

Millimetre-Wave Fibre-Wireless Technologies for 5G Mobile Fronthaul

Abayomi Temitope Latunde

*A thesis submitted to the University of Hertfordshire in partial
fulfilment of the requirements for the degree of Doctor of
Philosophy*

The programme of research was carried out in the Science and
Technology Research Institute (STRI),

Engineering and Technology,

University of Hertfordshire,

United Kingdom.

July 2018

Abstract

The unprecedented growth in mobile data traffic, driven primarily by bandwidth rich applications and high definition video is accelerating the development of fifth generation (5G) mobile network. As mobile access network evolves towards centralisation, mobile fronthaul (MFH) architecture becomes essential in providing high-capacity, ubiquitous and yet affordable services to subscribers. In order to meet the demand for high data rates in the access, Millimetre-wave (mmWave) has been highlighted as an essential technology in the development of 5G-new radio (5G-NR). In the present MFH architecture which is typically based on common public radio interface (CPRI) protocol, baseband signals are digitised before fibre transmission, featuring high overhead data and stringent synchronisation requirements. A direct application of mmWave 5G-NR to CPRI digital MFH, where signal bandwidth is expected to be up to 1GHz will be challenging, due to the increased complexity of the digitising interface and huge overhead data that will be required for such bandwidth. Alternatively, radio over fibre (RoF) technique can be employed in the transportation of mmWave wireless signals via the MFH link, thereby avoiding the expensive digitisation interface and excessive overhead associated with its implementation. Additionally, mmWave carrier can be realised with the aid of photonic components employed in the RoF link, further reducing the system complexity. However, noise and nonlinearities inherent to analog transmission presents implementation challenges, limiting the system dynamic range. Therefore, it is important to investigate the effects of these impairments in RoF based MFH architecture.

This thesis presents extensive research on the impact of noise and nonlinearities on 5G candidate waveforms, in mmWave 5G fibre-wireless MFH. Besides orthogonal frequency division multiplexing (OFDM), another radio access technology (RAT) that has received significant attention is filter bank multicarrier (FBMC), particularly due to its high spectral containment and excellent performance in asynchronous transmission. Hence, FBMC waveform is adopted in this work to study the impact of noise and nonlinearities on the mmWave fibre-wireless MFH architecture. Since OFDM is widely deployed and it has been adopted for 5G-NR, the performance of OFDM and FBMC based 5G mmWave RAT in fibre-wireless MFH architecture is compared for several implementations and transmission scenarios.

To this extent, an end-to-end transmission testbed is designed and implemented using industry standard VPI Transmission Maker® to investigate five mmWave upconversion techniques. Simulation results show that the impact of noise is higher in FBMC when the

signal-to-noise (SNR) is low, however, FBMC exhibits better performance compared to OFDM as the SNR improved. More importantly, an evaluation of the contribution of each noise component to the overall system SNR is carried out. It is observed in the investigation that noise contribution from the optical carriers employed in the heterodyne upconversion of intermediate frequency (IF) signals to mmWave frequency dominate the system noise. An adaptive modulation technique is employed to optimise the system throughput based on the received SNR. The throughput of FBMC based system reduced significantly compared to OFDM, due to laser phase noise and chromatic dispersion (CD). Additionally, it is shown that by employing frequency domain averaging technique to enhance the channel estimation (CE), the throughput of FBMC is significantly increased and consequently, a comparable performance is obtained for both waveforms.

Furthermore, several coexistence scenarios for multi-service transmission are studied, considering OFDM and FBMC based RATs to evaluate the impact inter-band interference (IBI), due to power amplifier (PA) nonlinearity on the system performance. The low out of band (OOB) emission in FBMC plays an important role in minimising IBI to adjacent services. Therefore, FBMC requires less guardband in coexistence with multiple services in 5G fibre-wireless MFH. Conversely, OFDM introduced significant OOB to adjacent services requiring large guardband in multi-service coexistence transmission scenario.

Finally, a novel transmission scheme is proposed and investigated to simultaneously generate multiple mmWave signals using laser heterodyning mmWave upconversion technique. With appropriate IF and optical frequency plan, several mmWave signals can be realised. Simulation results demonstrate successful simultaneous realisation of 28GHz, 38GHz, and 60GHz mmWave signals.

Acknowledgement

First of all, I will like to thank my supervisor Dr Pandelis Kourtessis, for allowing me to carry this research and his continuous support throughout the course of my study. I'm also privileged to have had Dr Milos Milosavljevic in my supervisory team, who constantly inspired and encouraged me to do more than just enough. I also want to thank Prof. John M. Senior for his advice every time we had team meetings.

Many thanks to my colleagues at D437 and D400 for their support, especially Matt Robinson for valuable discussions and ideas, and also for his help in times I had problems with my PC. I also want to specially thank my wife and daughter for their support, emotionally, psychologically and in prayers. You have been so wonderful, believing in me and always encouraging me. Whenever I get distracted or tired, Tolorunni says "*Daddy do your work*".

I will like to appreciate my sister for financial support since it all started; you sacrificed a lot for me to get here. My gratitude also goes to Mr Otunla for his financial support and helping with my scholarship.

I want to use this opportunity to thank the Niger Delta Scholarship scheme for sponsoring my research; I couldn't have done it without their financial support.

Above all, I give all glory to God Almighty for giving me the grace and strength to carry out this research, "*for by strength shall no man prevail*" (1 Sam: 2:9b)

Table of Content

Abstract.....	i
Acknowledgement.....	iii
Table of Content	iv
List of Figures	viii
List of Tables	xiii
Abbreviations	xiv
List of publications	xix
1. Towards High Capacity 5G Mobile Broadband Access Network	1
1.1. Introduction	1
1.2. State-of-the-Art 4G Mobile Broadband and Beyond	2
1.3. The IMT 2020 Requirements for 5G.....	2
1.3.1. Research Initiatives towards 5G.....	3
1.4. Research Motivation and Objectives	5
1.5. Research Contributions	6
1.6. Thesis Outline.....	7
2. Enabling Technologies for High-Capacity 5G Mobile Broadband Access.....	8
2.1. Introduction	8
2.2. Cloud Radio Access Network Architecture.....	8
2.3. Transport Technologies for Mobile Fronthaul.....	10
2.3.1. Radio over Fibre Technology	10
2.3.1.1. Digital Radio over Fibre	11
2.3.1.2. Analog Radio over Fibre	12
2.4. Millimetre-wave Technology.....	14
2.5. Photonics Techniques for Millimetre-wave Generation.....	17
2.5.1. Photonic-aided Millimetre-wave Generation using MZMs.....	17
2.5.2. Photonic-aided Millimetre-wave Generation using Lasers.....	21
2.5.3. Noise and Nonlinearities in Photonic-aided Millimetre-wave Signals.....	25

2.6.	Summary	26
3.	Design of Millimetre-Wave Fibre-Wireless Testbed for 5G Mobile Fronthaul	27
3.1.	Introduction	27
3.2.	The VPI Photonic Design Suite	27
3.2.1.	Simulation of ARoF in VPI.....	29
3.2.2.	MATLAB-VPI co-simulation Technique	31
3.3.	Self-Heterodyne Technique for Millimetre-wave Signal Downconversion	31
3.3.1.	System Model and Performance Analysis.....	33
3.4.	Filter Bank Multicarrier Systems Architecture.....	36
3.4.1.	Channel Estimation in FBMC	42
3.4.1.1.	Channel Estimation using Pairs of Pilots.....	43
3.4.1.2.	Channel Estimation using Interference Approximation	43
3.4.1.3.	Performance Evaluation of Preamble-based Channel Estimation for FBMC 44	
3.4.2.	Peak to Average Power Ratio in FBMC	45
3.5.	Summary	46
4.	Millimetre-wave Optical Transceivers for Next Generation Fibre-Wireless Architectures 48	
4.1.	Introduction	48
4.2.	Millimetre-Wave Upconversion Techniques for Fibre-Wireless 5G Mobile Fronthaul.....	48
4.2.1.	Millimetre-wave Upconversion using Electrical Local Oscillator.....	49
4.2.2.	Millimetre-wave Upconversion using MZM.....	58
4.2.3.	Millimetre-wave Upconversion using Laser heterodyning Technique	65
4.3.	Comparison of Millimetre-wave Techniques.....	70
4.4.	Summary	72
5.	Impact of Noise on Millimetre-Wave Signal Generated using Laser Heterodyning	73
5.1.	Introduction	73
5.2.	SNR of Millimetrewave IF over Fibre Signal Generated using Laser Heterodyning 73	

5.2.1.	Noise Generated in the Transmitter	74
5.2.1.1.	Relative Intensity Noise	74
5.2.1.2.	Laser Phase Noise	75
5.2.1.3.	Amplified Spontaneous Emission.....	78
5.2.2.	Noise Generated in the Receiver	79
5.2.2.1.	Thermal Noise	79
5.2.2.2.	Shot Noise	79
5.2.3.	SNR of the Millimetrewave Signal after O/E Conversion	80
5.3.	Noise Effects on Millimetre-wave IF over Fibre Signal based on uncorrelated Lasers	81
5.3.1.	Impact of RIN on the system performance	83
5.3.2.	Impact of ASE Noise.....	84
5.3.3.	Impact of CD-induced CPN.....	85
5.3.4.	Impact of Laser Linewidth	86
5.3.5.	Impact of Fibre Length	87
5.3.6.	Impact of Noise on IF Signal Bandwidth.....	89
5.4.	System Performance Optimisation based on the Received SNR and Frequency Domain Averaging	94
5.5.	Summary	100
6.	Nonlinear Impairments in Millimeter-Wave 5G Multi-Service over Fibre Systems.....	102
6.1.	Introduction	102
6.2.	Nonlinear Subcarrier Intermodulation in Multi-Service Systems	103
6.2.1.	Power Amplifier Modelling.....	103
6.3.	Impact of PA Nonlinearity in Millimetre-wave IF over Fibre Upconversion using Laser Heterodyning	105
6.3.1.	Scenario 1	107
6.3.2.	Scenario 2	109
6.3.3.	Scenario 3	110
6.3.4.	Scenario 4	111
6.4.	In-band Deployment of LTE Service in 5G Service	112

6.5.	Impact of PA Nonlinearity in Uplink Multi-User Access Systems	118
6.6.	Summary	119
7.	Coexistence of Multiple 5G Services in a Photonic Millimetre-wave Mobile Fronthaul	121
7.1.	Introduction	121
7.2.	Simultaneous Generation of Multiple Millimetre-wave Signals based on Optical Heterodyning	121
7.3.	Simulation Setup.....	124
7.3.1.	Performance Evaluation for 28GHz and 38GHz.....	127
7.3.2.	Performance Evaluation for 28GHz and 60GHz.....	130
7.3.3.	Performance Evaluation for 28GHz, 38GHz and 60GHz.....	133
7.4.	Summary	135
8.	Conclusion and Future Works	137
8.1.	Thesis Summary	137
8.2.	Future Works	140
	References	142

List of Figures

Figure 1.1: Cisco VNI Report for Global Mobile Data Traffic [1].....	1
Figure 1.2: High-Level Requirements for 5G	3
Figure 2.1: C-RAN Architecture.....	9
Figure 2.2: Radio-over-Fibre	11
Figure 2.3: Digital-over-Fibre (a) BB (b) IF (c) RF	12
Figure 2.4: Analog-over-Fibre (a) IF-over-Fibre (b) RF-over-Fibre.....	13
Figure 2.5: Atmospheric absorption at different frequency bands [39].....	15
Figure 2.6: Samsung end-to-end 5G FWA network [78].....	16
Figure 2.7: Schematic of DE-MZM (a) DE-MZM transfer function (b)	18
Figure 2.8: Optical signal after E/O at (a) Maximum point (b) Quadrature point (c) Null point	18
Figure 2.9: Cascaded MZM and phase modulator for frequency tripling [99].....	19
Figure 2.10: Cascaded DE-MZMs for frequency quadrupling [100]	20
Figure 2.11: Schematic of two stage upconversion to generate 8x the LO frequency [102].	20
Figure 2.12: The principle and schematic of the mmWave inter- and intra-RAT carrier aggregation in Het-Net based on optical band mapping [103]	21
Figure 2.13: Schematic of optical mmWave generation using gain-switched DFB laser [106]	22
Figure 2.14: Schematic of 60GHz RoF system based on PMLLD [107]	23
Figure 2.15: Different Schemes to generate mmWave carrier using unlocked LDs [110]	24
Figure 2.16: Principle of generation and transmission of 60GHz UWB Signal [111]	24
Figure 3.1: (a) Laser Bias current vs Output Power (b) and Bias current vs Linewidth	28
Figure 3.2: Bias current vs Laser RIN	28
Figure 3.3: OFDM Transceiver Design in VPI (a) Transmitter (b) Receiver	29
Figure 3.4: ARoF Simulation Schematic.....	29
Figure 3.5: Received constellation at (a) 0km (b) 25km (c) 50km (d) 100km	30
Figure 3.6: MATLAB VPI co-simulation Structure.....	31
Figure 3.7: Proposed network architecture.....	32
Figure 3.8: Simulation setup of the proposed architecture.....	33
Figure 3.9: Effect of Laser linewidths for BTB	35
Figure 3.10: BER vs Received Power at PD for BTB, 20km and 40km Fibre	36
Figure 3.11: (a) FBMC baseband transceiver (b) OFDM baseband transceiver	38
Figure 3.12: Frequency Time phase space lattice of the FBMC system	38
Figure 3.13: (a) OQAM-Pre-processing and SFB (b) AFB and OQAM Post-processing	39

Figure 3.14: Magnitude response of the prototype filter for $K = 1:4$	40
Figure 3.15: Preamble Structures for FBMC (a) POP (b) IAMR (c) IAMC	43
Figure 3.16: BER of FBMC for different preamble-based CE methods	45
Figure 3.17: Simulated PAPR for FBMC, FBMC with 25% clipping and OFDM	46
Figure 4.1: Schematic of mmWave RoF (a) Electrical spectrum after upconversion to 28GHz (b) Optical spectrum after E/O showing OSSB modulation (c) Electrical spectrum after downconversion to baseband.....	50
Figure 4.2: EVM vs RF drive power for mmWave RFoF using electrical LO (a) OFDM (b) FBMC	53
Figure 4.3: EVM vs Received Power for mmWave RFoF using electrical LO (a) OFDM BTB (b) FBMC BTB (c) OFDM 20km (d) FBMC 20km	54
Figure 4.4: mmWave IF-over-Fibre using electrical LO. (a) Optical spectrum after E/O showing OSSB modulation (b) Electrical spectrum after upconversion to 28GHz (c) Electrical spectrum after downconversion to baseband	56
Figure 4.5: EVM vs IF drive power for mmWave IFoF using electrical LO (a) OFDM (b) FBMC	57
Figure 4.6: EVM vs Received optical power for mmWave IFoF using electrical LO (a) OFDM BTB (b) FBMC BTB (c) OFDM 20km (d) FBMC 20km.....	58
Figure 4.7: mmWave IFoF using cascaded MZMs (a) Optical spectrum after second MZM (b) The spectrum of IF OFDM after downconversion (c) The spectrum of IF FBMC after downconversion.....	59
Figure 4.8: EVM vs IF drive power for mmWave IFoF using cascaded MZMs (a) OFDM (b) FBMC	61
Figure 4.9: EVM vs Received optical power for mmWave IFoF using cascaded MZMs (a) OFDM BTB (b) FBMC BTB (c) OFDM 20km (d) FBMC 20km	62
Figure 4.10: mmWave IFoF using DML and MZM (a) Optical spectrum after the MZM (b) The spectrum of IF OFDM after downconversion (c) The spectrum of IF FBMC after downconversion.....	63
Figure 4.11: EVM vs IF drive power for mmWave IFoF using DML and MZM (a) OFDM (b) FBMC	64
Figure 4.12: EVM vs Received optical power for mmWave IFoF using DML and MZM (a) OFDM BTB (b) FBMC BTB (c) OFDM 20km (d) FBMC 20km	64
Figure 4.13: mmWave IFoF using Laser Heterodyning (a) Optical spectrum after the optical coupler (b) The spectrum of IF OFDM after downconversion (c) The spectrum of IF FBMC after downconversion.....	66
Figure 4.14: EVM vs IF drive power for mmWave IFoF using laser heterodyning (a) OFDM (b) FBMC	68

Figure 4.15: EVM vs Received optical power for mmWave IFoF using laser heterodyning (a) OFDM BTB (b) FBMC BTB (c) OFDM 20km (d) FBMC 20km	69
Figure 5.1: Noise Source in mmWave System using laser heterodyning.....	74
Figure 5.2: Simulation Setup.....	81
Figure 5.3: DSP Transceiver design for the IF Signals: (a) FBMC (b) OFDM	82
Figure 5.4: Received SNR vs RIN for OFDM and FBMC.....	84
Figure 5.5: SNR degradation due to ASE.....	85
Figure 5.6: SNR degradation due to CPN	86
Figure 5.7: SNR degradation due to laser linewidth	87
Figure 5.8: SNR degradation due to fibre length	88
Figure 5.9: EVM vs Subcarrier Number after 40km fibre	89
Figure 5.10: EVM vs Subcarrier Number after 100km fibre	90
Figure 5.11: EVM vs IF bandwidth after 40km fibre.....	91
Figure 5.12: Received constellation after 40km fibre and 2MHz linewidth for 2nd, 64th and 128th subcarriers after equalisation in 2GHz (a) OFDM (b) FBMC.....	92
Figure 5.13 EVM vs IF Bandwidth for 100km fibre	93
Figure 5.14: Subcarrier SNR for 10.1MHz Laser Configuration and 2GHz IF bandwidth (a) 40km (b) 100km.....	93
Figure 5.15: Schematic of transmission channel with CSI feedback for adaptive modulation	94
Figure 5.16: ISFA averaging window for 2GHz OFDM and FBMC after 40km.....	95
Figure 5.17: Bit-loading profiles for 2MHz laser and 2GHz bandwidth after 40km (a) OFDM (b) FBMC	96
Figure 5.18: Received constellation after adaptive modulation with ISFA for 2MHz linewidth after 40km fibre (a)-(c) OFDM: 2-bits, 4-bits and 6-bits (d)-(f) FBMC: 2-bits, 4-bits and 6-bits	97
Figure 5.19: Bit-loading profiles for 10.1MHz linewidth and 2GHz bandwidth after 40km (a) OFDM (b) FBMC.....	97
Figure 5.20: Received constellation after adaptive modulation with ISFA for 10MHz linewidth after 40km fibre (a)-(c) OFDM: 2-bits, 4-bits and 6-bits (d)-(f) FBMC: 2-bits, 4-bits and 6-bits	98
Figure 5.21: ISFA averaging window for 1GHz OFDM and FBMC after 100km.....	98
Figure 5.22: Bit-loading profiles for 10.1MHz laser and 1GHz bandwidth after 100km (a) OFDM (b) FBMC.....	99
Figure 5.23: Received constellation after adaptive modulation with ISFA for 10MHz laser and 100km fibre (a)-(b) OFDM: 2-bits and 4-bits (c)-(d) FBMC: 2-bits and 4-bits	100
Figure 6.1: PA nonlinearity modelling in VPI	104

Figure 6.2: AM/AM conversion of the PA.....	104
Figure 6.3: Frequency-domain response of nonlinear PA with two-tone excitation.....	105
Figure 6.4: Simulation setup for the multi-service over fibre with remote mmWave upconversion	106
Figure 6.5: (a) EVM as a function PA input power for OFDM and FBMC (b) PSDs of FBMC and OFDM at input and output of the PA at points (i) to (iv) (i.e. -50dBm, -30dBm, -15dBm and -5dBm) and corresponding constellations	108
Figure 6.6: EVM as a function of input power of service 1.....	109
Figure 6.7: EVM as a function of input power of service 1.....	110
Figure 6.8: Coexistence of FBMC and OFDM in multi-service transmission scenario.....	111
Figure 6.9: EVM as a function nulled subcarriers on either side of the LTE-like signal (a) FBMC (b) OFDM.....	113
Figure 6.10: PSD of the integrated service (a) FBMC with the LTE zoomed out shown in the inset (b) OFDM with the LTE zoomed out shown in the inset	113
Figure 6.11: PSD of the Integrated Service before and after the notch filter (a) FBMC (b) OFDM	114
Figure 6.12: EVM as a function power difference between service 1 (FBMC and OFDM) and LTE signal as input power of LTE signal increased from -60dBm to -40dBm and the input of Service is fixed at -50dBm.....	114
Figure 6.13: EVM as a function power difference between service 1 (FBMC and OFDM) and LTE signal as input power of service 1 increased from -50dBm to -30dBm and the input of LTE is fixed at -50dBm.....	115
Figure 6.14: EVM as a function of received power for FBMC and OFDM with and without in-band LTE	116
Figure 6.15: Constellation at +1dBm received power (a) FBMC /w LTE (b) OFDM /w LTE (c) FBMC w/o LTE (d) OFDM w/o LTE	117
Figure 6.16: EVM of LTE integrated with FBMC and OFDM as a function of received power	117
Figure 6.17: EVM as a function of PA Input power for DFT-s-FBMC and DFT-s-OFDM uplink signals	118
Figure 7.1: The proposed concept of multi-service and multi-operator coexistence in a shared MFH infrastructure	122
Figure 7.2: Frequency Plan and Multiplexing of multiple services coexistence in a shared MFH infrastructure (a) WDM Multiplexer and Demultiplexer (b) 25GHz DWDM grid (c) 50GHz DWDM grid (d) Nx1 Port WSS	123
Figure 7.3: Schematic for the simultaneous generation of multiple mmWave signals using one optical LO.....	125

Figure 7.4: Spectrums (a) Optical spectrum before the PD (b) Electrical spectrum after the PD showing 28GHz and 38GHz (c) 28GHz Electrical spectrum (d) 38GHz Electrical spectrum.....	128
Figure 7.5: EVM as a function of received power using 200kHz combined laser linewidth (a) 28GHz OFDM and FBMC (b) 38GHz OFDM and FBMC (c) Constellation for 28GHz OFDM and FBMC at -7dBm received power (d) Constellation for 38GHz OFDM and FBMC at -7dBm received power	129
Figure 7.6: EVM as a function of received power using 2MHz combined laser linewidth (a) 28GHz OFDM and FBMC (b) 38GHz OFDM and FBMC (c) Constellation for 28GHz OFDM and FBMC at -7dBm received power (d) Constellation for 38GHz OFDM and FBMC at -7dBm received power	130
Figure 7.7: Spectrums at (a) Optical spectrum before the PD (b) Electrical spectrum after the PD showing 28GHz and 60GHz (c) 28GHz Electrical spectrum (d) 60GHz Electrical spectrum.....	131
Figure 7.8: EVM as a function of received power using 200kHz combined laser linewidth (a) 28GHz OFDM and FBMC (b) 60GHz OFDM and FBMC (c) Constellation for 28GHz OFDM and FBMC at -7dBm received power (d) Constellation for 60GHz OFDM and FBMC at -7dBm received power	132
Figure 7.9: EVM as a function of received power 2MHz combined laser linewidth (a) 28GHz OFDM and FBMC (b) 60GHz OFDM and FBMC (c) Constellation for 28GHz OFDM and FBMC at -7dBm received power (d) Constellation for 60GHz OFDM and FBMC at -7dBm received power.....	133
Figure 7.10: (a) EVM as a function of received power for 28GHz OFDM, 38GHz OFDM and 60GHz FBMC (b) constellations at -7dBm received power with and without ISFA using UL laser as LO	134
Figure 7.11: (a) EVM as a function of received power for 28GHz OFDM, 38GHz OFDM and 60GHz FBMC (b) constellations at -7dBm received power with and without ISFA using remotely delivered LO	135

List of Tables

Table 2-1: The frequency above 6GHz for future development of IMT 2020	16
Table 3-1: Simulation Parameters	30
Table 3-2: List of frequency coefficients for half Nyquist filter	37
Table 4-1: System parameters used in the simulation	52
Table 4-2: Performance Comparison of the investigated mmWave upconversion Techniques	71
Table 5-1: Source and type of noise generated by components	74
Table 5-2: Laser Configuration and Linewidth	86
Table 6-1: Scenarios used to investigate PA-induced IBI in multi-service mmWave MFH .	106
Table 6-2: System parameters used in the simulation	107
Table 7-1 System parameters used in the simulation	127

Abbreviations

3GPP	Third Generation Partnership Project
4G	Fourth Generation
5G	Fifth Generation
5GPP	Fifth Generation Partnership Project
5G-NR	5G-New Radio
ADC	Analog-to-Digital Converter
AFB	Analysis Filter Bank
AM/AM	Amplitude Modulation/Amplitude Modulation
AON	Active Optical Network
AWGN	Additive White Gaussian Noise
AR	Augmented Reality
ARoF	Analog Radio over Fibre
ASE	Amplified Spontaneous Emission
BB	Baseband
BBU	Baseband Unit
BER	Bit Error Rate
BPF	Bandpass Filter
BS	Base Station
BTB	Back-to-Back
BPSK	Binary Phase Shift Keying
BW	Bandwidth
BWA	Broadband Wireless Access
CA	Carrier Aggregation
CAGR	Compound Annual Growth Rate
CAPEX	Capital Expenditure
CC	Component Carrier
CD	Chromatic Dispersion
CCDF	Cumulative Complementary Distribution Function
CE	Channel Estimation
CFO	Carrier Frequency Offset
CFR	Channel Frequency Response
CMOS	Complementary Metal Oxide Semiconductor
CO	Central Office
CoMP	Cooperative Multipoint
CP	Cyclic Prefix

CPE	Customer Premises Equipment
CPN	Converted Phase Noise
CPRI	Common Public Radio Interface
C-RAN	Centralised Radio Access Networks
CSI	Channel State Indicator
CW	Continuous Wave
DAC	Digital-to-Analog Converter
DAS	Distributed Antenna System
DC	Direct Current
DE-MZM	Dual Electrode Mach Zehnder Modulator
DFB	Distributed Feedback
DFT	Discrete Fourier Transform
DL	Downlink
DML	Direct Modulated Laser
DPD	Digital Predistortion
DSB	Double Sideband
DSB-SC	Double Sideband-Suppressed Carrier
DSP	Digital Signal Processing
DU	Digital Unit
ECL	External Cavity Laser
ED	Envelope Detector
EDFA	Erbium Doped Fibre Amplifier
eMBB	Enhanced Mobile Broadband
EML	External Modulated Laser
E/O	Electrical-to-Optical
EVM	Error Vector Magnitude
FBMC	Filter Bank Multicarrier
FFT	Fast Fourier Transform
FT	Frequency-Time
FIR	Finite Impulse Response
FSPL	Free Space Path Loss
FWM	Four Wave Mixing
GFDM	Generalised Frequency Division Multiplexing
HetNets	Heterogeneous Networks
HPA	High Power Amplifier
HS	Hermitian Symmetry
HT	Hilbert Transform

IAM	Interference Approximation Method
IAM-R	Interference Approximation Method Real
IBBI	Inter-band Beating Interference
IBI	Interband Beat Interference
ICI	Intercarrier Interference
IEEE	Institute of Electrical and Electronic Engineering
IF	Intermediate Frequency
IFFT	Inverse Fourier Transform
IM-DD	Intensity Modulation-Direct Detection
IMD3	Intermodulation Distortion-3
IMI	Imaginary Interference
IMT-Adv.	International Mobile Telecommunications Advanced
IoT	Internet of Things
IQ	Inphase/Quadrature
ISFA	Intra-Symbol Frequency Domain Averaging
ISI	Inter-Symbol Interference
ITU	International Telecommunication Union
ITU-T	International Telecommunication Union Telecommunication
KPI	Key Performance Index
LD	Laser Diode
LNA	Low Noise Amplifier
LO	Local Oscillator
LTE	Long Term Evolution
LTE-A.	Long Term Evolution Advanced
LPF	Lowpass Filter
MBH	Mobile Backhaul
MFH	Mobile Fronthaul
ML	Modulated Laser
mMTC	Massive Machine Type Communications
mmWave	Millimetre-Waves
MIMO	Multiple In Multiple Out
MNO	Mobile Network Operators
MP	Maximum Point
NB-IoT	Narrowband-IoT
NF	Noise Figure
NG-PON	Next Generation Passive Optical Network
NLOS	Non-Line of Sight

NP	Null Point
O/E	Optical-to-Electrical
OBPF	Optical Bandpass Filter
OBSAI	Open Base Station Interface
OC	Optical Coupler
OCS	Optical Carrier Suppression
ODN	Optical Distribution Network
O/E	Optical-to-Electrical
OFM	Optical Frequency Multiplication
OFDM	Orthogonal Frequency Division Multiplexing
OFDMA	Orthogonal Frequency Division Multiple Access
OOB	Out-of-Band
OOK	On-Off Keying
QAM OFDM	Offset-QAM OFDM
OPEX	Operation Expenditure
OPLL	Optical Phase Lock Loop
ORI	Open Radio Interface
OSSB	Optical Single Sideband
PA	Power Amplifier
PAPR	Peak to Average Power Ratio
PD	Photodiode
PDC	Photonic Down Conversion
PDS	Photonic Design Suite
PHY	Physical Layer
PHYDYAS	Physical Layer For Dynamic Spectrum Access And Cognitive Radio
PM	Phase Modulator
PMLLD	Passive Mode-Locked Laser Diode
PON	Passive Optical Networks
POP	Pair of Pilots
PPL	Phase Locked Loop
PPN	Polyphase Network
PRT	Phase Rotation Term
P/S	Parallel-to-Serial
PSD	Power Spectrum Density
PTS	Partial Transmission Sequence
QAM	Quadrature Amplitude Modulator
QP	Quadrature Point

QPSK	Quadrature Phase Shift Keying
RAN	Radio Access Network
RAU	Radio Access Unit
RAT	Radio Access Technology
RC-SH	Receiver Carrier-Self Heterodyne
RF	Radio Frequency
RIN	Relative Intensity Noise
RoF	Radio over Fibre
RRH	Remote Radio Head
RU	Radio Unit
SC-FDMA	Single Carrier Frequency Division Multiple Access
SCM	Subcarrier Multiplexing
SE	Spectral Efficiency
SEL	Soft Envelope Limiter
SFB	Synthesis Filter Bank
SFDR	Spurious Free Dynamic Range
SLM	Selective Mapping
SMT	Staggered Multitone
SNR	Signal-to-Noise Ratio
SSBI	Signal Signal Beat Interference
SSMF	Standard Single Mode Fibre
SMP	Self-Phase Modulation
S/P	Serial-to-Parallel
TLD	Tunable Laser Diode
UE	User Equipment
UFMC	Universal Filtered Multicarrier
UHD	Ultra-High Definition
UL	Uplink
URLLC	Ultra Reliable Low Latency Communications
UWB	Ultra-Wide Band
VR	Virtual Reality
VPI	Virtual Photonics
WiMAX	Worldwide Interoperability for Microwave Access
WSS	Wavelength Selective Switch
XPM	Cross Phase Modulation
ZF	Zero Forcing

List of publications

Abayomi T. Latunde, Anastasios Papazafeiropoulos, Pandelis. Kourtessis, and John M. Senior, **"Co-existence of OFDM and FBMC in Resilient Photonic Millimeter-wave 5G Mobile Fronthaul,"** Photonic Network Communications (PNET) Journal 2019. (Accepted)

DOI: 10.1007/s11107-019-00845-z

(Invited) Abayomi T. Latunde, M. Milosavljevic, P. Kourtessis, and J. M. Senior, **"OQAM-OFDM RoF with IM-DD Remote Heterodyne 28GHz Upconversion for 5G Millimeter RANs,"** in 2016 18th International Conference on Transparent Optical Networks (ICTON) 2016, pp. 1-4.

1. Towards High Capacity 5G Mobile Broadband Access Network

1.1. Introduction

The proliferation of Internet-enabled mobile devices consuming a large amount of data and emerging applications such as ultra high-definition (UHD) video, augmented reality (AR), virtual reality (VR), online gaming as well as the Internet of things (IoT), are driving the explosive growth of mobile data traffic. According to Cisco virtual network index (VNI) report, the global mobile data traffic is expected to grow at a 47% CAGR (see Figure 1.1), reaching 49 exabytes per month by 2021 [1].

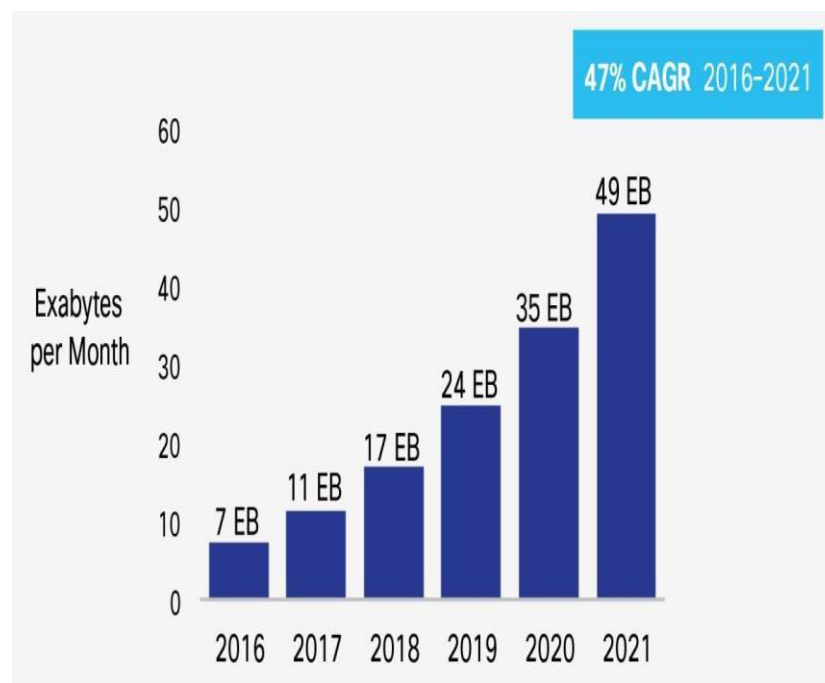


Figure 1.1: Cisco VNI Report for Global Mobile Data Traffic [1]

These smart devices accounted for 89% of mobile data traffic in 2017, of which 60% was video traffic. It has been forecasted that more than 75% of the world's mobile traffic will be video by 2021 [1]. As this trend continues, one direct consequence is that the last-mile access networks become a bottleneck of user bandwidth. Therefore, the wireless communication infrastructure that connects these devices must evolve to support this ever-increasing demand [2]. Currently, the dominant broadband wireless access (BWA) standards are Long Term Evolution (LTE), Worldwide Interoperability for Microwave Access (WiMAX) and Wi-Fi. The 4th generation (4G) mobile broadband primarily based on LTE represents the largest share of mobile data traffic by network type.

1.2. State-of-the-Art 4G Mobile Broadband and Beyond

The LTE mobile broadband since its standardisation by the Third Generation Partnership Project (3GPP) has been widely deployed by most service providers around the world. The introduction of LTE marked a paradigm shift in mobile broadband with the adoption of orthogonal frequency division multiple access (OFDMA) and single carrier frequency division multiplexing access (SC-FDMA), which are based on orthogonal frequency division multiplexing (OFDM) as the downlink (DL) and uplink (UL) access technology [3]. Techniques such as higher order modulation as well as multiple input multiple output (MIMO) spatial multiplexing are employed to improve spectral efficiency (SE) and increase network capacity. The peak throughput of LTE is 300Mbps and 75Mbps in DL and UL, respectively. In order to meet the International Telecommunication Union (ITU) recommendations for 4G mobile communications as defined in the International Mobile Telecommunication-Advanced (IMT-Advanced), LTE-Advanced (LTE-A) was specified in Rel. 10 by the 3GPP [4]. As an enhancement to LTE specified in Rel. 8, LTE-A was envisioned to provide a much higher peak data rate of up to 1Gbps and 500Mbps in the DL and UL, respectively [5]. The main feature of LTE-A is that it allows the combination of up to 5 component carriers (CCs) in a technique referred to as carrier-aggregation (CA). Therefore, a maximum of 100MHz can be realised by CA using five 20MHz LTE channels. CA can be achieved within the same band using a contiguous or non-contiguous stream of channels or between channels from two different bands. In addition, new techniques such as coordinated multipoint (CoMP) and higher order MIMO was introduced to improve SE and throughput. While LTE can support 4x4 MIMO configurations, LTE-A has the capability for 8x8 MIMO. Furthermore, LTE-A supports heterogeneous networks (HetNets) with coexisting Macro, Micro and Pico cells in the same infrastructure. Recently, LTE-A Pro was ratified by the 3GPP in Rel. 13 [6], to support the ever-growing demand for wireless resources as well as the emerging new class of services requiring more flexible network planning. An example of such service is the narrowband IoT (NB-IoT). The main feature in LTE-A Pro is the exploitation of unlicensed 5GHz band, which enables the support for up to 32 CCs in CA as well as higher order modulation (i.e. 256QAM) [6]. Evidently, more bandwidth is required in order to provide ubiquitous and high capacity services that meet mobile users' growing demand.

1.3. The IMT 2020 Requirements for 5G

The IMT 2020 key performance indicators (KPIs) outlined by the ITU is shown in Figure 1.2. The three main application scenarios are defined, namely, enhanced mobile broadband (eMBB), massive machine type communication (mMTC) and ultra-reliable low-latency communication (URLLC). As shown in Figure 1.2, the eMBB is of high importance and the

use case envisions a peak data rate of 20Gbps and 10Gbps in DL and UL, assuming all resources are utilised. Also, a minimum of 100Mbps user experienced data rate is expected, which is 100 times improvement over the cell edge data rate of 4G networks. These KPIs are important in meeting the explosive demand for high data rates anticipated in the 5th generation (5G) mobile network.

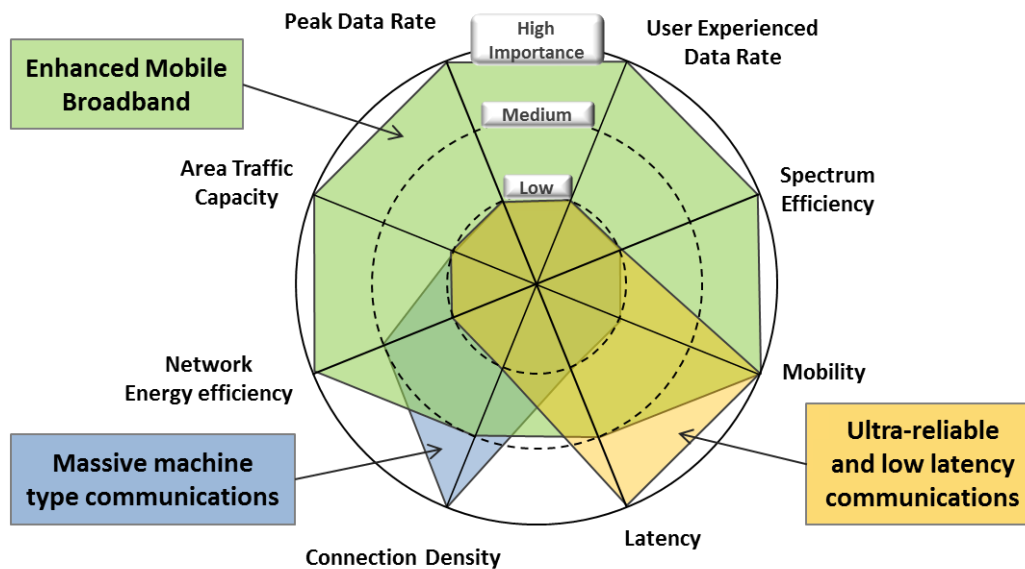


Figure 1.2: High-Level Requirements for 5G

1.3.1. Research Initiatives towards 5G

In recent years, several research initiatives involving equipment manufacturers, mobile network operators (MNOs) as well as the academic community have emerged, working towards the future 5G networks. Many of these consortia have been researching probable standardisation aspects of 5G, mainly focusing on two key areas that impact the eMBB use case, namely network architecture and air interface design. The projects are largely funded by the European Commission under the Seventh Framework Program for research and developments (FP7), Horizon 2020 program and the 5G Infrastructure Public-Private Partnership (5G-PPP). A few examples are Mobile and Wireless Communications Enablers for the Twenty-twenty Information Society (METIS) [7], 5th Generation Non-Orthogonal Waveforms for Asynchronous Signalling (5GNOW) [8], Millimetre-Wave Evolution for Backhaul and Access (MiWEBA) [9], Beyond 2020 heterogeneous Wireless Networks with Millimetre-Wave Small Cell Access and Backhauling (MiWaveS) [10], mm-Wave based Radio Access Network for 5G Integrated Communications (mmMAGIC) [11], 5G Crosshaul (XHaul) [12], and 5G Communication with Heterogeneous, Agile Mobile network in the PyeongChang winter Olympic competition (5G CHAMPION) [13]. A summary of the objectives of each of the above-mentioned projects are listed below:

- ❖ **METIS I&II:** METIS was the flagship EU project setup to provide valuable contributions to 5G pre-standardisation processes by developing a concept for the future mobile and wireless communication system. Spectrum management, air interface design and coexistence between legacy and new air interface were investigated. In terms of air interface design, METIS showed that Filter-Bank Multicarrier (FBMC) waveform can be a successful enabler for flexible air interface design.
- ❖ **5GNOW:** Flexible and unified frame structure was the main objective of the 5GNOW project. Flexible non-orthogonal waveforms were proposed that can support the IMT 2020 use cases (eMBB, mMTC and URLLC). The waveforms developed within the 5NOW project are the Universal Filtered Multi-Carrier (UFMC) and Generalised Frequency Division Multiplexing (GFDM).
- ❖ **MiWEBA:** The concept of HetNets, in which mmWave small cells are overlaid on larger macro cells was investigated within the MiWEBA project. MiWEBA also proposed a split between the control and data plane in order to overcome restricted coverage problem and reduce signalling overhead to the mmWave small cells.
- ❖ **MiWaveS:** The development of network function algorithms, radio and antenna technologies as well as the investigation of integrated small cell networks were the main objectives of the MiWaveS project.
- ❖ **mmMAGIC:** The suitability of a wide range of frequencies between 6GHz and 100GHz for 5G was the main objective of the mmMAGIC project. The mmMAGIC project investigated and developed robust channel models as well as transmission impairments (e.g. phase noise) characterisation at mmWave frequencies.
- ❖ **5G-Crosshaul:** The 5G-Crosshaul project aimed at developing a 5G integrated backhaul and fronthaul transport network enabling a flexible and software-defined reconfiguration of all networking elements in a multi-tenant and service-oriented unified management environment. The 5G-Crosshaul transport network proposed within the project is envisioned to consist of high-capacity switches and heterogeneous transmission links (e.g., fibre or wireless optics, high-capacity copper, mmWave) interconnecting remote radio heads (RRHs), 5GPoAs (e.g., macro and small cells), cloud-processing units (mini data centres), and points-of-presence of the core networks of one or multiple service providers.
- ❖ **5G CHAMPION:** The main objective of the 5G CHAMPION project was to demonstrate a proof-of-concept (PoC) 5G technology at the 2018 PyeongChang winter Olympics games. The PoC comprises of two interconnected 5G networks (one developed in South Korea and the other in Europe) operating in different frequency bands, using different air interface as well as core network specifications. Two use

cases: (i) short latency applications, (ii) broadband applications with stationary, high and ultra-high mobility. The 28GHz mmWave link was used as the backhaul for the radio access technology (RAT) hot-spot.

In order to fast track 5G developments, the 3GPP decided that the 5G-new radio (5G-NR) eMBB reuse the LTE core network and control plane [14]. A phased approach is considered in the standardisation of 5G-NR. Phase 1 will appear in the Rel.15 while phase 2 is expected to be captured in Rel.16 [15]. The key features addressed in phase 1 are carrier frequency, channel bandwidth, channel coding and spectrum occupancy. In terms of channel bandwidth, a maximum of 100MHz bandwidth can be supported for carrier frequencies below 6GHz, while up to 1GHz is supported for frequencies above 6GHz [15].

1.4. Research Motivation and Objectives

Several use cases are envisioned for 5G eMBB in order to meet the goal of providing pervasive Internet services to mobile users. As mentioned previously, network architecture and air interface design are key areas in the development of 5G. The integration of mmWave small cells into the centralised (or cloud) radio access network (C-RAN) will enable the design of robust mobile fronthaul (MFH) architecture, capable of addressing high-capacity data rate requirements. Due to the relatively short propagation distance at mmWave and the reduced coverage area of small cells, high-density deployment is necessary, which may be challenging with the present MFH architecture. Radio-over-Fibre (RoF) technology has long been deployed to extend the range and distribute radio signals in distributed antenna systems (DAS) and it is expected to play an important role in the next generation 5G access systems. Therefore, it will be interesting to explore fibre-wireless technologies that will enable mmWave small cells to be seamlessly integrated into future radio access networks (RANs).

The main objective of this research is to study enabling fibre-wireless technologies for cost-efficient, flexible and scalable deployment of integrated mmWave small cell in 5G RANs. Several impairments associated with the generation and transmission of mmWave signals in analog MFH is investigated. A simple frequency domain averaging technique is implemented to enhance the channel estimation (CE) process, in order to mitigate the effect of transmission impairments on the system performance. Furthermore, the impact of inter-RAT interference due to power amplifier (PA) nonlinearity is investigated with regards to the coexistence of multiple RATs over a single MFH architecture. Finally, a technique for flexible realisation of multiple mmWave signals in a multi-RAT scenario is proposed and investigated.

1.5. Research Contributions

The major contributions of this thesis are highlighted as follows:

- Carried out a comprehensive analysis of 5 mmWave upconversion techniques with respect to the impact of electrical-to-optical (E/O) and optical-to-electrical (O/E) interfaces on 5G candidate waveforms. In each of the techniques, OFDM and FBMC waveforms were employed for the investigation. The techniques were compared in terms of transmission performance, complexity and cost-efficiency in the application to dense deployment of mmWave small cells for 5G MFH.
- Derived an expression for the global signal-to-noise ratio (SNR) of the mmWave signal generated using laser heterodyning upconversion technique. Carried out an extensive study of the impact of various noise sources that limit the system performance. Although the total noise in the system is a combination of several noise sources, it was found that the system performance can be dominated by relative intensity noise (RIN) thereby masking other noise sources. However, for low RIN lasers, a combination of laser phase noise and fibre chromatic dispersion (CD) limits the system performance.
- Since the transmission impairments are inherent to the employed architecture, a link adaption technique was proposed and demonstrated by exploiting the channel state information (CSI) feedback from the user equipment (UE) to improve the system throughput based on the SNR. To further improve the system throughput, a frequency domain averaging algorithm was proposed and implemented to enhance the equalisation process at the UE. Results showed significant improvement in the system throughput compared to link adaption without frequency domain averaging technique.
- Carried out an extensive investigation of the inter-RAT interference in mmWave small cell deployment due to power PA nonlinearity in the coexistence of multiple 5G services employing OFDM and FBMC waveforms as well as legacy service such as LTE. Results showed that FBMC can successfully coexist with OFDM based services with the PA operating in the linear regime. On the other hand, OFDM based service contributes significant out-of-band (OOB) interference to adjacent services, even when the PA was operated in the linear regime.
- Proposed a novel scheme to generate multiple mmWave signals based on optical heterodyning in multi-RAT/ heterogeneous small cell MFH. The proposed technique can flexibly generate different mmWave signals by simply adjusting the centre emission wavelength of the heterodyning lasers. The 28GHz, 38GHz and 60GHz

were generated and successfully received by the UE after 40km fibre and 2m wireless transmission.

1.6. Thesis Outline

In chapter 2, enabling technologies for next-generation fibre-wireless MFH systems are discussed. In addition, some techniques that have been proposed in the literature to generate mmWave carrier with the aid of electrical and photonic components are also reviewed. In chapter 3, the industry standard VPI Transmission Maker® simulation platform used in this thesis is introduced and the integration with MATLAB in a cosimulation technique is discussed. The self-heterodyne detection technique is investigated for 28GHz offset-QAM OFDM generated using laser heterodyning. Additionally, FBMC system architecture and several preamble-based CE techniques that have been proposed for FBMC are reviewed. Finally, peak to average power ratio (PAPR) is briefly discussed and the effect of clipping technique in reducing PAPR is investigated in FBMC. In chapter 4, five mmWave upconversion techniques are investigated in terms of the complexity, scalability and impact of E/O and O/E conversion on the transmitted signal. Several noise sources in laser heterodyning architecture and their impact on the overall system SNR are studied in chapter 5. Link adaptation based on the received SNR is used to implement adaptive modulation so as to optimise the system throughput. A frequency domain averaging technique is employed to enhance CE in order to improve the equalisation process. Chapter 6 studies the impact of PA nonlinearity considering several multi-service /multi-RAT deployment scenarios in both DL and UL, respectively. A novel scheme is proposed in chapter 7 to flexibly generate multiple mmWave signals employing laser heterodyning. Finally, a summary of the work carried out in this thesis as well as suggestions for possible future research directions are presented in chapter 8.

2. Enabling Technologies for High-Capacity 5G Mobile Broadband Access

2.1. Introduction

In order to provide high-capacity, ubiquitous services in 5G, it is important that existing system architecture for radio access evolves to accommodate the ever-increasing demand for high-speed broadband access [2, 16]. With the emergence of new radio technologies, the cellular networks are moving away from the traditional Macro cell with tower mounted base stations (BSs) towards multi-tier HetNets, enabling the deployment of densely spaced small cells BSs [17, 18]. This deployment scenario is anticipated to include the integration of novel enabling technologies such as mmWave and massive MIMO to enhance capacity and offer improved SE to service subscribers. It is therefore important to ensure the future RAN architecture effectively support the integration of such technologies. The C-RAN architecture has been proposed to that effect [19, 20]. Also, evolving from this paradigm shift in RAN architecture is the concept of fronthauling. Specifically, MFH using optical access has been discussed as a key enabler for the deployment of a large number of small cell BSs in 5G access networks [21-24].

This chapter discusses potential technologies for next generation fibre-wireless MFH as well as the challenges of integrating high capacity mmWave small cells into 5G C-RAN architecture. Finally, several techniques that have been reported in the literature as a means to cost-effectively generate mmWave carrier for 5G wireless signals are discussed.

2.2. Cloud Radio Access Network Architecture

In conventional macro BSs, the two main functional units, namely baseband unit (BBU) or digital unit (DU) and radio unit (RU) also called radio element (RE) are located at the base of a tower or in a cabinet at close proximity (i.e. few metres). Functions such as baseband signal processing, radio network controller, management and control of BS are performed in the DU, while digital-to-analog/analog-to-digital (DAC/ADC), radio upconversion, filtering and amplification are performed in the RU. The RUs are connected to the antennas on top of the cell tower by bulky coaxial cables, via an interface known as X2. These configurations present some disadvantages such as transmit power loss in the cable and large equipment footprint [25]. Therefore, the conventional macro BS is physically separated into BBU and RRHs in distributed RAN architecture, where the RRHs are mounted on the cell tower close to the antennas and they require short coaxial jumper cables to connect them to the antennas. The connection between the BBU and RRHs is primarily an optical fibre, which

presents low loss and high bandwidth. This distributed RAN architecture has been deployed for high-capacity broadband access in LTE and 4G networks.

Evolving from the distributed RAN architecture is the concept of C-RAN, which is to pool several BBUs in a centralised location (i.e. Cloud) or BBU hotelling [26-28]. In C-RAN, the BBUs are co-located in the central office (CO) and several RRHs are connected to the CO via optical fibre link [27]. Figure 2.1 shows the C-RAN network architecture, consisting of Mobile Backhaul (MBH) link from the core network to the BBUs and MFH which connects the BBUs to the RRHs. In terms of management, the total cost of ownership (TCO) which includes capital expenditure (CAPEX) and operating expenditure (OPEX) is greatly reduced as several BBUs can share resources such as cooling and power [28]. In addition, C-RAN architecture enables flexibility and enhanced scalability, thus accelerating network integration. Moreover, advanced wireless network functionalities such as CoMP and enhanced Inter-cell Interference (eICIC) can be implemented more easily to enhance users' cell-edge coverage [28].

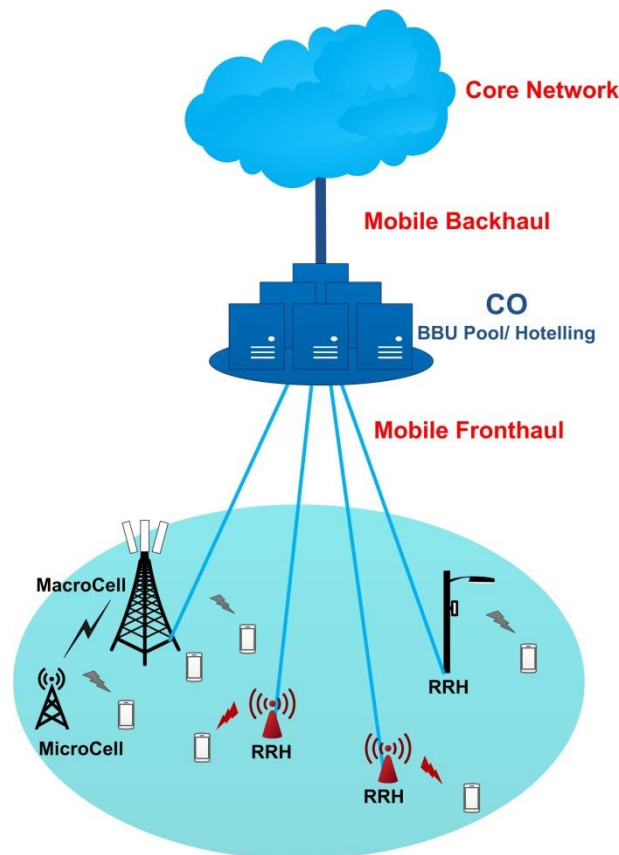


Figure 2.1: C-RAN Architecture

In the present MFH network installations, Common Public Radio Interface (CPRI) protocol is generally used to transmit digitised baseband IQ signals from the BBU to the RRH and vice versa using optical fibre link [29]. Other protocols which can be used are the Open Base

Station Architecture Initiatives (OBSAI) [30] or the Open Radio Initiatives (ORI) [31]. CPRI requires accurate synchronisation, strict latency control and constant bit rate having significantly high overhead data. For instance, 10.137Gbps (i.e. CPRI Rate-8) is required to transport 10 20MHz LTE signal. To deploy LTE-A with, 8x8 MIMO in a typical 3-sector cell site, the aggregated fronthaul data rate per RU in both direction will be approximately 60Gbps [32]. Considering that the huge bandwidth available in the mmWave frequency bands is expected to be exploited in 5G, a significantly high MFH data rate will be required in CPRI. Additionally, very high bandwidth optical components (e.g., modulators) will be required, which will significantly increase the MFH cost and complexity. Although several data compression techniques have been proposed [33-36], this will introduce additional delay and increase complexity and besides, the data rate is still relatively high [34, 36]. Another technique that has been proposed and extensively researched is functional split between the BBU and RRH [37]. By moving some processing close to the RRH, the MFH data rate requirement can be significantly reduced. The 3GPP has since initiated a study regarding the re-definition of function split between BBU and RRH. Several schemes, by which wireless signals can be transported over fibre that has been presented for MFH, as well as proposed modifications to the existing technologies, are discussed in the next section.

2.3. Transport Technologies for Mobile Fronthaul

The optical link in CPRI-based MFH is usually implemented using wavelength division multiplexing (WDM) technology or passive optical network (PON). Microwave radio link has long been used for MBH and it is anticipated that it may be deployed for the future MFH architecture [38], where the optical fibre is not in place and laying new fibre trunk is prohibitive either due to high cost or regulatory restrictions [39, 40]. However, microwave solutions will be subject to bandwidth constraints being experienced in current wireless systems. The bandwidth constraint can be avoided by using mmWave for wireless MFH, thanks to the vast amount of licence free bands present but the inherent high propagation losses limits the transmission range. Therefore, optical fibre transport technology appears to be a viable solution since it presents low loss transmission and high bandwidth. A number of means by which radio signals can be transported via optical fibre link are discussed in the next section.

2.3.1. Radio over Fibre Technology

The basic schematic structure of a RoF system is shown in Figure 2.2, comprising of the CO where multiple wireless signals are generated and multiplexed before the E/O conversion, and transported to the BSs via optical distribution network (ODN). At the BS, the signal is

radiated to the wireless user terminal after O/E conversion. In a typical RoF transmission scenario, the radio signal modulates the intensity of the laser diode (LD). The intensity modulation technique can be performed in two ways namely direct modulated laser (DML) and externally modulated laser (EML). The radio signal drives and directly modulates the intensity of the laser in DML, whereas, in EML, the intensity of a continuous wave (CW) laser is modulated in an optical modulator. After fibre transmission, the optical signal is directly converted to an electrical signal by a photodiode (PD). Thus, the E/O and O/E conversion is referred to as intensity modulation-direct detection (IM-DD) [41].

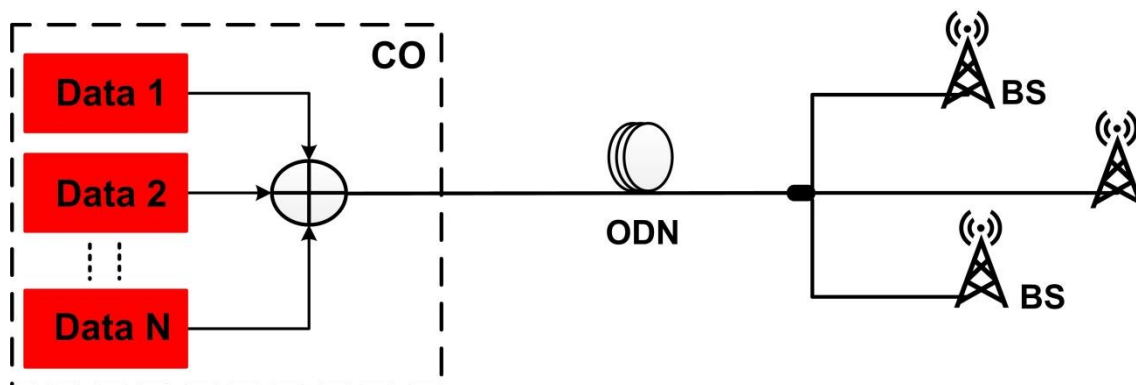


Figure 2.2: Radio-over-Fibre

The wireless signals in RoF can be transported at baseband (BB), intermediate frequency (IF) or at radio frequency (RF), and it can be implemented as either digital RoF (DRoF) or analog RoF (ARoF) as set out in the ITU recommendations for RoF technologies and their applications [42]. These two transmission schemes are discussed briefly in the next section.

2.3.1.1. Digital Radio over Fibre

The three basic implementations of DRoF are shown in Figure 2.3. The most common implementation of DRoF is the digital BB-over-Fibre (see Figure 2.3 (a)) used to transport wireless signals from BBU to RRH in C-RAN. The baseband IQ samples are digitised before optical transmission and converted to RF signals before transmitting from the antenna. The CPRI framing structure has both wireless sample data and management data segments, which are digitised based on the CPRI protocol resulting in high overhead data. In the case of digitised IF and digitised RF, shown in Figure 2.3 (b) and Figure 2.3 (c), digital IF and RF modulators are employed, to upconvert the IQ baseband signals prior to E/O conversion. Notice that the RF upconversion stage is not required in Digital RF-over-Fibre (see Figure 2.3 (c)), since the digitised signals are transmitted at the desired frequency. Although this configuration reduces the complexity of the BS, high sampling rate DAC that operates in the desired RF band will increase the overall system cost.

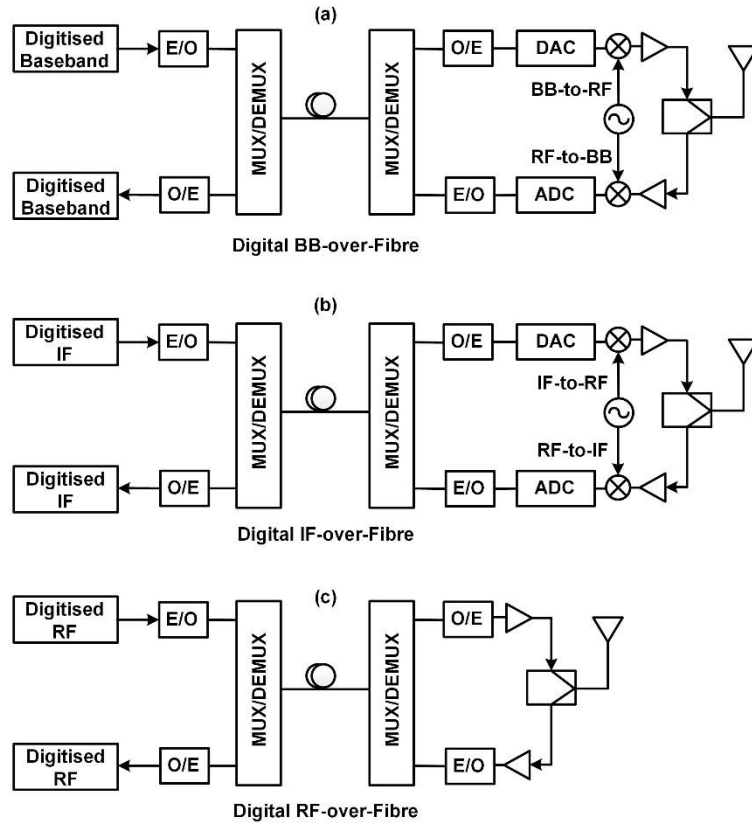


Figure 2.3: Digital-over-Fibre (a) BB (b) IF (c) RF

Alternative DRoF transmission scheme has been reported in the literature [43-46]. In [46], multiple IF signals are electrically combined and converted to digital samples using ADC after which they were transported over the optical link to the BS. In reconstructing the signals using DAC, a bandpass sampling technique was employed in order to select a high-frequency Nyquist zone; thus, IF-to-RF upconversion local oscillator (LO) is avoided. However, the bandwidth requirement of the DAC scales with the desired frequency of the wireless signals. Moreover, aliasing and jitter noise from the DAC/ADC may result in the degradation of the system SNR [47]. Recently, delta-sigma modulation has been proposed as an alternative fronthaul solution [48], which trades the quantization bits with the sampling rate. Nevertheless, the high sampling rate requirement makes delta-sigma scheme expensive. Therefore, a cost-effective solution is necessary, in order to design scalable fronthaul architecture for 5G mobile networks.

2.3.1.2. Analog Radio over Fibre

The two main implementations of ARoF is shown in Figure 2.4 (a) and Figure 2.4 (b), namely Analog IF-over-Fibre and Analog RF-over-Fibre. Alternatively, the baseband signals can be digitally shifted to IF in the frequency domain during the digital signal processing (DSP) process. In ARoF, the transmitted analog signal is generated by the DAC and upconverted to IF or RF before E/O conversion and subsequently, fibre transmission. The BS process

includes E/O conversion, upconversion (in the case of IF-over-Fibre), filtering and amplification. Thus, the BS complexity, as well as power consumption, is significantly reduced compared to DRoF systems since DAC/ADC is not required since most of the signal processing functions are centralised in ARoF featuring simple, scalable and low-cost implementations. Additionally, ARoF is transparent to signal waveforms and modulation formats, thus multiple wireless services from different RATs, e.g., LTE, WiFi, WiMAX and mmWave signals can be multiplexed and transported together via the same optical fibre link [49, 50].

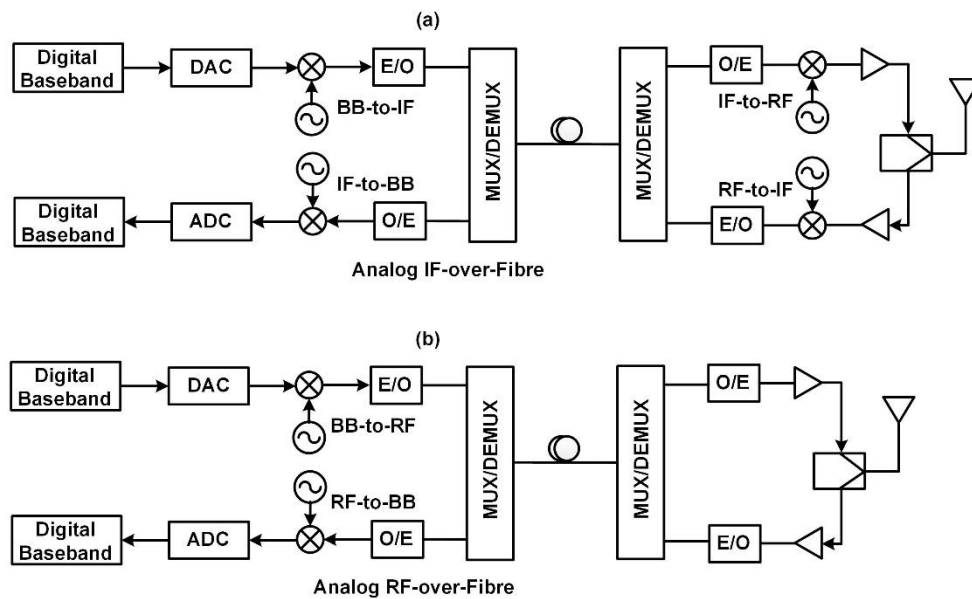


Figure 2.4: Analog-over-Fibre (a) IF-over-Fibre (b) RF-over-Fibre

More importantly, ARoF presents high SE and this advantage can be exploited in the future MFH to avoid the huge bandwidth in CPRI-based digital MFH [51]. The bandwidth efficiency of analog MFH has been demonstrated by several authors [52, 53], employing frequency domain multiplexing technique to transmit multiple aggregated LTE signals in multi-IF over fibre MFH. In [54], 36 LTE signals were aggregated using DSP technique and transmitted on a single wavelength occupying 1.1GHz. The channel aggregation/ de-aggregation were achieved using efficient inverse discrete/discrete Fourier Transform (IDFT/DFT) DSP techniques. The transmission of 48 20MHz LTE signals was demonstrated in [55], employing frequency-domain windowing to reduce the size of FFT/IFFT needed for channel aggregation and de-aggregation.

Besides the advantages of ARoF, nonlinearity is a major challenge in employing ARoF for multi-service MFH architecture. The nonlinearity can arise as a result of the nonlinear transfer function of E/O interface [56-58], induced by CD [59] or four-wave mixing (FWM) in WDM systems [60], resulting intermodulation distortions (IMDs). The IMDs from the E/O

interface can be generated by the laser in DML or Mach-Zehnder modulator (MZM) in EML RoF systems. Therefore, several linearisation techniques have been proposed to mitigate the effects of nonlinearity of the E/O interface [61-63]. The simplest and most common form of linearisation is predistortion. This technique can be implemented in analog [64] or digital domain [65]. The idea behind predistortion is to estimate and pre-compensate the nonlinear channel response by creating inverse characteristics of the channel response in the predistorter. Digital predistortion (DPD) is carried out at baseband before the DAC, which makes the technique much easier to implement, by avoiding the complexity of RF hardware. In [66], nonlinear inter-channel distortion in a multi-service/ multi-RAT MFH was investigated and DPD was applied to mitigate the inter-channel nonlinearity due to the PA and E/O interface. In order to avoid dispersion-induced distortion, efficient frequency plan was demonstrated in [67], such that the distortions were made to fall outside the useful signal bandwidth, while successfully transmitting up to 72 20MHz LTE-A carriers equivalent to 88.47Gbps in CPRI data rate over 30km fibre with low-cost 1.5GHz DML bandwidth.

Evidently, advanced DSP techniques can be employed to mitigate the impact of nonlinear impairments, thereby making ARoF a viable technology for the next-generation MFH architecture. Furthermore, the application of mmWave with bandwidth up to 1GHz (as proposed for 5G-NR) to MFH architecture featuring small cells is also straightforward, since no protocol or interface modification is required.

2.4. Millimetre-wave Technology

The mmWave frequency band is one of the enabling technologies for 5G mobile communications. The mmWave presents a huge amount of spectrum and has attracted significant attention within the research community, where the suitability of different mmWave frequencies for 5G mobile communication has been investigated [68-71]. The mmWave spectrum usually refers to frequency bands at 30-300GHz, but nearby 24-28GHz has been included in the discussion. The fact that most mmWave frequency band is license free or lightly licensed means it can be readily available to MNOs globally. However, mmWave transmissions can experience significant attenuations in the presence of heavy rain since raindrops have a similar wavelength (i.e. millimetres) [72]. Also, relatively high atmospheric absorption results in significant propagation loss. The atmospheric absorption across mmWave frequencies in dB/km is shown in Figure 2.5. The white circle shows the region where atmospheric attenuation is very small, the green circles show the attenuation similar to current communication systems, while the blue circles indicate frequencies with high attenuation.

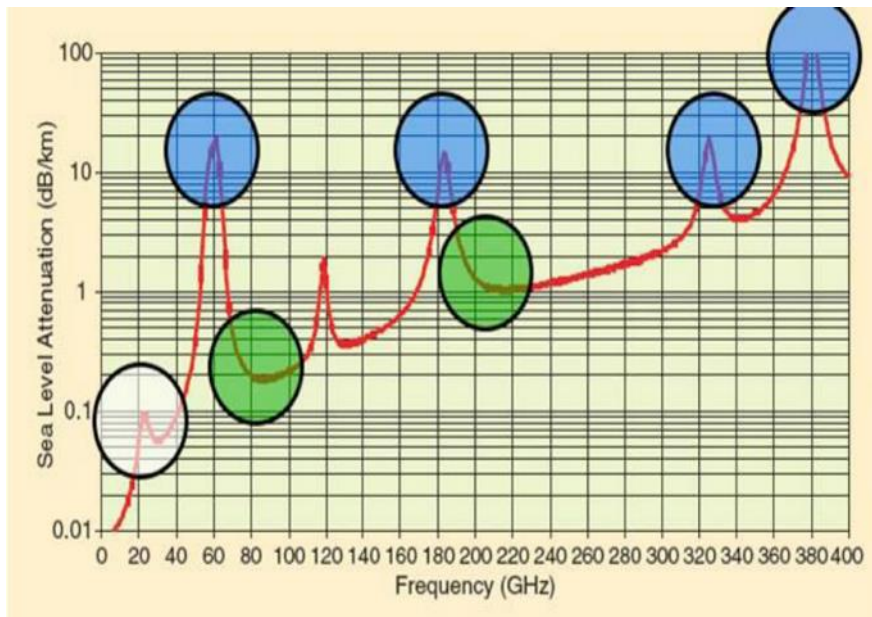


Figure 2.5: Atmospheric absorption at different frequency bands [39]

The 60GHz band due to its universal availability and license free has attracted the most interest and has been standardised for various applications, such as Wireless HD technology, ECMA-387, IEEE 802.11ac and IEEE 802.11ad. Enabled by the advent of advanced complementary metal-oxide semiconductor (CMOS) that now operates well in the mmWave band, these technologies are already being deployed [73]. Although the propagation loss is quite high for the 60GHz frequency band as shown in Figure 2.5, it is well suited for short-range communication, and it has been heavily researched for the next-generation small-cell backhaul. Apart from the 60GHz band, the 28GHz has received considerable attention from both industry and academia [73, 74]. Rappaport et.al have investigated the suitability of 28GHz, 38GHz and 73GHz for mobile communications in dense urban cities of New York and Texas, respectively [68]. The results demonstrated the possibility of employing 28GHz for small cell coverage of up to 200m employing highly directional antennas. Prior to this investigation, Samsung reported the feasibility of applying 28GHz in the next generation of mobile broadband systems. The ITU at the World Radiocommunication Conference in 2015 (WRC-15) selected several frequency bands [75] listed in Table 2-1 as candidates for 5G.

In the meantime, the FCC in the USA has released the 28GHz and 38GHz which were originally licensed locally for broadband services as well as the unlicensed spectrum at 64GHz - 71GHz for potential 5G developments. The 28GHz has been highlighted as a potential frequency for 5G in the USA, South Korea and Japan with proof of concept and field trials being carried out in preparation for the 5G standards. Samsung has been a leading advocate of the 28GHz band, demonstrating in 2013, a record speed of 7.5Gbps for a stationary vehicle and 1.2Gbps when the vehicle was moving at 100km/hr [76]. Handover

technique was demonstrated between two small cells for a vehicle moving at 192km/hr in September 2017.

Table 2-1: The frequency above 6GHz for future development of IMT 2020

24.25GHz – 27.5GHz	47.2GHz – 50.2GHz
37GHz – 40GHz	50.4GHz – 52.6GHz
42.5GHz – 43.5GHz	66GHz – 76GHz
45.5GHz – 47GHz	81GHz – 86GHz

Other field trials have been carried in collaboration with KDDI in South Korea, NTT Docomo in Japan, and Verizon in the USA to test 5G technologies. Recently, the world’s first fully integrated end-to-end 5G prototype was demonstrated at the 2018 Winter Olympic Games in PyeongChang, South Korea [73].

Fixed wireless access (FWA) is another application, where the 28GHz is being investigated [77]. The idea behind the FWA concept is to replace the last-mile optical fibre infrastructure with 5G wireless. The radio link from the mmWave radio unit to the outdoor/indoor customer premises equipment (CPE) is fixed ranging between 10 - 100m and it is anticipated to offer speeds comparable to fibre installations (see Figure 2.6) [78]. The Verizon 5G Technology Forum (V5GTF) was formed in cooperation with Cisco, Qualcomm, Intel, Nokia, Samsung and LG to set out 5G technical specifications for FWA, and to facilitate trials leading to commercial deployment [73].



Figure 2.6: Samsung end-to-end 5G FWA network [78]

In the UK, Arqiva (telecom mast operator) recently announced that it will be conducting FWA trials at 28GHz in conjunction with Samsung. Meanwhile, Qualcomm has announced that the first commercial products featuring 5G-NR modem is expected to be available in 2019 and it

will initially support the 28GHz band with 800MHz bandwidth via 8x100MHz CA [79]. There is a high priority for bands around the 28GHz in the USA, South Korea and Japan, even though the 28GHz band was excluded from the mmWave candidate frequencies recommended by the ITU (see Table 2-1). The 3GPP proposes to treat the spectrum from 24.25GHz - 29.5GHz as one band and adapt the actually used channel based on local regulations. The first mmWave 5G standard will most likely be around the 28GHz for both fixed and mobile broadband. On the other hand, cost-efficient generation of the mmWave carrier for 5G small cell MFH leveraging fibre-wireless architecture is actively researched. In the next section, photonics-aided techniques that have been reported in the literature as a means to generate mmWave carrier for 5G small cells are discussed.

2.5. Photonics Techniques for Millimetre-wave Generation

Photonic-aided techniques have proved to be a viable alternative in generating spectrally pure mmWave carrier for high-capacity 5G small cell MFH. Since most of the signal processing functionalities is concentrated in the CO, the mmWave carrier can be remotely generated and delivered to the RRH along with the DL signal. Basically, the mmWave carrier is generated by optical heterodyning at O/E conversion, thereby significantly reducing the BS complexity. Several mmWave generation techniques that have been proposed in the literature are highlighted in [80, 81]. These techniques rely on a combination of electrical LO and optical components or all-optical technique to realise mmWave carrier. The optical carriers for heterodyning can be generated using MZMs or by mixing of optical tones from lasers. In the MZM based optical heterodyning technique, the nonlinear transfer function of MZM is exploited to generate multiple phase-correlated optical carriers [82-84]. In laser based optical heterodyning, gain-switched laser [85-87], passive mode-locked laser diode (PMLLD) [88, 89] and unlocked lasers techniques have been reported [90-92]. These photonic mmWave upconversion techniques are discussed next.

2.5.1. Photonic-aided Millimetre-wave Generation using MZMs

External modulators, especially the dual electrode-MZM (DE-MZM) are a key component in the design of future proof fibre-wireless systems for 5G MFH. Aside from the ability to eliminate frequency chirp in the generation of the optical signal [93], DE-MZM has been widely employed in literature for the generation of spectrally pure mmWave carrier [94-97], mainly focusing on the conventional push-pull configuration.

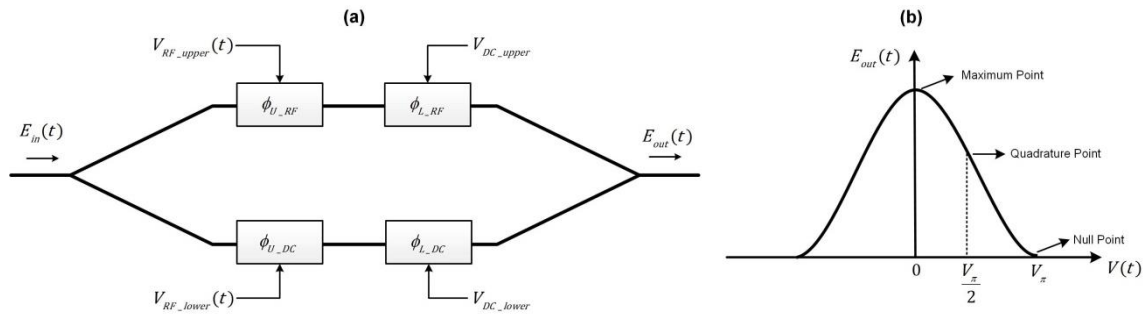


Figure 2.7: Schematic of DE-MZM (a) DE-MZM transfer function (b)

Figure 2.7 shows the schematic (a) and the intensity transfer function (b) of the DE-MZM. The driving RF signal and bias are applied to the upper and lower arm of the MZM to create a phase shift ϕ between the two interferometric branches with opposite signs (i.e. push-pull). The bias voltage required to create a relative phase shift of 180° between the two arms is V_π . The three operating points of DE-MZM is shown in Figure 2.7 (b), namely maximum point (MP), quadrature point (QP) and null point (NP), respectively.

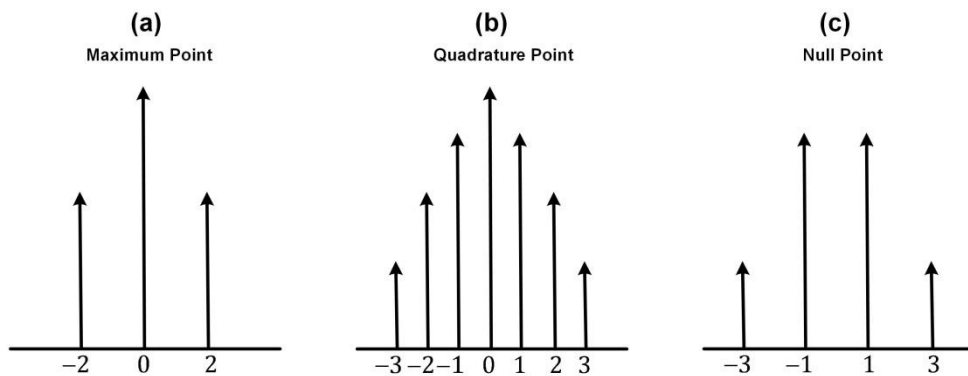


Figure 2.8: Optical signal after E/O at (a) Maximum point (b) Quadrature point (c) Null point

Due to the sinusoidal transfer function of the MZM, optical sidebands are generated at multiple frequencies of the driving RF signal on either side of the optical carrier. Figure 2.8 (a)-(c) shows the optical signal resulting from the three bias points of DE-MZM. As shown in Figure 2.8 (a), when the DE-MZM is biased at MP, the intensity is at maximum and all odd order sidebands are suppressed after E/O conversion. The output of MZM biased at QP is an optical double sideband (ODSB) modulation as depicted in Figure 2.8 (b). The maximum linearity of the transfer function is achieved when the DE-MZM is biased at QP. When an ODSB modulated signal is transmitted over optical fibre, the sidebands experience different propagation delay due to fibre CD. As a consequence, constructive or destructive interference may occur between the beating sidebands at O/E conversion. The transmitted signal will experience total extinction at certain frequencies depending on the transmission distance. When the DE-MZM is biased at NP, the optical carrier and even order sidebands

are suppressed and thus, referred to as optical carrier suppression (OCS) modulation technique.

Although, NP bias point results in 2x the modulating RF after O/E conversion, OCS modulation is generally realised by multiple MZMs arranged either in series or parallel. The series configuration often referred to as cascaded MZMs is used to separate the data modulation from optical mmWave generation [98]. With the cascaded MZM configuration, higher order harmonics can be used to generate, for example, frequency tripling [99] or frequency quadrupling [100] of the modulating RF. In [99], DE-MZM and a phase modulator (PM) was cascaded in series as shown in Figure 2.9, to generate a DSB-suppressed carrier (DSB-SC) and optical single sideband (OSSB) modulation, respectively.

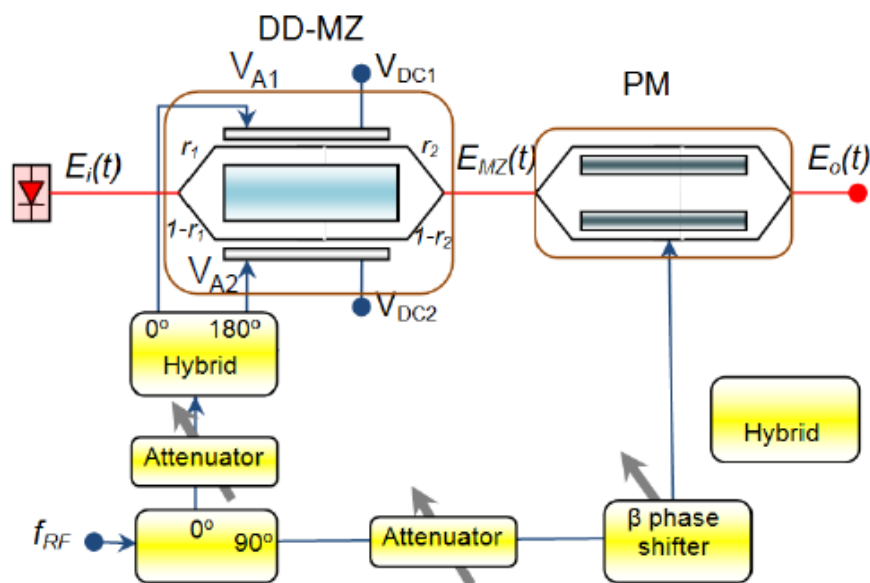


Figure 2.9: Cascaded MZM and phase modulator for frequency tripling [99]

By varying the bias and modulation indices ratios, the sideband suppression ratio in OSSB and optical carrier to sideband suppression ratio in DSB-SC were significantly improved and consequently, improving fibre CD tolerance. In [100], two DE-MZMs were biased at NP as depicted in Figure 2.10 to generate a frequency quadrupled mmWave carrier. A single RF source was used to drive the two MZMs, with the bias symmetrical about the NP, i.e. the MZM1 was biased at the positive slope of the transfer curve while MZM2 was biased at the negative slope of the transfer curve. With the configuration, the two first-order sidebands and the optical carrier at the output of MZM1 were modulated in MZM2. The output of the second MZM is a coherent overlap between the modulated coherent frequency components. Furthermore, by adding an offset to the bias of both MZMs, the optical carrier is almost completely suppressed such that two even order sidebands beat in the PD. Since the RF bandwidth of most commercially available MZMs is 20-40GHz [101], the implementation of

DE-MZM used in this research work is a datasheet model with 40GHz RF bandwidth and it takes into account parameters such as microwave loss, index mismatch and extinction ratio in the modelling of its transfer function [101]. The frequency response of MZM can be limited by velocity mismatch between the electrical and optical signals as well as microwave attenuation in the electrical circuit [101]. However, due to the relatively small RF bandwidth of the modulating signal, the effect relating to the frequency response of the MZM is not a limiting factor.

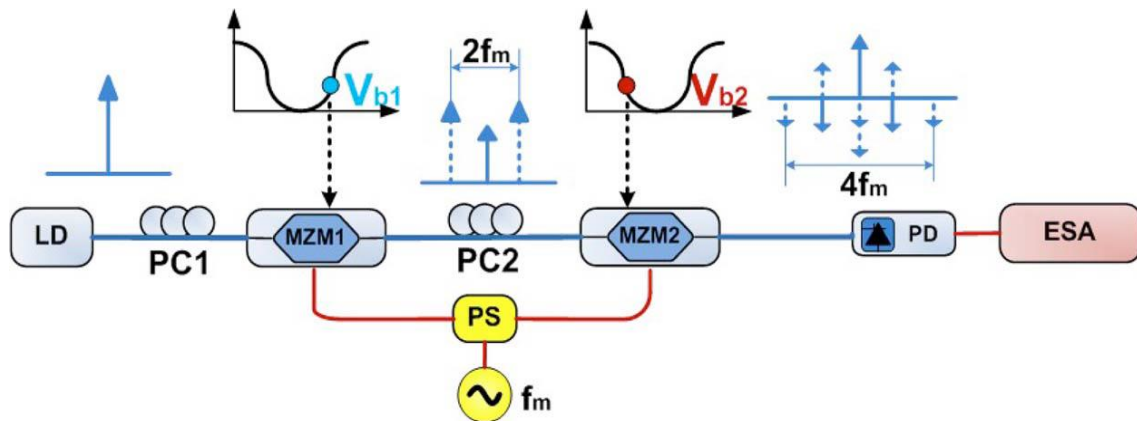


Figure 2.10: Cascaded DE-MZMs for frequency quadrupling [100]

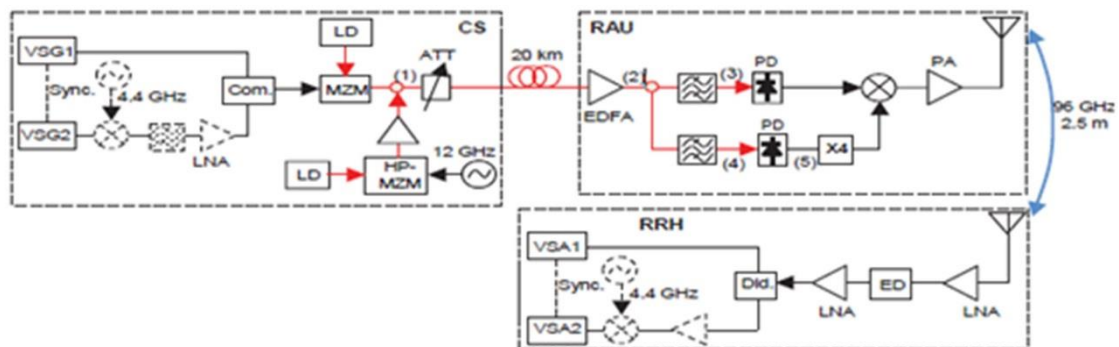


Figure 2.11: Schematic of two stage upconversion to generate 8x the LO frequency [102]

Recently, a technique was demonstrated to generate 8x the LO frequency employing two-stage upconversion [102]. Figure 2.11 shows the schematic of the two-stage upconversion technique that generates a mmWave carrier at 8x the LO frequency. Two LTE-A signals were generated at IF to represent 2x2 MIMO and used to modulate an optical carrier. Another optical source was modulated by a 12GHz LO to generate an OCS modulation and combined with the output of the first MZM. After fibre transmission, two optical bandpass filters (OBPFs) were used to select the modulated optical carrier and the OCS signal before the PD. Thus, a frequency doubled RF carrier was generated at 24GHz, which was then upconverted to 96GHz (i.e. frequency quadrupling) by a frequency synthesiser (see Figure 2.11). Subsequently, the 96GHz mmWave carrier was mixed with the IF signal to realise mmWave signal at 96GHz. In the RRH, the mmWave signal was

downconverted to IF by an ED. The idea was to propose a mmWave wireless bridge in the W-band that can be used to connect the CO to the RRH locations where fibre installation is difficult due to the terrain or due to a fibre cut. However, the proposed scheme is not flexible and may be difficult to upgrade since OBPFs usually have a fixed wavelength.

An optical band mapping technique was proposed in [103], based on OCS optical mmWave generation. The modulating signals (LTE and mmWave) were generated as IF signals and used to modulate separate optical carriers, after which a reconfigurable switch dynamically selects the signal to be transmitted and subsequently map these optical signals to the optical mmWave generation module as shown in Figure 2.12. After fibre transmission, the composite signal was converted to 60GHz by the PD in the RRH and radiated out of the mmWave antenna to the UE where an envelope detector (ED) downconverts the mmWave signal to IF.

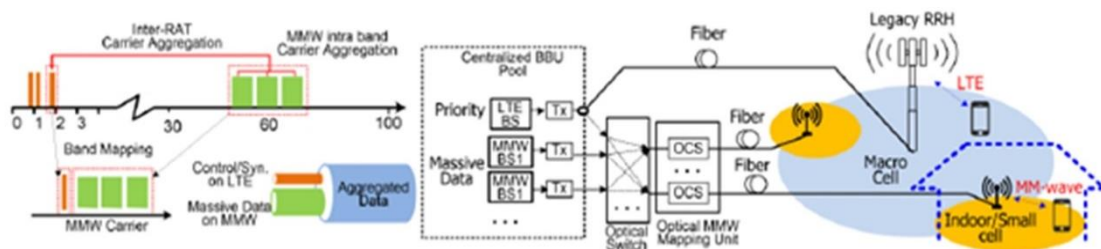


Figure 2.12: The principle and schematic of the mmWave inter- and intra-RAT carrier aggregation in Het-Net based on optical band mapping [103]

A drawback of this technique is that it is prone to phase noise since an optical source is required when adding new services. In addition, the architecture will be expensive to upgrade due to the high cost of optical modulators. In [104], the coexistence of 60GHz OFDM/ FBMC with legacy LTE service was reported. The mmWave carrier was generated photonicly by OCS and ED was used at UE for downconversion. It was shown in the experiments that only one subcarrier guardband is sufficient for FBMC to achieve orthogonality in asynchronous multiband transmission, whereas, OFDM due to its stringent orthogonality requirement can only achieve orthogonality with about 26 subcarrier guardband. However, the work reported considers only the effect of asynchronous transmission on OFDM and FBMC waveforms, whereas, the impact of noise and nonlinear can be detrimental to the system in the real application.

2.5.2. Photonic-aided Millimetre-wave Generation using Lasers

One of the ways by which mmWave carrier can be photonicly generated is to gain-switch a LD [105]. In order to gain-switch a LD, a high power RF signal is used to drive the laser such that it produces several harmonics at a repetition frequency of the RF signal, after which an OBPF is then used to select the desired sidebands that will beat in the PD to generate the

mmWave carrier. The optical mmWave generation based on a gain-switched LD can be achieved either by DML or EML configuration. In the DML case, the modulating signal is combined with high power RF signal before directly modulating the LD, which is externally injected by a master laser to reduce the phase noise by reducing the linewidth and mitigate the effect of chirp. Afterwards, a wavelength selective switch (WSS) is used to select the desired modulated optical signals before optical transmission which will eventually beat in the PD to generate the mmWave signal [105].

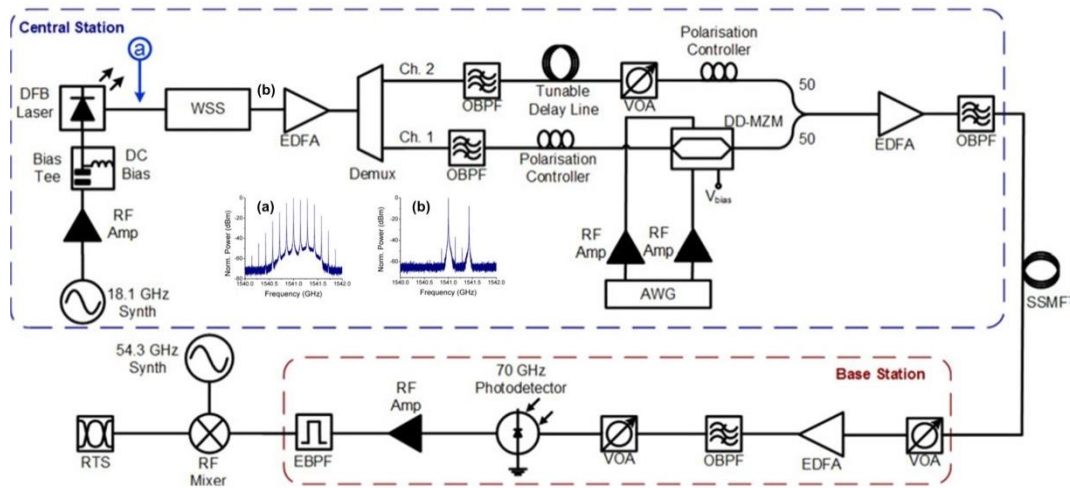


Figure 2.13: Schematic of optical mmWave generation using gain-switched DFB laser [106]

Figure 2.13 shows the schematic setup to generate an optical mmWave carrier based on a gain-switched distributed feedback (DFB) in an EML configuration [106]. The output optical signals after gain-switching the DFB and after the WSS are shown in Figure 2.13 (a) and Figure 2.13 (b), respectively. Since the frequency spacing of the generated optical comb is dependent on the frequency of the LO, and the WSS usually have fixed optical frequency, the RF frontend must be replaced in order to generate mmWave carrier outside the LO frequency band. While it is possible to generate a widely tunable frequency using the laser gain-switching technique, the actual implementation will entail replacing the LOs in both CO and RRH. Further, the complexity of the RRH is increased by employing electrical LO and therefore, this technique may not be suitable for massive deployment of high-capacity mmWave small cells for 5G MFH.

PMLLD generates a wide spectrum of equally spaced and phase-locked optical signal at its output. The free spectral range (FSR) of the generated spectrum is determined by the laser cavity length at the time of fabrication. One difference between gain-switched laser and PMLLD is that the FSR of the gain-switched laser is determined by the driving LO while that of PMLLD is fixed at fabrication. Figure 2.14 shows the schematic of the investigation of 60GHz signals generated using PMLLD [107]. Although, PMLLD can be employed to generate mmWave carrier, the linewidth of individual comb can be relatively large and

imperfect phase coherence between two beating optical tones may result in significant phase noise and moreover, mode partition noise will limit the system performance.

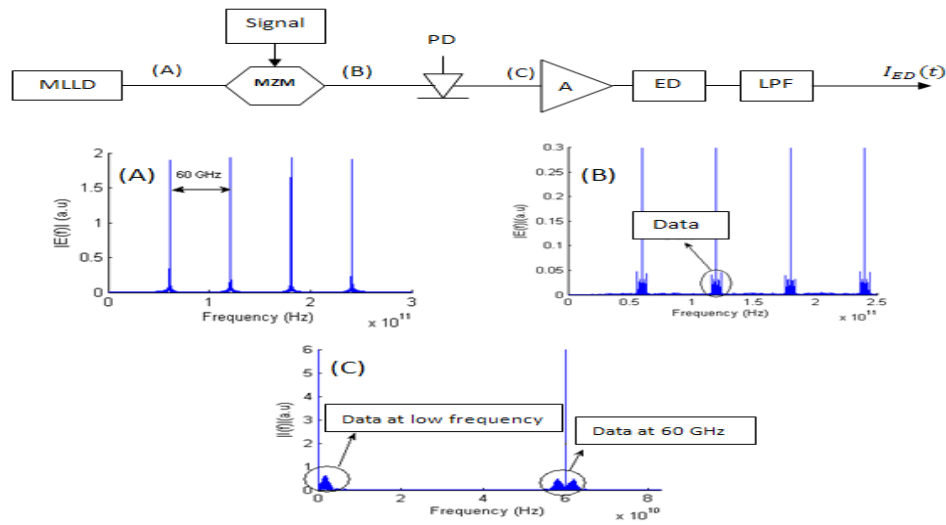


Figure 2.14: Schematic of 60GHz RoF system based on PMLLD [107]

As an alternative, the beating optical tones for the mmWave carrier can be generated from different LDs. A significant difference between this technique and the previous two laser-based mmWave generation schemes is that the optical carriers are not coherent since they are generated from different optical sources whereas, gain-switched laser and PMLLD require a suitable amount of phase coherence between the heterodyne optical tones, in order to avoid phase noise. This implies that the impact of phase noise may be higher when using independent lasers to generate mmWave carrier compared to other techniques. However, the phase of the two optical tones can be locked by a phase locked loop (PLL) [108] or a DSP technique [109] can be employed to mitigate the effect of phase noise. Alternatively, phase noise can be reduced by employing narrow linewidth lasers such as external cavity lasers (ECLs).

Figure 2.15 shows different schemes by which mmWave carrier can be generated by heterodyning two uncorrelated LDs [110]. In scheme A, the two optical tones separated by the desired mmWave frequency are modulated by the data signal, and the output of the MZM is shown as an inset in Figure 2.15 (a), similar to OCS modulation. Scheme B and C are essentially the same apart from the location of the second LD which serves as the LO. Furthermore, the output of the MZM in schemes A and B is an OSSB. As mentioned previously, this technique is susceptible to phase noise, therefore an RF self-homodyne receiver was proposed [110] (see Figure 2.15 (d)) to downconvert the mmWave signal to baseband, thereby avoiding the need for LO and consequently PLL or DSP to compensate for phase noise. In [90], it was shown that although ED has limited bandwidth, it exhibits

better sensitivity compared with RF self-homodyne downconversion, which is not limited in bandwidth.

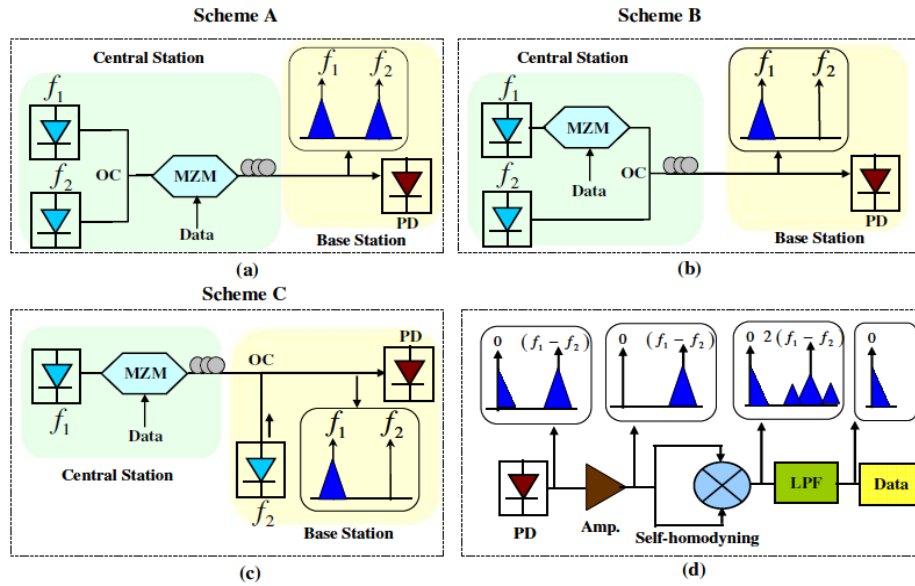


Figure 2.15: Different Schemes to generate mmWave carrier using unlocked LDs [110]

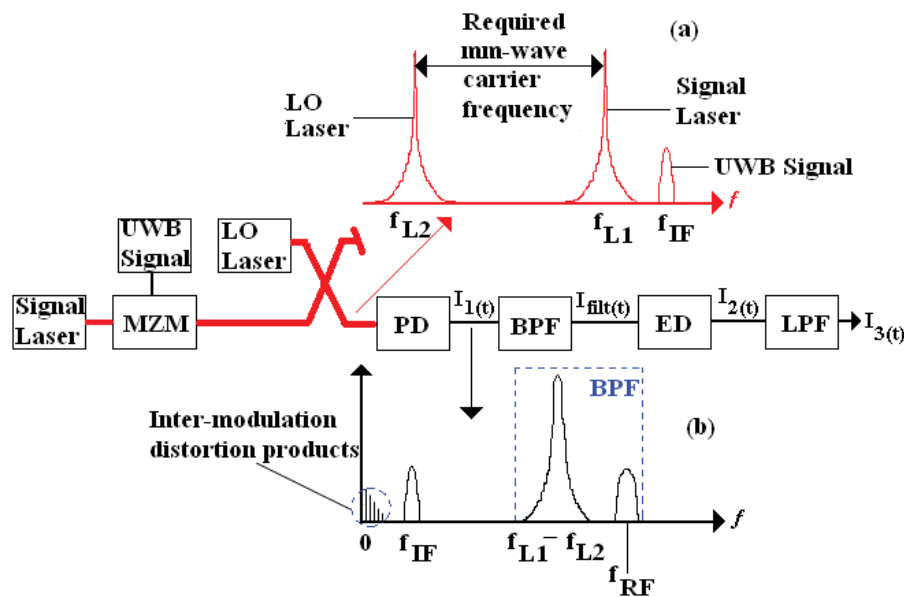


Figure 2.16: Principle of generation and transmission of 60GHz UWB Signal [111]

Uncorrelated heterodyning of LDs was adopted in [111], to generate 60GHz mmWave carrier for multiband-OFDM (MB-OFDM) while an ED was employed in the downconversion of the mmWave signal. Two thermally cooled tunable ECLs were used in the experiment, having a combined linewidth of ~ 900 kHz. Figure 2.16 shows the concept of optical generation of mmWave signals employing uncorrelated laser heterodyning, where Figure 2.16 (a) and Figure 2.16 (b) represent the spectrum before O/E conversion and electrical after O/E conversion, respectively. The ultra-wideband (UWB) signal was modulated on one

sideband of the signal laser (i.e. OSSB). By employing ED for mmWave downconversion, phase noise is avoided as no LO is required. In addition, sideband-sideband interference (SSBI), which usually appears close to DC in multicarrier modulation, is avoided.

A key advantage of the uncorrelated laser heterodyning technique is its ability to generate the widely tunable mmWave frequency. In addition to the simple BS configuration, since LO for upconversion is optically generated remotely, low-cost optical modulator can be employed, which further reduces the overall system implementation cost. However, a common drawback with the photonic realisation of the mmWave carrier using lasers is that noise intrinsic to the optical source significantly impacts the system performance.

2.5.3. Noise and Nonlinearities in Photonic-aided Millimetre-wave Signals

Generally, noise and nonlinearities can originate from electrical and optical components in ARoF systems. Moreover, the presence of the mmWave generation stage in the system can further increase these effects. The optical modulation technique employed in the architecture also plays an important role and the impact of different optical modulation schemes on the performance of mmWave ARoF MFH has been studied in [112]. In the generation of mmWave carrier based on optical heterodyning, transceiver noise such as laser phase noise and RIN as well as the impact of CD on the optical carriers used to generate mmWave was investigated in [89, 113-115]. In [116], it was shown that the spectral purity of the remotely generated mmWave carrier is dependent on the laser linewidth and the effect of fibre CD. However, the generated carriers in many cases were not modulated by data signals. In scenarios where data is modulated on the mmWave carrier, non-spectrally efficient on-off keying (OOK) [92, 110] or binary phase shift keying (BPSK) [114] was employed in the investigation.

On the other hand, OFDM has been investigated [117-121], since it is a candidate waveform for 5G and has been widely deployed in most wireless communication systems. The relationship between CD and laser phase noise in OFDM based optical fibre transmission has been reported [122, 123]. Additionally, the effect of RIN on the performance of OFDM ARoF system has been studied extensively [124]. Besides OFDM, FBMC is another spectrally efficient waveform that has been proposed as a candidate waveform for 5G [125]. Compared to OFDM, FBMC has better control of OOB leakage, due to the frequency-time (F-T) well-localised prototype function employed for pulse shaping. Furthermore, a cyclic prefix (CP) longer than the channel delay spread is used in OFDM to mitigate the effect of multipath delays, but FBMC is robust to multipath delays. Therefore, it is anticipated that these benefits in FBMC will be exploited in future 5G networks [125]. However, FBMC has

only recently been reported for mmWave 5G MFH [104, 126]. It is therefore important to investigate the effects of noise and nonlinearities on the performance of FBMC based mmWave small cell MFH architectures. The system architecture of the FBMC waveform is discussed in chapter 3. The impact of noise on the performance of mmWave fibre-wireless MFH is investigated in detail in chapter 5, while in chapter 6, nonlinear distortion in multi-service coexistence is investigated in the DL and UL, respectively.

2.6. Summary

In this chapter, several enabling technologies for high-capacity 5G mobile broadband access have been discussed. With the paradigm shift from state-of-the-art distributed RAN architecture to centralisation in C-RAN, comes the concept of MFH which is now being actively researched for 5G. Optical transport based on RoF technology is an attractive option for next generation MFH since it centralises signal processing, thus making the system easy to upgrade, manage and enabling multiple operators to share the same infrastructure. Furthermore, mmWave which is regarded as critical in meeting the target data rate for 5G has been discussed. Finally, photonic-aided techniques to generate mmWave carrier that has appeared in the literature have been reviewed in terms of complexity and also the impact of noise and nonlinearities associated with mmWave RoF transmission.

3. Design of Millimetre-Wave Fibre-Wireless Testbed for 5G Mobile Fronthaul

3.1. Introduction

The main focus of this chapter is the design of fibre-wireless testbed to be used in subsequent chapters to investigate the performance of the mmWave 5G MFH architecture. The testbed is implemented using industry standard VPI photonics simulation platform. An end-to-end ARoF transmission design is performed in VPI, and subsequently, the integration of the MATLAB signal processor with VPI is discussed. A self-heterodyne detection technique is proposed to downconvert the mmWave signal generated by heterodyning remotely delivered optical LO (OLO) and the downlink optical signal. The proposed detection scheme is then investigated using the MATLAB-VPI co-simulation technique. Finally, the system architecture of FBMC waveform employed for investigation in subsequent chapters is discussed.

3.2. The VPI Photonic Design Suite

The VPI photonics design suite (PDS) platform is a simulation tool for an end-to-end design of optical communication systems [127]. The system modelling is performed in a graphical user interface known as photonic design environment (PDE), thus, allowing for accelerated design and analysis of different optical transmission scenarios. The PDE has a rich library of electrical, optical, E/O and O/E components that can be configured/ characterised to exhibit performance closely matching commercially-available components [127]. The system parameters can be flexibly configured to test and analyse the performance of existing technology or to propose a completely new system design. Moreover, it offers the possibility to explore different transmission scenarios, which may be challenging in practice due to hardware limitations. In addition, component nonlinearities and transmission impairments (e.g. CD) can be investigated independently and its effects analysed for various transmission scenarios.

Figure 3.1 (a)-(b) show the output power and linewidth of a DFB laser as a function of bias current, characterised in VPI. The laser is a datasheet model, similar in configuration to commercially available high power multi-quantum well DFB laser. It can be seen from Figure 3.1 (a) that the laser threshold current is about 30mA and the maximum output power of the laser is 13mW at 100mA bias current. Similarly, Figure 3.1 (b) shows the laser linewidth as a function of bias current, and it can be seen that the linewidth is ~1MHz at 100mA bias. Therefore, the DFB laser must be biased well above its threshold current in order to obtain optimum output power and low linewidth.

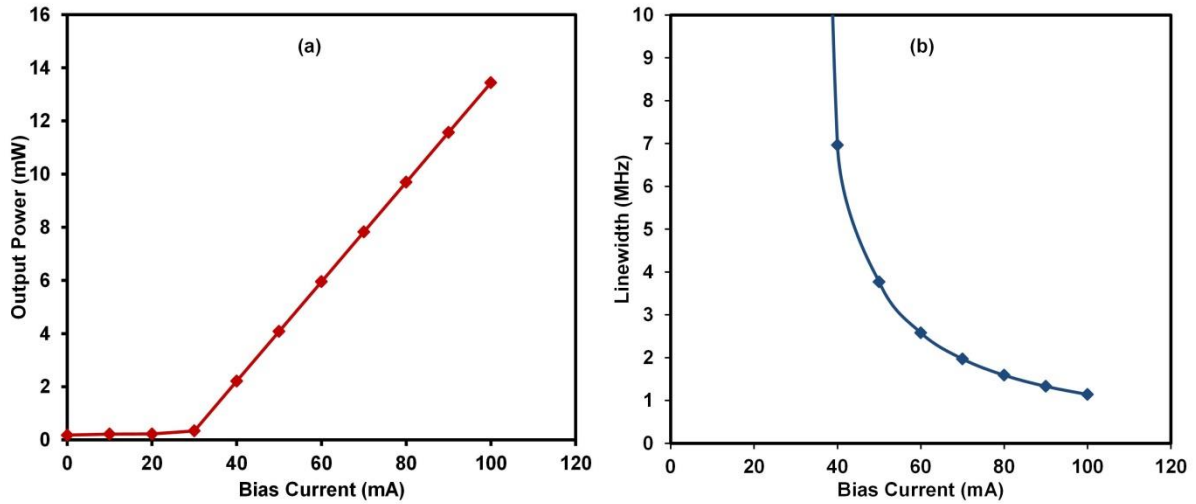


Figure 3.1: (a) Laser Bias current vs Output Power (b) and Bias current vs Linewidth

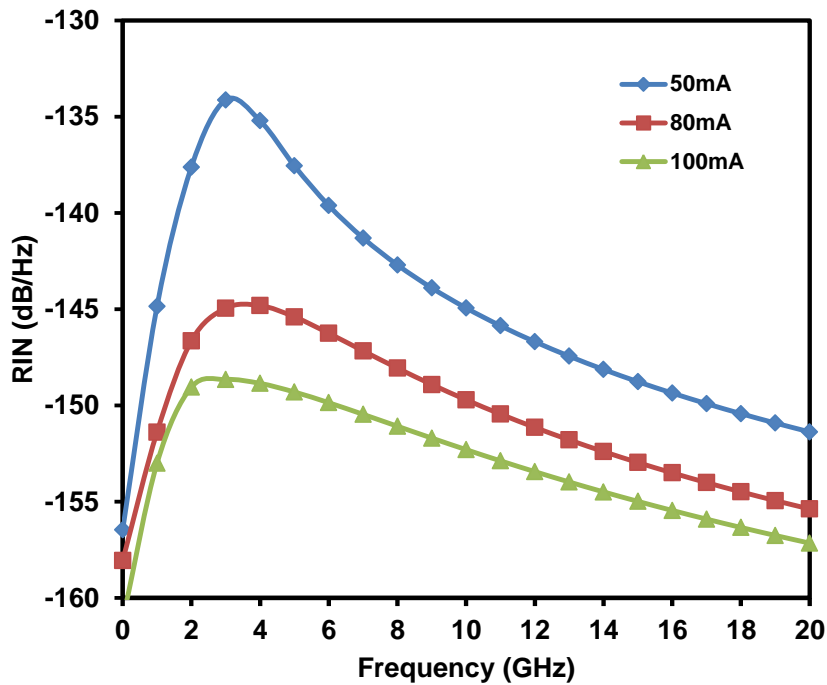


Figure 3.2: Bias current vs Laser RIN

In the same way, Figure 3.2 shows the simulation of the DFB laser RIN in terms of bias current. The RIN peaks at the laser relaxation oscillation frequency which is around 3GHz and it reduced from -134dB/Hz to -148dB/Hz when the laser bias current is increased from 50mA to 100mA. It is therefore important to set the appropriate laser bias as high RIN value will limit the dynamic range of the system [128]. In addition, it is necessary in the design of fibre-wireless 5G MFH systems to consider lasers with low intrinsic RIN in order to reduce its effect on the system performance. The impact of laser intrinsic RIN is investigated extensively in chapter 5.

3.2.1. Simulation of ARoF in VPI

A simple RoF transmission scheme is designed in VPI Transmission Maker® to evaluate the effect of fibre CD on the system performance. OFDM signal having a bandwidth of 500MHz is generated in VPI using the inbuilt OFDM transceiver coder. Figure 3.3 shows the OFDM transceiver designed using inbuilt functionalities in VPI. The transmitter (see Figure 3.3 (a)) comprises of the random bit generator, OFDM coder, a square root raised cosine (SRRC) pulse shaping filter with roll-off factor of 0.2, and RF up-conversion. The random bit is fed into the OFDM coder, where QAM, IFFT, CP insertion is done. The real and imaginary output of OFDM coder is connected to two SRRC pulse shaping filters, after which the baseband OFDM signal is upconverted to RF by an electrical LO. The reverse of the OFDM transmitter process is done in the receiver (see Figure 3.3(b)).

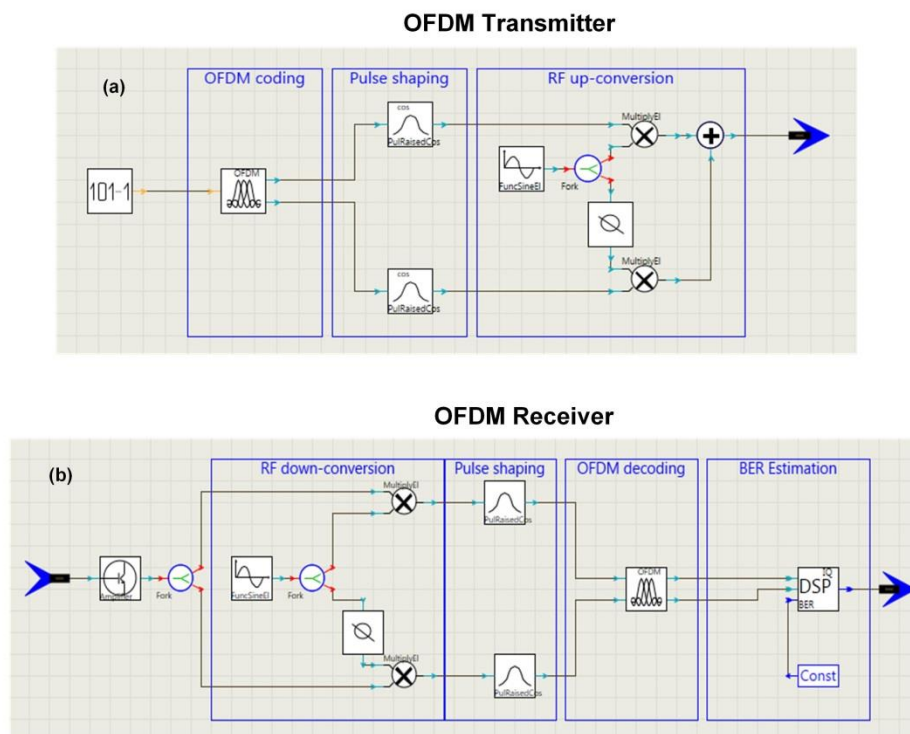


Figure 3.3: OFDM Transceiver Design in VPI (a) Transmitter (b) Receiver

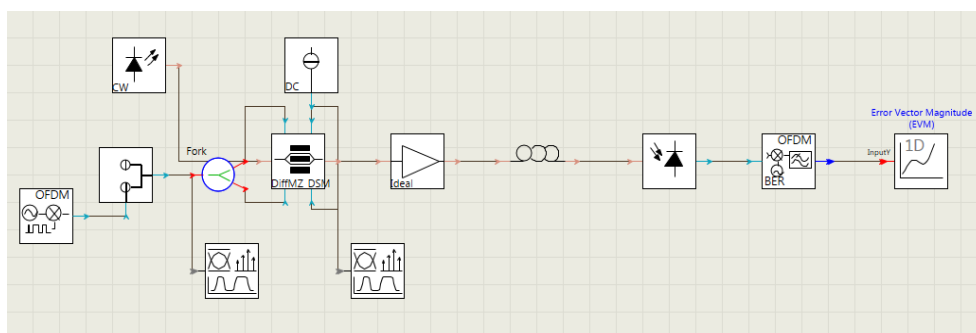


Figure 3.4: ARoF Simulation Schematic

Figure 3.4 shows the ARoF simulation set up in VPI. A 1550nm DFB laser was modulated by the OFDM signal in the DE-MZM biased at QP and the resulting ODSB signal was

transmitted over 25km, 50km and 100km standard single mode fibre (SSMF), respectively. The parameters used in the simulation are listed in Table 3-1.

Table 3-1: Simulation Parameters

Parameter	Value	Parameter	Value
Signal Bandwidth	500MHz	Laser Linewidth	10MHz
CP	4	Laser RIN	~-150dB/Hz
IFFT/FFT	64	Laser Power	10dBm
Modulation	16QAM	MZM Insertion Loss	5dB
LO Frequency	2GHz	MZM Extinction Ratio	35dB
Thermal Noise	10x10 ⁻¹² A/H1/2	Fibre Length	0 – 100km
RRC Filter Roll-off	0.2	Fibre Dispersion	17ps/(nm.km)
Data Rate	2Gbps	Fiber Attenuation	0.2dB/km
PD Responsivity	1A/W	EDFA Noise Figure	5dB

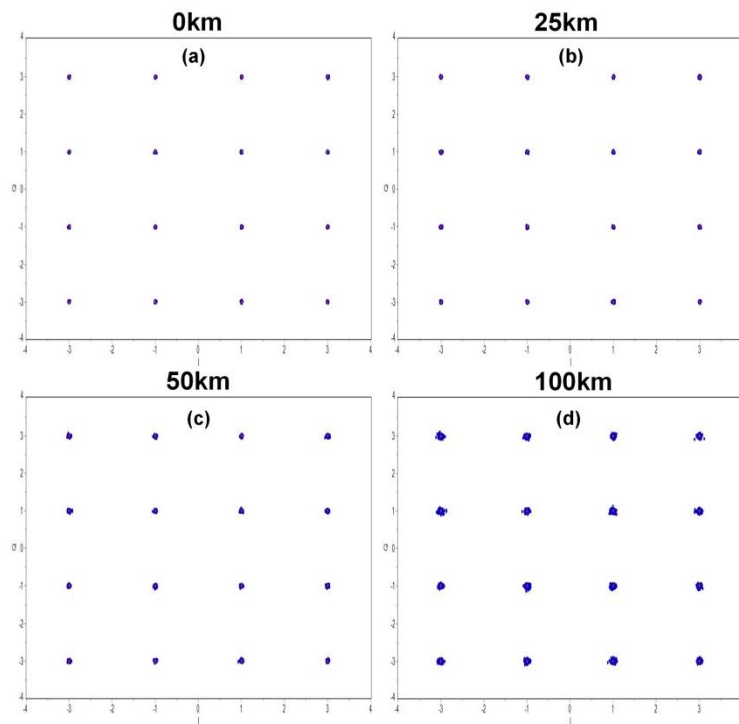


Figure 3.5: Received constellation at (a) 0km (b) 25km (c) 50km (d) 100km

Figure 3.5 shows the received constellation for 0km, 25km, 50km and 100km with corresponding EVM of 0.5%, 0.6%, 0.8% and 1.5%, respectively. The increase in EVM can be attributed mainly to increased accumulation of fibre CD.

In order to investigate other 5G candidate waveforms such as FBMC for fibre-wireless MFH, using VPI simulation platform. The waveforms can be programmed offline using DSP tools such as MATLAB and imported into VPI to simulate optical transmission. This scheme, referred to as co-simulation technique is discussed next.

3.2.2. MATLAB-VPI co-simulation Technique

The PDS can interface with third-party software packages such as MATLAB in co-simulation as shown in Figure 3.6. In co-simulation with MATLAB, special libraries known as libeng and libmx allow VPI access to all the functionalities in MATLAB via the cosimInterface. This implies that custom or standard based components can be designed in MATLAB and implemented in the target environment which is the PDE in this case. For instance, baseband transmitter can be modelled in MATLAB as shown in Figure 3.6 while the transmission channel is implemented in PDE, after which the data is passed onto MATLAB to implement the baseband receiver. Therefore, throughout this thesis, the MATLAB-VPI co-simulation scheme is used to design, implement, test and optimise the performance of integrated fibre-wireless systems for 5G MFH.

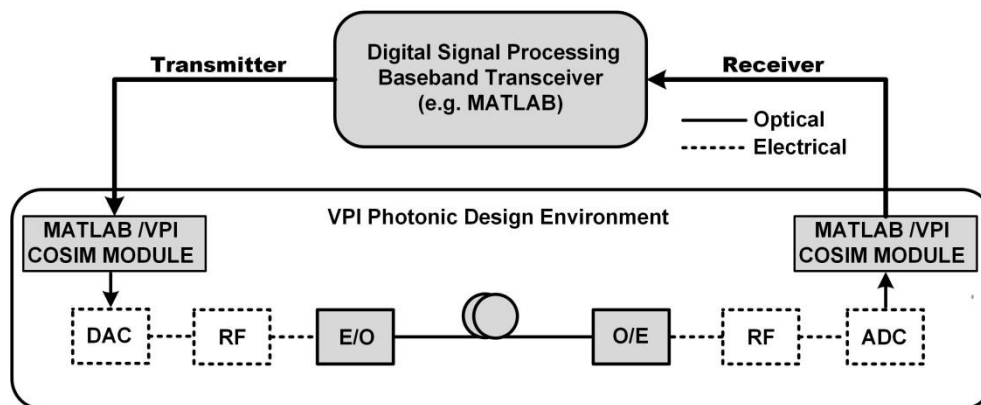


Figure 3.6: MATLAB VPI co-simulation Structure

3.3. Self-Heterodyne Technique for Millimetre-wave Signal Downconversion

In this section, an alternative receiver technique is employed to downconvert the mmWave signal generated using laser heterodyning. At the UE, the mmWave carrier is extracted by a narrowband filter and used as input to the LO port of a mixer. For simplicity, this technique is referred to as the receiver carrier self-heterodyne (RC-SH). This receiver can be applied in a scenario where the ED has limited IF bandwidth compared to the received mmWave signal. Therefore, the system performance using the RC-SH is investigated for UWB mmWave signal. In addition, offset QAM-OFDM (OQAM-OFDM) waveform which is commonly referred to as FBMC is employed as the UWB signal. The proposed distributed RoF mmWave 5G RAN architecture is shown in Figure 3.7. Several RRHs are connected to a common CO via optical fibres and a passive splitter. Complete layer-1 and 2 processing are performed by the CO and only O/E, E/O, electrical filtering and amplification is required at the RRH, before the wireless signal is transmitted to the UE. This simplifies the operation of the RRH allowing for

densely populated BSs and increased overall radio capacity. As shown in Figure 3.7, UWB OQAM-OFDM signalling was employed in order to achieve a minimum of 10Gbps data rate per each RRH. The UWB OQAM-OFDM signal is generated at the CO using DSP; the output of which modulates an optical carrier. In order to avoid transmitting high RF frequencies on the fibre, since they are susceptible to fibre impairments, the signal was digitally upconverted to an IF frequency before it is fed to the E/O converter. To generate the 28GHz carrier needed for the downstream transmission, another CW laser source (λ_{LO}) which is exactly 28GHz apart is coupled with the transmitted signal (λ_{DL}), as seen in Figure 3.7 from the output of the optical coupler (OC). The carrier beating at the O/E converter of the RRH will generate the desired 28GHz carrier that can then be transmitted in the air. The BPF selects the desired frequency and feeds the antenna via the high power amplifier (HPA) and duplexer for bidirectional transmission. It is worth highlighting that the 28GHz was considered instead of the widely investigated 60GHz [80] because higher distances can be achieved even in non-line-of-sight (NLOS) transmission [68].

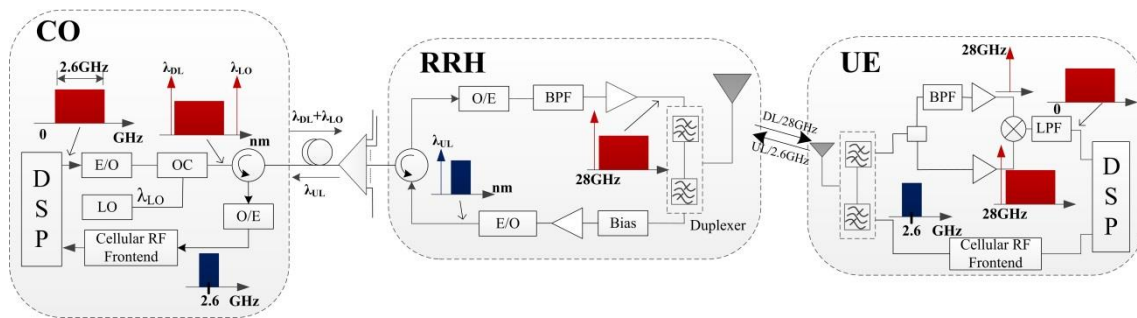


Figure 3.7: Proposed network architecture

A notable feature of the proposed architecture is the RC-SH technique employed in the UE. The received mmWave signal was split by a power divider after the duplexer, as shown in Figure 3.7. The mmWave carrier was then extracted by a narrowband BPF since the received signal has the carrier component embedded and used as an LO for downconversion. The mixer outputs a 2.6GHz IF signal which after low pass filtering was passed to DSP. Thus, high-frequency LO is avoided at the UE when the RC-SH technique was employed. In addition, stringent frequency synchronisation is not required which further relaxes the transceiver architecture.

For uplink transmission from UE to the CO the architecture assumes frequency division duplex approach in which mmWave and cellular sub-6GHz are paired instead of frequencies from the same band as it is currently deployed in cellular networks. It is obvious that the upstream transmission will have significantly smaller bandwidth compared to downstream. However, this is justified from the fact that the upstream data rates are considerably smaller compared to its downstream counterpart. Using microwave frequencies in upstream significantly simplifies the design of UEs and RRHs as well as the upstream RoF

transmission. The standard RF cellular front end of UEs is used to send the signal to RRH. At the RRH, the cost-effective DML can be used for E/O conversion due to smaller bandwidths and frequencies compared to downstream. Otherwise, a 28GHz LO will need to be generated instead which will increase the complexity of RRH. Therefore, as demonstrated in Figure 3.7, the received uplink signal modulates a laser at λ_{UL} that is transmitted back to the CO. In order to distinguish between individual remote antennas, each RRH can be assigned a different wavelength in which case WDM multiplexer would be required at either a distribution point or at the CO. Alternatively, RoF subcarrier multiplexing (SCM) on a single wavelength [80] can be applied by electrically shifting received uplink signal in frequency before modulating a laser. Finally, at the CO, an optical circulator splits the uplink signal which is then fed into an O/E component. RF downconversion, amplification and filtering are performed by the cellular RF frontend before it is passed onto the DSP for baseband processing.

3.3.1. System Model and Performance Analysis

The downstream transmission of the proposed architecture using industry standard VPI and MATLAB is investigated. The complete system model for downstream is shown in Figure 3.8.

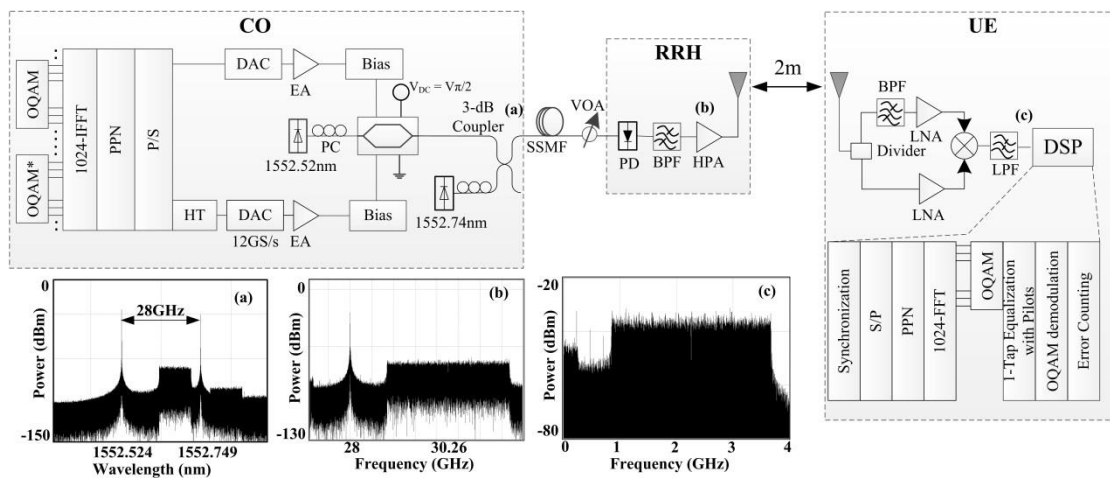


Figure 3.8: Simulation setup of the proposed architecture

The OQAM-OFDM waveform [129] was generated at the CO using MATLAB. The 1024-IFFT size is assumed. Since the signal is upconverted to IF digitally, the real-valued symbols for the laser modulation were obtained by using the Hermitian symmetry (HS) property of the IFFT [130]. Therefore, out of 1024 IFFT inputs, the first 73 and last 71 subcarriers are set to zero while 230 subcarriers between subcarrier numbers 74-314 are modulated with OQAM symbols taken from the 16QAM constellation. In addition, 1 pilot subcarrier is inserted after every 23 data subcarriers for equalisation purposes and the rest of 398 subcarriers are filled with zero. Complex conjugates of the OQAM symbols are mapped onto subcarriers 713-953

to realise HS. Setting the first 73 subcarriers to zero ensures that the signal is digitally shifted from baseband to the IF in order to avoid subcarrier beating noise at the output of the PD that normally falls into the baseband and degrades the SNR. After pulse shaping filtering [129] and parallel-to-serial (P/S) conversion the resulted OQAM-OFDM signal is split and fed to the two 12GS/s 10 bits DACs. As shown in Figure 3.8, the Hilbert transform (HT) of the OQAM-OFDM signal is applied to one of the DACs in VPI in order to eliminate one of the electrical sidebands. This will allow for OSSB transmission reducing the overall effect of the fibre CD. The HT is implemented via DSP thus avoiding the need for high bandwidth analog electrical phase shifter. The bandwidth of the OQAM-OFDM signal after the DAC is 2.695GHz centred at 2.26GHz. Using symbols from the 16QAM constellation this corresponds to 10.78Gbps data rate.

As shown in Figure 3.8, implemented in VPI Transmission Maker®, the outputs of each DAC were used to drive a DE-MZM which is biased at the quadrature point. The laser centre emission wavelength is set to 1552.524nm. The output of the DE-MZM is combined with the LO laser at 1552.749nm via a 3dB OC. The optical wavelength difference between the two lasers corresponds to 28GHz in frequency, as shown in Figure 3.8(inset (a)), which is required for optical remote heterodyne in order to generate a carrier for wireless mmWave transmission. The signal is fed over various fibre lengths to the RRH.

At the RRH, the two wavelengths beat at the PD and generate required 28GHz electrical carrier which is modulated with the transmitted data. This is then filtered, amplified and fed to the antenna for wireless transmission. Inset (b) of Figure 3.8 shows clearly the 28 GHz carrier and data shifted by IF from the carrier. Once the signal is received by the UE antenna, the RC-SH, as discussed in the previous section, separates the carrier using the BPF and demodulates the data. The received spectrum is shown as inset (c) in Figure 3.8 demonstrating clearly that the signal is at the correct IF frequency and bandwidth. This is then applied to MATLAB which implements the synchronisation algorithm in order to find the start of the frame, reverses the filtering and after selecting the desired subcarriers, from 74-314 since the others are complex conjugate, it applies a zero-forcing (ZF) equaliser on each data subcarrier in order to equalise the received signal. The coefficients for the ZF equaliser are obtained from the pilot tones. After the OQAM demodulation, the bit error (BER) rate is calculated.

The input power at the DE-MZM is an important parameter to consider in optimising the transmission with respect to the SNR and component nonlinearities. In addition, as optical remote heterodyne involves beating of the two optical carriers, the laser linewidths can affect the system overall performance. Therefore, the IF drive power at the DE-MZM versus BER for various laser linewidths of both ML and the LO was initially plotted for BTB transmission. This is considered necessary in order to establish an optimum electrical power to be applied

at the DE-MZM arms. The obtained result is shown in Figure 3.9. The optical received power was fixed at +1dBm and both lasers output powers were set to +10dBm. As it can be seen from Figure 3.9, for all combination of laser linewidths the typical ‘bathtub’ response is obtained with respect to various drive powers. At power levels below +14dBm, the system is affected by noise while at powers above this value the nonlinearities introduce unwanted distortions. Therefore, +14dBm can be considered as an optimum power that is used for further analysis. The BER of 10^{-3} was assumed as error-free transmission since it represents the limit for forward error correction (FEC) algorithms.

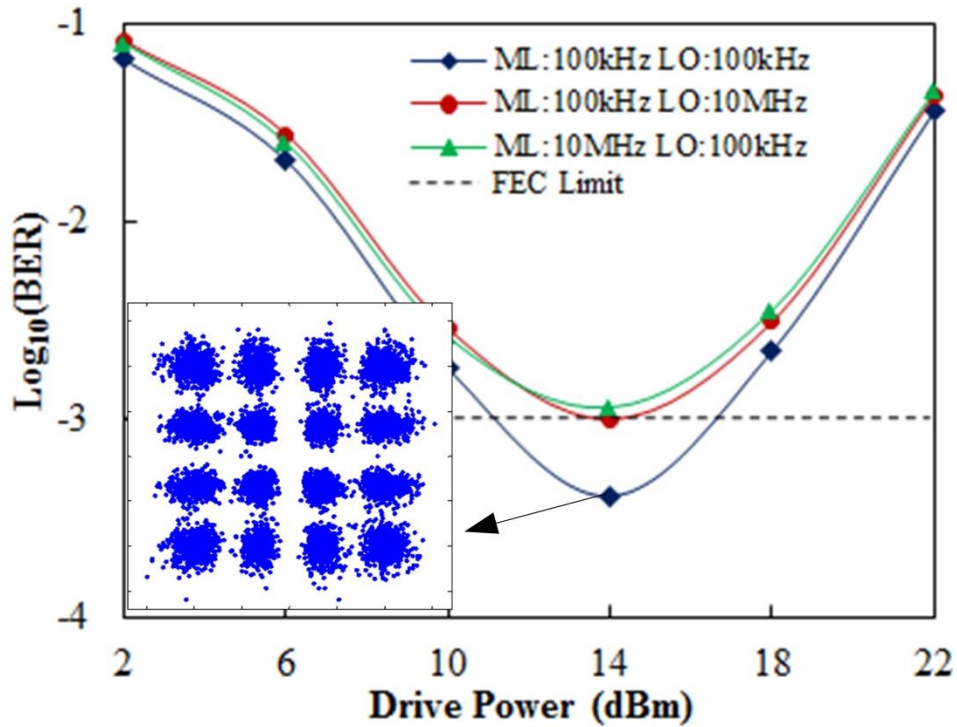


Figure 3.9: Effect of Laser linewidths for BTB

It can be observed from Figure 3.9 that the best performance is obtained when both ML and LO linewidth is 100kHz. However, the results also demonstrate that the BER of 10^{-3} can be achieved if any of the lasers have much wider linewidth compared to the other. As can be seen, if either of the lasers has a 10MHz linewidth the desired performance targets are still met. The wider laser linewidths allow for improved transceiver design in terms of the cost-effectiveness. Therefore, cheaper OLO lasers for photonic upconversion can be used at RRHs potentially improving the performance as the LO would not need to be transmitted on the fibre.

In addition to the above, the BER at UE was then evaluated with respect to the received optical power at the PD. The obtained results are displayed in Figure 3.10. Both ML and LO laser linewidths were set to 100 kHz and the wireless transmission distance of 2 meters was considered. As can be seen in Figure 3.10, the 10.78Gbps error-free transmission was achieved for all fibre distances. There is however a 1dB power penalty between 20km and

40km because of the fibre CD that affects the wideband transmission. Although not shown, in order to validate this conclusion the BER was evaluated with the fibre CD disabled. The obtained results showed no significant penalty. Therefore, it was concluded that the CD, even for IF frequencies with UWB, can have an effect on the overall performance of the proposed architecture. Finally, the received constellation diagrams plotted after the ZF equaliser for the optical received power of -7dBm and 40km fibre show clear 16QAM-OFDM constellation points.

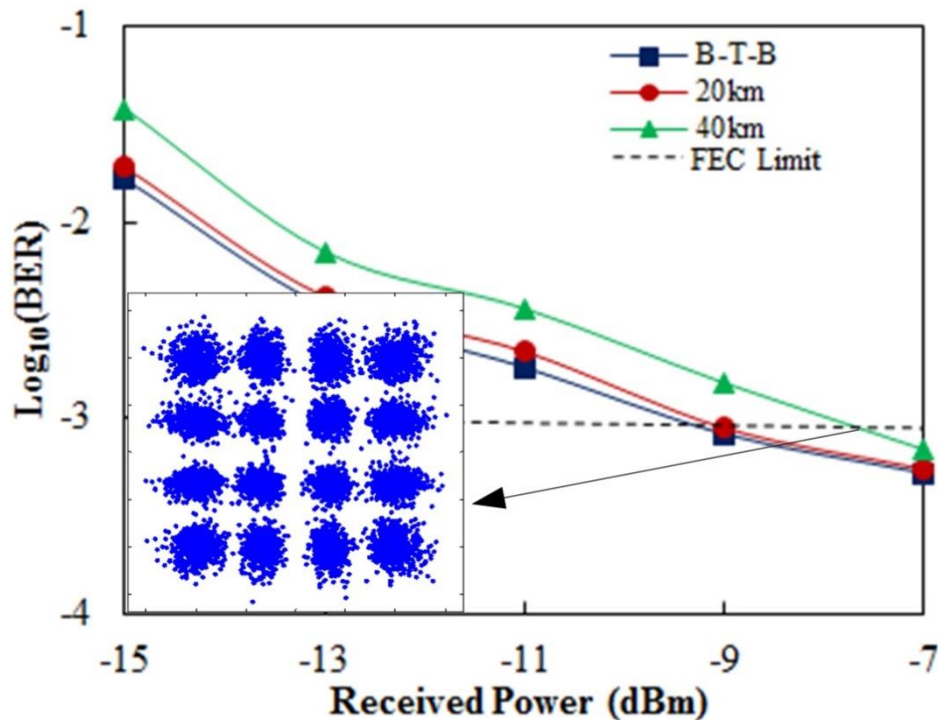


Figure 3.10: BER vs Received Power at PD for BTB, 20km and 40km Fibre

3.4. Filter Bank Multicarrier Systems Architecture

FBMC has recently received significant attention as an alternative modulation technique for the next generation broadband wireless technology [131-135]. Although, OFDM has been adopted and widely deployed in many of today's broadband wireless standards. However, the main drawback in OFDM is that it exhibits significant OOB spectral leakage [134]. Consequently, to avoid OOB interference when OFDM is employed in multi-access non-contiguous frequency bands, frequency bandgap is introduced between adjacent bands which results in a loss in SE [134]. In addition, a redundant cyclic prefix (CP) is required in OFDM to combat intersymbol interference (ISI) due to channel propagation delays. The basic idea of FBMC is to apply well-localised pulse-shape filters at the subcarrier level to reduce the sidelobes [136], thus, improving the SE. The concept of FBMC was initially proposed in 1967 by Saltzberg [137], showing that baud-rate frequency spacing between

adjacent subcarrier channels can be achieved in a multichannel QAM system, and the information is still recovered free of ISI and intercarrier interference (ICI). To achieve this, a properly designed transmit pulse-shape is required and a half symbol delay between the in-phase and quadrature components of the subcarrier symbols. The half symbol delay is referred to as OQAM and it is the basis of the Staggered Multi-Tone (SMT) variant of FBMC [138, 139].

In terms of filter banks, the IFFT and FFT can be considered as set of filters that modulate each subcarrier in a multicarrier system. The first filter is referred to as the prototype filter, which corresponds to the zero-frequency filter, from which other filters are derived via frequency shift. These set of filters constitutes transmit pulse-shape which invariably determines the spectrum of each modulated subcarrier. The IFFT/FFT filters used in OFDM have Sinc-shaped frequency response and exhibits high sidelobes. On the other hand, these high OOB ripples are reduced in FBMC by well-designed pulse shape filters with much steeper roll-off and higher stopband attenuation. The Mirabassi-Martin filter [140] is a special linear-phase finite impulse response (FIR) prototype filter having up to eight coefficients. The FIR filters have stopband attenuation exceeding 40dB for coefficients higher than 4 [140]. This prototype filter was later adopted for FBMC in the PHYDYAS project [136], and the coefficients (listed in Table 3-2) suggested that K be set to 3 or higher for good OOB attenuation. Moreover, setting $K = 4$ achieves an OOB attenuation of about 40dB which is sufficient to significantly reduce OOB interference to adjacent channels [138]. Note that the factor $K = 1$ corresponds to the FFT filters employed in CP-OFDM.

FBMC is essentially a variant of OFDM with some of the baseband transceiver processing blocks such as the insert/remove CP blocks in OFDM transceiver replaced by the polyphase filtering blocks in the synthesis/analysis filter bank (SFB/AFB) (see Figure 3.11). The SFB includes the IFFT, polyphase network (PPN) filtering implementation and P/S conversion, while the AFB is a reverse of the SFB

Table 3-2: List of frequency coefficients for half Nyquist filter

K	H ₀	H ₁	H ₂	H ₃
1	1	-	-	-
2	1	$\sqrt{2}/2$	-	-
3	1	0.911438	0.411438	-
4	1	0.971960	$\sqrt{2}/2$	0.235147

In addition, to fulfil the condition stated by Saltzberg [137], OQAM Pre-/Post-processing block is required before/after the SFB/AFB in the transmitter and receiver, respectively. In

the OQAM Pre-processing block, complex-valued QAM symbols are converted into real-valued symbols by separating the real and the imaginary parts of the QAM symbols.

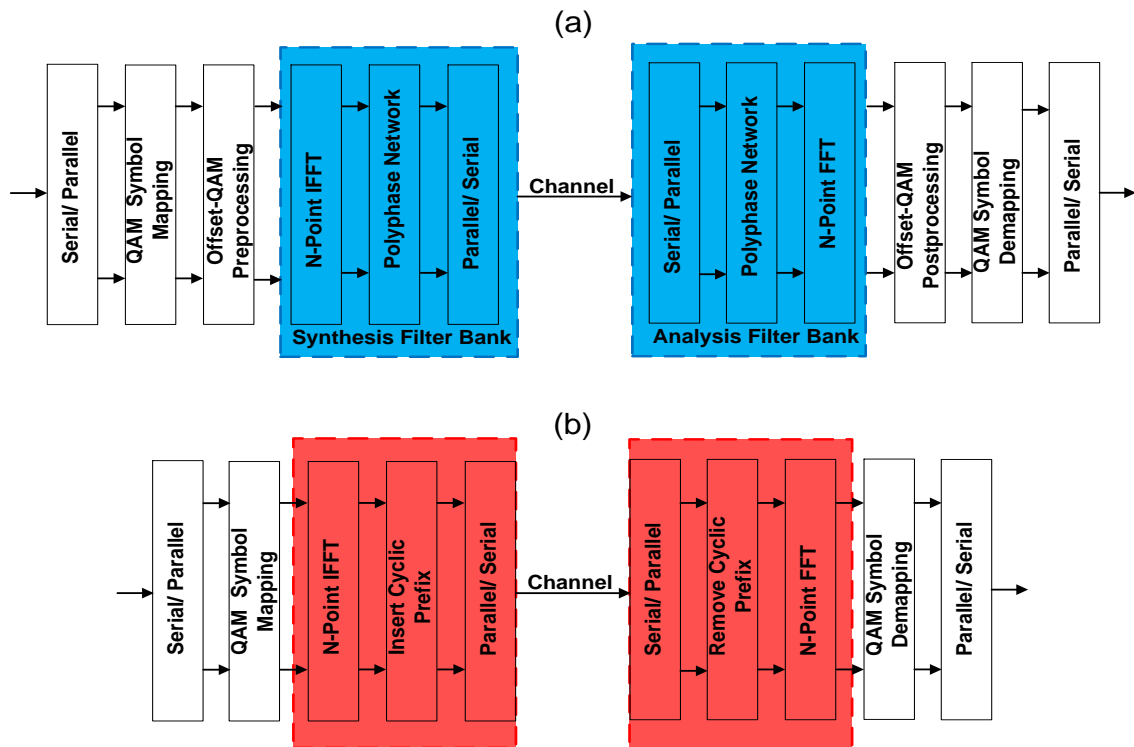


Figure 3.11: (a) FBMC baseband transceiver (b) OFDM baseband transceiver

The OQAM symbol mapping can be described in terms of its projection onto the F-T plane referred to as lattice as shown in Figure 3.12. The real and imaginary parts are separated by half symbol period. In terms of system lattice density, FBMC has twice system lattice density as it transmits only real-valued symbols and the SE can be compared to CP-OFDM without CP.

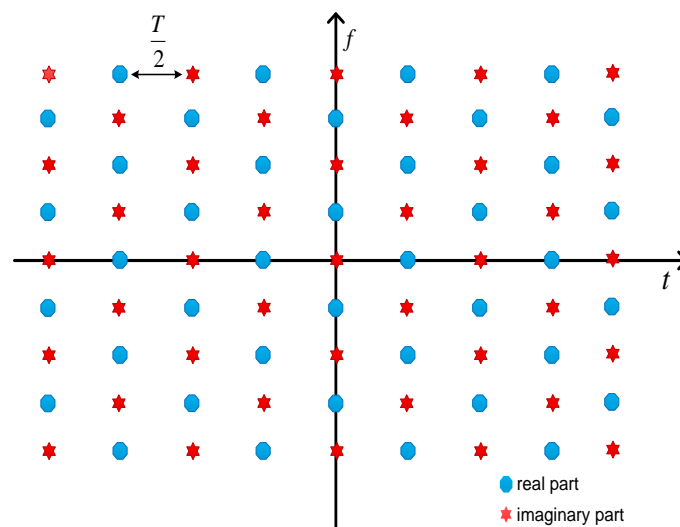


Figure 3.12: Frequency Time phase space lattice of the FBMC system

The real and the imaginary are both upsampled by a factor of 2 as illustrated in Figure 3.13 (a), and a half symbol period ($\frac{\tau_0}{2}$, τ_0 is the complex QAM symbol period) offset is applied to imaginary part for even subcarrier index while for the odd subcarrier index, the $\frac{\tau_0}{2}$ offset is applied to the real part. Next is the multiplication with a phase term $\theta_{m,n} = j^{m+n}$ to introduce a phase shift of $\frac{\pi}{2}$ on adjacent symbols where subscript k and n represents the subcarrier index and time index, respectively. It should be noted that $n = 2\tau_0$ for OQAM symbols since the real-valued and imaginary-valued symbols alternate on adjacent subchannel.

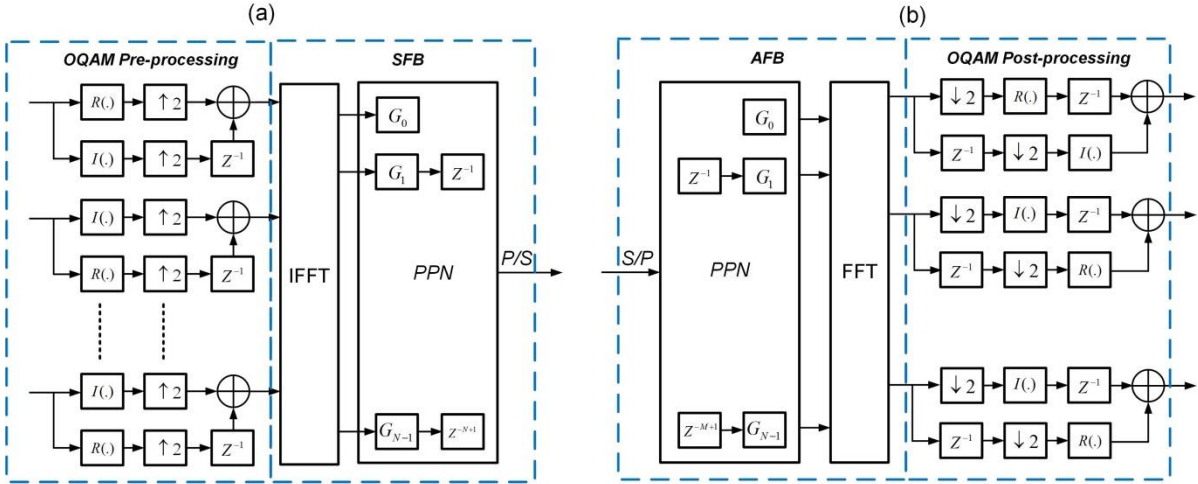


Figure 3.13: (a) OQAM-Pre-processing and SFB (b) AFB and OQAM Post-processing

The OQAM symbols are fed into the SFB where IFFT, polyphase filtering with PPN and P/S is performed successively before transmitting over the channel. The orthogonality condition is greatly relaxed by transmitting OQAM symbols. This, however, can only be achieved in the real-field by well-localised prototype function. The frequency response of the PHYDYAS prototype filter can be expressed as [136]:

$$H(f) = \sum_{k=-(K-1)}^{K-1} H_k \frac{\sin\left(\pi\left(f - \frac{k}{MK}\right)MK\right)}{MK \sin\left(\pi\left(f - \frac{k}{MK}\right)\right)} \quad (3.1)$$

The length of the prototype filter is MK , where M is the FFT size of the multicarrier symbols (assuming all FFT outputs are considered), and K is the overlapping factor, which denotes the number of multicarrier symbols that overlap the filter impulse response in the time domain. The filter roll-off is set to 1 such that the maximum OOB attenuation of a subchannel filter is achieved at the centre of adjacent subchannel filter, thus, higher overlapping factor K improves the OOB attenuation of the prototype filter. The impulse response of the prototype filter is obtained by taking the IFFT of its frequency response, and it can be expressed as:

$$h(t) = 1 + 2 \sum_{k=1}^{K-1} H_k \cos\left(2\pi \frac{kt}{KT}\right) \quad (3.2)$$

The filter bank is obtained basically by shifting the prototype function in frequency, as in the case of FFT. For instance, the filter with index k is obtained by multiplying the prototype filter coefficients by $e^{j2\pi ki/M}$. The PPN is an efficient technique to reduce the computational complexity of the filtering process so that the FFT size can be maintained. At the receiver, the PPN is applied prior to the FFT and subsequently the reconstructed signal is fed into the OQAM Post-processing block as illustrated in Figure 3.13 (b). The OQAM Post-processing is essentially the reverse of the OQAM Pre-processing, while the remainder of the receiver processing block is similar to the OFDM receiver block.

Figure 3.14 shows the magnitude response for the prototype filter for $K = 1:4$. Obviously, the OOB attenuation of the prototype filter is increased for higher overlapping factor K , thus increasing the frequency selectivity of the filter. Observe from Figure 3.14 that the magnitude of the first OOB ripple for $K = 4$, (normalised to 0dB) is -40dB. On the other hand, the first OOB ripple for $K = 1$ has a magnitude -13dB, which is due to the Sinc-shaped prototype function employed in CP-OFDM [141].

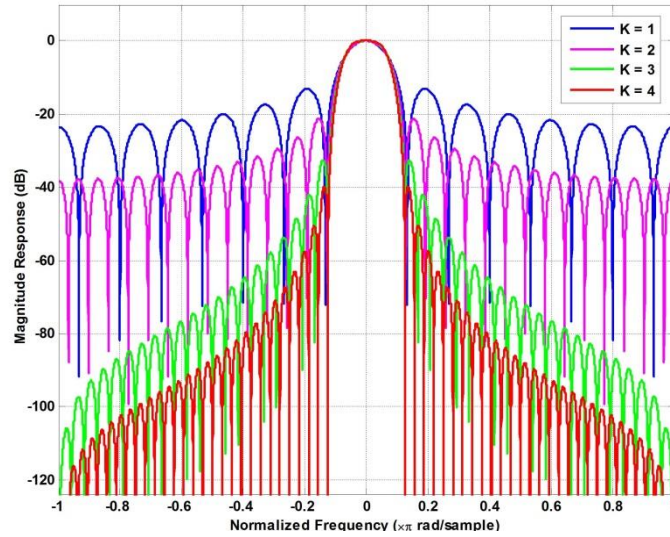


Figure 3.14: Magnitude response of the prototype filter for K =1:4

The baseband transmitted FBMC signal can be expressed as:

$$s(t) = \sum_{m=0}^{M-1} \sum_{n=0}^{N-1} a_{m,n} g_{m,n}(t) \quad (3.3)$$

$$g_{m,n}(t) = g(t - nT/2) e^{j(m+n)\frac{\pi}{2}} e^{j2\pi m f_o t}$$

where $a_{m,n}$ represents the real-valued symbol transmitted on m th subcarrier and n th FBMC symbol. The pulse shape function $g_{m,n}(t)$ is a time and frequency shifted version of the prototype function $g(t)$. The subcarrier bandwidth $f_0 = 1/T$, where $T = 2\tau_0$ is the FBMC symbol duration. $\theta_{m,n} = e^{j(m+n)} = 1, j, 1, j, \dots$ for k even and $j, 1, j, 1, \dots$ for k odd in order to ensure orthogonality. Assuming a distortion free channel, perfect (neglecting the background noise generated due to near perfect filter bank design) reconstruction can be achieved due to real orthogonality condition:

$$\Re\{\langle g_{m,n} | g_{p,q} \rangle\} = \Re\{\int g_{m,n}(t)g_{p,q}^*(t)dt\} = \delta_{m,p}\delta_{n,q}, \quad (3.4)$$

where $\delta_{k,p} = 1$ if $k = p$ and $\delta_{k,p} = 0$ if $k \neq p$. Hence, $\langle g \rangle_{m+p,n+q}^{m,n} = -j\langle g_{m+p,n+q} | g_{m,n} \rangle$, where $\langle g \rangle_{m+p,n+q}^{m,n}$ is the ambiguity function of $g(t)$ [142]. This implies that even in the absence of distortion and synchronisation errors, there will be some ISI and/or ICI at the output of the AFB [142]. This intrinsic interference is purely imaginary and it has a real value corresponding to the ambiguity function of $g(t)$ [142]. Furthermore, in a transmission over a realistic channel, such as optical fibre, the signal is filtered by the channel impulse response $h(t, \tau)$. Also, noise is added to the system which could be generated by the E/O and O/E components along the transmission link. The impulse response of the optical channel is basically due to fibre CD. Thus, the received FBMC signal after the channel can be expressed as a convolution of the transmitted FBMC signal and the channel impulse response, and it can be written as follows:

$$r(t) = (h \otimes s)(t) + \eta(t) \quad (3.5)$$

where \otimes denotes the convolution operator and $\eta(t)$ represents the combined noise in the link. Equation (3.5) can be further expressed for the received signal at F-T points (m, n) as [142]:

$$\begin{aligned} r_{m,n}(t) &= \int_0^\Delta g_{m,n}^*(t) \{h(t) s(t - \tau) d\tau\} + \eta(t) \\ &= \sum_{m=0}^{M-1} \sum_{n=0}^{N-1} a_{m,n} \int_0^\Delta h(t, \tau) g_{m,n}(t - \tau) d\tau \end{aligned} \quad (3.6)$$

For a prototype filter L_g of length ≥ 1 , the channel can be assumed to be a flat fading channel at each subchannel, which implies that $1/L_g < B_c$, where $B_c \approx 1/(2\Delta)$ is the channel coherence bandwidth and Δ is the maximum delay spread of the channel, which is typically small for optical fibre. Based on these assumptions, the prototype function will have

low variation in the time interval $[0, \Delta]$. Consequently, $g(t - n\tau_0 - \tau) \approx g(t - n\tau_0)$ for $\tau \in [0, \Delta]$. Hence, (3.6) can be expressed as:

$$r_{m,n}(t) = \sum_{m=0}^{M-1} \sum_{n=0}^{N-1} a_{m,n} g_{m,n}(t) \int_0^{\Delta} h(t, \tau) e^{-j2\pi m f_0 \tau} d\tau + \eta(t) \quad (3.7)$$

After, demodulation, (3.7) can be written as:

$$r_{m,n}(t) = h_{m,n} a_{m,n} + \sum_{(p,q) \neq (0,0)} h_{m+p,n+q} a_{m+p,n+q} \langle g_{m,n}, g_{m+p,n+q} \rangle + \eta(t) \quad (3.8)$$

Since the channel is slowly varying, and considering that the prototype function is well localised in F-T, it can be assumed that in the first order neighbours of the received block $(m+p, n+q)(p, q) \in \Omega_{1,1}$ that:

$$h_{m+p,n+q} \approx h_{m,n} \quad (3.9)$$

Hence, the following equality holds $\langle g_{m,n}, g_{m+p,n+q} \rangle \approx 0$, $(p, q) \notin \Omega_{1,1}$, which means that only the first order neighbour is significantly affected by imaginary interference (IMI). The index of these blocks can be defined as $\Omega_{(1,1)}^* = \Omega_{(1,1)} - (0,0)$, and (3.9) can be written as:

$$r_{m,n}(t) = h_{m,n} a_{m,n} + j \underbrace{\sum_{(p,q) \in \Omega_{(1,1)}^*} h_{m+p,n+q} a_{m+p,n+q} \langle g_{m,n}, g_{m+p,n+q} \rangle}_{\text{IMI}} + \eta(t) \quad (3.10)$$

This IMI must be taken into account when estimating the channel response in order to sufficiently mitigate the channel effects [142, 143]. Thus, a different approach to CE that considers the IMI is required as the conventional CE methods used in CP-OFDM cannot be applied directly in FBMC. In the next section, some preamble-based CE methods that have been proposed in the literature for FBMC are reviewed.

3.4.1. Channel Estimation in FBMC

Typically, a sequence of reference signals referred to as pilots, known to the receiver are embedded in the transmitted signal, which is then extracted at the receiver and used to estimate the channel frequency response (CFR). It is possible to estimate the CFR at the receiver based on the received data by employing some complex algorithm to perform blind CE. With that, no prior knowledge of the channel characteristics is required, and the redundancy of pilots is eliminated, however, the complexity of the receiver is increased.

Several preamble-based CE schemes for FBMC that have appeared in the literature have been reviewed in [143]. While some of these techniques aim at exploiting the intrinsic

interference to improve the estimation performance, others aim at cancelling/avoiding the effect in the CE process. The pair of pilots (POP) and interference approximation (IAM) are common examples of preamble structure used in FBMC [143].

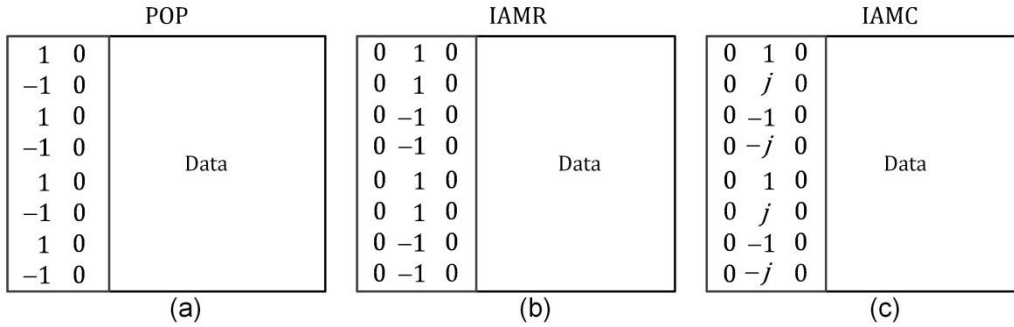


Figure 3.15: Preamble Structures for FBMC (a) POP (b) IAMR (c) IAMC

3.4.1.1. Channel Estimation using Pairs of Pilots

The POP aims at estimating the CFR from two symbols, where $n_0 = (-1)^d$ for $d = 1, 2, \dots, M - 1$ and n_1 is all zero as can be seen (Figure 3.15 (a)). An advantage of the POP estimation method is its simplicity. Moreover, it does not explicitly depend on the type of prototype function employed for the filter bank. However, noise is not considered in its derivation, thus, the performance can become unpredictable in the presence of noise.

3.4.1.2. Channel Estimation using Interference Approximation

Interference approximation estimation method (IAM) exploits the IMI from neighbouring F-T points to construct complex pilots which are used to estimate the complex CFR. To this extent, it requires that all input symbols in the neighbourhood of $(\cdot)_{m,n}$ be known in order to sufficiently compute an approximation of this interference. Compared to OFDM, 1.5 complex symbols are required for training. Hence, a simple preamble arrangement that seems to reach this goal is to place zeros in time instants n_0 and n_2 and $1, 1, -1, -1, \dots, 1, 1, -1, -1$ in n_1 , for $x_{m,1}, k = 0, 1, \dots, M - 1$. This is referred to as IAM-Real (IAMR), since the real symbols are placed in the middle time instant of the preamble as shown in Figure 3.15 (b). The IAMR preamble structure can be modified slightly, by multiplying the even indexed subcarriers with j (see Figure 3.15 (c)). This is referred to as IAM-Complex (IAMC) to distinguish it from IAMR. An alternative approach that aims at cancelling the IMI which, aside from placing zeros in the first and third symbol of IAMR, zeros are transmitted at all even- (odd-) indexed subcarriers [144]. In that way, the CFR can be obtained for even- (odd-) indexed subcarriers, while the rest of the channel is estimated via interpolation. Although, this implies an additional computation in the CE process to perform interpolation, nevertheless, the slightly increased computation could be justified by the degree of CE accuracy [144]. The interference cancellation preamble structure can be extended to accommodate even and

odd index subcarriers by inserting extra preamble symbols. Note that the resulting preamble is basically IAMR with the pilots for odd and even index subcarriers on different symbols [143]. In that way, it ensures zero is placed around all F-T points of the pilots to cancel the IMI for first-order neighbourhood of the F-T points. However, this is achieved at the expense of increased preamble overhead [143]. Next, the performance of POP, IAMR and IAMC preamble is investigated by simulation in MATLAB considering an additive white Gaussian noise (AWGN) channel.

3.4.1.3. Performance Evaluation of Preamble-based Channel Estimation for FBMC

A Monte Carlo simulation was carried out in MATLAB to evaluate the performance of the POP, IAMR and IAMC preamble methods. FBMC waveform was programmed in MATLAB following the transceiver structure depicted in Figure 3.11 (a). The FBMC in each case has 1024 FFT and 1000 OQAM symbols taking from 4QAM alphabet. The PHYDYAS prototype filter has been adopted in the simulation with overlapping factor $K = 4$, such that $MK - 1 = 4095$. One preamble symbol as presented in Figure 3.15 was appended to the FBMC frame before transmission. An AWGN channel was assumed for the simulation and a single-tap ZF equalisation was performed in the receiver with the obtained CE estimates.

Figure 3.16 shows the BER performance of FBMC when POP, IAMR and IAMC preamble methods were used for CE. BER is high at low SNR values for the three preamble-based CE methods considered. The IAMR preamble outperforms both POP and IAMC preambles as SNR values increased. Also, POP preamble exhibits better performance compared to the IAMC preamble. Note that channel time dispersion is not considered in the simulation, of course, the CE performance will be different. Due to its superior performance over other preamble structures for CE, the IAMR preamble method will be used in subsequent FBMC experiments.

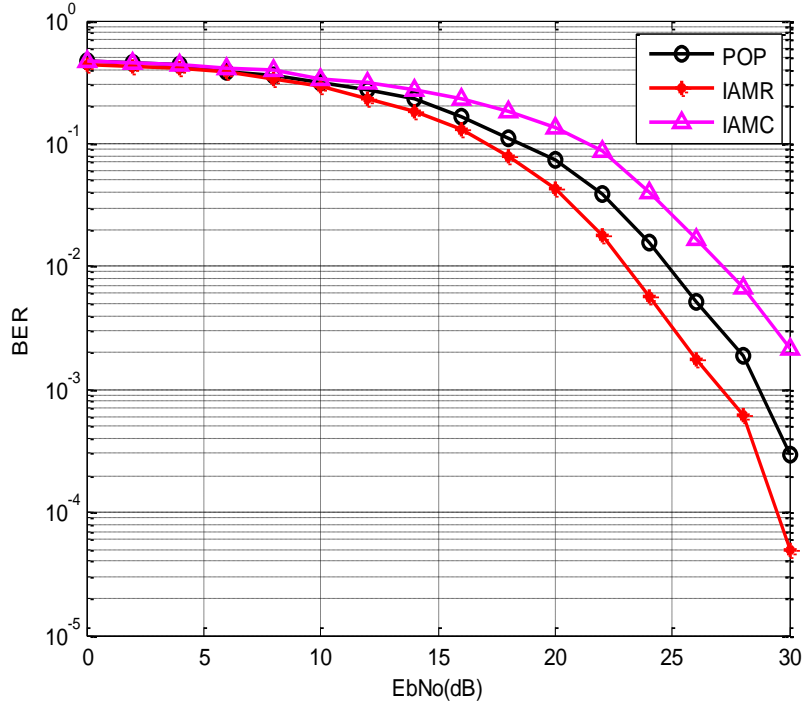


Figure 3.16: BER of FBMC for different preamble-based CE methods

3.4.2. Peak to Average Power Ratio in FBMC

Despite the advantages, FBMC as a multicarrier waveform is susceptible to the PAPR [145]. Due to high PAPR, the low OOB spectrum, which is uniquely a merit in FBMC, disappears in the presence of nonlinearities [146]. Compared to OFDM, FBMC exhibits higher PAPR and thus, higher sensitivity to nonlinearities [147, 148]. Furthermore, with the preamble method used in FBMC for CE, PAPR will be significantly increased. For instance, the IAM preamble proposed in [142], was chosen so as to maximise its power, in order to improve the CE. A direct consequence is that in practice, high peak amplitude will result in high PAPR and limits the dynamic range of the PA. In ARoF architecture, lasers, optical modulators, ADC and PA are the source nonlinearities. In WDM transmission systems, FWM arises in the optical fibre as a result of the Kerr effect.

The PAPR can be defined as:

$$PAPR = \frac{\max\{|S(t)|^2\}}{E\{|S(t)|^2\}}, \quad t \in [0, T] \quad (3.11)$$

where $E\{\cdot\}$ represents the expectation operator. The cumulative complementary distribution function (CCDF) is a parameter that can be used to measure the PAPR, and it can be defined as the probability that PAPR will exceed a given threshold. PAPR reduction techniques such as clipping, selective mapping (SLM) and partial transmit sequence (PTS) have been reported by several authors [147, 149, 150]. Clipping is the simplest form of PAPR reduction, where signal amplitudes above a predetermined threshold are limited to the amplitude threshold.

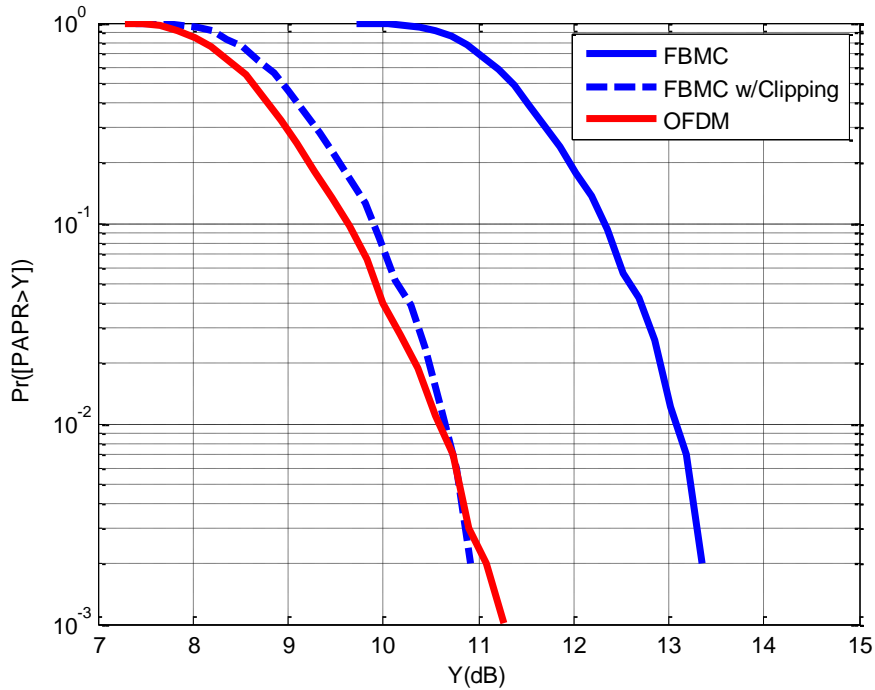


Figure 3.17: Simulated PAPR for FBMC, FBMC with 25% clipping and OFDM

Figure 3.17 shows the simulated CCDF of PAPR for FBMC and OFDM symbols. In order to reduce the PAPR, a 25% clipping was applied to FBMC waveform. The signals were implemented with 128 subcarriers. As it can be seen from Figure 3.17, the PAPR of FBMC without clipping is 2dB higher than OFDM for 10^{-2} CCDF. However, by clipping the signal amplitude of FBMC waveform to 75% of its maximum amplitude, the PAPR is comparable to OFDM. One demerit of clipping is that it increases both OOB and in-band distortion. Therefore, the clipping ratio must be selected so as to minimise the OOB and in-band distortion. Clipping technique is applied throughout this thesis to the FBMC signal to reduce the effect of PAPR.

3.5. Summary

The industry standard VPI simulation platform used in this thesis to design and implement novel 5G fibre-wireless transmission schemes has been discussed. The rich library of optical, electrical and transmission components in VPI has been discussed. As an example, a datasheet model of DFB laser has been characterised, by sweeping the laser bias current to determine the laser threshold current, linewidth as well as the relationship between RIN and bias current. A simulation testbed was implemented to study the effect of fibre CD using the inbuilt VPI DSP library to generate an OFDM signal. Results show that CD is an important system performance limiting factor in ARoF.

In addition to the above, the VPI co-simulation technique which allows the integration of third-party software such MATLAB was discussed. A key advantage of the MATLAB-VPI co-simulation technique is that it enables complex transceiver design and DSP processes to

be executed in MATLAB while VPI is used to model the optical transmission channel. For instance, other 5G candidate waveforms such as FBMC which cannot be modelled using VPI DSP library can be investigated using the co-simulation technique. To this extent, using the MATLAB-VPI co-simulation technique, an UWB OQAM-OFDM transmission was successfully investigated. A unique concept of self-heterodyne detection was employed to downconvert mmWave signal at the UE. Notably, the self-heterodyne receiver can be applied in UWB transmission scenarios where for example, the IF bandwidth of commonly used ED is limited.

FBMC system architecture has been discussed, in comparison with conventional OFDM. Moreover, the implementation of the PHYDYAS prototype filter applied in FBMC was also discussed. Due to the IMI at the output of the AFB, conventional CE methods used in OFDM cannot be applied directly to FBMC. Therefore, several preamble-based CE techniques that have been proposed in literature were reviewed, and performance evaluation was carried out via MATLAB simulations on POP, IAMR and IAMC preamble structures, respectively. The IAMR preamble outperforms the other two preamble structures and hence, IAMR preamble will be used in FBMC transceiver design for experiments in subsequent chapters. Finally, the effect of PAPR has been discussed, and the clipping technique was applied to reduce the PAPR of FBMC.

4. Millimetre-wave Optical Transceivers for Next Generation Fibre-Wireless Architectures

4.1. Introduction

In chapter 2, several photonic mmWave generation techniques have been discussed. These techniques generally rely on heterodyning of optical carriers for the generation of the mmWave wireless carrier. In this chapter, 5 different mmWave RoF architectures are investigated. Since the generation of the mmWave carrier is largely dependent on the transceiver configuration, the effect of upconversion/downconversion is investigated for these architectures from the perspective of E/O and O/E conversion, respectively. Furthermore, as a potential candidate technology for 5G, FBMC waveform is considered for the analysis, and in order to compare their performance, OFDM is also transmitted over these architectures. Note that OFDM has been investigated in some recent work [111, 151-153], but it should be highlighted that a study comparing the performance of OFDM and FBMC in photonic generated mmWave signals has not been done. Therefore, the work presented in this chapter investigates and compare the performance of the two waveforms over the 5 mmWave architectures in terms of nonlinearity of the E/O interface and noise at O/E conversion.

4.2. Millimetre-Wave Upconversion Techniques for Fibre-Wireless 5G Mobile Fronthaul

In this section, 5 mmWave upconversion techniques are investigated for FBMC and OFDM respectively. The architectures are numbered #1 to #5 for comparison purposes; taking into consideration factors such as complexity in terms of mmWave realisation and scalability of the system. The first two schemes rely on electrical LO for upconversion to mmWave and downconversion to baseband, respectively. However, they differ only in the frequency of the signal transmitted over the fibre and the number of stages involved in the upconversion/downconversion. These upconversion techniques are based on the transmission of RF and IF signals over fibre, thus, referred to in this study as mmWave RoF and mmWave IFoF architectures, since the resultant signal after O/E conversion is at the mmWave frequency. The third and fourth schemes rely on both electrical LO and OCS optical modulation to realise frequency doubled carrier at O/E conversion. These techniques are similar in that they both employ two stage optical modulations, to achieve frequency doubling, but the order of modulation and optical components employed are different. Finally, the fifth technique is based on heterodyning uncorrelated optical carriers for mmWave upconversion.

This technique can be seen as all-optical mmWave upconversion as electrical LO is not involved.

The 28GHz frequency band is considered as the carrier frequency for the evaluation since it has been proposed as a candidate carrier frequency for 5G [14, 68]. Although the 28GHz is considered in this work, it should be noted that other candidate mmWave frequencies that have been highlighted for 5G can be employed.

For the investigation, an end-to-end transmission testbed was implemented using VPI Transmission Maker®. The waveforms were generated in MATLAB and loaded onto the VPI platform via the cosimInterface as described in chapter 3. The components used in VPI such as lasers, MZMs and amplifiers have been characterised and their parameters set to what is commonly found on the datasheet of commercially available devices. Therefore, the simulation setup can be used as a basis for an experimental testbed since the platform presents more flexibility, allowing investigations to be carried out for various transmission scenarios. The system performance is determined by calculating the error vector magnitude (EVM) since this is a commonly used figure of merit in a wireless communication system. It should be noted that some system parameters vary for each transmission scheme, as the components are different.

4.2.1. Millimetre-wave Upconversion using Electrical Local Oscillator

The diagram of mmWave RoF architecture and the spectrum at points (a)-(c) is illustrated in Figure 4.1. The shaded areas in the schematic denote points at which there is upconversion/downconversion. The data is a baseband IQ signal upconverted to 28GHz by an electrical LO in the CO prior to E/O conversion.

Assuming the baseband IQ signal has been upconverted to RF in an IQ mixer. The RF signal is then split and used to drive the two arms of the DE-MZM in a push-pull configuration. The signal after splitting can be expressed as:

$$V_{RF_1}(t) = V_{RF} \cos(\omega_{RF}t + \phi_{RF}(t)) \quad (4.1)$$

$$V_{RF_2}(t) = V_{RF} \cos(\omega_{RF}t + \phi_{RF}(t))$$

where V_{RF} represents the amplitude of the RF signal, $\omega_{RF}(t) = 2\pi f_{RF}$ is the angular frequency and $\phi_{RF}(t)$ is the random phase fluctuation of the oscillator. The MZM is quadrature biased with a DC voltage of V_{DC} , where the DC voltage on each arm of the MZM

is given as $V_{DC_1} = V_{DC_2} = V_\pi/4$ and V_π represents the switching voltage. Hence, the field at the output of the MZM can be expressed as:

$$E_o(t) = \frac{E_i(t)}{2} \left\{ \exp \left[j\pi \frac{V_{RF_1}(t) + V_{DC_1}}{2V_\pi} \right] + \exp \left[-j\pi \frac{V_{RF_2}(t) + V_{DC_2}}{2V_\pi} \right] \right\} \quad (4.2)$$

where $E_i(t) = Ee^{j\omega_c t + \phi_c(t)}$ is the electric field of the CW laser signal. E , ω_c and ϕ_c are the field amplitude, the angular frequency of the optical carrier and random phase fluctuation of the laser, respectively.

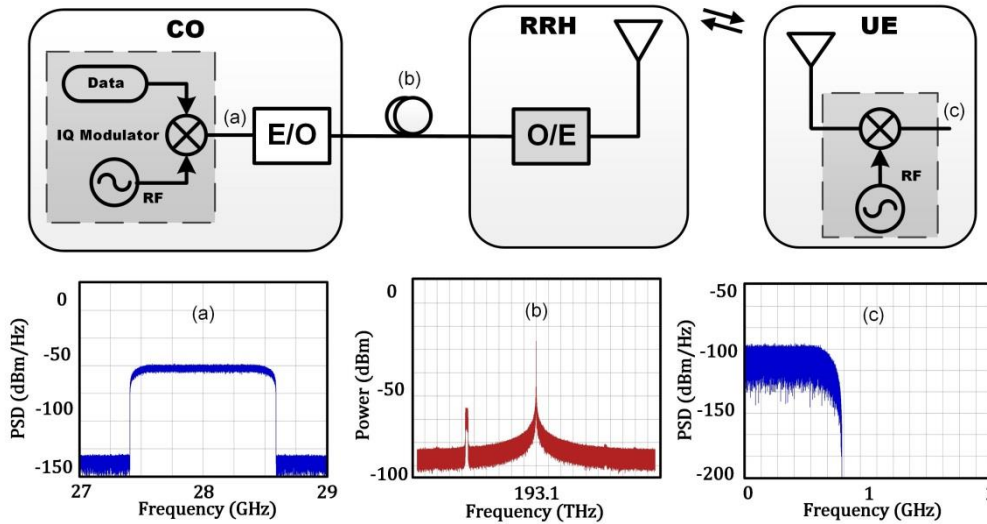


Figure 4.1: Schematic of mmWave RoF (a) Electrical spectrum after upconversion to 28GHz (b) Optical spectrum after E/O showing OSSB modulation (c) Electrical spectrum after downconversion to baseband

Equation (4.2) can be further expressed as:

$$E_o(t) = \frac{E_i(t)}{2} \left\{ \cos \left(\pi \frac{V_{RF}(t) + V_{DC}}{2V_\pi} \right) \right\} \quad (4.3)$$

$$= \frac{E_i(t)}{2} \left\{ \begin{array}{l} \cos \left(\frac{\pi V_{DC}}{2V_\pi} \right) \cos \left(\frac{\pi V_{RF} \cos(\omega_{RF}t + \phi_{RF}(t))}{2V_\pi} \right) \\ -\sin \left(\frac{\pi V_{DC}}{2V_\pi} \right) \sin \left(\frac{\pi V_{RF} \cos(\omega_{RF}t + \phi_{RF}(t))}{2V_\pi} \right) \end{array} \right\}$$

Using Jacobi-Anger expansion [154]:

$$\cos(z \cos \theta) = J_0(z) + 2 \sum_{n=1}^{\infty} (-1)^n J_{2n}(z) \cos(2n\theta) \quad (4.4)$$

$$\sin(z \cos \theta) = -2 \sum_{n=1}^{\infty} (-1)^n J_{2n-1}(z) \cos[(2n-1)\theta]$$

where $J_n(\cdot)$ is the Bessel function of the first kind of order n . Equation (4.3) can be written as:

$$\begin{aligned}
E_o(t) = \frac{E_i(t)}{2} & \left\{ \cos\left(\frac{\pi V_{DC}}{2V_\pi}\right) \left(J_0\left(\frac{\pi V_{RF}}{2V_\pi}\right) \right. \right. \\
& + 2 \sum_{n=1}^{\infty} (-1)^n J_{2n}\left(\frac{\pi V_{RF}}{2V_\pi}\right) \cos\left(2n\omega_{RF}t + \phi_{RF}(t)\right) \\
& + \sin\left(\frac{\pi V_{DC}}{2V_\pi}\right) \left(-2 \sum_{n=1}^{\infty} (-1)^n J_{2n-1}\left(\frac{\pi V_{RF}}{2V_\pi}\right) \cos\left((2n \right. \\
& \left. \left. - 1)\omega_{RF}t + \phi_{RF}(t)\right) \right) \left. \right\} \quad (4.5)
\end{aligned}$$

The first and second term in (4.5) represents even harmonics for $n = 0, 1, 2, \dots$ and odd optical harmonics for $n = 1, 2, \dots$, respectively. To generate an OSSB modulation for the RFoF architecture, an additional phase shift of $\pi/2$ is applied to the RF signal at one arm of the MZM. Depending on where the phase shift is applied, one of the first odd order harmonics is suppressed. The upper sideband is suppressed if the phase shift is negative while the lower sideband is suppressed if the phase shift is positive. A negative phase shift is applied in this case, and thus, the upper sideband is suppressed. Furthermore, considering that $\frac{V_{RF}}{V_\pi} = m_{RF} \ll 1$, where m_{RF} is the modulation index of the RF signal, higher order sidebands for $n > 1$ can be ignored since the optical carrier beats only with the first order sideband. Also, ignoring the bias, (4.5) can be expressed as:

$$E_o(t) = \frac{E_i(t)}{2} \left\{ J_0(\pi m_{RF}) + 2J_1(\pi m_{RF}) \cos(\omega_{RF}t + \phi_{RF}(t)) \right\} \quad (4.6)$$

The OSSB signal shown in the inset (b) of Figure 4.1 is then transmitted over fibre. At the RRH, the optical carrier beat with the lower first-order sideband signal in the PD to generate the mmWave signal for wireless transmission. Neglecting the effect of the optical channel, and assuming a responsivity $\mathfrak{R} = 1$, the photocurrent at the output of the PD can be expressed as:

$$I(t) = \{|E_o(t)|^2\} = \frac{E^2}{2} \left\{ \left(\begin{aligned} & [J_0^2(\pi m_{RF}) + 2J_1^2(\pi m_{RF})] + \\ & 2J_1^2(\pi m_{RF}) \cos(2\omega_{RF}t + \phi(t)) + \\ & 4J_0(\pi m_{RF})J_1(\pi m_{RF}) \cos(\omega_{RF}t + \phi(t)) \end{aligned} \right) \right\} \quad (4.7)$$

The first two terms in (4.7) are DC and higher frequency components. These terms can be ignored since they will be experimentally filtered out by BPF before the antenna emits the

mmWave signal. Also, the phase fluctuation term $\phi(t)$ is due to the phase noise of the electrical LO and that of the CW laser. Consequently, the third term which is the mmWave signal is transmitted over a wireless channel to the UE. The transmitted mmWave signal can be compactly written as:

$$I(t) = \frac{1}{2} m_{RF} \cos(\omega_{RF}t + \phi(t)) \quad (4.8)$$

An IQ downconversion is performed at the UE using a matching LO, and subsequently baseband demodulation.

A key benefit of this technique is that the mmWave upconversion/downconversion is straight forward to implement involving only one stage. Nevertheless, the drawback is that high-speed optical modulator is employed, which besides the high-frequency LO increases the system complexity. These components must be replaced if the system configuration changes. In addition, the mmWave signal transmitted over the fibre is susceptible to RF power fading due to fibre CD. Moreover, the system is prone to hardware impairments such as phase noise of the electrical LO which can become worse with fibre CD. Thus, a complex phase noise cancellation algorithm or PLL may be required [155] in the UE to track the phase of the transmitter LO, and mitigate the effect of phase noise which obviously increases the system complexity.

To investigate the performance of the mmWave RFoF scheme, a simulation testbed was implemented in VPI based on the parameters listed in Table 4-1. In the simulation, OFDM and FBMC were transmitted over the architecture. The effect of the wireless channel was not considered in the simulation since it is not critical at mmWave frequencies due to short distance transmission. Therefore, system performance analysis was based on the impact of RF drive power at the E/O interface and received optical power at O/E conversion.

Table 4-1: System parameters used in the simulation

Parameter	Value	Parameter	Value
Signal Bandwidth	1GHz	Laser Linewidth	1MHz
CP (OFDM)/ K (FBMC)	4/4	Laser RIN	~-160dB/Hz
IFFT/FFT	256	Laser Power	10~16dBm
DAC/ADC Sampling Rate	4 /96GSa/s	MZM Insertion Loss	5dB
DAC/ADC Resolution	14-bits	MZM Extinction Ratio	35~50dB
Modulation	16QAM	Fibre Length	20km
LO Frequency	28GHz	Fibre Dispersion	17ps/(nm.km)
Thermal Noise	$10 \times 10^{-12} \text{A/H}^{1/2}$	Fiber Attenuation	0.2dB/km
RRC Filter Roll-off	0.18	EDFA Noise Figure	5dB
Data Rate	4Gbps	PD Responsivity	0.68A/W

FBMC signal was generated at baseband in MATLAB and converted to an analog baseband signal by 14-bit DAC sampling at 4GS/s. The FFT length was 256 and the overlapping factor $K = 4$. Similarly, OFDM was generated with the same parameter and a CP of 1.56% was used. The small CP sample is reasonable because the channel delay spread is relatively small for the fibre length used in the simulation. One preamble symbol was appended at the start of each frame for CE and a single-tap ZF equalisation was applied to undo the channel effects. IAMR preamble discussed in chapter 3 was used in FBMC while 1 QPSK symbol was used in OFDM. The analog bandwidth of the signal after DAC was 1GHz. The IQ baseband signal was upconverted to RF by electrical LO in an IQ mixer assumed to be lossless. The 28GHz signal was then amplified by a 20dB low noise amplifier (LNA) and fed into a 90° hybrid coupler to provide the $\pi/2$ phase shift required at one arm of the DE-MZM for OSSB modulation. The output of the hybrid coupler was applied to the two arms of the DE-MZM. The half-wave voltage of the MZM is 2.5 volts and the electrical bandwidth is 40GHz. After E/O conversion, the optical signal was amplified by an EDFA, and an optical attenuator was used to set the input power at the PD to +1dBm.

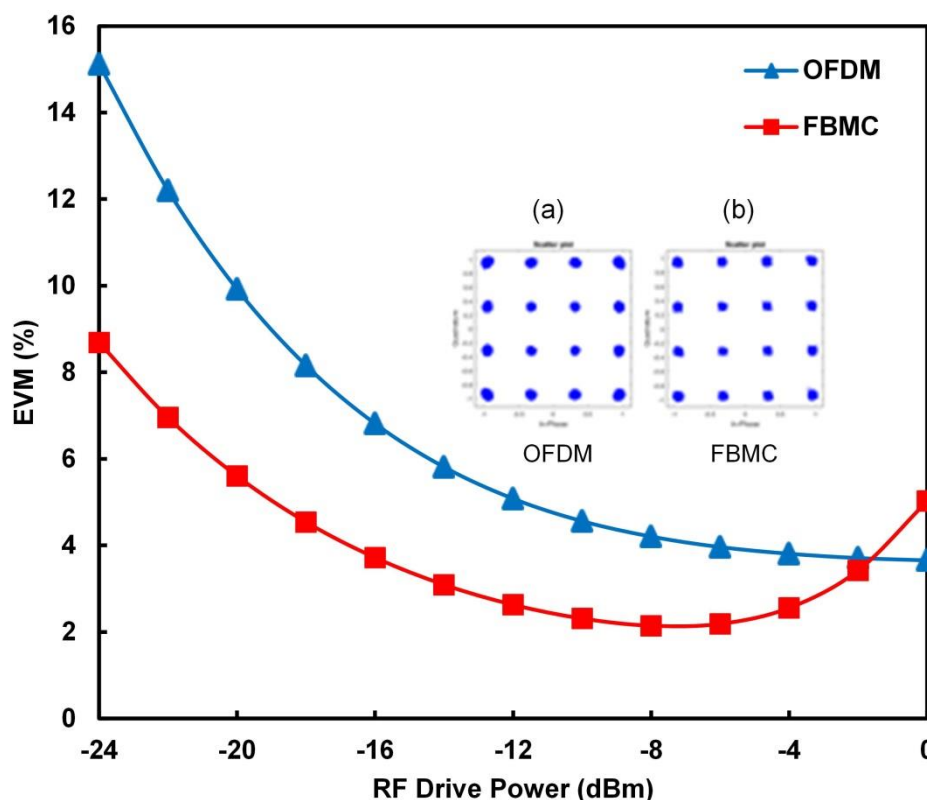


Figure 4.2: EVM vs RF drive power for mmWave RFoF using electrical LO (a) OFDM (b) FBMC
 Firstly, the impact of RF drive on the system performance was evaluated in an optical back-to-back (BTB). An electrical attenuator was placed before the hybrid coupler to sweep the input power into the MZM. Figure 4.2 shows the EVM in terms of RF drive power for

OFDM and FBMC. It can be seen that the EVM is high at low drive powers and reduced gradually as the drive power increases. The high EVM value at low power is due to low SNR at E/O conversion as noise dominates the system. This appears to be more severe in OFDM compared to FBMC. As it can be seen from Figure 4.2, at -24dBm, the EVM of FBMC is +6.5dB better than OFDM. However, for RF power higher than -8dBm, the EVM of FBMC starts to degrade due to the nonlinearity of the E/O interface, as a result of MZM nonlinear response. The nonlinear effect is more noticeable in FBMC as the EVM increased by more than 3%, while OFDM exhibits a better tolerance to MZM nonlinearity as the EVM value increased by ~0.4% at 0dBm drive power. Therefore, to avoid the effect of nonlinearity in subsequent investigations, the optimum drive was considered to be -8dBm. The received constellation of OFDM and FBMC at -8dBm RF drive power is shown in Figure 4.2 (a) and Figure 4.2 (b).

Next, to investigate the impact of O/E conversion on the received EVM, an optical attenuator was used to sweep the optical power input to the PD at BTB and after 20km, respectively. The 20km fibre length is considered practical since it corresponds to the installed capacity of most PONs deployed in the access network.

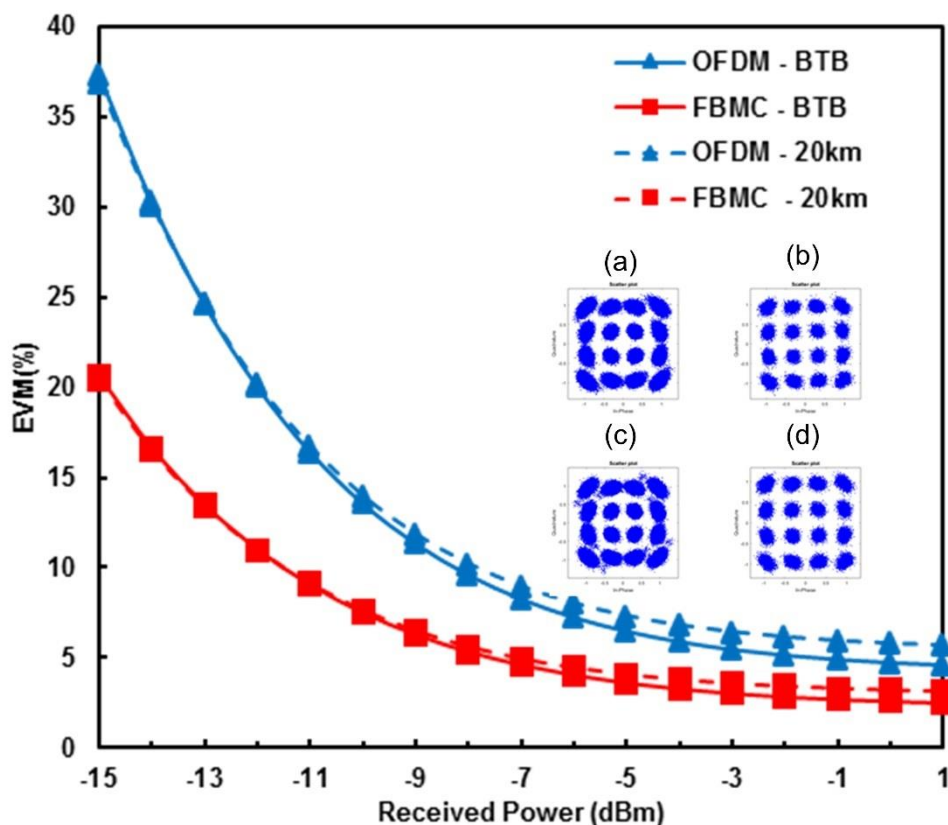


Figure 4.3: EVM vs Received Power for mmWave RFoF using electrical LO (a) OFDM BTB (b) FBMC BTB (c) OFDM 20km (d) FBMC 20km

Figure 4.3 shows the EVM values of OFDM and FBMC vs received optical power. The constellations at -9dBm received power are shown in the inset (a)-(d) of Figure 4.3

corresponding to BTB and 20km, respectively. The high EVM values for low received powers at BTB and after 20km fibre is mainly due to low SNR at receiver as noise contribution from laser intrinsic RIN, Amplified spontaneous emission (ASE) noise and thermal noise dominate the system performance. However, EVM improves as the received power increases. The EVM error floor can also be observed at around -6dBm for OFDM and FBMC signal at BTB and 20km, respectively. Moreover, the EVM penalty after 20km is less than 1% for OFDM and FBMC, respectively. This implies that the effect of CD is not noticeable in the system. The robustness of the system against fibre CD is enhanced by employing OSSB modulation at E/O conversion [156]. Of course, the effect will become more noticeable for increased fibre lengths. Additionally, increasing the mmWave frequency or signal bandwidth will also increase the impact of CD on the system.

Alternatively, to avoid transmitting high-frequency signal over the fibre, two-stage upconversion can be employed, where the baseband signal is first upconverted to IF and transported via optical fibre to the RRH. The mmWave upconversion is then performed in the RRH by another LO. This transmission technique is similar to the RFoF scheme but differs in the point where mmWave upconversion is performed. This is technique #2 and it is referred to as mmWave IFoF architecture since the resulting wireless signal is centred at mmWave, which is 28GHz in this case. As shown in Figure 4.4, the baseband IQ signal is first upconverted to IF frequency by an electrical LO before E/O conversion. After fibre transmission, another LO is used to convert the IF signal to mmWave after O/E conversion. At the UE, mmWave downconversion is done by an electrical LO centred at the frequency equal to $IF+RF$ (i.e. 28GHz in the case). An obvious advantage of this scheme compared to technique #1 is that coupled with OSSB modulation, transmitting IF signals will further improve the system robustness to CD. Thus, signal bandwidth and transmission distance can be increased as required. Furthermore, complexity is reduced in the CO as it eliminates the need for a high bandwidth optical modulator for E/O conversion. Moreover, legacy services having fixed frequency can be generated in the CO and upconverted to mmWave in the RRH. However, the complexity has been shifted to the RRH where LO is required for upconversion to mmWave. In the future 5G heterogeneous access networks, massive deployment of mmWave small cell BSs is anticipated to increase capacity and improve coverage in dense urban environments. Hence, antenna units are expected to be compact and have small form factors such that it can be deployed on street lamp posts, building facades or indoors in mmWave DAS. Moreover, considering that the upconversion/downconversion in mmWave IFoF architecture using LO involves multiple stages, the system may become more susceptible to LO frequency/phase offsets which will further degrade the system performance. Consequently, besides the already increased complexity of the UE, DSP algorithms may be required to track the phase noise and mitigate the effects.

The performance of OFDM and FBMC was considered over the mmWave IFoF architecture. As previously, the impact of input power at the O/E interface and received power at O/E was investigated. The system parameters are the same as before and can be seen in Table 4-1. However, the frequency of mmWave LO in the RRH was set to 26GHz and the IF frequency was 2GHz. Thus, the mmWave transmission was still at 28GHz.

Figure 4.5 shows the EVM as a function of IF drive power and corresponding constellation plots at the optimum input power of -6dBm for OFDM and FBMC, respectively. EVM values for both IF signals are in general similar at low drive powers, but OFDM exhibits 2% better EVM compared to FBMC at -24dBm. The EVM value was the same for both waveforms at -18dBm, after which the EVM of FBMC reduced gradually to 2.4% for -6dBm drive power while EVM of OFDM reduced to 3.7%. For IF drive powers higher than -6dBm, the effect of MZM nonlinearity becomes noticeable in FBMC as shown previously in Figure 4.2, while OFDM appears to exhibit resilience to MZM nonlinearity, with EVM increasing by just 0.6% for 0dBm drive power. The constellation at the optimum drive power of -6dBm for OFDM and FBMC is shown in Figure 4.5 (a) and Figure 4.5 (b).

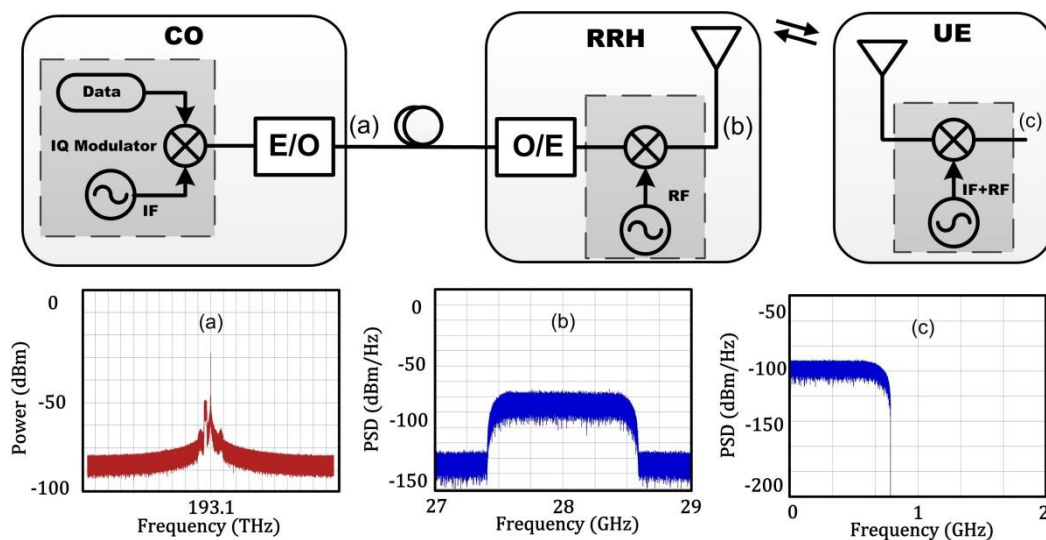


Figure 4.4: mmWave IF-over-Fibre using electrical LO. (a) Optical spectrum after E/O showing OSSB modulation (b) Electrical spectrum after upconversion to 28GHz (c) Electrical spectrum after downconversion to baseband

Next, the impact of received optical power at O/E conversion was investigated. The EVM vs received optical power plot and constellation at -9dBm received power for BTB and after 20km fibre is shown in Figure 4.6 for OFDM and FBMC, respectively. As expected, EVM was high for both IF signals at low received powers, which then decreased steadily as the received power increased. This is due to low SNR at O/E conversion where noise influence is high primarily from laser RIN, ASE noise and thermal noise. EVM reached an error floor at -7dBm for both IF signals showing no significant improvement as the received power was

increased up to +1dBm. The EVM penalty after 20km was observed to be less than 1% for OFDM and FBMC, respectively.

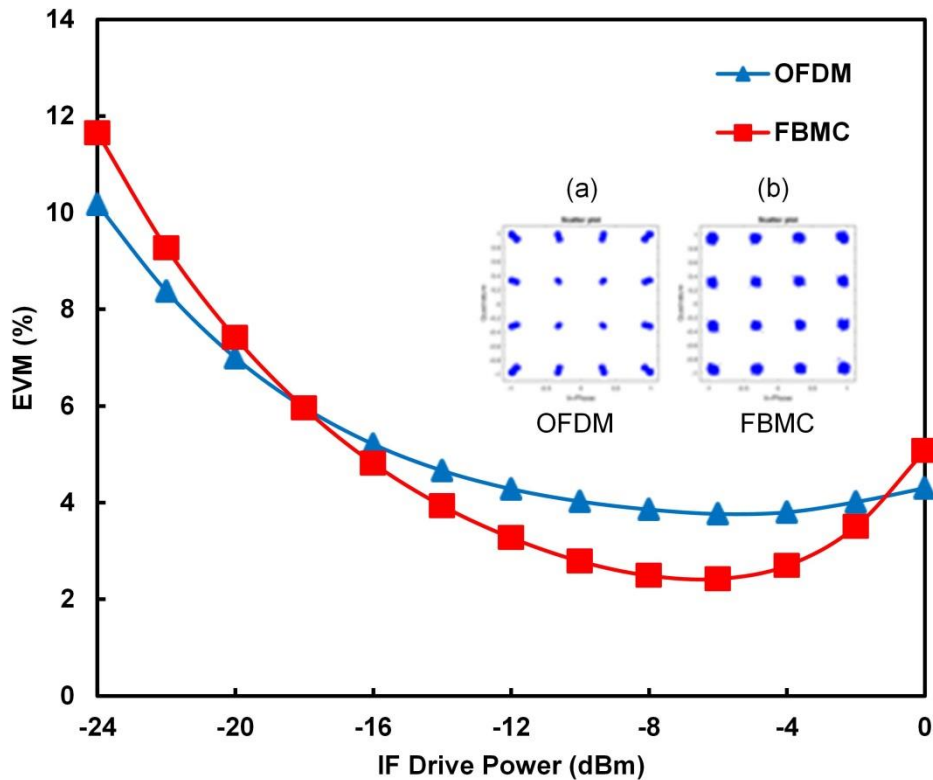


Figure 4.5: EVM vs IF drive power for mmWave IFoF using electrical LO (a) OFDM (b) FBMC

In practice, the frequency offset may arise due to transmit-receive LO mismatch or Doppler effect [157]. However, in the scenario presented here, it is assumed that the UE is stationary and fibre CD is negligible. Thus, LO mismatch is the only likely source of carrier frequency offset (CFO) in the architecture. This effect leads to loss of orthogonality among adjacent subcarriers which can result in severe ICI [157, 158]. For instance, the transceiver oscillators for standard communication systems are specified to have a maximum frequency tolerance of ± 20 ppm (parts per million). Consequently, for mmWave signal centred at 28GHz, the subcarrier spacing $\Delta f = BW/N_s$, where BW is the bandwidth of the signal and N_s is the total number of data subcarriers. Thus, the maximum frequency synchronisation error resulting from LO mismatch can be expressed as:

$$\delta f = 40\text{ppm} \times f_c = 40 \times 10^{-6} \times 28\text{GHz} = 1.12\text{MHz} \quad (4.9)$$

The normalised CFO is $\varepsilon = \delta f / \Delta f = 1.12\text{MHz} / 3.90625\text{MHz} \approx 0.3$ for a 1GHz bandwidth signal. This is relatively large and can significantly degrade system performance.

Alternatively, the stringent frequency synchronisation in upconversion/downconversion can be relaxed by employing photonic techniques for the mmWave upconversion. In addition, a

less complex receiver can be used for downconversion if symbols are not encoded on the carrier signal phase. Thus, mmWave transceiver can be simply and cost-efficiently implemented. The design and performance of these photonic transceivers are investigated next.

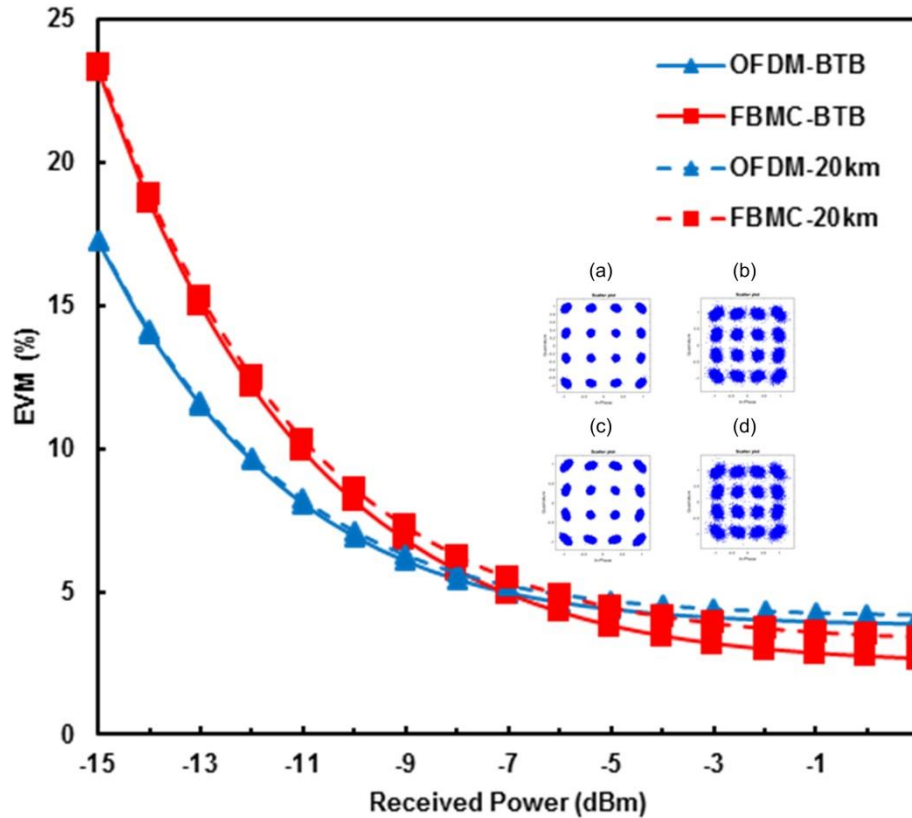


Figure 4.6: EVM vs Received optical power for mmWave IFoF using electrical LO (a) OFDM BTB (b) FBMC BTB (c) OFDM 20km (d) FBMC 20km

4.2.2. Millimetre-wave Upconversion using MZM

A common method of generating and remotely delivering mmWave carrier to the RRH photonicly is based on cascaded MZMs [128, 159]. Two MZMs are employed in this technique in which one is used for mmWave carrier generation while the second MZM is used for E/O conversion. Since the carrier is generated separately, the mmWave frequency can be changed based on the optical modulation employed at the carrier generation stage. Additionally, low bandwidth optical modulator can be used if E/O conversion is done before OCS to reduce the system complexity. Depending on the desired mmWave frequency and the flexibility requirements in terms of optical carriers for remote mmWave upconversion, the centre optical carrier can be suppressed, along with even harmonics generated to realise OCS modulation. In that way, first-order sidebands beat in the PD to generate the desired mmWave carrier. Thus, the LO frequency used in the mmWave upconversion stage is only half the desired mmWave carrier. Note that higher order sidebands can be generated at O/E

conversion as reported in [97, 98, 160-164]. However, these techniques are complex involving multiple stages of optical filtering, bias and phase shifters. While optical filter makes the system frequency dependent, bias and phase shifters require precise control, further increasing system complexity. Therefore, OCS for frequency doubling is a preferred option to realise the mmWave carrier due to its simplicity.

The diagram of cascaded MZMs transmitting IF signals and remote delivery of mmWave carrier is depicted in Figure 4.7, where inset (a)-(c) shows the optical spectrum after second MZM, and the received IF signal after downconversion for OFDM and FBMC, respectively.

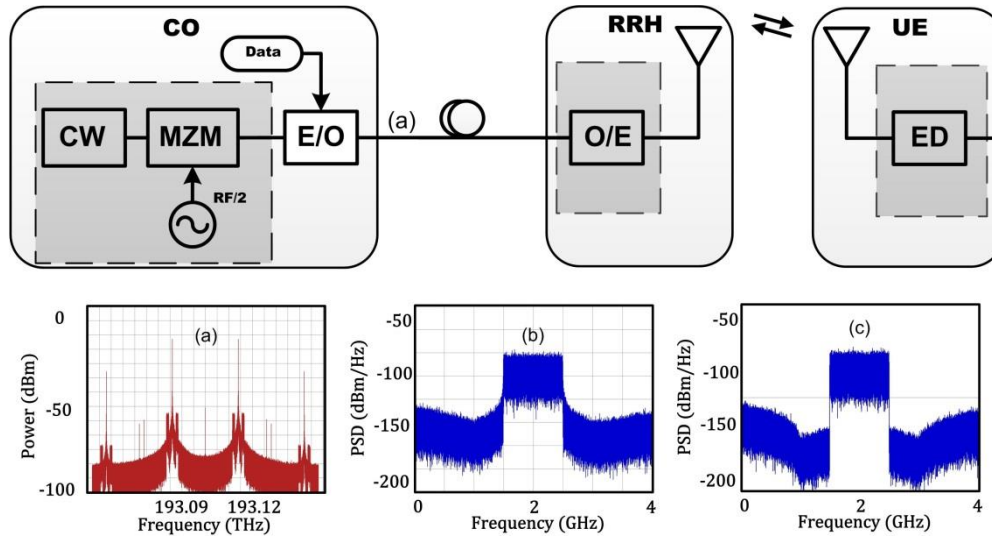


Figure 4.7: mmWave IFOF using cascaded MZMs (a) Optical spectrum after second MZM (b) The spectrum of IF OFDM after downconversion (c) The spectrum of IF FBMC after downconversion

For this scheme, the OCS generation is done in the shaded area of the CO as shown in Figure 4.7, before the E/O conversion. Note that it is possible to perform the E/O prior to OCS generation, by switching the order of modulation. In that way, E/O conversion will be part of the mmWave carrier generation. The main advantage of this technique compared to technique #2 is that CFO and phase noise is not an issue since an ED is used for downconversion in the UE. The ED is essentially a square law detector and it requires that the signal is carried on IF. Moreover, since it only detects envelope variation, carrier phase information is discarded.

The LO signal at the input of the first MZM is as given in (4.1), but the RF frequency ω_{RF} is half the desired mmWave carrier. The DE-MZM is biased at the null point to suppress the optical carrier and even order sidebands. Recall from (4.5), that the optical signal at the output of the MZM has both odd and even harmonics. When $V_{DC} = V_{\pi}$, the optical carrier and all even order sidebands are suppressed. Thus, the field at the output of the first MZM can be expressed as:

$$E_{MZM_1}(t) = \frac{E_i(t)}{2} \left\{ \pm 2 \sum_{n=1}^{\infty} (-1)^n J_{2n-1}(\pi m_{RF}) \cos((2n-1)\omega_{RF}t + \phi_{RF}(t)) \right\} \quad (4.10)$$

The OCS signal is then fed into the second MZM. Consequently, the IF signal is modulated on all odd order sidebands (see Figure 4.7 (a)). Since the beating in the PD involves only the first odd order sidebands, the field at the output of the second MZM considering $n = 1$ is given as:

$$E_{MZM_2}(t) = \frac{E}{2} \left\{ 2J_1(\pi m_{IF}) \cos((\omega_c + \omega_{RF})t + \hat{\phi}(t)) - 2J_1(\pi m_{IF}) \cos((\omega_c - \omega_{RF})t + \hat{\phi}(t)) \right\} \cdot \cos(\omega_{IF}t) \quad (4.11)$$

Where m_{IF} and ω_{IF} represents the modulation index and angular frequency of the IF signal, respectively. The phase term $\hat{\phi}(t)$ results from the phase fluctuation of the electrical LO and the laser. Ignoring the effect of fibre CD and considering only the beating between first-order sidebands, the photodetected signal is expressed as:

$$I(t) = |E_{MZM_2}(t)|^2 = \frac{E^2}{2} \left\{ \cos 2\omega_{RF}t + \hat{\phi}(t) + 2J_2\pi m_{IF} \left(\cos(\omega_{IF}t + \hat{\phi}(t)) + \frac{1}{2} \cos((2\omega_{RF} \mp \omega_{IF})t + \hat{\phi}(t)) \right) \right\} \quad (4.12)$$

The first term in (4.12) is the mmWave carrier generated by beating of the first order sidebands, the second and third term represents a copy of the IF signal at baseband and the IF signal modulated on the mmWave carrier, respectively. Note that the responsivity \mathfrak{R} has been dropped since it is assumed for simplicity to be equal to 1. In practice, terms outside the frequency of interest can be ignored, since they will be filtered out. Therefore, the transmitted mmWave signal can be expressed as:

$$I_{mmWave}(t) = \frac{m_{IF}}{2} \left\{ \left(\cos(2\omega_{RF}t) + \cos((2\omega_{RF} - \omega_{IF})t) + \cos((2\omega_{RF} + \omega_{IF})t) \right) \right\} \quad (4.13)$$

At the UE, an ED is used to downconvert the mmWave signal to IF before receiver baseband demodulation. Assuming an ideal ED with sufficient IF bandwidth, the IF signal is extracted by a lowpass filter (LPF), and it can be written as:

$$I_{IF}(t) = \frac{m_{IF}^2}{2} \cos(\omega_{IF}t) \quad (4.14)$$

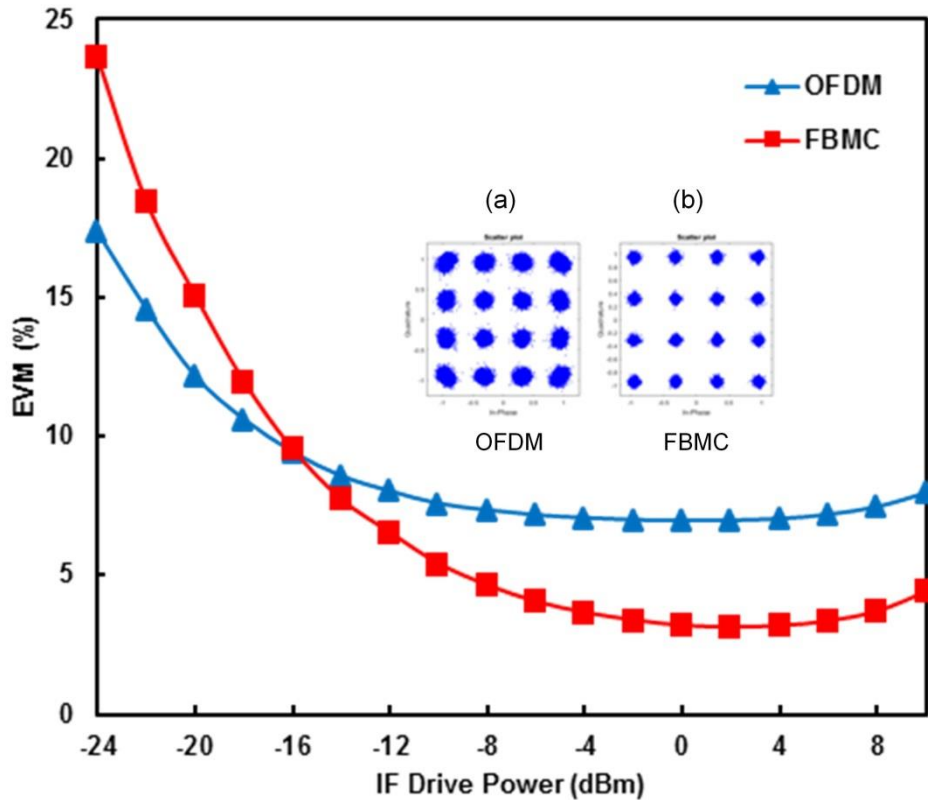


Figure 4.8: EVM vs IF drive power for mmWave IFoF using cascaded MZMs (a) OFDM (b) FBMC

A simulation testbed was implemented for mmWave IFoF architecture using cascaded MZMs, representing technique #3 in VPI, to evaluate the transmission performance of FBMC and OFDM, respectively. A real-valued data was generated in MATLAB having FFT size of 1024, where 128 subcarriers were used for data. The first 192 subcarriers were filled with zero to digitally shift the time-domain signal to IF. Also, corresponding negative frequencies were filled with the complex conjugate of the data symbols for HS, to realise a real-valued IF signal after IFFT. A 16 samples CP was appended to each OFDM symbol. After passing through a 8GSa/s 10-bits DAC, the IF signal bandwidth was 1GHz, centred at 2GHz which was then amplified by an amplifier providing 30dB gain. Subsequently, the IF power was swept between -24dBm and +10dBm using an electrical attenuator in optical BTB, to investigate the effect of MZM nonlinearity at E/O conversion.

The EVM as a function of IF drive power is shown in Figure 4.8 and the constellation at an optimum drive of +4dBm are inset in Figure 4.8. As previously, the EVM values are high for

low drive powers, which was primarily due to low SNR at E/O conversion. Nevertheless, OFDM exhibits better performance than FBMC at low IF powers. The EVM then decreased gradually until the IF power reached -16dBm, where the corresponding EVM value was 9.4% and 9.5% for OFDM and FBMC respectively. EVM values for FBMC reduced steadily up to +2dBm drive power while OFDM reached an error floor at -8dBm IF drive power. This suggests that FBMC is more susceptible to noise and will require a high SNR system for optimal performance. On the other hand, OFDM exhibits better resilience to noise but it does not benefit from increased drive power. Furthermore, as the IF power increased beyond +2dBm, the MZM nonlinearity effect comes into play becoming more obvious in FBMC than in OFDM.

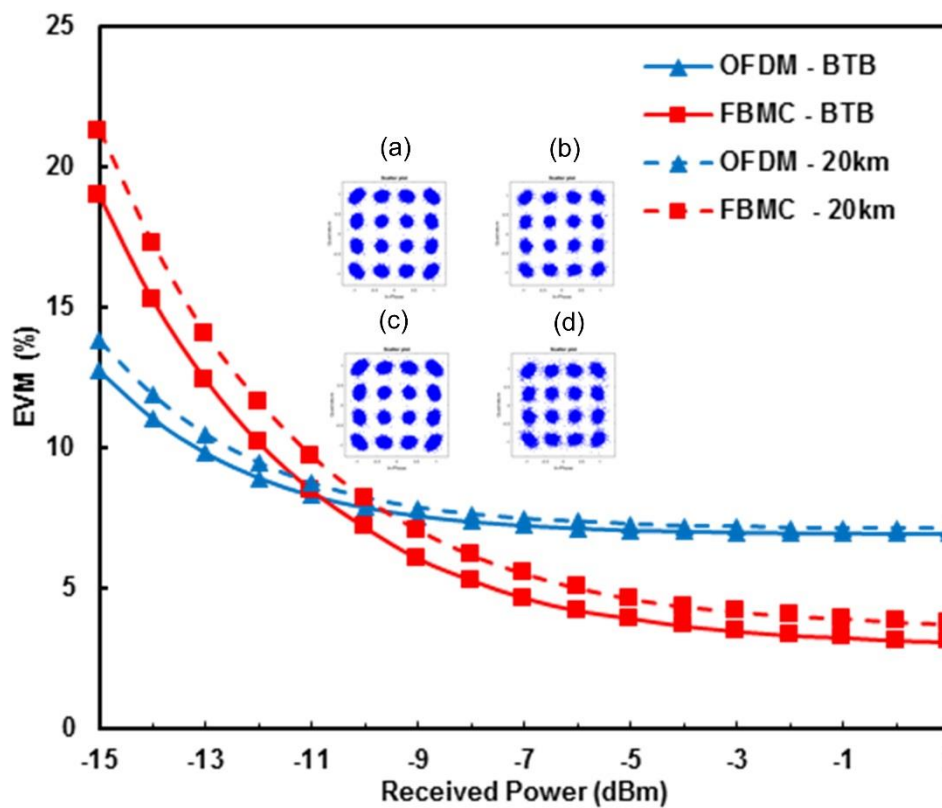


Figure 4.9: EVM vs Received optical power for mmWave IFoF using cascaded MZMs (a) OFDM BTB (b) FBMC BTB (c) OFDM 20km (d) FBMC 20km

Although, OFDM and FBMC exhibit the same EVM value at -16dBm drive power, the optimum IF power was considered to be +2dBm for both signals, since it is the EVM value for both waveforms just before the MZM nonlinear response starts to degrade the EVM. This value was subsequently used to investigate the impact of received optical power on the IF signals. The EVM as a function of received optical power is shown in Figure 4.9. A similar trend to the results for the previously investigated techniques can be observed, with OFDM reaching an error floor at -10dBm received power while the EVM value for FBMC reduced gradually until -5dBm before reaching an error floor. The constellation plots are

shown in inset (a) - (d) of Figure 4.9, which corresponds to -9dBm received power at BTB and after 20km fibre, respectively. Notice that the EVM values for FBMC are worse at low received powers even though it was more than 3% better than OFDM at optimum IF power. In technique #4, the order of modulation is changed as previously stated, thereby having the modulating signal as part of the mmWave carrier generation. Also, a low-cost direct modulation is employed at E/O to further drive down the cost of transceivers. Consequently, low power modulation is necessary to operate the DML to ensure that the transfer function is in the linear regime and free from distortion due to clipping.

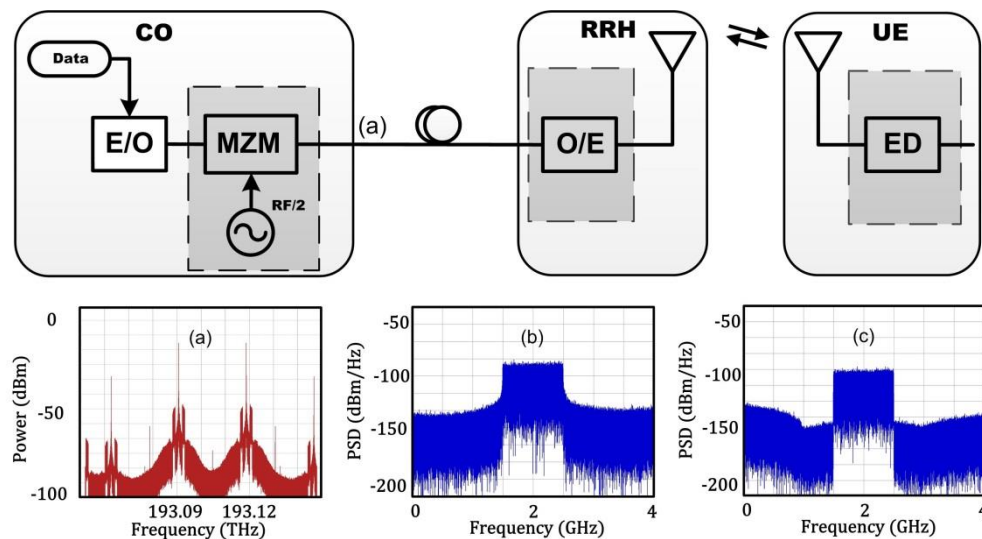


Figure 4.10: mmWave IFoF using DML and MZM (a) Optical spectrum after the MZM (b) The spectrum of IF OFDM after downconversion (c) The spectrum of IF FBMC after downconversion

Figure 4.10 shows the schematic of mmWave IFoF architecture using DML and MZM. The OCS spectrum after the MZM is shown in inset (a) of Figure 4.10 where the IF signal is superimposed on all odd sidebands. The DML threshold current was 37mA and was biased at 100mA which is well above the threshold current. At this bias voltage, the laser RIN and linewidth is ~ 155 dB/Hz and ~ 1 MHz, respectively. After passing through the DAC, the signal was amplified and fed into the laser for direct modulation. As before, the IF power was swept from -24dBm to -8dBm to evaluate the EVM of OFDM and FBMC, respectively.

The EVM vs IF power for mmWave IFoF using DML and MZM is shown in Figure 4.11. Interestingly, the EVM values between -24dBm and -12dBm improved by only 2.8% and 3.5% for OFDM and FBMC after which the EVM starts to degrade due to laser clipping. As previously stated, DML requires a lower modulation index compared to MZM, therefore, the EVM value at -24dBm is much better than it was for mmWave IFoF using cascaded MZMs. Likewise, nonlinear distortion sets in at much lower drive powers since DML is typically driven by a lower power compared to EML. The optimum drive power was found to be -12dBm, which was used for subsequent investigation.

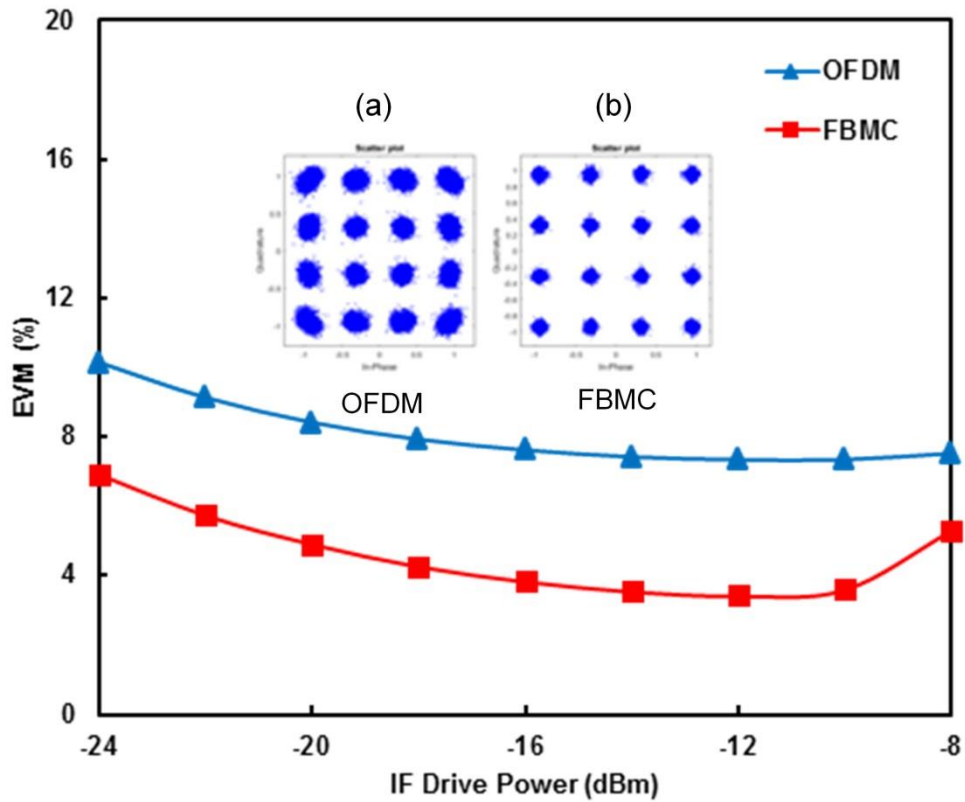


Figure 4.11: EVM vs IF drive power for mmWave IFoF using DML and MZM (a) OFDM (b) FBMC

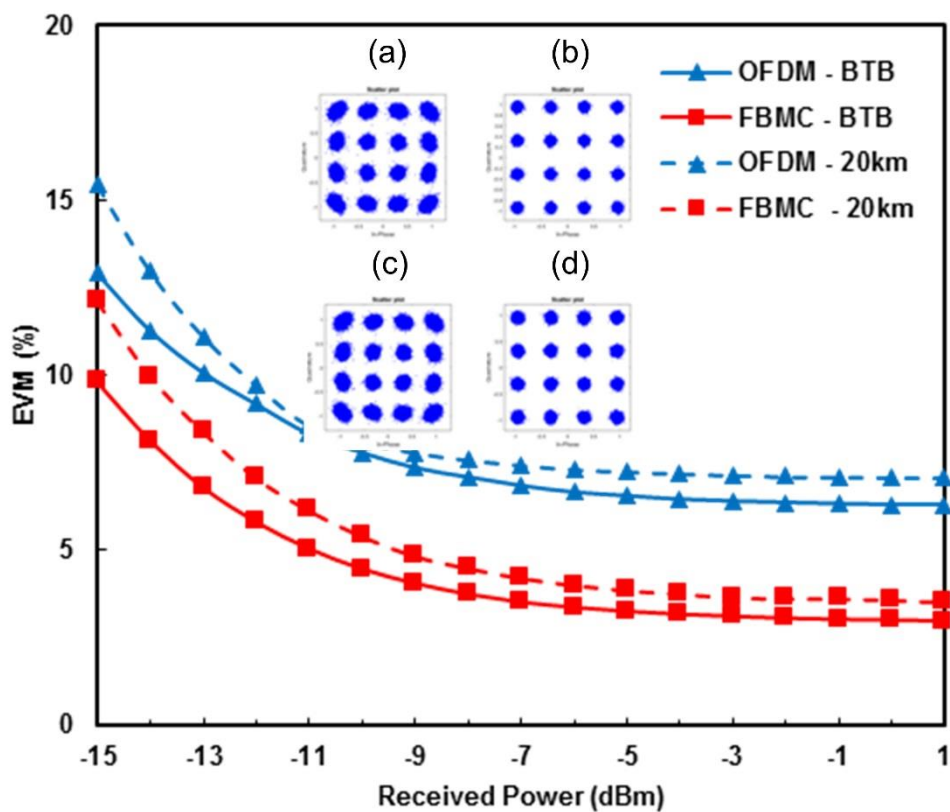


Figure 4.12: EVM vs Received optical power for mmWave IFoF using DML and MZM (a) OFDM BTB (b) FBMC BTB (c) OFDM 20km (d) FBMC 20km

Figure 4.12 shows the EVM vs received power at BTB and after 20km fibre transmission, respectively. The constellation at -9dBm received power for OFDM and FBMC are inset in Figure 4.12 (a)-(d). The EVM values reduce gradually until -9dBm, after which an error floor was reached for OFDM and FBMC respectively. In addition, the EVM penalty after 20km was less than 0.5% and 1% for OFDM and FBMC, respectively. In terms of complexity and cost, employing DML reduces the component cost in the CO. However, DML typically have low modulation bandwidth which may limit the deployment to low-cost short-reach networks. Further, since the transmitted signal is a DSB, fibre CD effect will limit the transmission distance.

4.2.3. Millimetre-wave Upconversion using Laser heterodyning

Technique

To avoid high-frequency LO and optical modulator electrical bandwidth bottleneck, associated with generating mmWave using frequency multiplication, laser heterodyning technique has been proposed as a cost-efficient alternative for generating frequency tuneable mmWave signals [90, 120, 128]. A wide range of mmWave frequency can be realised, limited only by PD bandwidth. In addition, since high-speed optical modulators and RF devices are avoided in the CO and RRH, system complexity is significantly reduced. However, employing unlocked laser sources for mmWave upconversion implies that the phase fluctuations of the optical carriers are uncorrelated, which in effect will degrade the system performance [110, 111]. The laser phase noise is usually characterised by its linewidth, thus a typical DFB laser having 10MHz linewidth will introduce higher phase noise compared to a 100kHz linewidth ECL. The phase noise effect becomes worse when it interacts with fibre CD, resulting in amplitude noise which usually falls within the useful signal bandwidth. This effect was referred to as converted phase noise (CPN) in [165]. While phase noise is not an issue when the self-homodyne receiver is employed in downconverting digital baseband signals upconverted to mmWave using uncorrelated laser heterodyning as reported in [110], phase noise will severely impact multicarrier waveforms such as OFDM and FBMC, resulting in ICI. To this extent, the impact of laser phase noise on the mmWave OFDM signal generated by laser heterodyning has been investigated in [111, 151]. However, the effect of phase noise on the mmWave signal generated by laser heterodyning has not been investigated on FBMC to date.

Therefore, the mmWave upconversion by laser heterodyning was implemented in VPI to investigate the transmission of FBMC over such architecture. An ED was used for mmWave downconversion since it discards the signal phase information. In order to compare their performance, OFDM was also transmitted over the architecture. Furthermore, the system

parameters are the same as in previous schemes to enable a fair comparison among the mmWave upconversion techniques.

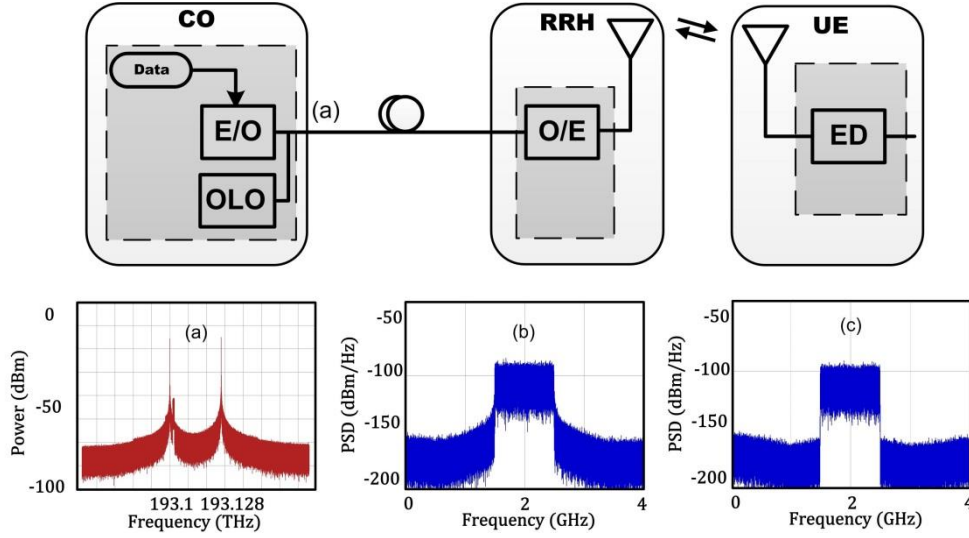


Figure 4.13: mmWave IFOF using Laser Heterodyning (a) Optical spectrum after the optical coupler (b) The spectrum of IF OFDM after downconversion (c) The spectrum of IF FBMC after downconversion

The schematic of mmWave upconversion architecture using unlocked lasers is depicted in Figure 4.13. The IF signal modulates the DE-MZM generating an OSSB at its output. A 3dB OC was used to combine the OLO from a TLD with the OSSB signal. The centre frequency of the OLO was set to 28GHz apart from the ML centre frequency. Inset (a) - (c) of Figure 4.13 shows the downstream optical signal after the coupler, OFDM and FBMC after downconversion, respectively. At the RRH, the optical carriers beat in the PD to generate the mmWave signal. The electric field of the lasers can be written as:

$$E_{ML}(t) = E_{ML} \cos(\omega_{ML}t + \phi_{ML}(t)) \quad (4.15)$$

$$E_{LO}(t) = E_{LO} \cos(\omega_{LO}t + \phi_{LO}(t))$$

where E_{ML} , $\phi_{ML}(t)$, E_{LO} and $\phi_{LO}(t)$ are the field amplitude of the ML, phase fluctuation of the ML, field amplitude of the LO laser and phase fluctuation of the LO laser, respectively. Assuming an IF signal modulates the laser to realise an OSSB signal after E/O conversion, which can be expressed as:

$$E_o(t) = E_{ML}(t)[1 + x(t)] \quad (4.16)$$

where $x(t) = \cos(\omega_{IF}t)$, and ω_{IF} represents the angular frequency of the IF signal. The OSSB signal is then combined with the optical carrier from the LO laser by an OC. Neglecting the loss due to the OC, the combined signal can be written as:

$$E_{oc}(t) = E_{ML}(t)[1 + x(t)] + E_{LO}(t) \quad (4.17)$$

After fibre transmission, the composite signals beat in the PD and the output can be expressed as:

$$I(t) = |E_{oc}(t)|^2 \quad (4.18)$$

$$= \left\{ \begin{aligned} & (E_{ML}^2(t) + E_{LO}^2(t)) + 2E_{ML}^2(t)x(t) + E_{ML}^2x^2(t) \\ & + 2E_{LO}(t)E_{ML}(t) + 2E_{LO}(t)E_{ML}x(t) \end{aligned} \right\}$$

The PD output in (4.18) comprises of the DC terms, a high frequency component, a copy of the IF signal, second order intermodulation term, the mmWave carrier term and the desired mmWave signal, respectively. Again, unwanted terms can be ignored since they will be experimentally filtered out by HPA and a BPF. Thus, the mmWave signal emitted from the mmWave antenna can be derived from the last two terms in (4.18) and can be written as:

$$I(t) = 2\{E_{ML}(t)E_{LO}(t) + E_{ML}(t)E_{LO}x(t)\} \quad (4.19)$$

$$= 2 \left\{ \left(\frac{E_{ML}E_{LO}}{2} (\cos(\omega_{LO}t - \omega_{ML}t + (\phi_{LO} - \phi_{ML})t) + \cos(\omega_{LO}t + \omega_{ML}t + (\phi_{LO} + \phi_{ML})t)) \right) [1 + x(t)] \right\}$$

$$= 2RE_{ML}E_{LO} \{ \cos(\omega_{mm}t + \Delta\phi(t)) + \cos((\omega_{mm} + \omega_{IF})t + \Delta\phi(t)) \}$$

where $\omega_{mm} = \omega_{LO} - \omega_{ML}$ is the desired mmWave carrier. $\Delta\phi(t)$ results from the mixing of the phase noise of the lasers. An ED is used in the UE to downconvert the mmWave signal to IF. Considering only the term of interest, the output of the ED can be expressed as:

$$I_{ED}(t) = xE_{ML}E_{LO} \left\{ \begin{aligned} & \cos(\omega_{mm}t - (\omega_{mm} + \omega_{IF})t + (\Delta\phi(t) - \Delta\phi(t))) \\ & + \cos(\omega_{mm}t + (\omega_{mm} + \omega_{IF})t + (\Delta\phi(t) + \Delta\phi(t))) \end{aligned} \right\} \quad (4.20)$$

It can be seen from (4.20) that the IF signal is recovered successfully, free from phase noise using an ED. After passing through a LPF, the resulting IF signal can be expressed as:

$$I_{ED}(t) = xE_{ML}E_{LO}\cos(\omega_{IF}t) \quad (4.21)$$

Although phase noise is cancelled at downconversion using an ED, CPN due to fibre CD will significantly impact the system performance at O/E. In the previously investigated architectures, the beating terms were assumed to be phase correlated since the optical carriers were generated from the same laser source. Therefore, for short fibre transmission and moderate signal bandwidth, the optical tones remained correlated, hence, the CPN effect was minimised. However, since free-running lasers are employed for mmWave upconversion in this architecture, the impact of CPN will be more noticeable.

As previously, OFDM and FBMC were transmitted over this architecture to compare their performance in terms of IF drive power at E/O conversion and received optical power at O/E conversion.

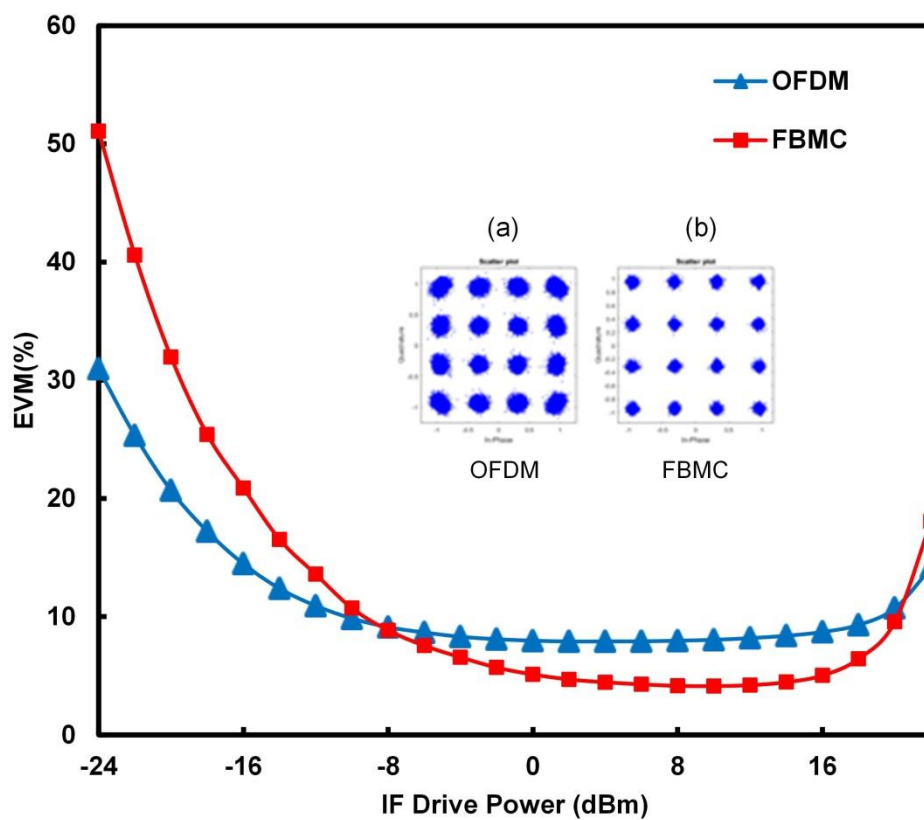


Figure 4.14: EVM vs IF drive power for mmWave IFoF using laser heterodyning (a) OFDM (b) FBMC

Figure 4.14 shows the EVM of OFDM and FBMC as a function of IF drive powers, the trend can be observed as similar to previous architectures. FBMC exhibit worse performance compared with OFDM at low drive powers and as the power increased to -8dBm, OFDM reached an error floor while further EVM improvement was observed for FBMC. The received constellations at +4dBm are shown as an inset in Figure 4.14 for OFDM and FBMC, respectively. For drive powers higher than +4dBm, EVM starts to degrade due to MZM nonlinearity. Therefore, the optimum drive power was set to +4dBm for subsequent investigation.

The EVM as a function of received optical power is shown in Figure 4.15, and the received constellations at -9dBm are inset in Figure 4.15 for BTB and 20km, respectively. The EVM penalty after 20km at -9dBm received power was less than 0.5% and 1% for OFDM and FBMC, respectively. It can also be noticed that both OFDM and FBMC reached an error floor at -5dBm. Observe that EVM values are high for this technique compared to other mmWave techniques previously investigated. This is due to excess noise generated in the PD from the laser phase noise.

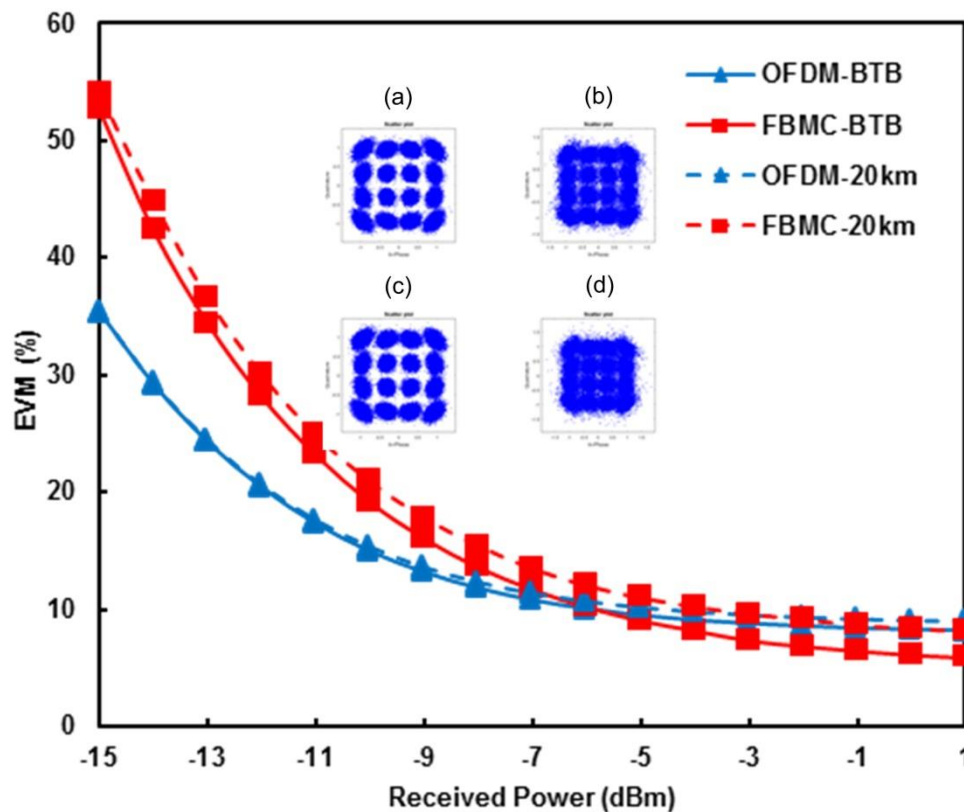


Figure 4.15: EVM vs Received optical power for mmWave IFOF using laser heterodyning (a) OFDM BTB (b) FBMC BTB (c) OFDM 20km (d) FBMC 20km

Although, the phase noise of the generated mmWave carrier is theoretically cancelled using ED for downconversion as shown in (4.21), prior to upconversion, the interaction between the optical carriers used for upconversion with CD results in amplitude noise which further degrades the system performance. Since this architecture offers the benefit to achieve a wide-range frequency tunability while avoiding high-speed optical modulators and high-frequency LO for upconversion/downconversion. The laser heterodyning technique can be adopted flexibly as MFH architecture to support densely spaced mmWave 5G small cells. The effect of each noise sources and its contribution to the received SNR is further investigated in chapter 5 so as to optimise the system performance for future 5G mmWave small cell MFH.

4.3. Comparison of Millimetre-wave Techniques

In the previous section, 5 mmWave upconversion techniques have been investigated, in terms of their performance at E/O and O/E conversion, respectively. To compare the mmWave upconversion techniques, a summary of the results are shown in Table 4-2, for OFDM and FBMC based on the investigated parameters. In all cases, the EVM value at the optimum drive for FBMC is better than for OFDM ranging from 1.4% to 4%. However, the benefit of high SNR at E/O conversion disappears in FBMC for low received powers at O/E conversion. In addition, for a fair comparison, -9dBm was considered as a reference received optical power in all upconversion techniques. At this received power, the EVM of FBMC is worse compared to OFDM in 4 of the investigated techniques. However, as the SNR improves, FBMC exhibits better EVM values compared to OFDM. This suggests that in the optical transmission scenario where channel delay spread is low, the performance of FBMC will be limited at low SNR. It should be recalled that the waveforms were hard-clipped prior to the DAC, to achieve similar PAPR. However, the sensitivity of FBMC to nonlinearity is obvious in the 5 investigated techniques for high drive powers. Note that the electrical amplifier (EA) before the MZM was assumed to have operated in the linear regime thus the nonlinear impairments experienced by the signals was due to the nonlinear transfer function of the MZM. The impact of nonlinearity due to PA will be studied in chapter 6.

To further analyse the performance of the architectures, the received power at O/E conversion required to achieve the 12.5% EVM threshold as set out by the 3GPP for 16QAM LTE signal [166] was considered. The EVM and corresponding power at which the EVM was achieved are illustrated in Table 4-2. The receiver sensitivity is lowest in #5 and highest in #4. The noise level in #5 is increased due to RIN of the lasers and considering that the laser linewidth is increased, the effect of CPN also increased, thus requiring more power to achieve the desired SNR. Moreover, OFDM shows 2dB better sensitivity compared to FBMC in #5. On the other hand, FBMC has 2dB better sensitivity in #4 compared to OFDM. This is because FBMC exhibits 6dB better SNR at E/O conversion in #4. In addition, the laser was biased well above the threshold, so RIN is relatively low and the effect of CPN is reduced since the beating terms are assumed to be phase correlated for short fibre transmission. However, #4 may be limited by modulation bandwidth if the IF signal bandwidth is wide as expected in mmWave transmission. Furthermore, to realise OSSB modulation which makes the system robust against CD for long reach fibre transmission, an optical filter will be required to remove one of the sidebands. Therefore, due to low modulation bandwidth and susceptibility to fibre CD, #4 may be limited to short distance low-cost implementation such as indoor DAS. On the contrary, # 5 can achieve OSSB and is not limited by modulation bandwidth as typical MZM has an electrical bandwidth of the order of 10s of GHz.

Additionally, the architecture is simple and can be easily reconfigured to realise a wide range of mmWave frequency. This is beneficial since there is a huge bandwidth in the mmWave spectrum that can potentially be employed for 5G. Hence, #5 is a more attractive option as it appears suitable for various transmission scenarios, but noise limitation which is typical in ARoF limits the dynamic range. Therefore, it is important to optimise the SNR in #5, by further studying the effect of noise if the architecture is to be employed for 5G heterogeneous access networks. This noise impact and SNR optimisation are investigated in the next chapter.

Table 4-2: Performance Comparison of the investigated mmWave upconversion Techniques

E/O and O/E performance	OFDM	FBMC
#1: mmWave RoF using electronic LO		
Optimum Drive Power (dBm)	-8dBm	-8dBm
EVM (%) at Optimum Drive Power	4.2%	2.1%
EVM (%) penalty after 20km at -9dBm	0.5%	0.2%
Receiver Sensitivity at 12.5% EVM Threshold (20km)	-9dBm	-11dBm
#2: mmWave IFoF using electronic LO		
Optimum Drive Power (dBm)	-6dBm	-6dBm
EVM (%) at Optimum Drive Power	3.8%	2.4%
EVM (%) penalty after 20km at -9dBm	0.8%	1%
Receiver Sensitivity at 12.5% EVM Threshold (20km)	-13dBm	-12dBm
#3: mmWave IFoF using Cascaded MZMs		
Optimum Drive Power (dBm)	2dBm	2dBm
EVM (%) at Optimum Drive Power	6.9%	3.1%
EVM (%) penalty after 20km at -9dBm	1.5%	1.8%
Receiver Sensitivity at 12.5% EVM Threshold (20km)	-13dBm	-12dBm
#4: mmWave IFoF using DML and MZM		
Optimum Drive Power (dBm)	-12dBm	-12dBm
EVM (%) at Optimum Drive Power	7.4%	3.4%
EVM (%) penalty after 20km at -9dBm	0.5%	0.8%
Receiver Sensitivity at 12.5% EVM Threshold (20km)	-13dBm	-15dBm
#5: mmWave IFoF using Laser Heterodyning		
Optimum Drive Power (dBm)	4dBm	4dBm
EVM (%) at Optimum Drive Power	7.9%	4.5%
EVM (%) penalty after 20km at -9dBm	0.4%	1.7%
Receiver Sensitivity at 12.5% EVM Threshold (20km)	-8dBm	-6dBm

4.4. Summary

In this chapter, five mmWave upconversion techniques have been investigated in terms of their performance at E/O at O/E conversion, respectively. The first two techniques are based on conventional RoF and IFoF architectures, using an electrical LO for mmWave upconversion. The third and fourth architectures employed two stages optical modulation, using a combination of electrical LO and an optical modulator for mmWave upconversion. In addition, the third architecture employed a common two stage upconversion using cascaded MZMs while the E/O MZM was replaced by a DML in the fourth architecture, to reduce the system cost. The fifth architecture relies on a tunable optical source to provide the LO required for mmWave upconversion and therefore, referred to as laser heterodyning.

Theoretical analysis showed that for the first two architectures, frequency and phase offset can severely degrade the system performance if present as high-frequency LO was employed for upconversion/downconversion. Moreover, these architectures are complex and may not be suitable for the massive deployment of mmWave small cell BSs in 5G networks. The third and fourth architectures, on the other hand, reduce the frequency requirement by half, using MZM for frequency doubling. These techniques are more convenient to implement because the stringent frequency/ phase locking requirements for the previous techniques is eliminated by using an ED for downconversion at the UE receiver. However, high-speed optical modulator is employed for upconversion which is an expensive component. The system cost can be reduced by employing a DML as in technique #4, but may be limited by DML modulation bandwidth. The fifth technique employed an OLO for mmWave upconversion, thus eliminating the need for a high-speed optical modulator. Additionally, using OSSB modulation improves robustness against fibre CD, allowing the possibility of long reach transmission. Moreover, the system can be reconfigured to achieve any mmWave carrier as desired, which is subject to the limit of PD bandwidth.

The performance of OFDM and FBMC has been investigated over the five architectures. It was found that FBMC exhibits worse EVM compared to OFDM when the SNR is low at E/O and O/E, respectively. The EVM value improves, however, as the SNR increased, indicating that FBMC requires a high SNR system for optimal performance. This phenomenon was more obvious for the fifth technique where two lasers were employed for mmWave upconversion because the noise due to laser RIN doubled. Also, the laser linewidth was doubled which will equally contribute to the effect of CPN at O/E conversion.

It was observed in the simulation that nonlinearity of the E/O interface affects FBMC more than OFDM as the EVM degradation was higher for powers above the optimum.

5. Impact of Noise on Millimetre-Wave Signal Generated using Laser Heterodyning

5.1. Introduction

In the previous chapter, 5 mmWave upconversion techniques was investigated subject to the impact of E/O and O/E conversion on the transmitted signal. Although limited by the noise of the mmWave generator, from the economic point of view, mmWave upconversion employing laser heterodyning appears to be a desirable technique in scaling the traditional RoF architecture to accommodate mmWave signals [128, 167]. This is necessary for dense deployment of mmWave small cell BSs in a 5G MFH system. However, as observed in the previous chapter, noise limits system performance. Therefore, the contribution of different noise sources and their effects on the system SNR is investigated in this chapter. By quantifying the impact of noise generated at specific points, the system performance can be optimised in terms of SNR.

Firstly, an expression for the system SNR is derived in terms of noise power spectral density (PSD). The impact of different noise sources are then studied by simulation. The system performance evaluation is done by observing SNR degradation and EVM, respectively. SNR degradation is calculated by considering the overall system SNR with and without the noise contribution from the component that introduces noise into the system. As previously, OFDM and FBMC waveforms are employed for the analysis and their transmission performance are compared.

Finally, to optimise the system performance in the presence of noise, the adaptive modulation technique is applied to select a subcarrier modulation level based on CSI feedback from the receiver [5]. To further improve the SE with adaptive modulation, while keeping in mind the system complexity, an intra-symbol frequency domain averaging (ISFA) technique [168] is applied to improve the CE by averaging the CFR over multiple adjacent subcarriers. The result shows significant improvement in the SE compared to when adaptive modulation is used without ISFA.

5.2. SNR of Millimetrewave IF over Fibre Signal Generated using Laser Heterodyning

In this section, we derive an expression for the system SNR in terms of noise contribution from the transmitter, channel and receiver as depicted in Figure 5.1. The noise originates from uncorrelated sources and therefore can be modelled as a zero-mean Gaussian random process. The SNR degradation due to the nonlinearity of the E/O interface can be ignored

since IF drive power is fixed throughout the investigation. Furthermore, since the effect of PA nonlinearity will be investigated in the next chapter, all electrical amplifiers are operated in the linear regime and therefore do not contribute to the system impairments.

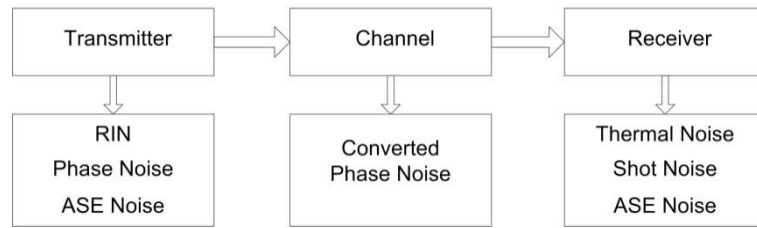


Figure 5.1: Noise Source in mmWave System using laser heterodyning

The type of noise generated by each component and the source is shown in Table 5-1. It can be observed that noise arises from a source due to the properties of the component. However, since the interaction of laser phase noise and dispersive fibre link results in laser phase noise being converted to intensity noise, the CPN is considered to originate from the fibre [165]. Also, ASE noise from the optical amplifier depends on where the amplifier is employed within the system.

Table 5-1: Source and type of noise generated by components

Noise	Source	Component	Noise Type
RIN	Intensity fluctuations	Laser	Additive
Phase Noise	Phase fluctuations	Laser	Multiplicative
ASE	Spontaneous emission	Optical Amplifier	Beating
CPN	Chromatic Dispersion	Optical Fibre	Multiplicative
Thermal	Thermal agitation	PD	Additive
Shot	Photons fluctuation	PD	Additive

5.2.1. Noise Generated in the Transmitter

5.2.1.1. Relative Intensity Noise

The intensity noise is an intrinsic property of a laser which results from optical intensity fluctuations. Generally, spontaneous emission and thermal variations are responsible for the fluctuations in optical intensity. The electric field of a laser can be written in terms of the constant and time-varying fields [169]:

$$E(t) = [E_o + \Delta E(t)]\exp[j\omega t + \phi(t)] \quad (5.1)$$

where $P_o = E_o^2$, ω_c and ϕ are the average optical power, angular centre frequency and random phase of the laser, respectively. Laser RIN is specified as the ratio of the time

averaged intensity fluctuations to the average optical power emitted by the laser, and it can be expressed as:

$$RIN = \frac{\langle \Delta P^2 \rangle}{P_o^2} \quad (5.2)$$

where ΔP is the time varying fluctuations in the laser intensity and $\langle \rangle$ denotes the time average. The PSD of the intensity noise $\Delta P(t)$ can be expressed in terms of its autocorrelation function using the Weiner-Kinchintin theorem as [116]:

$$S_{\Delta P}(\omega) = \frac{1}{2T} \int_{-T}^T R_{\Delta P}(\tau) \exp(-j\omega\tau) d\tau \quad (5.3)$$

where $R_{\Delta P} = \langle \Delta P(t)\Delta P(t + \tau) \rangle$ is the autocorrelation function of $\Delta P(t)$. T represents the observation interval. Thus the PSD of RIN in (5.2) can be expressed as:

$$S_{RIN}(\omega) = \frac{S_{\Delta P}(\omega)}{P_o^2} \quad (5.4)$$

It can be seen from (5.4) that RIN contribution to the receiver noise is dependent on average optical power. Therefore, RIN can exceed other noise effects in the receiver at low laser output powers.

5.2.1.2. Laser Phase Noise

Considering a quasi-monochromatic laser operating far above the lasing threshold, phase fluctuations of such laser is primarily due to quantum noise as a result of spontaneous emission in the laser's gain medium, which results in finite linewidth of the laser. Due to the intrinsic property of noise and the central limit theorem, phase fluctuations can be treated as a stationary zero-mean Gaussian process using small signal approximation [116]. However, laser phase fluctuation exhibits a nonstationary random walk. Therefore, the phase fluctuation of the optical carrier in (5.1) is characterised by the Wiener-Levy process [116, 170]. However, the laser electric field is a zero-mean Gaussian random process. In addition, the frequency fluctuation is a constant, and the PSD of frequency noise is proportional to the phase noise PSD. Therefore, the autocorrelation function of the laser electric field can be written as:

$$R_E(t) = \langle E(t)^* E(t + \tau) \rangle \quad (5.5)$$

Considering the phase fluctuation part in (5.5), the autocorrelation can be further expressed as:

$$R_E(t) = Re[\langle j\Delta\phi(t, \tau) \rangle \exp(j\omega_c t)] \quad (5.6)$$

$\Delta\phi(t, \tau) = \phi(t + \tau) - \phi(t)$ is the phase jitter between t and $t + \tau$ having probability density function between t and $t + \tau$ which can be written as:

$$W_T[\Delta\phi(\tau)] = \frac{1}{\sqrt{2\pi\langle\Delta\phi^2(\tau)\rangle}} \exp\left[-\frac{\Delta\phi^2(\tau)}{2\langle\Delta\phi^2(\tau)\rangle}\right] \quad (5.7)$$

$\langle\Delta\phi^2(\tau)\rangle$ is the mean-squared phase jitter, and since $\Delta\phi(t, \tau)$ follows Gaussian distribution, there is a well-known relation:

$$\langle j\Delta\phi(t, \tau) \rangle = \exp\left[-\frac{1}{2}\langle\Delta\phi^2(\tau)\rangle\right] \quad (5.8)$$

Inserting (5.8) into (5.5) we have:

$$Re\{\langle \exp[j\Delta\phi(t, \tau)] \exp(j\omega_c t) \rangle\} = \exp\left[-\frac{1}{2}\langle\Delta\phi^2(\tau)\rangle\right] \cos\omega_c t \quad (5.9)$$

The laser spectrum is obtained by taking the Fourier Transform of (5.9):

$$S_E(\omega) = Re \int_0^{\infty} \exp(-[1/T_{coh} + j\omega]t) dt \quad (5.10)$$

where T_{coh} represents the laser coherent time which is related to the laser linewidth and can be written as:

$$\Delta\nu = \frac{1}{\pi T_{coh}} \quad (5.11)$$

By solving (5.10), it is easy to see that the laser has a Lorentzian line shape:

$$\begin{aligned} S_E(\omega) &= Re \left[\frac{\exp(-[1/T_{coh} + j\omega]t)}{-[1/T_{coh} + j\omega]} \right]_0^{\infty} \\ &= \frac{1/T_{coh}}{(1/T_{coh})^2 + (\omega - \omega_c)^2} \\ &= \frac{\Delta\nu}{\pi(\Delta\nu)^2 + (\omega - \omega_c)^2} \end{aligned} \quad (5.12)$$

The frequency noise spectrum of the laser above is white noise (i.e. constant), and it is related to the phase noise PSD through Ω , which represents the noise frequency. Hence, the PSD of phase noise can be expressed as:

$$S_\phi(\omega) = S_f(\omega)\Omega^{-2} \quad (5.13)$$

The mean-squared phase jitter may be expressed in terms of the laser instantaneous frequency-fluctuations spectrum $S_f(\omega)$:

$$\langle \Delta\phi^2(\tau) \rangle = R_\phi(\tau) = \frac{1}{2\pi\Omega^2} \int_{-\infty}^{\infty} |H(\omega)|^2 S_f(\omega) d\omega \quad (5.14)$$

where $H(\omega) = \frac{\sin(\frac{\omega\tau}{2})}{\frac{\omega\tau}{2}}$ is the transfer function of an LPF which has impulse response $h(t) =$

$$\begin{cases} \frac{1}{|\tau|} & -\frac{|\tau|}{2} < t \leq \frac{|\tau|}{2} \\ 0 & \text{others} \end{cases}. \text{ The mean-squared phase jitter increases linearly with time. Therefore, (5.14)}$$

results in [171]:

$$\langle \Delta\phi^2(\tau) \rangle = 2\Delta\nu|\tau| \quad (5.15)$$

$2\Delta\nu$ is the angular full width at half maximum (FWHM) of the laser field spectrum. Note that the PSD of laser phase noise expressed in (5.13) is considered as a general case, for a laser subject to quantum noise and exhibiting Shawlow-Tones linewidth [171].

Due to square-law detection of the PD, the phase noise is converted to intensity noise which can be as a result of delay between the two arms of the MZM interferometer or time delay due to fibre CD [172, 173]. This is usually referred to as converted RIN to distinguish it from the laser intrinsic RIN [174]. Here, we consider time delay due to the fibre CD as a source of converted RIN. Furthermore, to distinguish its effect from laser intrinsic RIN, it is referred to as CPN in this thesis since the phase noise term in the mmWave signal is cancelled by the envelope detection in the UE.

In the proposed laser heterodyning architecture, the lasers are completely uncorrelated, hence, the phase noise spectrum is the Lorentzian linewidth expressed in (5.12). Consequently, the effect of phase noise is increased compared to the other architectures studied in the previous chapter. Further, the interplay between the phase noise and fibre CD causes different spectral components to experience differential delays, thus leading to a frequency dependent phase variation among the spectral components. This phenomenon introduces a phase rotation term (PRT) particular to each subcarrier at conversion [165]. It has been reported that phase noise due to PRT is dependent on transmission length and symbol duration [175]. Also, due to the time delay, the phase noise spectrum is enlarged leading to significant ICI among the subcarriers [175]. Therefore, since CD-induced PRT and ICI are mutually independent zero-mean Gaussian random variables, then the total phase fluctuation effect on k th subcarrier is a summation of mutually independent Gaussian random variables [165].

In this analysis, the phase noise is assumed to be completely converted to intensity noise at O/E. Therefore, considering the fibre link as a linear time-invariant system, the PSD of CPN after dispersive fibre can be expressed as:

$$S_{CPN}(\omega) = S_{\phi}(\omega)|H_{CD}(\omega)|^2 \quad (5.16)$$

where $H_{CD}(\omega)$ is the fibre CD transfer function expressed as:

$$H_{CD}(\omega) = \exp\left(j\frac{1}{2}\beta_2 L \omega_k^2\right) \quad (5.17)$$

where $\beta_2 = -\lambda^2 DL/c$ is the group velocity dispersion coefficient of the fibre. Here, the optical carrier is modulated by IF signal where $\omega_k = (k + GB)\Delta\omega$ is the angular frequency of k th subcarrier symbol and GB is the guard band. It can be seen from (5.17) that the PSD of CPN is dependent on fibre length and frequency of the modulating signal. Moreover, CPN is a multiplicative noise since it follows the signal frequency. Consequently, noise contribution from CPN can dominate the receiver noise for long fibre transmission and/or wide signal bandwidth.

5.2.1.3. Amplified Spontaneous Emission

ASE noise is an additive noise generated at the output of an optical amplifier. Due to the gain mechanism of the amplifier, the intensity and phase fluctuations from the laser as a result of spontaneous emission is amplified along with the input optical signal. As a square-law detection device, the PD generates beating noise from the ASE field, which includes ASE-ASE beat noise and ASE-Signal beat noise. Consequently, the ASE-Signal beat noise spectrum is superimposed on the signal field. The ASE-ASE beat noise, on the other hand, contributes to the optical SNR and the spectrum depends on the optical filter employed [176]. Generally, ASE noise is spectrally flat and can be modelled as a zero-mean stationary Gaussian random process. Therefore, the noise PSD of ASE-Signal beat noise and ASE-ASE beat noise can be expressed as follows:

$$S_{A-S}(\omega) = S_x(\omega)|H_{op}(\omega)|^2 \quad (5.18)$$

$$S_{A-A}(\omega) = S_x(\omega)|H_{op}(\omega)|^2$$

where the subscript $A - S$ and $A - A$ represent ASE-Signal and ASE-ASE, respectively. $H_{op}(\omega)$ is an ideal OBPF with a rectangular function. $S_x(\omega)$ is the PSD of the input signal $x(t)$ to the optical amplifier, assumed to be zero-mean Gaussian and spectrally flat within the amplifier's gain medium. Depending on where the amplifier is placed within the architecture,

$x(t)$ may represent the signal at the input or output of the fibre. The total ASE field noise PSD contribution at the receiver is a linear combination of $S_{A-S}(\omega)$ and $S_{A-A}(\omega)$. However, $S_{A-S}(\omega)$ is the dominant ASE noise source that degrades the system SNR. Hence, ASE-Signal beat noise PSD of the optical amplifier can be expressed as:

$$S_{A-S}(\omega) = \frac{\eta_{ASE} \hbar BW_{op}(G-1)}{2} \quad (5.19)$$

where η_{ASE} is the ASE noise factor, typically referred to as noise figure (NF) when expressed dB, \hbar is Planck's constant, BW_{op} is the effective bandwidth of the optical filter and G represents the gain of the amplifier. ASE noise in optical amplifier is usually quantified by NF which is 4~5dB for EDFAs [176]. ASE noise dominated by the contribution from the ASE-signal field can exceed other noise contribution in the receiver for low input optical power.

5.2.2. Noise Generated in the Receiver

Apart from the noise generated in the transmitter and the channel, noise added by the PD also contributes to the system SNR. The PD noise is intrinsic to electrical systems which include thermal noise, shot noise, respectively.

5.2.2.1. Thermal Noise

Thermal noise is generated by the PD due to thermal fluctuation of electrons within its conductor. Thermal noise does not depend on frequency thus regarded to as white noise. However, thermal noise depends on temperature and load resistance of the conductor. The noise PSD of thermal noise can be expressed as:

$$S_{Th}(\omega) = S_x(\omega)|H_e(\omega)|^2 \quad (5.20)$$

$$S_{Th}(\omega) = 2k_B TR$$

where $H_e(\omega)$ is the transfer function of the electrical filter in the receiver, which is usually the detection bandwidth.

5.2.2.2. Shot Noise

Shot noise results from the discrete nature of the photons incident on the PD. The shot noise contribution to the receiver noise is proportional to the received average optical power, and the PSD can be expressed as:

$$S_{Sh}(\omega) = S_x(\omega)|H_e(\omega)|^2 \quad (5.21)$$

$$S_{Sh}(\omega) = 2qI_{dc}$$

where q denotes the electron charge and I_{dc} is the average DC current generated at O/E conversion. Considering an ideal receiver with responsivity $\mathfrak{R} = 1$, it can be seen that shot noise is dependent on the received optical power.

5.2.3. SNR of the Millimetrewave Signal after O/E Conversion

To determine an expression for the SNR of the mmWave signal generated at O/E conversion, we consider that the noise is from uncorrelated sources and that the PSD of noise generated at the PD is a linear superposition of the noise PSDs. Therefore, the mmWave signal at the output of the PD that has been corrupted by noise is written as:

$$S_{mm}(\omega) = P_i S_{IF}(\omega) + S_{N_T}(\omega) \quad (5.22)$$

where P_i is the average power of the incident light on the PD. $S_{N_T}(\omega)$ is the total noise spectral density of the system:

$$\begin{aligned} S_{N_T}(\omega) = & S_{RIN}(\omega) + S_{\phi}(\omega) + S_{CPN}(\omega) + S_{ASE}(\omega) + S_{Th}(\omega) \\ & + S_{Sh}(\omega) \end{aligned} \quad (5.23)$$

$S_{IF}(\omega)$ is the PSD of the transmitted IF signal which can be computed using the Parseval's theorem:

$$P_x(f) = \lim_{T \rightarrow \infty} \left(\frac{1}{T} E\{|\mathcal{F}\{X_T(t)\}|^2\} \right) \quad (5.24)$$

$E\{\cdot\}$ and $\mathcal{F}\{\cdot\}$ denotes the expectation and Fourier Transform operator, respectively.

Therefore, the total SNR of the mmWave signal can be expressed as:

$$SNR_{mm}(\omega) = \frac{S_{mm}(\omega) - S_{N_T}(\omega)}{S_{N_T}(\omega)} \quad (5.25)$$

We can observe the impact of each of the noise sources on the SNR of the mmWave signal. Generally, for some fixed parameters, noise contribution of some noise sources can be ignored in some cases. For instance, for a fixed average optical power, and increased fibre length, CPN will dominate the system noise while shot noise power is negligible. In addition, noise due to CPN will increase with the laser linewidth. On the other hand, RIN and ASE noise contribution will increase at low optical power. Even though thermal noise is constant, its effect will increase at low received optical power.

Notably, a comprehensive study on the noise performance of mmWave signal generated using uncorrelated lasers has not been done simultaneously for OFDM and FBMC, to the best of our knowledge. To this extent, a holistic investigation is necessary to gain an insight into the performance limitations associated with such system. Furthermore, it may be possible with such information to optimise the system performance in the presence of noise, since transmission scenario such as distance and channel in an optical fibre are largely invariant. It will, therefore, be interesting to investigate the impact of these noise sources on the system SNR. In the next section, the effect of different noise sources on the system SNR is studied by simulation.

5.3. Noise Effects on Millimetre-wave IF over Fibre Signal based on uncorrelated Lasers

In order to study the impact of different noise sources on the mmWave signal generated after O/E, a simulation testbed was implemented in VPI Transmission Maker®. The schematic for the simulation setup is depicted in Figure 5.2.

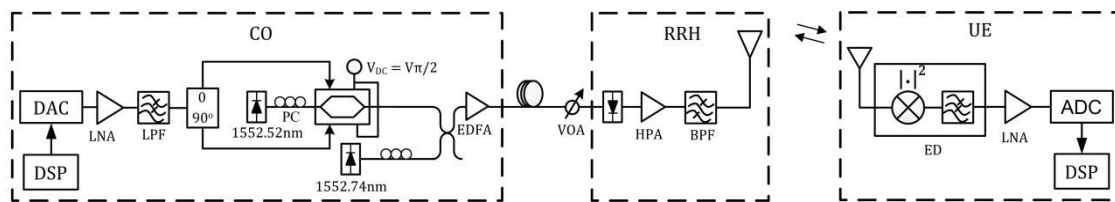


Figure 5.2: Simulation Setup.

The transmitter and receiver for IF signals (i.e. OFDM and FBMC) were implemented in DSP using MATLAB based on Figure 5.3. Here the total FFT size was 2048 and 128 subcarriers were used for data. The large FFT size was primarily chosen to ensure sufficient oversampling and allow for more carriers to be used for data transmission as needed. Moreover, subcarriers from DC to 192 were filled zero to digitally shift the signal to IF, which is necessary for envelope detection. In addition, signal-signal beat interference (SSBI) around DC usually generated at O/E is avoided completely since the unmodulated subcarriers amount to 1.5x the IF signal bandwidth. The subcarriers were modulated with symbols generated from M-QAM alphabets, where M represents the number of constellation points. For FBMC, the QAM symbols were fed into the OQAM Pre-processing module as shown in Figure 5.3 (a). Then, the generated OQAM symbols were mapped to subcarriers 193:320 while the complex conjugate OQAM symbols were mapped to the corresponding negative IFFT frequency to realise HS. The SFB implements the IFFT, pulse shaping and P/S conversion, respectively. The pulse-shape filter is based PHYDYAS prototype function with overlapping factor $K = 4$ [136]. Similarly, OFDM was generated based on the same parameters, and 128 subcarriers was used for CP. As illustrated in Figure 5.2, the digital

signal either FBMC or OFDM was converted to an analog signal after passing through the DAC sampling at 8GSa/s. The analog signal was then amplified by a LNA providing around 30dB gain. A LPF was placed after the LNA to remove aliasing that results from DAC. The IF signal after DAC was centred at 2GHz having bandwidth 500MHz.

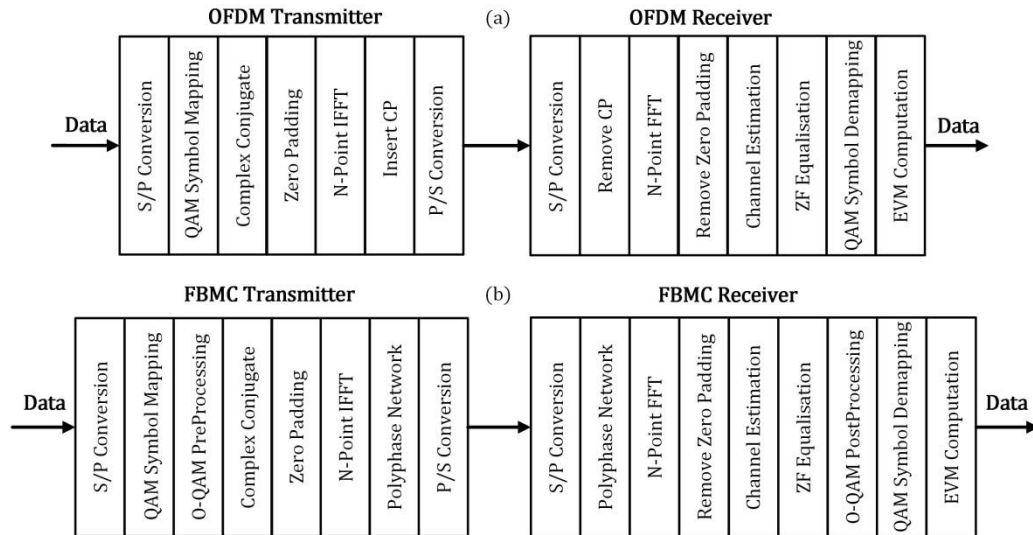


Figure 5.3: DSP Transceiver design for the IF Signals: (a) FBMC (b) OFDM

In the simulation, DFB lasers having 1MHz linewidth were employed as the ML and LO laser, respectively. To improve robustness against fibre CD, the IF signal after amplification was sent to a hybrid coupler which splits the signal and adds 90° phase shift at one of its output. The output of the hybrid coupler was then applied to the two arms of the DE-MZM, biased at quadrature point to generate OSSB modulation. The centre emission frequency the ML was set to 1552.524nm. After the E/O conversion, a 3dB coupler was used to combine the OSSB signal with the OLO. The centre emission frequency of the LO laser was set to 1552.749nm which is exactly 28GHz apart from the ML centre frequency. The combined signal was then amplified by an EDFA before 40km fibre transmission. The EDFA noise figure is 5dB and it provides 9dB gain so no inline or pre-amplification was required at the receiver. This is typical in short reach fibre access networks such as PON. The input optical power to the PD was fixed at +1dBm. In that way, thermal and shot noise effects are assumed constant. The mmWave signal was generated in the PD via heterodyning of the two optical tones. The mmWave signal was then amplified by a 30dB gain HPA, and a BPF was used to remove unwanted beatings around the desired carrier frequency. At the UE, the mmWave signal was downconverted by an ED and a LPF extracts the desired signal before the LNA. The received IF signal was converted to digital samples by a 64GSa/s ADC before the receiver DSP was performed offline in MATLAB based on the design shown in Figure 5.3. The system performance evaluation was carried out for different transmission scenarios by computing the SNR degradation with and without the noise generating source. The

system SNR was calculated after symbol demodulation from the received EVM using the relationship [177]:

$$SNR \approx \frac{1}{EVM^2} \quad (5.26)$$

Since the total noise PSD is the sum of the PSDs of all noise generated within the system, the following assumptions are made regarding how noise effect is investigated:

- The impact of each noise source on the system performance can be examined independently. This is done by fixing some parameters while the parameter associated with the noise source of interest is swept.
- In situations where noise is dependent on a transmission parameter, it can be assumed that such noise influence will remain constant as long as the parameter value remains unchanged.
- Although, total system noise performance is a combination of multiple noise sources, as transmission scenario changes, the impact of one or more of the noise sources will exceed others. Thus, it can be inferred that the system performance is limited by the dominant noise term.

In the next section, the impact of noise is investigated based on the simulation setup depicted in Figure 5.2 for OFDM and FBMC, respectively.

5.3.1. Impact of RIN on the system performance

To study the impact of RIN on the system performance, the laser RIN parameter was swept from -135dB/Hz to -165dB/Hz in 5dB steps. The laser employed in the simulation allows the RIN to be set independent of the average optical power. Thus, the optical power delivered to the PD was fixed at +1dBm. Moreover, optical BTB transmission was considered so ASE noise and impact of CPN due to CD is excluded from the noise calculation. In addition, the IF drive power was kept as -8dBm for all evaluations. At this drive power level, OFDM and FBMC showed similar performance, hence, the nonlinearity of the E/O interface was not accounted for in the setup. For the evaluation, OFDM and FBMC were modulated with 4, 16 and 64QAM and their performance compared. The received SNR as a function of RIN values is shown in Figure 5.4 for OFDM and FBMC, respectively. As expected, the SNR reduces with an increase in RIN. Observe that OFDM exhibits 2dB better performance in SNR compared to FBMC for all modulation formats and at all RIN levels.

Generally, the SNR was degraded by ~10dB as RIN increased from -150dB/Hz to -135dB/Hz whereas SNR floor can be noticed from -150dB/Hz to -165dB/Hz. This suggests that RIN contribution to the overall system noise was reduced at low RIN values.

Further, laser intrinsic RIN contribution to the overall system noise reduced significantly for RIN values lower than -155dB/Hz . Consequently, system SNR performance can be improved by employing low RIN lasers.

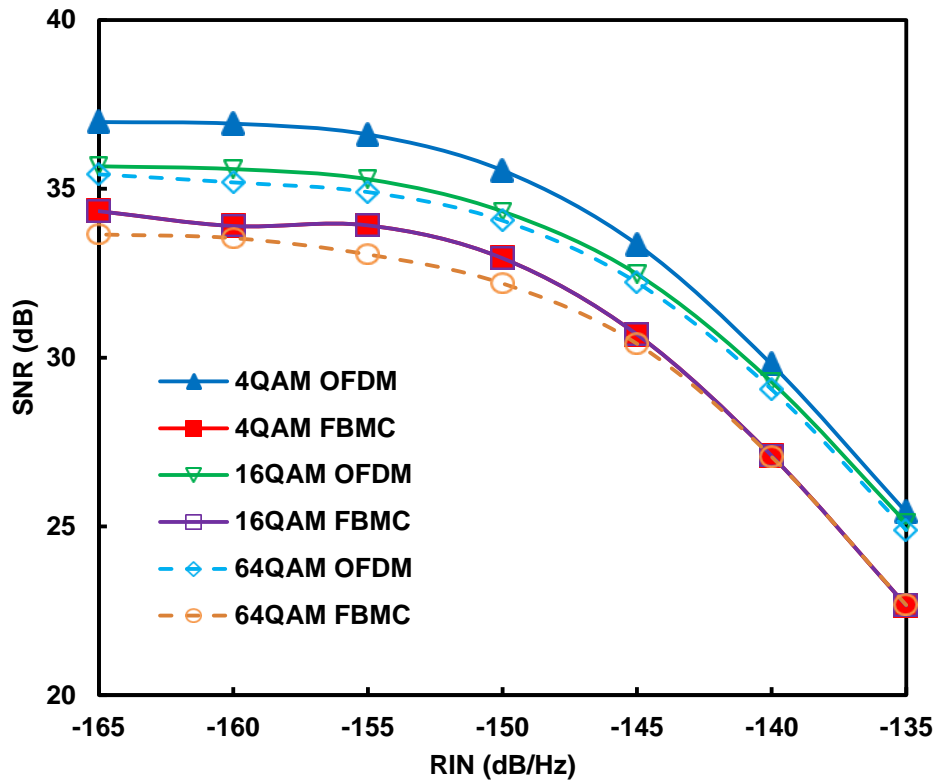


Figure 5.4: Received SNR vs RIN for OFDM and FBMC

5.3.2. Impact of ASE Noise

Next, noise due to ASE is studied by placing a 5dB NF EDFA after the coupler. The EDFA output power was set to +9dBm. An optical attenuator was used to set the PD input power to +1dBm. As mentioned earlier, shot noise power is assumed constant for this power level since it depends on the input power level. Also, thermal noise power does not change. Therefore, it is expected that for low RIN values, further system SNR degradation will be as a result of ASE noise.

The RIN value was swept from -165dB/Hz and -155dB/Hz to evaluate how the introduction of EDFA will impact the system SNR. To achieve this, the input optical power to EDFA was set to +1dBm and -7dBm, respectively. In a practical scenario, the EDFA serves as a power booster in the former while in the latter it serves as a preamplifier to improve receiver sensitivity. Here, the performance evaluation was performed without fibre in order to determine the dominant noise source in the system. The SNR degradation was calculated by comparing the SNR for the two configurations for different RIN values. SNR degradation is shown in Figure 5.5 for 4, 16, and 64QAM, respectively.

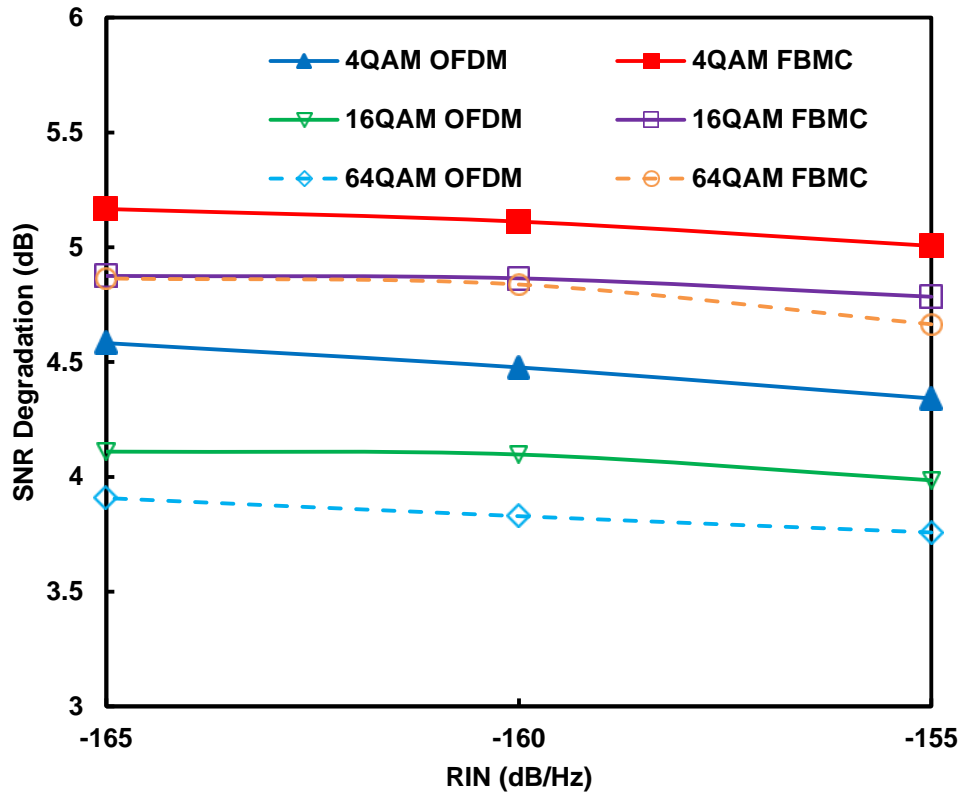


Figure 5.5: SNR degradation due to ASE

For all RIN values, the system noise is a combination of RIN and ASE noise. It can be seen from Figure 5.5 that when the EDFA was employed as a power booster (i.e. +1dBm input power), it does not contribute significantly to system noise. This is due to high optical SNR at the input of the EDFA. On the contrary, when the EDFA was employed as a preamplifier with -7dBm input power, the effect of ASE noise becomes noticeable exhibiting 4~5dB degradation. This implies that ASE noise generally depends on the input optical power level.

5.3.3. Impact of CD-induced CPN

To investigate the impact of CPN on the system SNR performance, the RIN values were swept as before, from -165dB/Hz to -135dB/Hz. The EDFA was placed after the OC to provide +9dBm launch power into the fibre. In that way, ASE noise contribution due to EDFA is minimised as shown in Figure 5.5. The SNR degradation was computed by observing the received SNR at BTB and after 40km fibre, respectively.

It is interesting to see from Figure 5.6, that there was no effect on SNR degradation for -135dB/Hz value. This implies that even in the presence of other noise sources such as ASE and CPN, the system noise was dominated by RIN. Moreover, CPN dominates SNR degradation as the RIN value reduced. To validate this, the fibre CD effect was switched off and the SNR degradation was observed for the 4QAM signal, which is also shown in Figure

5.6. This can be achieved in practice by employing a dispersion compensating fibre at the end of the fibre span to mitigate the CD effect.

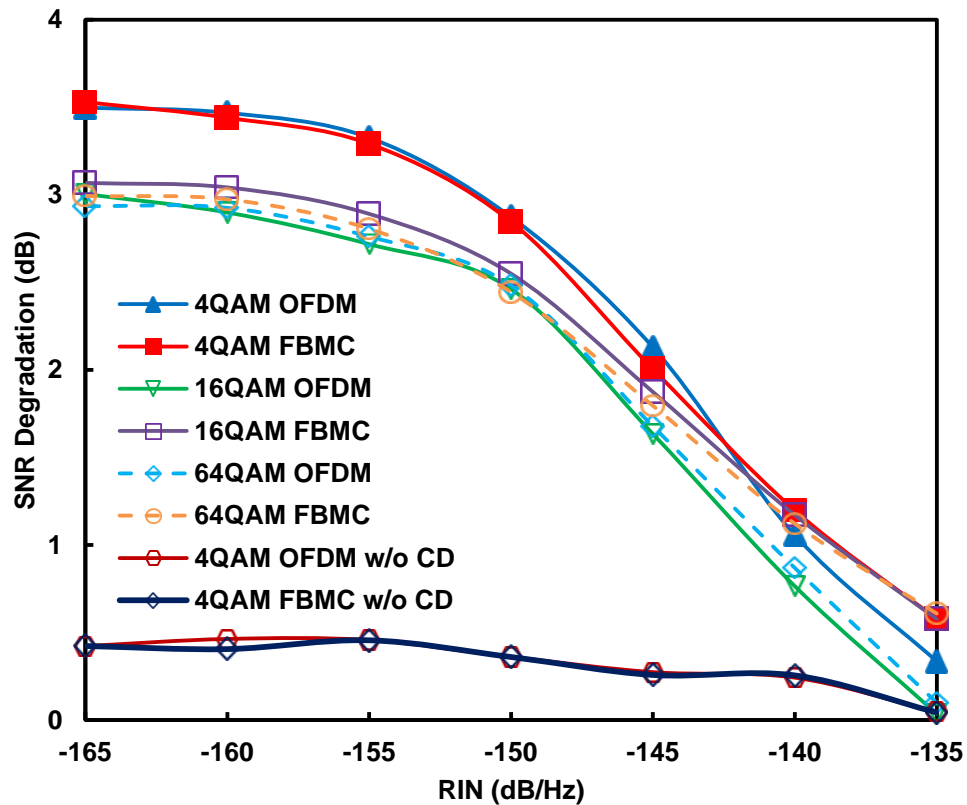


Figure 5.6: SNR degradation due to CPN

It can, therefore, be concluded that CPN will dominate the noise contribution to system SNR for low RIN values but its effect may become insignificant when the laser RIN is extremely high.

5.3.4. Impact of Laser Linewidth

Since the laser linewidth is the phase noise spectrum of the laser, it is important to study the impact of linewidth on SNR degradation due to CPN.

Table 5-2: Laser Configuration and Linewidth

Laser Configuration	ML Linewidth	LO Linewidth	Total Linewidth
FL-FL	1kHz	1kHz	2kHz
FL-ECL	1kHz	100kHz	101kHz
ECL-ECL	100kHz	100kHz	200kHz
ECL-DFB	100kHz	1MHz	1.1MHz
DFB-DFB	1MHz	1MHz	2MHz
FL-DFB	1kHz	10MHz	10.1MHz
DFB-DFB	10MHz	10MHz	20MHz

The linewidth of both ML and LO was swept to reflect different laser configurations and types, as shown in Table 5-2. The laser types considered are fibre laser (FL), ECL and DFB, respectively.

The SNR degradation due to laser linewidth was computed by observing the SNR at BTB and after 40km fibre transmission. The RIN value was set to -155dB/Hz, and the optical launch power was +9dBm, so as to maintain the PD input power of +1dBm.

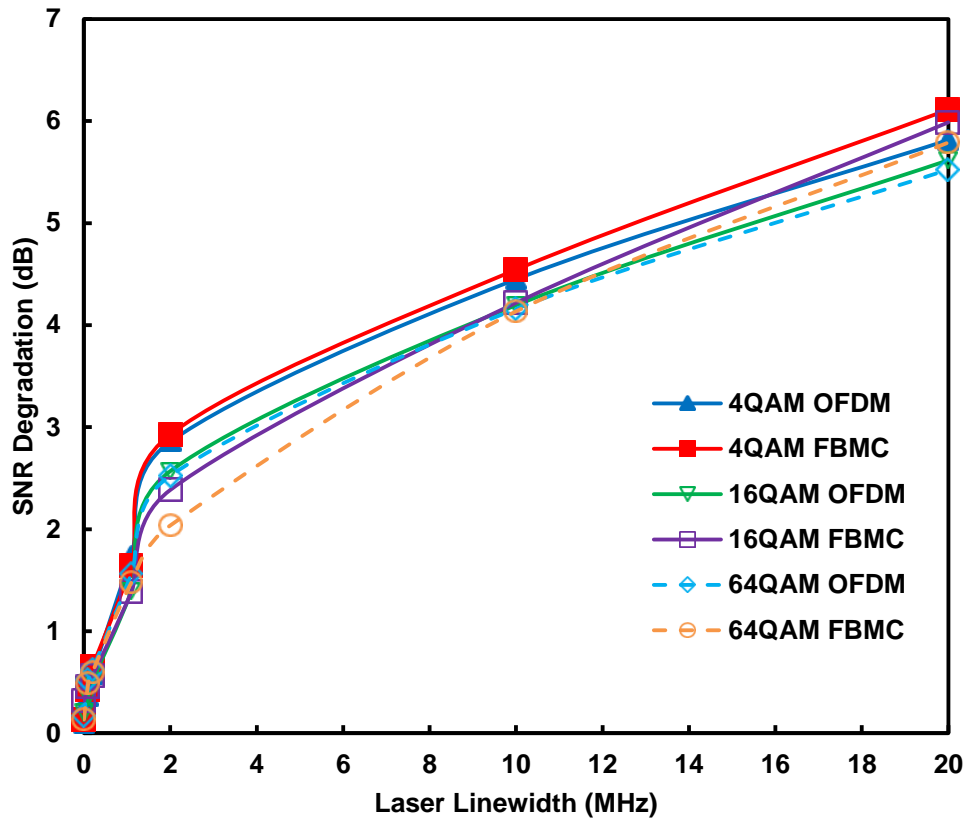


Figure 5.7: SNR degradation due to laser linewidth

Figure 5.7 shows SNR degradation as a function of laser linewidth. It can be seen that SNR degradation for linewidth configurations below 2MHz is less than 1dB whereas the SNR degradation for the 20MHz laser is ~6dB. Here, the noise contribution is assumed to be due to CPN only as all other noise parameters were unchanged. Therefore, low linewidth lasers are desirable to reduce the effect of noise on the system performance

5.3.5. Impact of Fibre Length

In this section, the impact of fibre length is studied for transmission up to 100km. For previous investigations, the fibre length was fixed at 40km which is equivalent to the Next Generation-PON2 (NG-PON2) standard [178]. Here, we consider long-reach optical access network as it has been proposed as an alternative solution to the currently installed fibre capacity [179]. In the investigation, two laser linewidth configurations were used and only 16QAM modulation format was employed. Also, the RIN was set to -165dB/Hz. In order to

avoid the effect of fibre nonlinearity, the optical launch power kept at +9dBm. After 40km, another EDFA was placed before the PD to ensure a +1dBm input optical power to the PD throughout the investigation. The fibre length was increased in steps of 10km and the SNR degradation was calculated w.r.t the SNR at optical BTB.

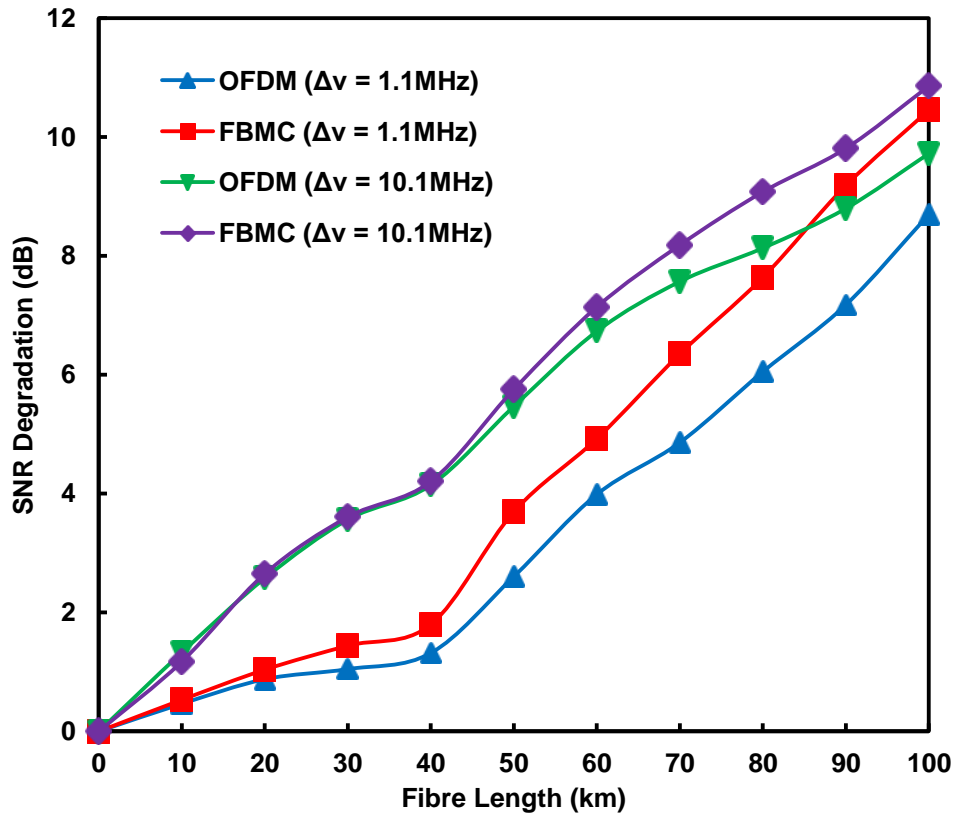


Figure 5.8: SNR degradation due to fibre length

Figure 5.8 shows the SNR degradation as a function of fibre length for two laser linewidth configurations. As can be seen from Figure 5.8, the SNR degradation in both OFDM and FBMC increased significantly for 10.1MHz linewidth, while it is less than 2dB up to 40km for 1.1MHz. In addition, the steeper trend after 40km is due to the introduction of another EDFA as a preamplifier before the PD. Hence, optical power at the EDFA reduced by +2dBm for every 10km increase in fibre length, and on average SNR was degraded by 0.8dB and 1dB for OFDM and FBMC, respectively. As shown previously, we can deduce that given a maximum 5dB NF from the preamplifier EDFA, SNR degradation is dominated by CPN after 70km fibre. Therefore, for fibre lengths further than 40km, the noise contribution consists mainly of ASE and CPN. Moreover, SNR degradation is 2.5dB and 3dB worse for OFDM and FBMC, respectively as the linewidth was increased from 1.1MHz to 10.1MHz. Further, FBMC can be observed to exhibit more SNR degradation compared to OFDM. This is clear at 90km fibre where for 1.1MHz FBMC was degraded more than 10.1MHz linewidth OFDM. This suggests that FBMC is more sensitive to CD-induced phase-to-intensity noise compared to OFDM.

5.3.6. Impact of Noise on IF Signal Bandwidth

In this section, the impact of noise is investigated considering different IF signal bandwidth for 40km and 100km fibre, respectively. Since mmWave frequency presents huge bandwidth that can be used for 5G networks, it is necessary to study the effect of noise on increasing the signal bandwidth. Two laser linewidth configurations were used for the evaluation.

Firstly, the subcarrier bandwidth was fixed while more carriers were allocated to increase the transmitted IF signal bandwidth. It is well known that phase noise impact is minimised if subcarrier bandwidth is larger than the laser linewidth [180, 181]. Therefore two laser configurations are related to the subcarrier spacing as:

$$\Delta\omega_{IF} = 3.90625\text{MHz} > 2\text{MHz} \quad (5.27)$$

$$\Delta\omega_{IF} = 3.90625\text{MHz} < 10.1\text{MHz}$$

Increasing subcarrier number can be seen as allocating more bandwidth to the UE in terms of subcarriers, where the subcarrier frequency is fixed and the resultant IF signal bandwidth is calculated as $\Delta\omega_{IF} * \text{Subcarrier Number}$. Figure 5.9 shows the received EVM as a function of subcarrier number after 40km fibre. Obviously, the SNR degrades as the subcarrier number was increased, which is explained by (5.17).

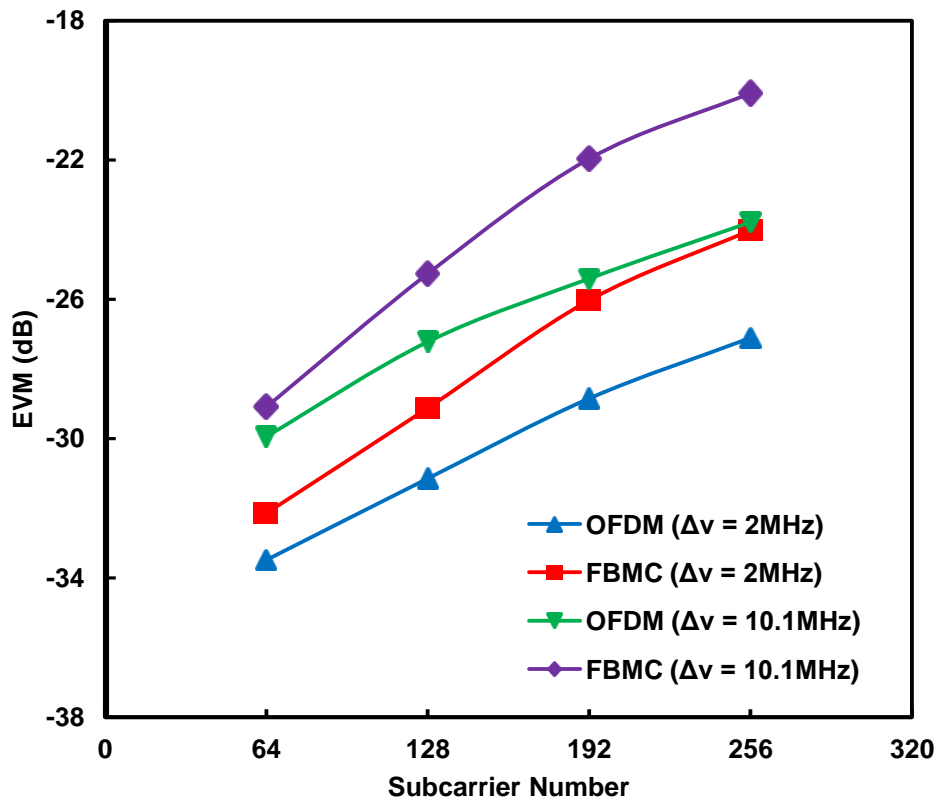


Figure 5.9: EVM vs Subcarrier Number after 40km fibre

The EVM was degraded by 2~3dB as the subcarrier number increased from 64 to 256 (i.e. 250MHz-1GHz) and as a consequence 8~9dB loss in SNR. Moreover, FBMC exhibits 3dB worse SNR when the subcarrier number increased to 256 for 10.1MHz laser configuration. The SNR degradation as more subcarriers were added can be attributed to the increased accumulation of CPN per subcarrier. Even though the subcarrier bandwidth is larger than the phase noise spectrum of 2MHz laser linewidth configuration, the CD effect increased with subsequent increase in signal bandwidth. Similarly, the EVM as a function of the subcarrier number after the 100km fibre is shown in Figure 5.10. Compared to Figure 5.9, it can be seen that the EVM value for 64 subcarriers reduced by 6~7dB as the fibre was increased to 100km. This is due to CD-induced CPN and ASE noise since another EDFA was placed just before the PD.

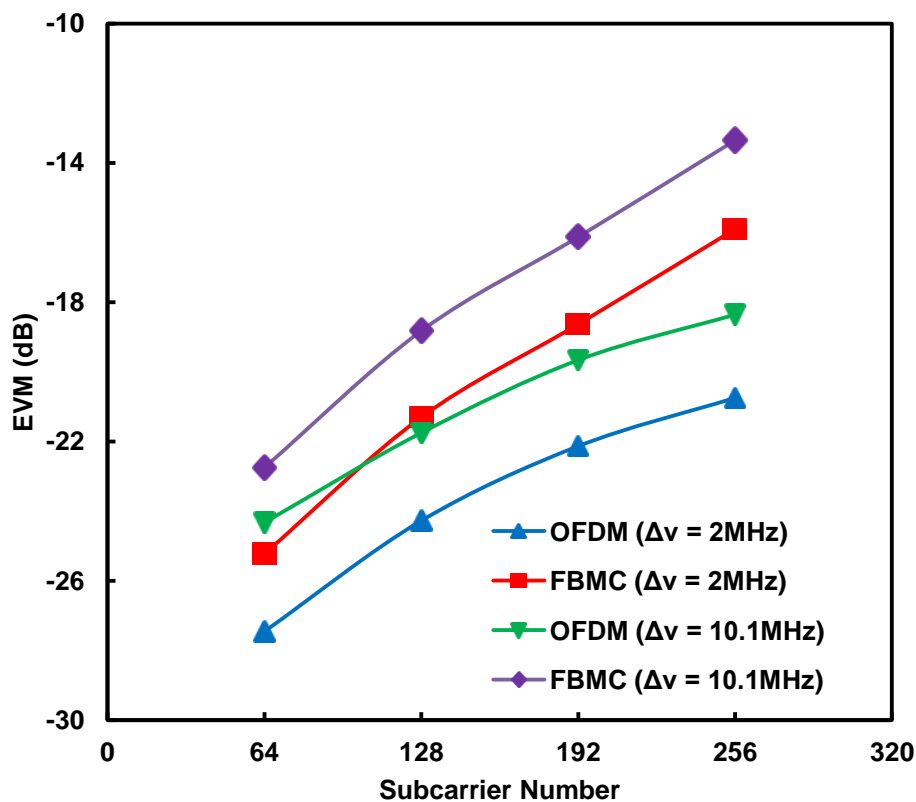


Figure 5.10: EVM vs Subcarrier Number after 100km fibre

Considering the 18dB SNR threshold for 16QAM signal, the maximum number of subcarriers that can be allocated in FBMC is 192 (i.e. 750MHz) for 2MHz linewidth configuration. The number of achievable subcarrier allocation reduced to 128 (i.e. 500MHz) for 10.1MHz linewidth configuration. On the other hand, OFDM can allocate all subcarriers as the SNR is higher than 18dB after 100km for 10.1MHz configuration. This implies that FBMC requires more stringent laser linewidth configuration to reduce the effect of phase noise on mmWave signals generated using laser heterodyning.

Next, the subcarrier number was fixed while the subcarrier sampling interval was increased. The same linewidth configuration was used and the received EVM for OFDM and FBMC was compared after 40km and 100km fibre, respectively. The bandwidth was increased from 250MHz to 2GHz in 250MHz step. To avoid SSBI around DC at O/E conversion, the centre frequency of the IF signal was shifted as the signal bandwidth increased. The allocated guardband is $\geq BW_{IF}$. The two laser configurations are related to the subcarrier spacing as:

$$\Delta\omega_{IF} \leq 2MHz \text{ for } 250MHz$$

$$\Delta\omega_{IF} > 2MHz \text{ for } 500MHz - 2GHz$$

(5.28)

$$\Delta\omega_{IF} < 10.1MHz \text{ for } 250MHz - 1GHz$$

$$\Delta\omega_{IF} > 10.1MHz \text{ for } 1.5GHz - 2GHz$$

The relation in (5.28) is necessary to evaluate the influence of laser linewidth and CD on the transmitted signal. Figure 5.11 shows the EVM as a function IF signal bandwidth after 40km for the two laser configurations.

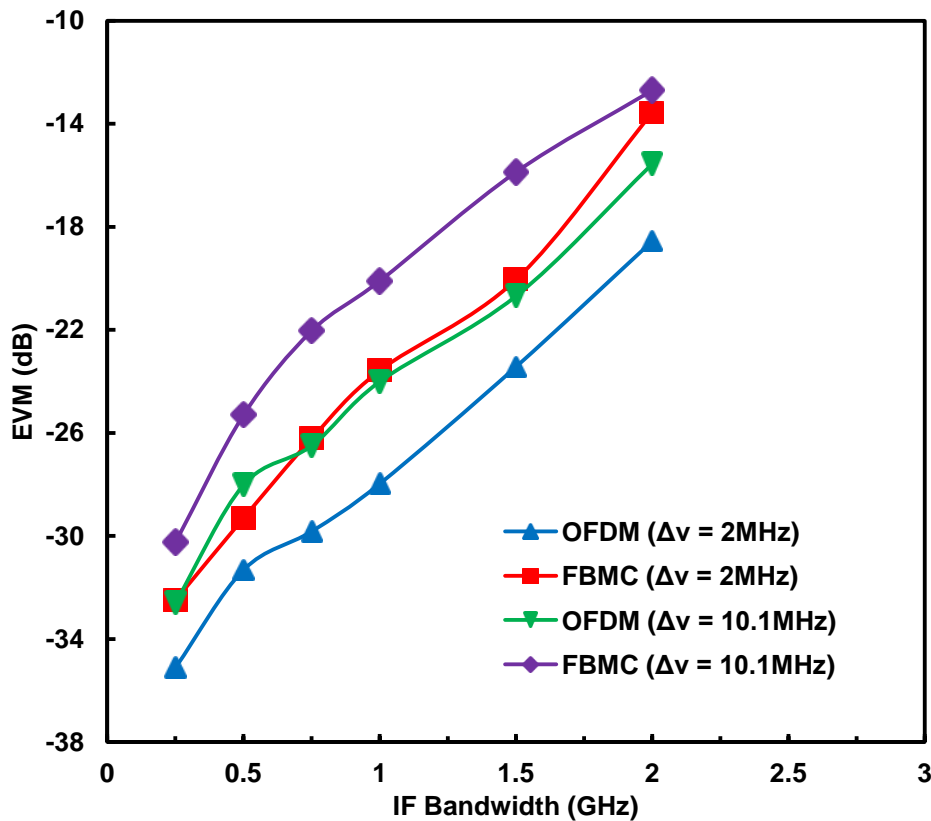


Figure 5.11: EVM vs IF bandwidth after 40km fibre

The maximum achievable IF bandwidth considering 18dB SNR threshold in FBMC is 1.5GHz for 2MHz and 1GHz for 10.1MHz laser configuration. Compared to the 100km shown in Figure 5.10, the maximum achievable bandwidth is doubled by reducing fibre length to 40km. Even though the subcarrier bandwidth was increased relative to the laser linewidth, which should sufficiently improve tolerance against laser phase noise. The CPN spectrum becomes enlarged with increased signal bandwidth leading to significant ICI and consequently loss of orthogonality [165]. This effect is more pronounced in FBMC since it suffers from IMI due to real-field orthogonality constraint leading to ICI/ISI, which in effect can be made worse with phase noise [182].

On the other hand, transmission of 2GHz and 1.5GHz OFDM signal can be achieved over the architecture for 2MHz and 10.1MHz laser configuration, respectively. This implies that OFDM presents 25% and 33% (i.e. for 2MHz and 10.1MHz linewidth) better SE in terms of IF bandwidth over this architecture due to its robustness against CPN compared to FBMC. However, if we consider that the CP overhead in OFDM is not required in FBMC, the SE margin will be reduced. The received constellation for the 2nd, 64th, and 128th subcarrier is shown in Figure 5.12. The effect of CD induced ICI can be noticed on the 128th subcarrier since the relative time delay is increased.

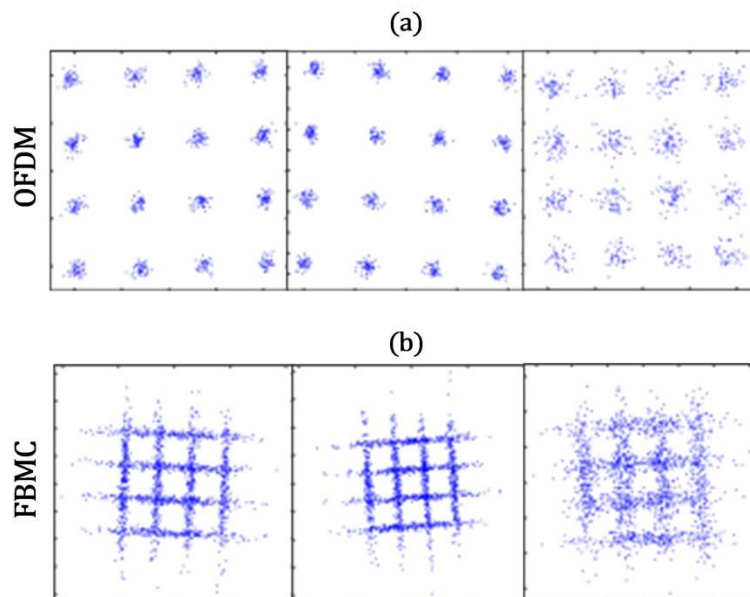


Figure 5.12: Received constellation after 40km fibre and 2MHz linewidth for 2nd, 64th and 128th subcarriers after equalisation in 2GHz (a) OFDM (b) FBMC

The same transmission scenario was considered for 100km fibre as shown in Figure 5.13. The difference in SNR between OFDM and FBMC was 3dB and 5dB for 250MHz and 2GHz IF bandwidths, respectively. Obviously, the effect of CD increased with fibre length and signal bandwidth, further degrading the EVM. Additionally, the input optical power at EDFA was -11dBm after 100km, thus ASE noise from the preamplifier also contributed to EVM degradation.

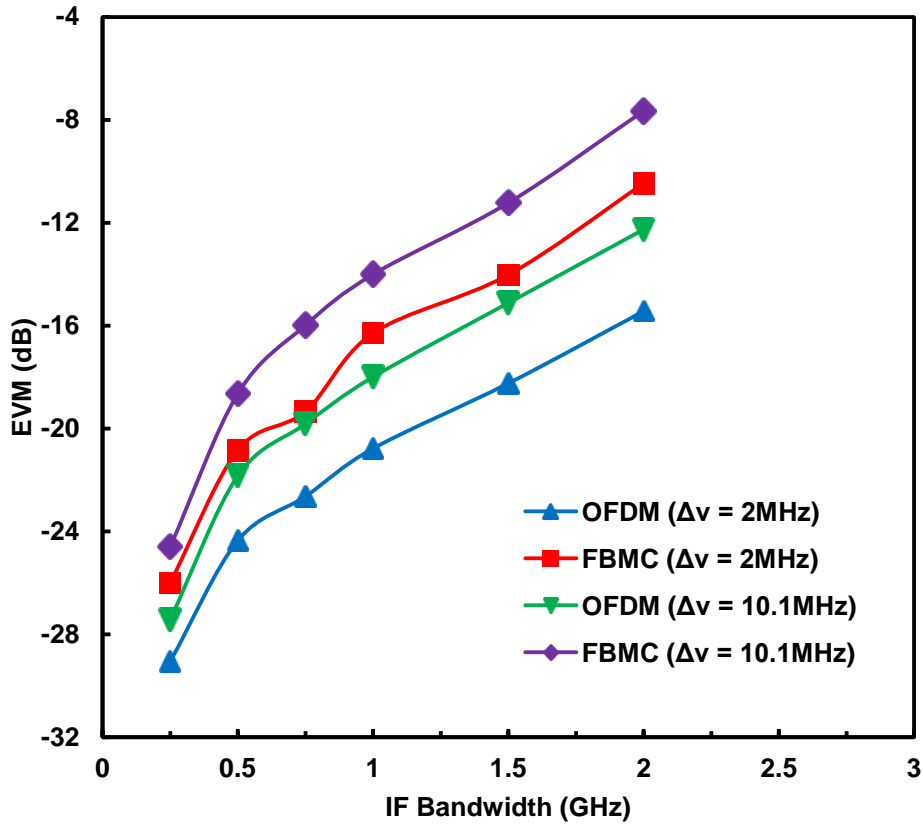


Figure 5.13 EVM vs IF Bandwidth for 100km fibre

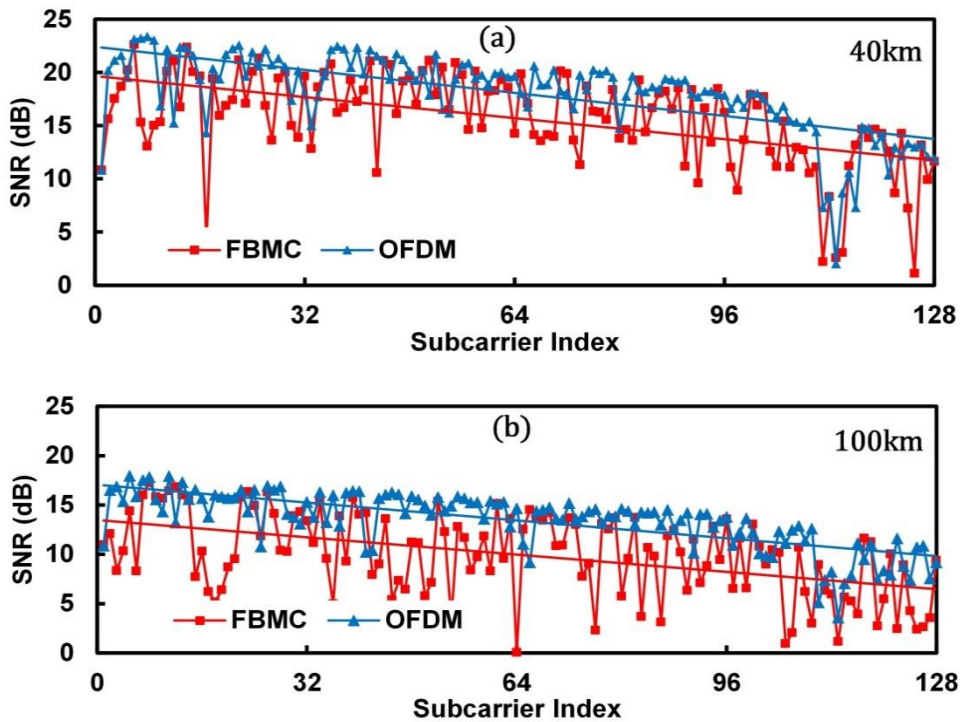


Figure 5.14: Subcarrier SNR for 10.1MHz Laser Configuration and 2GHz IF bandwidth (a) 40km (b) 100km

The maximum achievable bandwidth for 2MHz laser linewidth is 1.5GHz and 0.75GHz for OFDM and FBMC, respectively. As the laser linewidth increased to 10.1MHz, the maximum

achievable bandwidth reduced to 1GHz and 0.5GHz for OFDM and FBMC, respectively. This shows that the CPN effect is more detrimental in FBMC than in OFDM. To verify this, the SNR value of the 128 subcarriers was computed after 40km and 100km considering 2GHz bandwidth and 10.1MHz laser configuration as shown in Figure 5.14. The trend lines indicate how SNR degrades with the subcarrier number. It can be observed that SNR per subcarrier of FBMC after 100km is worse, with several dips. In addition, the trend lines in Figure 5.14 (a)-(b) show an average of 3dB difference in subcarrier SNR of OFDM and FBMC.

In order to employ the laser heterodyning technique for optical backhauling of mmWave small cell BSs, system performance optimisation is necessary. This can be achieved by employing very narrow linewidth lasers for mmWave carrier generation, reducing the signal bandwidth or fibre length. However, narrow linewidth lasers are quite expensive, while in practice; fibre length is usually fixed based on the deployed architecture. In addition, it is desirable to exploit the huge bandwidth that is present in the mmWave band.

To this extent, system optimisation can be achieved by considering the transmission channel characteristics and adapting the signal modulation scheme suitable for the available SNR. This technique is referred to as link adaptation in the present 4G mobile networks and it is expected to be employed in 5G. Further, if the estimation of the channel response is enhanced, the received SNR can be improved. Therefore, system performance employing link adaptation technique and channel noise averaging optimisation is investigated in the next section.

5.4. System Performance Optimisation based on the Received SNR and Frequency Domain Averaging

The transmission schematic of adaptive modulation based on CSI feedback from the UE is depicted in Figure 5.15.

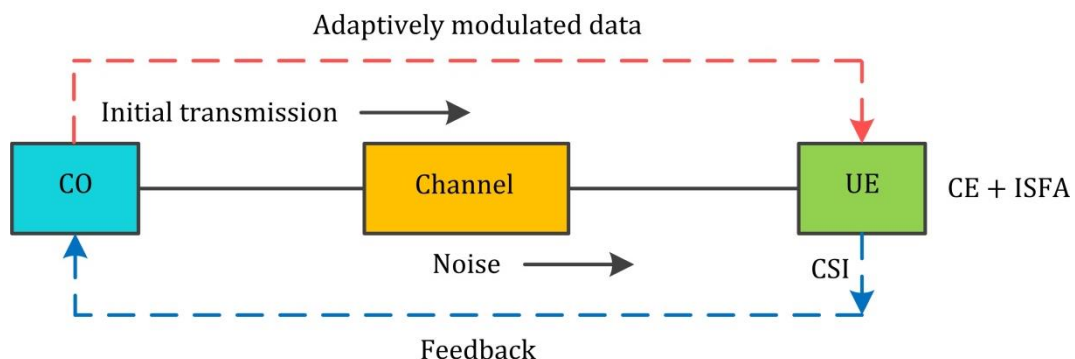


Figure 5.15: Schematic of transmission channel with CSI feedback for adaptive modulation

To optimise transmission throughput in the presence of noise, the UE receives the downlink data corrupted by noise and subsequently, the CE is done and the UE computes the CSI,

which is then fed back to the CO. The SNR information contained in the CSI is used to select the appropriate modulation scheme based on the SNR threshold for each modulation format [5]. In the CO, the subcarriers are then modulated with different modulation formats and transmitted back to the UE via the channel.

By taking the advantage that channel transfer function is usually highly correlated for adjacent subcarriers, ISFA was employed to average the noise over data-carrying subcarriers. The CE was based on least squares using the preamble appended at the start of each frame. Subsequently, the ISFA scheme was applied to average a total of $(2m + 1)$ subcarriers. Thus, the channel matrix for k th subcarrier can be written as [183]:

$$H(k) = \frac{1}{2m + 1} \sum_{i=k-m}^{k+m} H(i) \quad (5.29)$$

where $H(k)$ is the channel matrix for k th subcarrier and m is the averaging window. The averaging window is selected from m neighbour subcarriers to the left and right of the k th subcarrier. A ZF equalisation was then applied to the received signal after ISFA. To implement the system optimisation, adaptive modulation was initially used to improve the throughput of 2GHz signal considering 40km fibre and the two linewidth configurations.

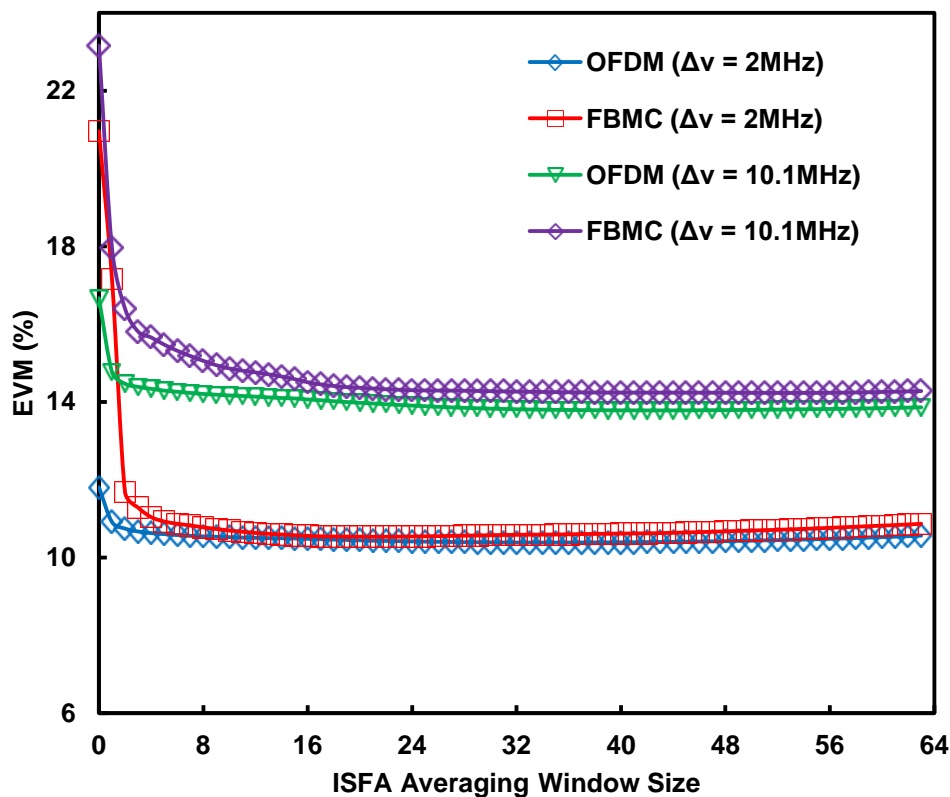


Figure 5.16: ISFA averaging window for 2GHz OFDM and FBMC after 40km

Afterwards, ISFA was employed to enhance the CE, and a comparison was made on the number of loaded bits with and without ISFA. The ISFA window size was first swept to obtain

an optimum number of subcarriers required before implementing the ISFA. Figure 5.16 shows the EVM as a function of the ISFA window for OFDM and FBMC. The zero averaging window size corresponds to when ISFA averaging was not applied. The optimum ISFA window size for 2MHz laser configuration was 29 and 22 for OFDM and FBMC, while the optimum window size for 10.1MHz was 35 for both waveforms.

The bit-loading profile after 40km fibre for 2MHz laser linewidth is shown in Figure 5.17. It can be seen that with ISFA more subcarriers were loaded with a higher bit number compared to when ISFA was not applied. In addition, it can be observed that high subcarrier numbers were modulated with lower bits. This is due to the increased SNR degradation as a result of accumulated CPN on high subcarrier numbers as shown in Figure 5.14, thus lower modulation format was employed. After adaptive modulation, the signal was retransmitted over the architecture with the same configuration and subcarrier demodulation was performed after using the optimum ISFA window to average the channel response. Figure 5.18 shows the received constellations for subcarriers loaded with 2-, 4- and 6-bits when ISFA was applied for 2MHz linewidth and 40km fibre length, respectively.

Given that the preamble used in CE constitutes 1% symbol overhead for both waveforms and another 5.3% CP overhead in OFDM. The effective data rate of OFDM and FBMC before adaptive modulation was 7.45Gbps and 7.92Gbps, respectively. After adaptive modulation, the effective data rate of OFDM increased by 21% without ISFA and 32% when ISFA was applied. However, the effective data rate of FBMC after adaptive modulation was reduced to 94% without ISFA, but it increased by 31% when ISFA was applied to enhance the CE process before adaptive modulation.

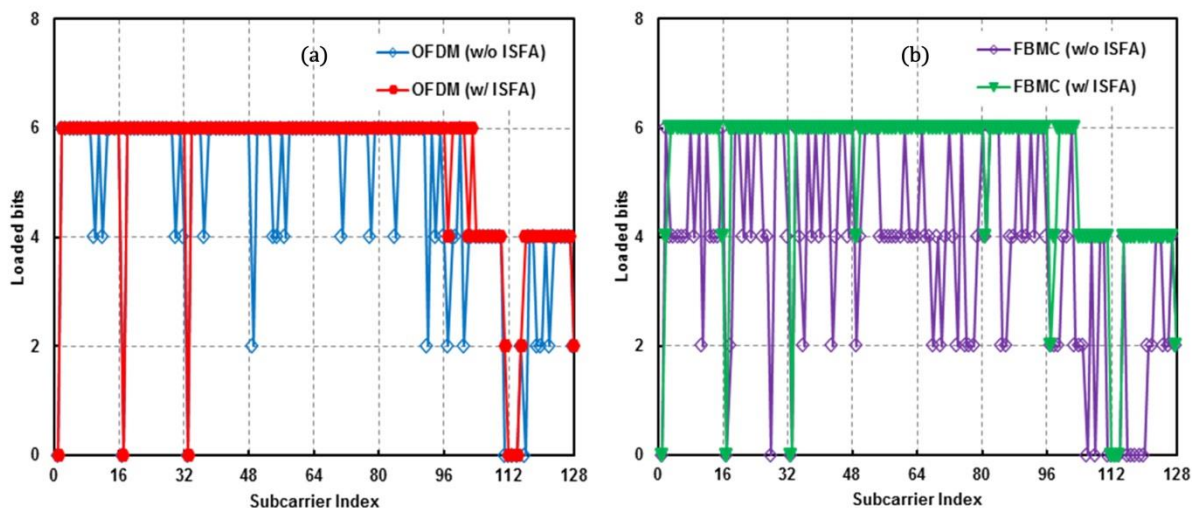


Figure 5.17: Bit-loading profiles for 2MHz laser and 2GHz bandwidth after 40km (a) OFDM (b) FBMC

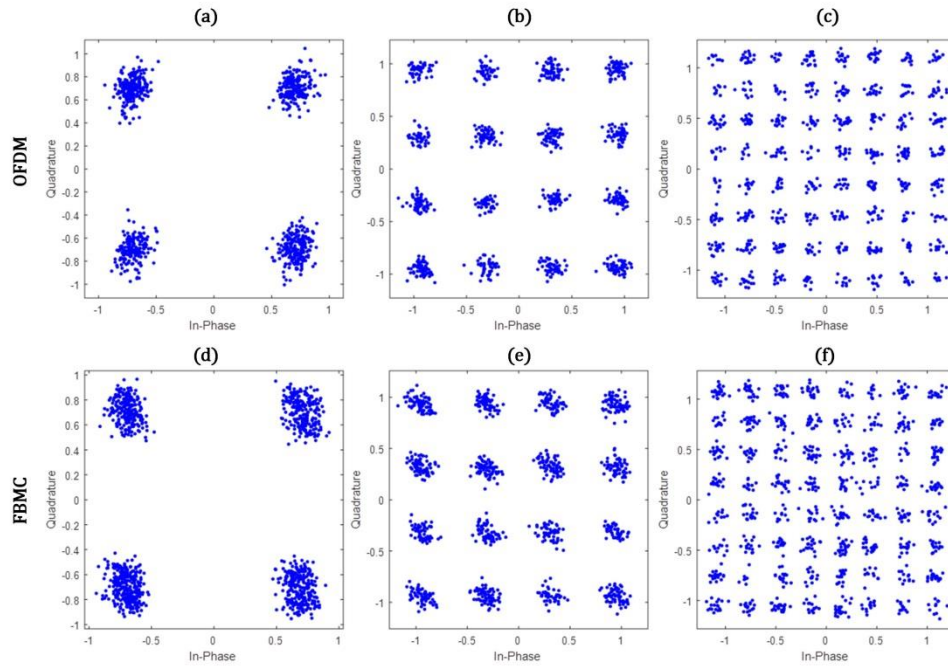


Figure 5.18: Received constellation after adaptive modulation with ISFA for 2MHz linewidth after 40km fibre (a)-(c) OFDM: 2-bits, 4-bits and 6-bits (d)-(f) FBMC: 2-bits, 4-bits and 6-bits

Similarly, the bit-loading profile is shown in Figure 5.19, with and without ISFA for 2GHz bandwidth and 10.1MHz laser linewidth after 40km fibre. It can be observed that bits are not loaded from around 112th subcarrier to 128th subcarrier. This is due to the enlarged laser phase noise spectrum as the linewidth was increased. Note that it is possible to shift the IF signal further away as the linewidth increases, but it means increasing the signal frequency which then means the CD effect will be increased. Figure 5.20 shows the received constellations for the subcarriers loaded with 2-, 4- and 6-bits after the signal was retransmitted over the architecture using the same configuration.

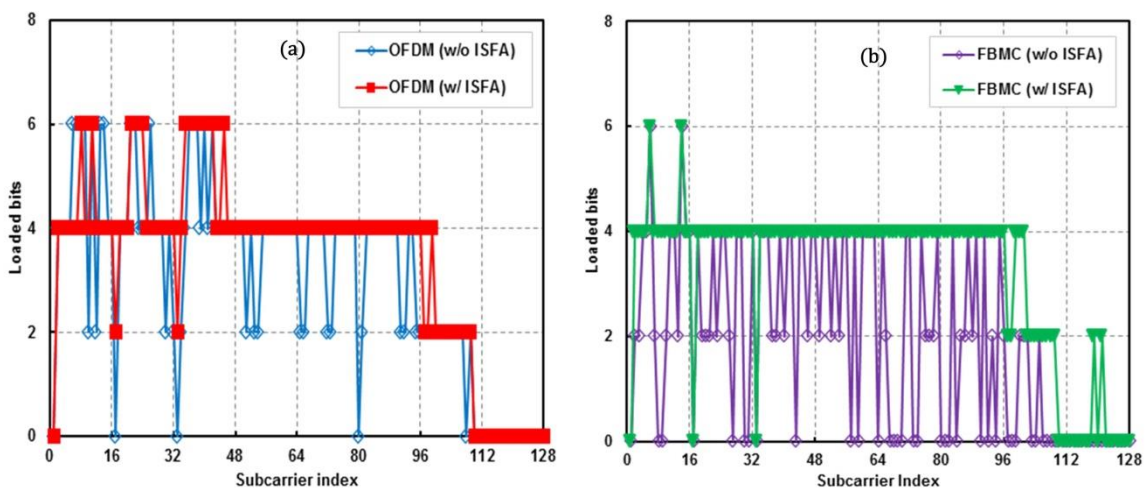


Figure 5.19: Bit-loading profiles for 10.1MHz linewidth and 2GHz bandwidth after 40km (a) OFDM (b) FBMC

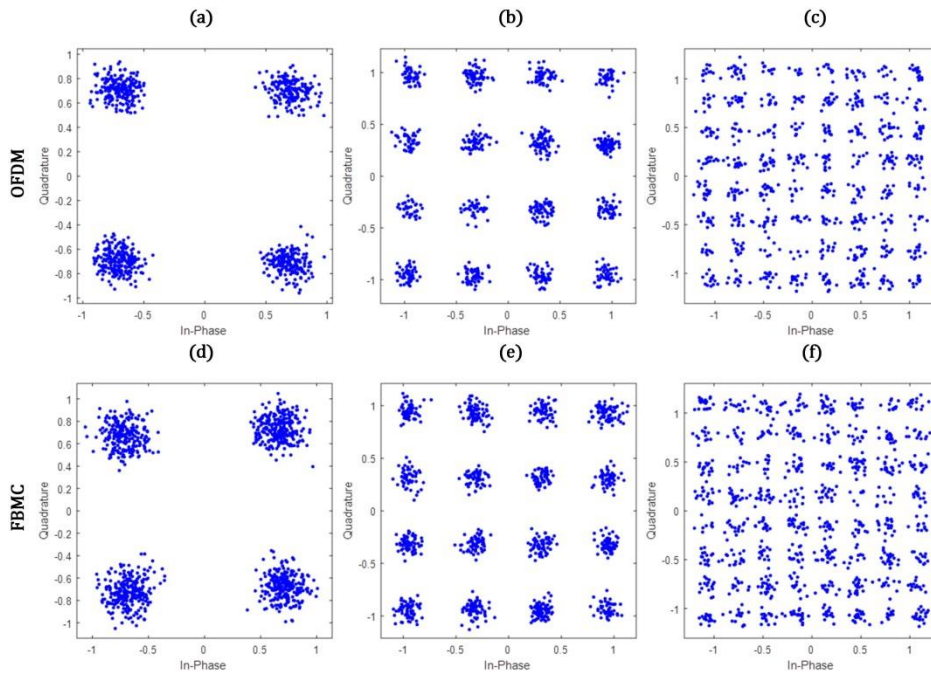


Figure 5.20: Received constellation after adaptive modulation with ISFA for 10MHz linewidth after 40km fibre (a)-(c) OFDM: 2-bits, 4-bits and 6-bits (d)-(f) FBMC: 2-bits, 4-bits and 6-bits

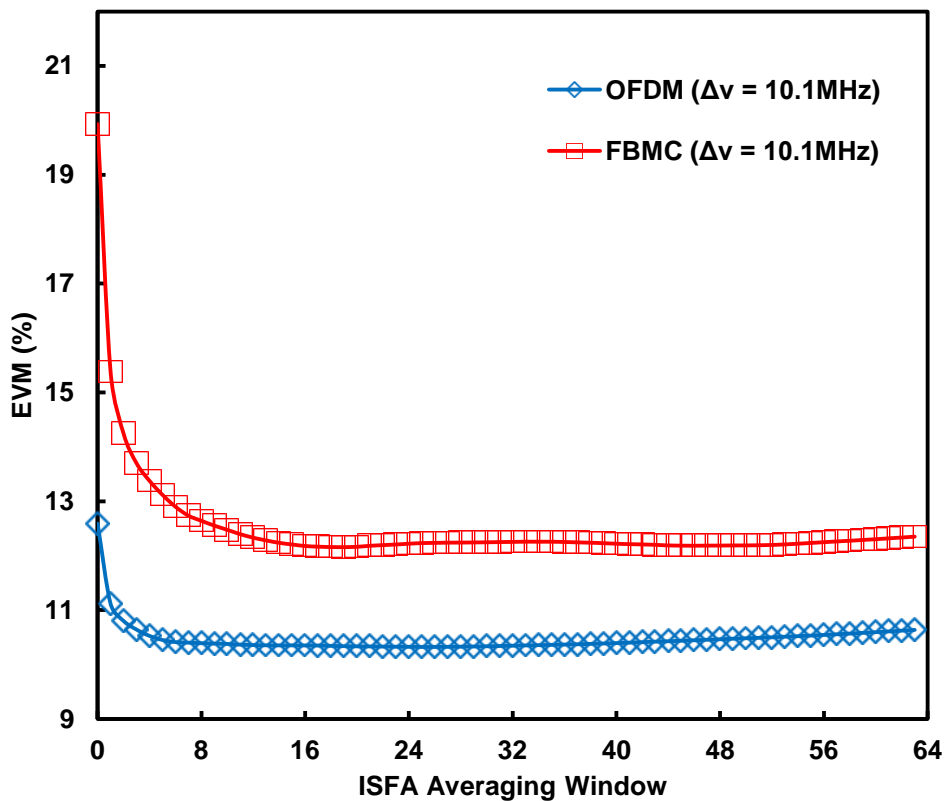


Figure 5.21: ISFA averaging window for 1GHz OFDM and FBMC after 100km

The total effective data rate after adaptive modulation in OFDM was 5.65Gbps, which represents 75% of the 7.45Gbps initial transmission data rate before adaptive modulation. The effective transmission data rate increased to 85% when ISFA was applied. Similarly, the

total effective data rate in FBMC after adaptive modulation was 3.77Gbps which amounts to 48% of the initial transmission data rate. However, the effective data rate increased significantly to 80% when ISFA was applied. It is worth highlighting that the received EVM before adaptive modulation was -15dB and -12.5dB for OFDM and FBMC which is below the -18dB threshold for 16QAM LTE signal. Clearly, the transmission throughput has been significantly improved by combining ISFA with adaptive modulation, in the presence of transmission impairments.

Finally, in order to optimise the system throughput after long-reach fibre transmission, adaptive modulation was implemented for 1GHz signal considering 10.1MHz linewidth after 100km. As previously, the ISFA averaging window was swept to determine the optimum ISFA window size as shown in Figure 5.21, which was found to be 24 for OFDM and FBMC, respectively. As can be seen from Figure 5.21, the EVM improved significantly from 20% to 15.2% even with an averaging window of 1 for FBMC, while it only improved by less than 2% in OFDM.

Figure 5.22 shows the bit-loading profile of OFDM and FBMC with and without ISFA. Clearly, more bits were loaded when ISFA was applied compared to without ISFA thus improving SE and system throughput. In the case of FBMC, less number of bits was loaded on the high subcarrier numbers, which is consistent with the previous result using 10.1MHz laser linewidth configuration. However, the received constellations for subcarriers loaded with 2- and 4-bits as shown in Figure 5.23 demonstrates successful transmission for OFDM and FBMC, respectively.

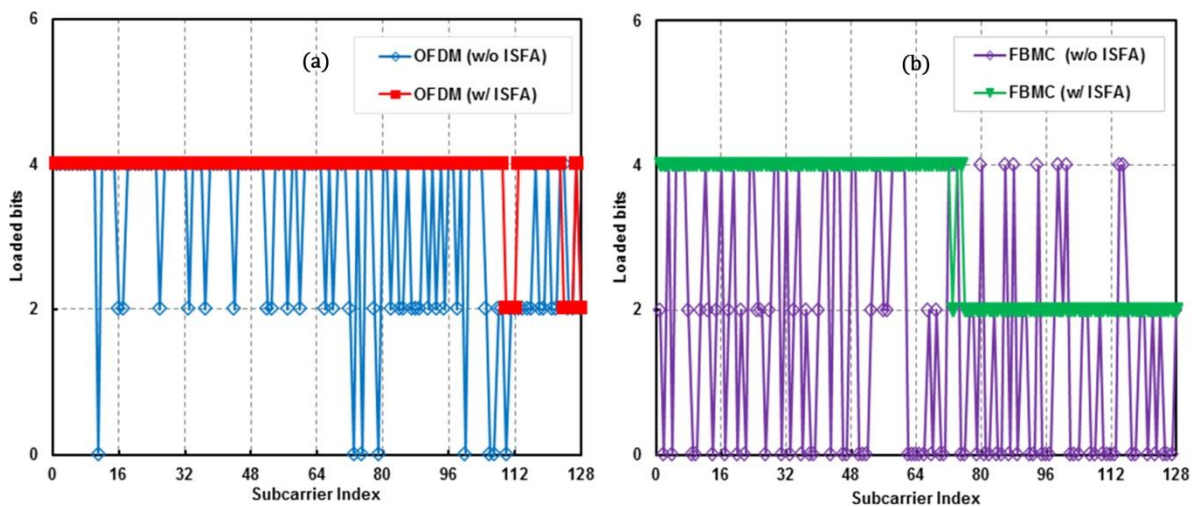


Figure 5.22: Bit-loading profiles for 10.1MHz laser and 1GHz bandwidth after 100km (a) OFDM (b) FBMC

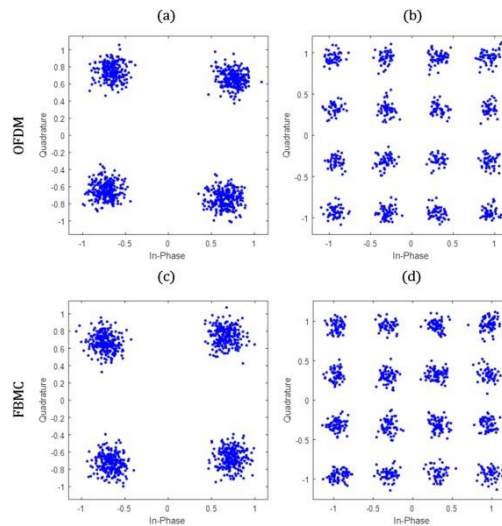


Figure 5.23: Received constellation after adaptive modulation with ISFA for 10MHz laser and 100km fibre (a)-(b) OFDM: 2-bits and 4-bits (c)-(d) FBMC: 2-bits and 4-bits

A maximum of 4-bits was loaded on all subcarriers for both waveforms. The initial transmission data rate was 3.96Gbps and 3.73Gbps for FBMC and OFDM when all the 128 subcarriers were modulated with 16QAM symbols. Due to transmission impairments dominated by CPN and ASE noise, the data rate after adaptive modulation without ISFA reduced by 33% in OFDM and more significantly by 51% in FBMC. When ISFA was applied, the effective data rate was significantly increased to 95% and 79% of the initial transmission data rate for OFDM and FBMC, respectively. Therefore, ISFA can be employed to reduce the effect of noise on system performance and improve the transmission data rate.

5.5. Summary

In this chapter, different noise sources that limit the system performance in employing laser heterodyning for mmWave upconversion has been investigated. Firstly, an expression for the system SNR was derived in terms of the PSD of each noise source. The impact of each noise source was then studied considering different parameters that influence the noise contribution. For high RIN values about -135dB/Hz, RIN dominates the system noise, thereby masking all other noise contribution. In addition, ASE noise is within the limit of NF and it is dependent on optical power at the EDFA input. Therefore, it can be concluded that for high optical power and consequently, low RIN values, the system performance is limited by laser phase noise and its interaction with CD. While the effect of laser phase noise can be reduced by increasing subcarrier bandwidth, the impact of CD increases with signal bandwidth. It was found that SNR degrades by ~1dB for every 10km increase in fibre length. In addition, an increase in linewidth from 2MHz to 10.1MHz for 100km fibre results in a reduction in the achievable bandwidth of FBMC from 750MHz to 500MHz. On the other hand, the maximum achievable signal bandwidth for 10.1MHz linewidth and 40km fibre is

1.5GHz and 1GHz for OFDM and FBMC, respectively. This implies a 33% loss in SE in FBMC compared to OFDM. In all investigated transmission scenarios, FBMC exhibits more sensitivity to noise compared to OFDM.

Finally, system performance in the presence of noise generated by the transmitter and the transmission channel has been optimised by adaptively modulating the subcarrier based on the SNR feedback from the UE. Additionally, by combining ISFA with adaptive modulation the system throughput was significantly increased. Therefore, since noise is mostly intrinsic to the component, by employing adaptive modulation with ISFA, the maximum achievable data rate can be scaled in terms of laser linewidth, modulation format and fibre length if laser heterodyne technique is employed for mmWave upconversion in the future 5G small cell MFH architecture.

6. Nonlinear Impairments in Millimeter-Wave 5G Multi-Service over Fibre Systems

6.1. Introduction

This chapter investigates the impact of PA nonlinearity for mmWave single and multi-service over fibre systems. The future 5G network is anticipated to support several services, multi-RATs and provide backward compatibility with legacy services [7, 184, 185]. In the meantime, the development of 5G-NR is underway, considering coexistence between multiple RATs and the emerging class of service [14, 15]. Integrating this new class of service with existing services has been highlighted in the standardisation of 5G NR [14]. An important issue under consideration is the interference among different services as they are transported over the same architecture [186, 187]. This is due to OFDM employed in most of the wireless broadband access is known to exhibit poor spectral containment, thereby requiring large frequency guard bands to avoid interference among adjacent services. As a candidate waveform for 5G, FBMC among others has the most superior control of OOB spectral leakage [133]. Additionally, frequency synchronisation which makes OFDM challenging in uplink is also relaxed in FBMC [134]. This makes FBMC an attractive candidate waveform in multi-service/ multi-access systems [134]. To this extent, some research initiatives have been exploring the possibility of coexistence of multiple RATs employing FBMC and OFDM in a heterogeneous architecture [48, 104, 121]. While the results demonstrate the successful transmission of FBMC and OFDM, the effect of inter-band interference (IBI), which can be severe in multi-service transmission systems, was not considered. The impact of IBI in OFDM based multi-service systems have been studied extensively in [66] considering several transmission scenarios, however, such analysis has not been done for FBMC. As mentioned earlier, several RATs employing different waveforms may likely coexist on the same infrastructure in the future 5G heterogeneous access networks. It is, therefore, important to study the impact of IBI among RATs employing different waveforms. In addition, since DFT-spread-OFDM (DFT-s-OFDM) is employed in uplink LTE to reduce the effect of PAPR and improve PA efficiency, it will be interesting to investigate DFT-spread-FBMC (DFT-s-FBMC) in uplink multi-service transmission.

In order to study the effect of PA-induced IBI in multi-service/ multi-RAT transmission systems, several transmission scenarios are considered for the coexistence of OFDM and FBMC waveforms in 5G mmWave small cell MFH architecture. The investigated scenarios depict possible coexistence schemes for both legacy and 5G services.

6.2. Nonlinear Subcarrier Intermodulation in Multi-Service Systems

Multicarrier systems are generally sensitive to nonlinear impairments due to their continuously varying waveform and high PAPR [188-190]. Intermodulation among subcarriers results in both in-band and out-of-band distortion [191]. The in-band distortion resulting from third-order IM is the most challenging as it usually has a frequency close to the signal frequency and thus it cannot be filtered out [192]. On the other hand, out-of-band distortion occurs at a frequency away from the signal frequency band, hence this can be filtered out. The even and odd order IMs accounting for out-of-band distortion can be easily filtered out. However, this could be an issue in multi-service systems, where different services are allocated adjacent frequency bands. It has been reported that the PSD of OOB emission is two times the signal bandwidth [66]. Therefore, IBI between two services depends on their subcarrier bandwidth and their relative amplitudes [56]. The high OOB spectral leakage in OFDM means large frequency guardband is always inserted between adjacent services in OFDM based systems to reduce the effect of IBI. FBMC, on the other hand, exhibits highly suppressed OOB emissions. Based on these characteristics, it is therefore expected that the sensitivity of both waveforms to IBI will differ.

A simulation testbed was implemented in VPI Transmission Maker® employing MATLAB/VPI cosimulation technique to investigate the impact IBI in a multi-service over fibre architecture using laser heterodyning for remote mmWave upconversion. Considering the employed architecture, PA and MZM are the source nonlinear IMs. Since the impact of MZM nonlinearity has been studied in chapter 4, evaluations carried out in this chapter focuses only on nonlinear impairments due to the PA. Therefore, it is important to accurately model the nonlinear transfer function of the PA.

6.2.1. Power Amplifier Modelling

The PA nonlinearity was characterised in VPI based soft envelope limiter (SEL), due to its simplicity [193], which assumes linear gain up to an input saturation level. Beyond the saturation level, the amplified signal is clipped resulting in nonlinear distortion of the input signal amplitude. The transfer function of the PA can be described as [194]:

$$|y(t)| = \begin{cases} Gx(t), & x(t) \leq V_0 \\ V_0, & x(t) > V_0 \end{cases} \quad (6.1)$$

where $|y(t)|$ is the magnitude of the output signal envelope, G is the small signal gain of the PA, $x(t)$ is the envelope of the input signal and V_0 is the saturation level.

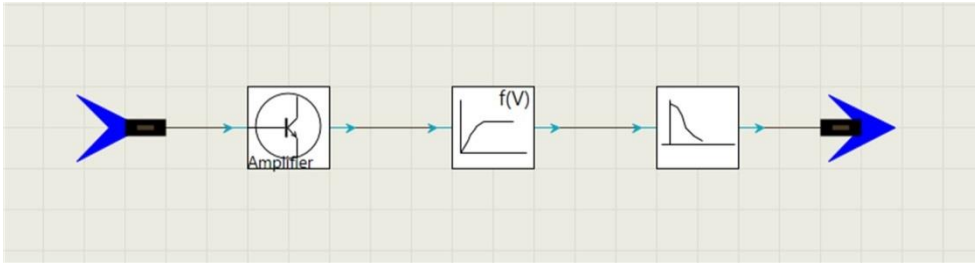


Figure 6.1: PA nonlinearity modelling in VPI

The VPI model of a PA exhibiting input saturation is depicted in Figure 6.1. The first module provides a linear gain to the input signal and adds noise. The second module is the nonlinear element which sets limiting function by clipping the input signal level and consequently, distorting the signal amplitude as the input power increases. The third module represents the frequency response. Since the focus here is the amplitude distortion of the input signal, the frequency response is assumed to be flat over the range of signal bandwidth. A single tone was used to characterise the AM/AM conversion of the PA having a small signal gain of 30dB. Figure 6.2 shows the AM/AM conversion of the PA with a single tone excitation for different input saturation levels. It can be seen that the input-output relationship is linear up to around -30dBm input power, after which the PA gradually tends towards the compression region. The transition from the linear regime to the saturation point is dependent on V_0 .

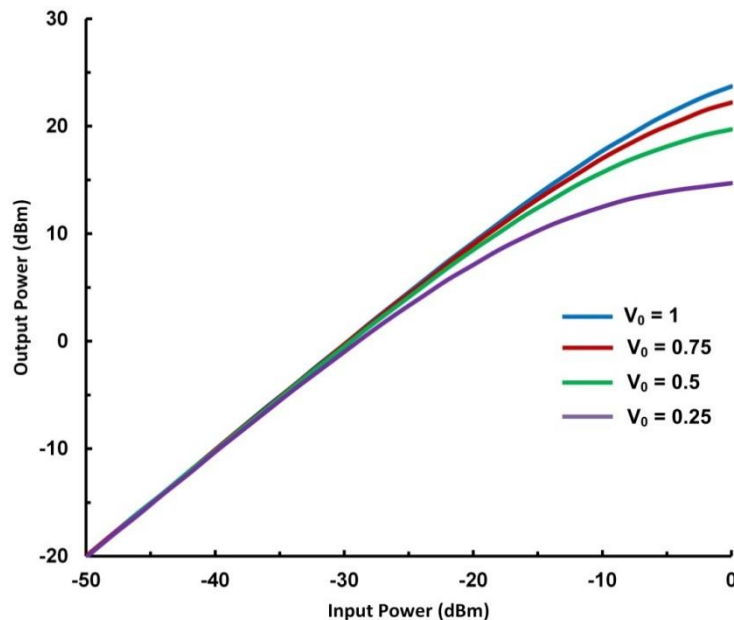


Figure 6.2: AM/AM conversion of the PA

For instance, two-tone excitation is described in Figure 6.3, where the two fundamental frequencies represent two subcarriers from one service. It can be seen that the two subcarriers after passing through a nonlinear PA will generate both in-band distortion and out-of-band distortion. The IMD represents the in-band distortion which is formed by $2f_1 - f_2$

and $2f_2 - f_1$. The second and third harmonics result in OOB distortion. The third harmonic is of particular interest in the multi-service systems since it will be closer to the fundamental frequency of the adjacent service.

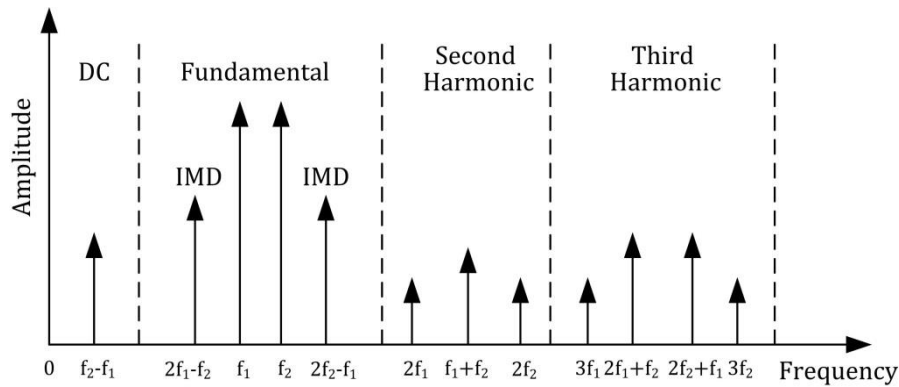


Figure 6.3: Frequency-domain response of nonlinear PA with two-tone excitation

It should be noted that the amplitude of the generated IM products depends on the amplitude of the fundamental frequencies which in this case are the subcarriers, whereas, the frequency is dependent on the sum/difference of the subcarriers. Therefore, high amplitude service will most likely generate higher out-of-band distortion which will consequently become in-band distortion to the adjacent low amplitude service. In the next section, the impact of IBI as a result of PA nonlinearity is investigated considering the simultaneous transmission of multiple IF services over fibre with remote mmWave upconversion

6.3. Impact of PA Nonlinearity in Millimetre-wave IF over Fibre Upconversion using Laser Heterodyning

In order to evaluate the impact of PA nonlinearity on the proposed architecture, it is important to consider different transmission scenarios. Since several works have studied nonlinear impairments in OFDM based services, the main focus here is to investigate IBI due to PA nonlinearity in a multi-service over fibre systems with remote mmWave upconversion. For all transmission scenarios, OFDM and FBMC waveforms were transmitted in order to compare their performance. Table 6-1 lists the scenarios considered in the evaluation of PA-induced distortions in multi-service multi-RAT mmWave architecture.

In scenario 1, OFDM and FBMC were transmitted separately over the architecture and the input power of the PA was swept to evaluate the effect of in-band distortion on the transmitted waveform. To emulate non-contiguous CA, two OFDM services having the same bandwidth were transmitted simultaneously in the second scenario. To compare the performance of FBMC with OFDM in multi-service transmission, the FBMC waveform was transmitted using the same configuration in scenario 2. In scenario 3, the bandwidth of

service 2 was reduced to half the bandwidth of service 1 to study the effect of IBI when the services have different bandwidths. In scenario 4, the possible coexistence of different RATs employing different waveforms was investigated to evaluate the effect of IBI between OFDM and FBMC.

Table 6-1: Scenarios used to investigate PA-induced IBI in multi-service mmWave MFH

Scenario	No. of Services	Service 1	Service 2	FFT Size	Data Subc.	BW (MHz)	C.F (GHz)	GB (MHz)
1	1	FBMC	-	4096	128	250	0.625	-
		OFDM						
2	2	FBMC	FBMC	4096	128/	250/	0.625/	750
		OFDM	OFDM		128	250	1.625	
3	2	FBMC	FBMC	4096	128/	250/	0.625/	750
		OFDM	OFDM		64	125	1.5625	
4	2	FBMC	OFDM	4096	128/	250/	0.625/	750
		OFDM	FBMC		128	250	1.625	

In the three multi-service investigations, the input power of service 1 was swept while the input power of service 2 was fixed. In that way, out-of-band emission from service 1 results in IBI to service 2. The subcarrier spacing and frequency guardband between the two services was fixed for all evaluations.

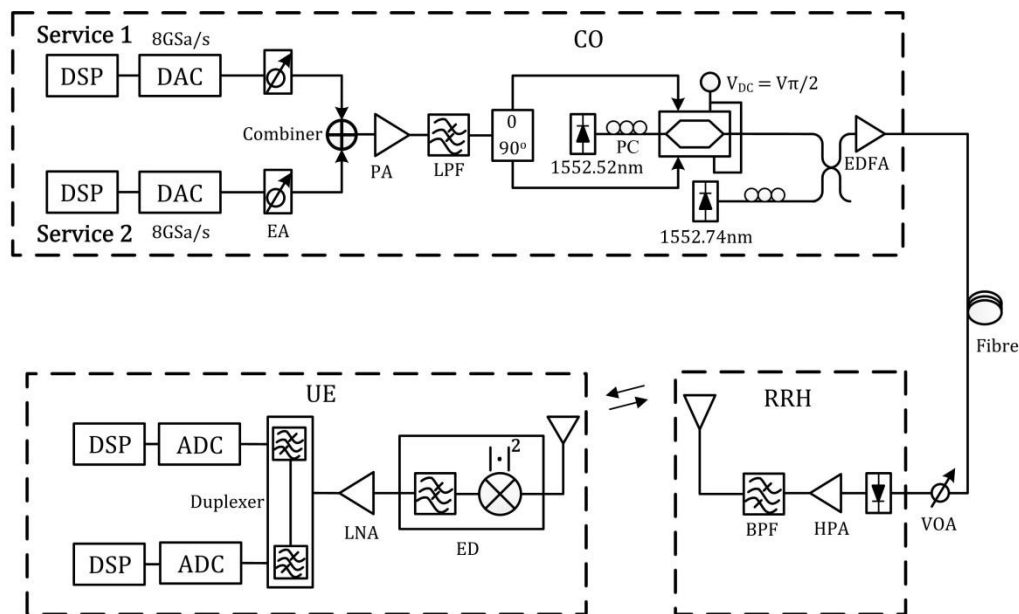


Figure 6.4: Simulation setup for the multi-service over fibre with remote mmWave upconversion

Figure 6.4 shows the schematic employed for simulation in scenario 2 - 4. The schematic earlier used in chapter 5 was employed for the first scenario since only one service was transmitted. As previously, the waveforms were programmed in MATLAB and loaded onto

separate DAC sampling at 8GSa/s via the cosimulation module. An electrical attenuator was used to adjust the power of the signals before they were combined and fed into the PA. The PA as described in section 6.2.1 has a small signal gain of 30dB. After amplification, a LPF was used to remove aliasing from the DACs. Subsequently, the combined signal was applied to two arms of the DEMZM with $\pi/2$ phase shift through a hybrid coupler as shown in Figure 6.4. The OLO was coupled with the OSSB output of the MZM and amplified by an EDFA before it was sent over 20km fibre. A VOA was used to fix the input optical power at +1dBm. For such fibre distance, the effect of CD is negligible. In addition, as seen in chapter 5, noise added by the PD can be ignored at +1dBm input optical power. Therefore, system impairments are expected to be dominated by the PA nonlinearity. At the UE, the IF signal after ED, was amplified by a LNA, after which it was fed into a duplexer to extract each service from the composite signal. Subsequently, the extracted signals were converted to digital samples by a 64GSa/s ADC before passing to MATLAB for offline DSP via the *cosim module*. The system parameters used in the simulation are listed in Table 6-2.

Table 6-2: System parameters used in the simulation

Parameter	Value	Parameter	Value
Signal Bandwidth	250MHz	Laser Linewidth	100kHz
Total IFFT/FFT	4096	Laser RIN	-155dB/Hz
Data Subcarriers	128	Laser Power	10dBm
Modulation	16QAM	MZM Insertion Loss	5dB
CP (OFDM)	0	MZM Extinction Ratio	35dB
K (FBMC)	4	Fibre Length	20km
DAC/ADC Sampling Rate	8 /64GSa/s	Fibre Dispersion	17ps/(nm.km)
DAC/ADC Resolution	10bits	Fiber Attenuation	0.2dB/km
Thermal Noise	$10 \times 10^{-12} \text{A}/\text{H}^{1/2}$	EDFA Noise Figure	5dB
		PD Responsivity	0.68A/W

In order for the SE of OFDM and FBMC to be comparable, the OFDM waveform was generated without CP. Moreover, there was no significant difference in the received EVM after 20km fibre when compared to BTB transmission. The nonlinear impairment was evaluated by observing the EVM as a function of the PA input power.

6.3.1. Scenario 1

Scenario 1 studies the effect of PA nonlinearity on a single service considering OFDM and FBMC, respectively. The waveforms were transmitted separately using the same configuration and the received EVM as a function of the PA input power was observed.

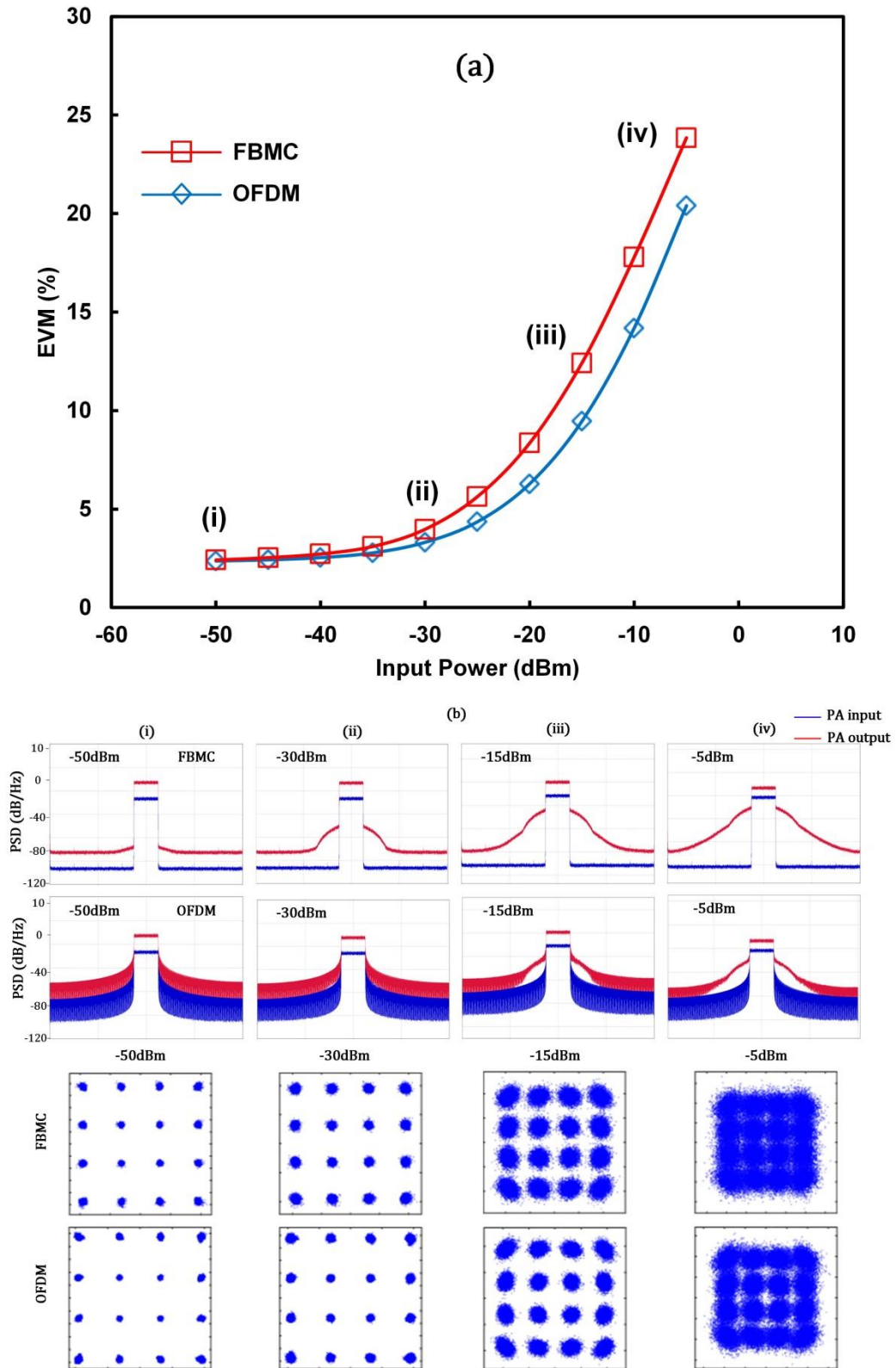


Figure 6.5: (a) EVM as a function PA input power for OFDM and FBMC (b) PSDs of FBMC and OFDM at input and output of the PA at points (i) to (iv) (i.e. -50dBm, -30dBm, -15dBm and -5dBm) and corresponding constellations

Figure 6.5 shows the EVM plot as the input was swept between -50dBm to -5dBm, the EVM increases slightly with an increase in the input power between -50dBm and -30dBm. Beyond this point, the EVM increased sharply as the PA starts to introduce significant distortion to the input signal. Observe that FBMC exhibits higher sensitivity to PA-induced in-band distortion which can be attributed to the high PAPR and the OQAM modulation scheme employed [193, 195]. The PSDs and corresponding constellation at points labelled (i) to (iv) are shown in Figure 6.5 (b). In addition, the fact that PSD of OOB emission is 2x the signal bandwidth can be observed, as its spectrum extending outside the signal bandwidth on either side is equivalent to the signal bandwidth. This is noticeable in FBMC from -30dBm PA input power but it only becomes obvious in OFDM at -5dBm. As can be seen from Figure 6.5, the EVM value of FBMC is 4% worse than OFDM. This implies that FBMC is more sensitive to PA-induced nonlinearity than OFDM.

Since the OOB emission will most likely extend to the signal spectrum of the adjacent signal in a multi-service scenario, subsequent investigations consider the coexistence of multi-service.

6.3.2. Scenario 2

In this scenario, the effect of IBI on service 2 is investigated. The input power of service 1 was swept between -50dBm and -25dBm in 5dB step, while the input power of service 2 was fixed at -50dBm.

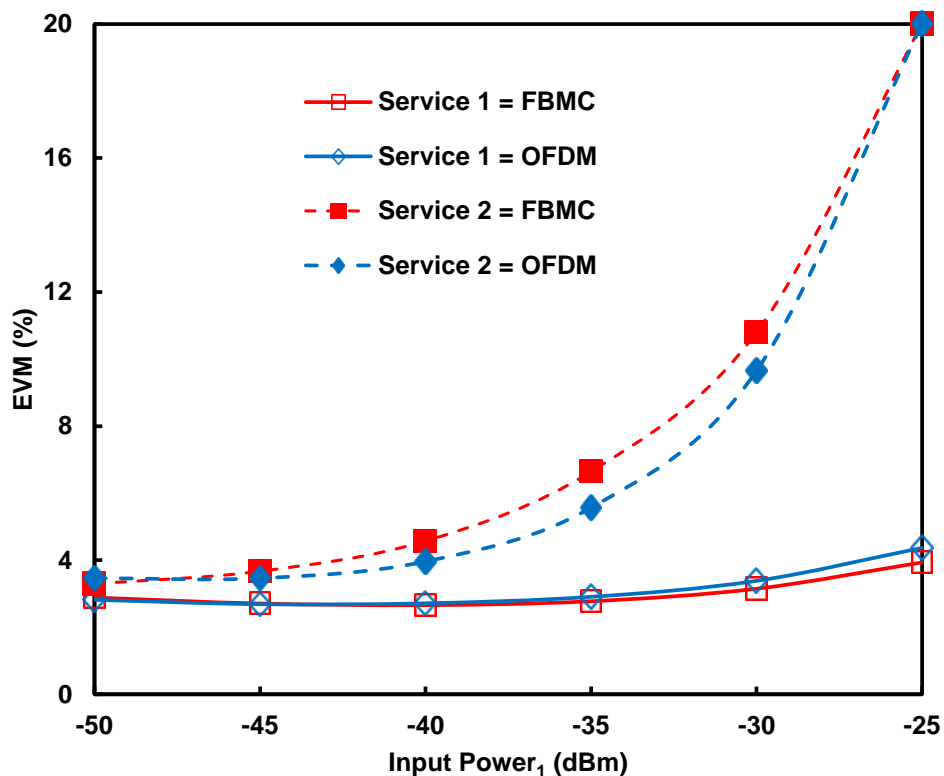


Figure 6.6: EVM as a function of input power of service 1

By fixing the input power of service 2, it experiences IBI as the input power of service 1 increases, driving the PA into the nonlinear regime. This means that OOB distortion from service 1 will result in IBI to service 2. As shown in Table 6-1, service 1 and service 2 have the same bandwidth and the guard band between the two services was set to 750MHz, which is 3 times the signal bandwidth. The two services are from the same RAT, either OFDM or FBMC.

Figure 6.6 shows the EVM of service 1 and service 2 as a function of the input power of service 1. Service 2 experiences high IBI as the input power of service 1 was increased, resulting in significant EVM degradation. It can be seen from Figure 6.6 that both OFDM and FBMC will introduce IBI to adjacent services in a multi-service transmission scenario. This implies that the benefit of low OOB emission, and consequently, low IBI in FBMC cannot be achieved when the PA is driven in the nonlinear regime. Next, it will be shown that the impact of PA-induced IBI on the system performance depends on the bandwidth of participating signals.

6.3.3. Scenario 3

In order to study the dependence of IBI on the signal bandwidth, the number of data subcarriers in service 2 was reduced to 64. As a result, the bandwidth of service 2 is half the bandwidth of service 1 and the guard band was kept constant.

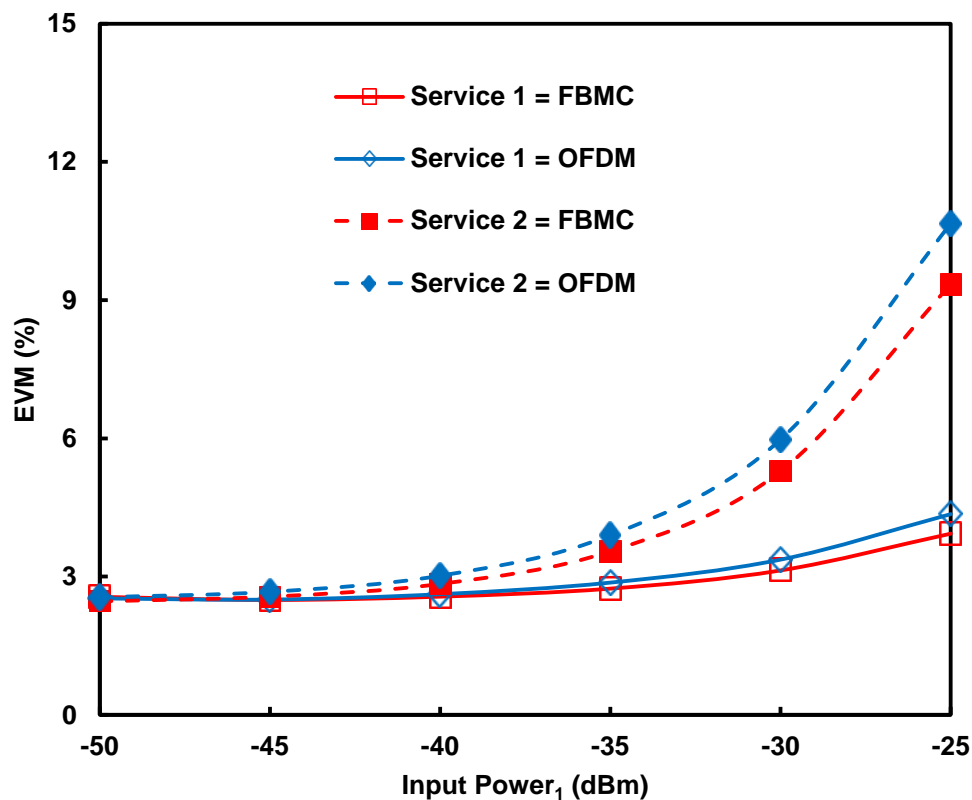


Figure 6.7: EVM as a function of input power of service 1

As previously, the performance of FBMC and OFDM was compared for this configuration. Figure 6.7 shows the received EVM as a function of the input power of service 1. The EVM of service 2 is 9.3% and 10.6% for FBMC and OFDM, respectively. Compared to the EVM in scenario 2 where the bandwidth of service 2 was 250MHz, the EVM reduced by 10% for both waveforms. This is because most OOB distortion from service 1 fall out of the signal bandwidth of service 2, therefore, service 2 experiences less IBI from service 1. The result demonstrates that the impact of IBI on adjacent low input power service is dependent on the bandwidth of participating signals. Next scenario investigates the coexistence of FBMC and OFDM and their interaction due to IBI.

6.3.4. Scenario 4

This scenario studies the coexistence of FBMC and OFDM deployed as multi-service signals in a common infrastructure. An example could be a new class of service from different RATs coexisting in the same 5G architecture. The bandwidth of service 1 and service 2 is the same (i.e. 250MHz).

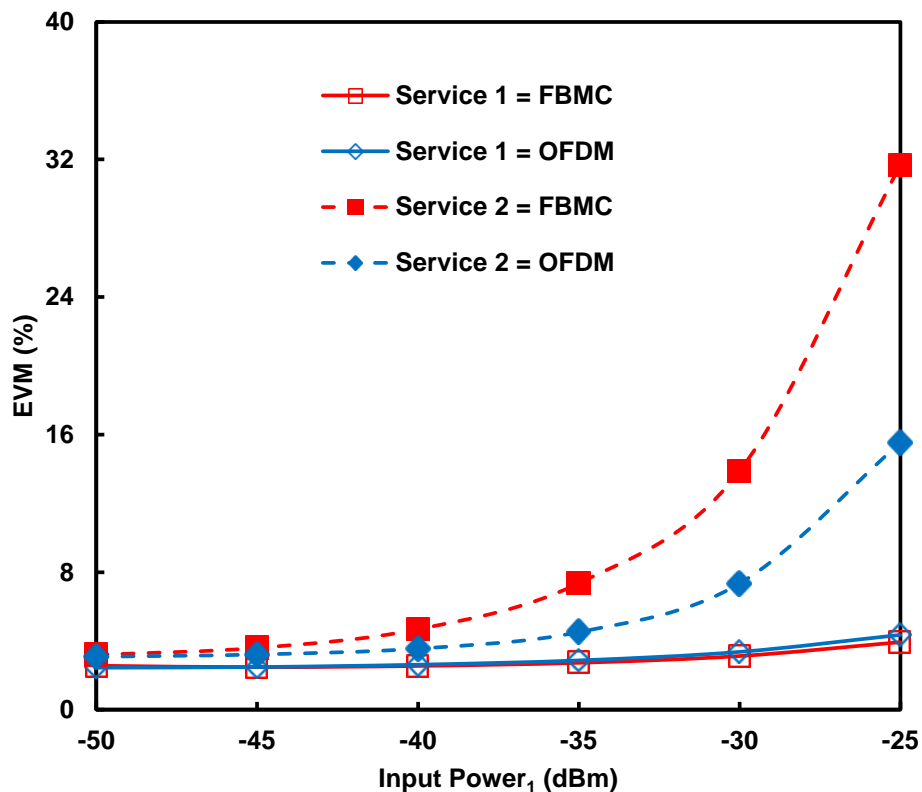


Figure 6.8: Coexistence of FBMC and OFDM in multi-service transmission scenario

The input power of service 1 was swept between -50dBm and -25dBm. FBMC was deployed as service 1 while OFDM was deployed as service 2. OFDM was also deployed as service 1 while FBMC was deployed as service 2 to enable a fair comparison between the waveforms in terms of sensitivity to IBI when they are transmitted together. Figure 6.8 shows the EVM

as a function of the input power of service 1 for FBMC and OFDM, respectively. Both waveforms exhibit similar EVM performance as service 1. However, due to the large OOB emission in OFDM, FBMC when deployed as service 2 experiences high IBI, resulting in significant EVM deterioration. On the contrary, the much steeper roll-off of OOB emission in FBMC means less IBI is experienced by service 2 based on OFDM, which is clearly seen in Figure 6.8. As it can be observed from Figure 6.8, the EVM of service 2 at -30dBm input power of service 1 is 13.8% and 7.3% for FBMC and OFDM, respectively. This implies that FBMC can coexist with services from different RATs at moderate powers without any significant impact on system performance.

6.4. In-band Deployment of LTE Service in 5G Service

In this section, a unique transmission scenario is investigated where legacy service such as LTE is integrated with a wideband signal. In this case, the bandwidth and carrier frequency of the legacy service is fixed. Previous investigations considered wideband signals having bandwidth >200MHz, enabled by the huge spectrum available in the mmWave band. The coexistence of these wideband signals with legacy services such as LTE is a key direction in the next phase of 5G-NR standardisation [14]. For example, one way by which narrowband-IoT (NB-IoT) service can be deployed in the present LTE systems as specified in the 3GPP Rel. 13 standard is to deploy the NB-IoT service in-band LTE service [196]. To better utilise the available spectrum, the aforementioned concept is adopted here to access the coexistence of multiple services over the same architecture. To achieve this, a spectral hole is created during the baseband signal generation of the 5G wideband signal, corresponding to the carrier frequency of the legacy service. This will allow seamless integration of legacy service such as LTE with 5G wideband signal. Notably, the large OOB emission in OFDM which is employed in LTE will impact the combined signal. It will, therefore, be interesting to examine the effect of IBI within the architecture. To this extent, an LTE-like signal having 128 data subcarriers and 15MHz bandwidth was programmed in MATLAB and deployed as service 2 in the architecture shown in Figure 6.4. FBMC and OFDM waveforms are deployed as service 1 at different times to evaluate their performance with LTE signal. A total of 128 subcarriers are used for data in service 1 resulting in 500MHz bandwidth and 3.90625MHz subcarrier spacing. The subcarrier spacing of service 1 is 32 times the subcarrier spacing service 2 which is 122kHz. Thus, the LTE signal is a NB service w.r.t to service 1. In that case, 4 subcarriers in service 1 correspond to the whole bandwidth of service 2. The subcarrier allocation of service 1 was selected such that it is centred at 2.5GHz. Also, the centre frequency of the LTE signal was set to 2.5GHz. This implies that the in-band LTE signal is symmetric around the centre frequency of service 1.

First, the input IF power to the PA was set to -50dBm and -60dBm for service 1 and service 2, to investigate the required number of nulled service 1 subcarriers that will be sufficient as guardband on either side of the LTE signal.

Figure 6.9 shows the EVM as a function of nulled subcarriers around the LTE signal when FBMC and OFDM are employed as service 1 (see Figure 6.10). The drawback in employing OFDM for seamless multi-service transmission is clearly seen here as it requires about 28 subcarriers to avoid interference from the LTE signal. This is as a result of a strict frequency synchronisation requirement in OFDM. Conversely, only one subcarrier guardband is required in FBMC to achieve seamless integration of the LTE signal. While this true when the power ratio between the two signals is well-balanced, it is not the case in the presence of PA nonlinearity. Therefore, 28 subcarriers are used as a guard band for subsequent investigations.

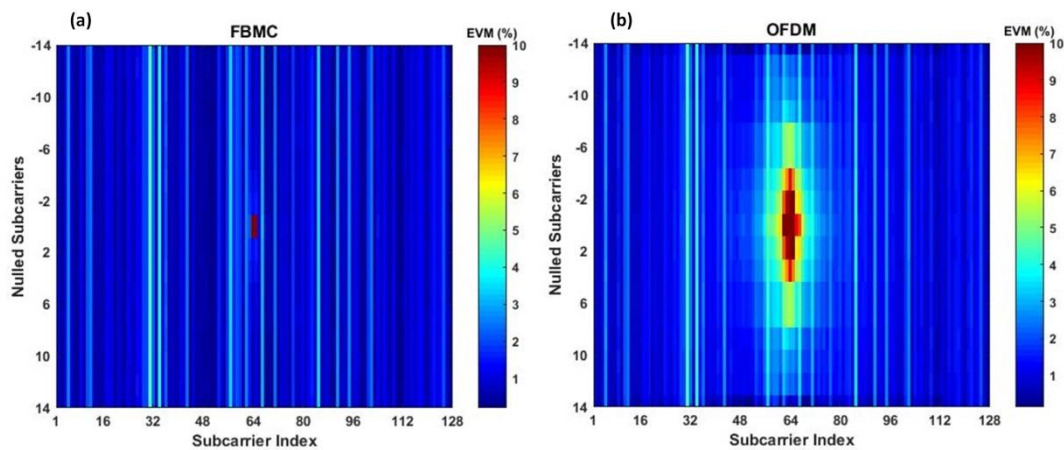


Figure 6.9: EVM as a function nulled subcarriers on either side of the LTE-like signal (a) FBMC (b) OFDM

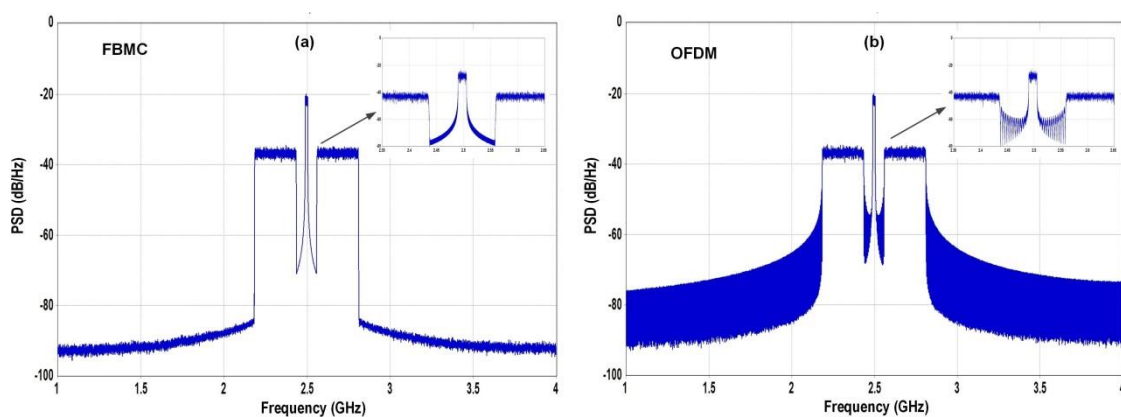


Figure 6.10: PSD of the integrated service (a) FBMC with the LTE zoomed out shown in the inset (b) OFDM with the LTE zoomed out shown in the inset

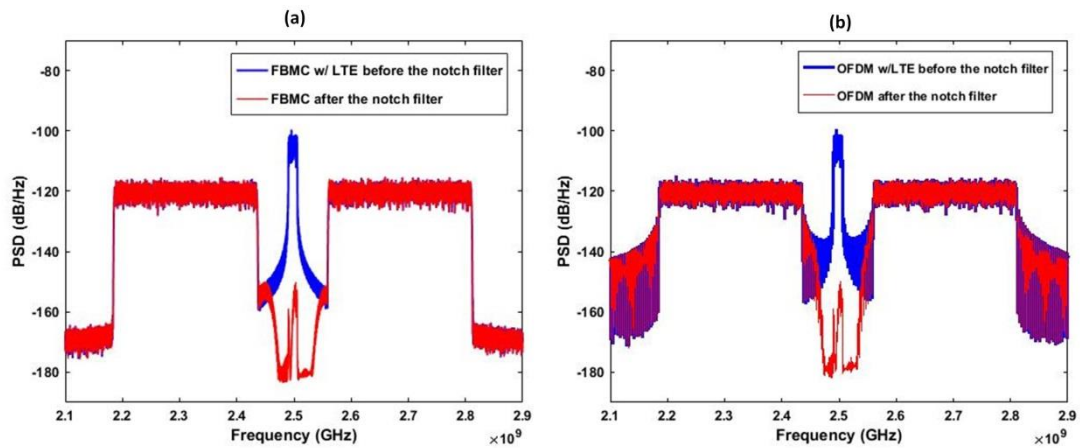


Figure 6.11: PSD of the Integrated Service before and after the notch filter (a) FBMC (b) OFDM

Next, the impact of IBI between the two services was studied by varying the power of one service while the input power of the other service is fixed.

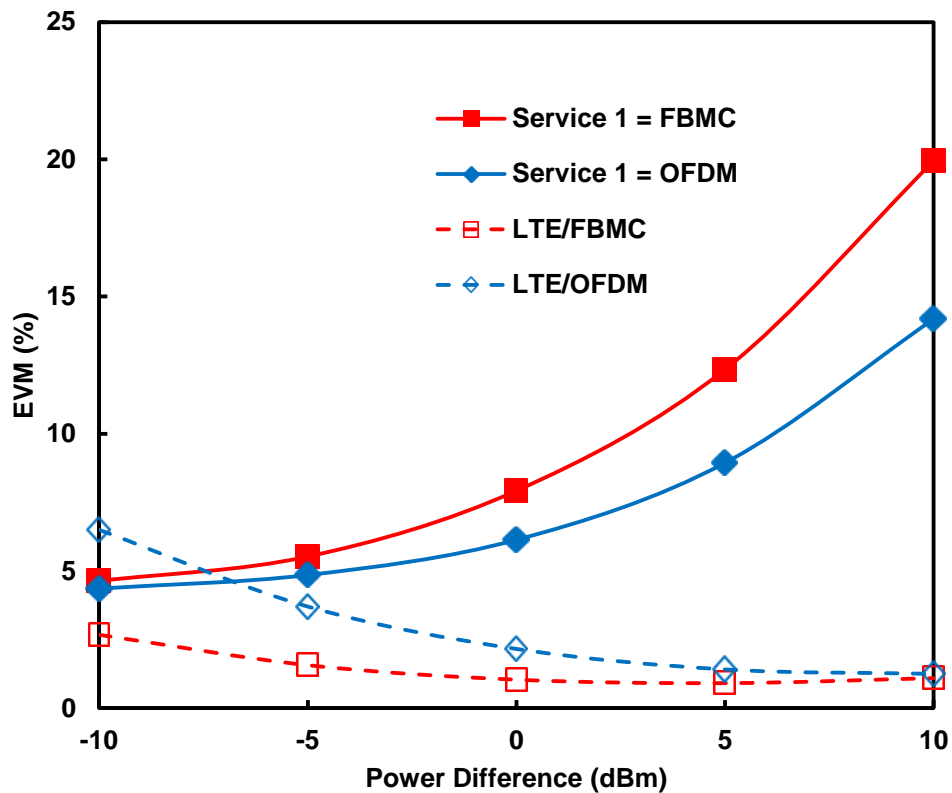


Figure 6.12: EVM as a function power difference between service 1 (FBMC and OFDM) and LTE signal as input power of LTE signal increased from -60dBm to -40dBm and the input of Service is fixed at -50dBm

Prior to processing the received signal in MATLAB, 465-tap notch filter was implemented in MATLAB using a Kaiser window to reject the LTE signal from the combined signal [186]. Similarly, a 185-tap BPF was used to extract the LTE signal before demodulation. The high filter order is due to the sharp roll-off requirement to avoid suppressing the sidelobe of the adjacent signal. The guardband can be increased to further relax the filter order

requirements. The PSD of the wideband signal is plotted in Figure 6.11 before and after the notch filter for FBMC and OFDM, respectively. It can be seen that the NB signal is fully rejected after the notch filter with almost 50dB attenuation.

The input power of the LTE signal was then swept between -60dBm and -40dBm while the input power of service 1 was fixed at -50dBm. The EVM as a function of the power difference between service 1 and the LTE signal is shown in Figure 6.12. Observe that EVM of LTE at -10dBm power difference is 4.4% lower when integrated with FBMC compared to when integrated with OFDM. This is due to lower OOB emission in FBMC as the effect of PA nonlinearity has yet to influence the system performance. Further, the effect of enlarged OOB emission in the OFDM based LTE signal can be seen significantly impacting the EVM of FBMC as the power difference approaches +10dBm. In the same way, the input power of service 1 was swept between -50dBm and -30dBm while the input power of the LTE signal was fixed at -50dBm.

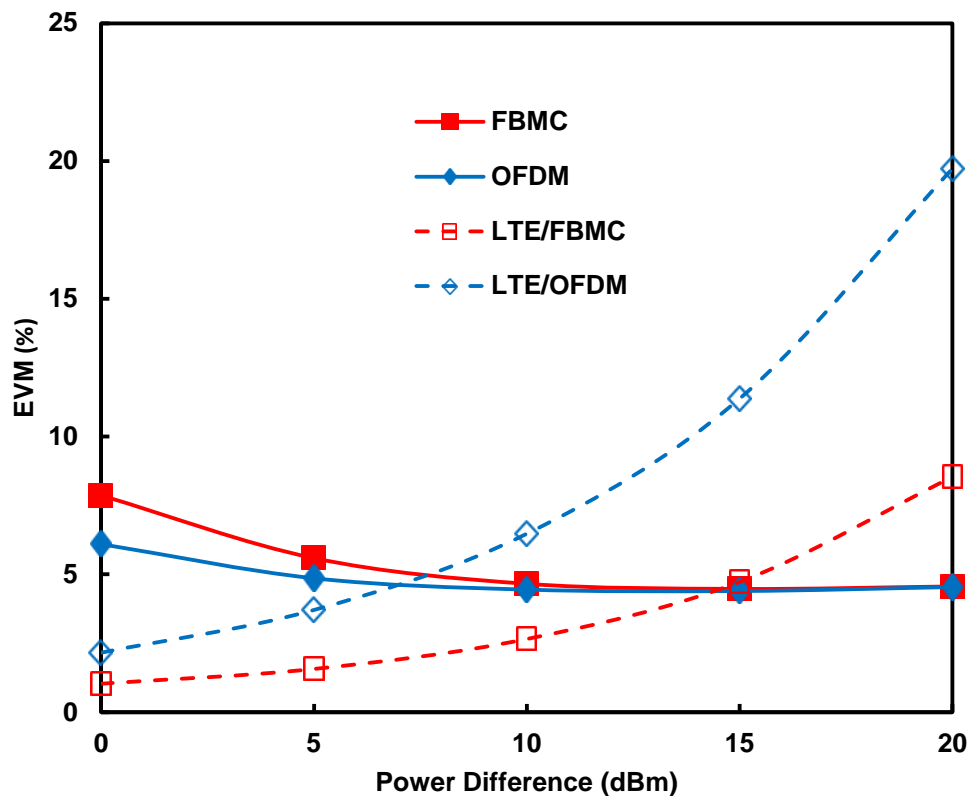


Figure 6.13: EVM as a function power difference between service 1 (FBMC and OFDM) and LTE signal as input power of service 1 increased from -50dBm to -30dBm and the input of LTE is fixed at -50dBm

Figure 6.13 shows the EVM as a function of the power difference as the input power of service 1 was swept. Notice that the LTE suffers severely from IBI when OFDM was employed as service 1, whereas IBI is greatly reduced when FBMC was employed as service 1. The EVM of LTE increased by 17.5% as the input power difference with OFDM

increased from 0dBm to 20dBm while it only increased by 7.5% with FBMC. This is consistent with the previous results as FBMC contribute minimal interference to adjacent service thanks to the highly suppressed OOB emission. Even in the absence of PA nonlinearity, a large guardband is required in OFDM due to its sensitivity to guardband spacing as shown in Figure 6.9. Therefore, OFDM appears to be less efficient in terms of spectrum utilisation in a multi-service transmission scenario. FBMC, on the other hand, shows good spectral containment which means it contributes less IBI to adjacent service. However, as shown in previous results, this advantage vanishes when PA nonlinearity comes into play. To demonstrate the benefit of FBMC, the number of guardband subcarriers was reduced to 16 and the power difference between service 1 and the LTE signal was set to 0dBm. Service 1 was then transmitted with and without in-band LTE signal to evaluate the impact of the LTE signal on service 1.

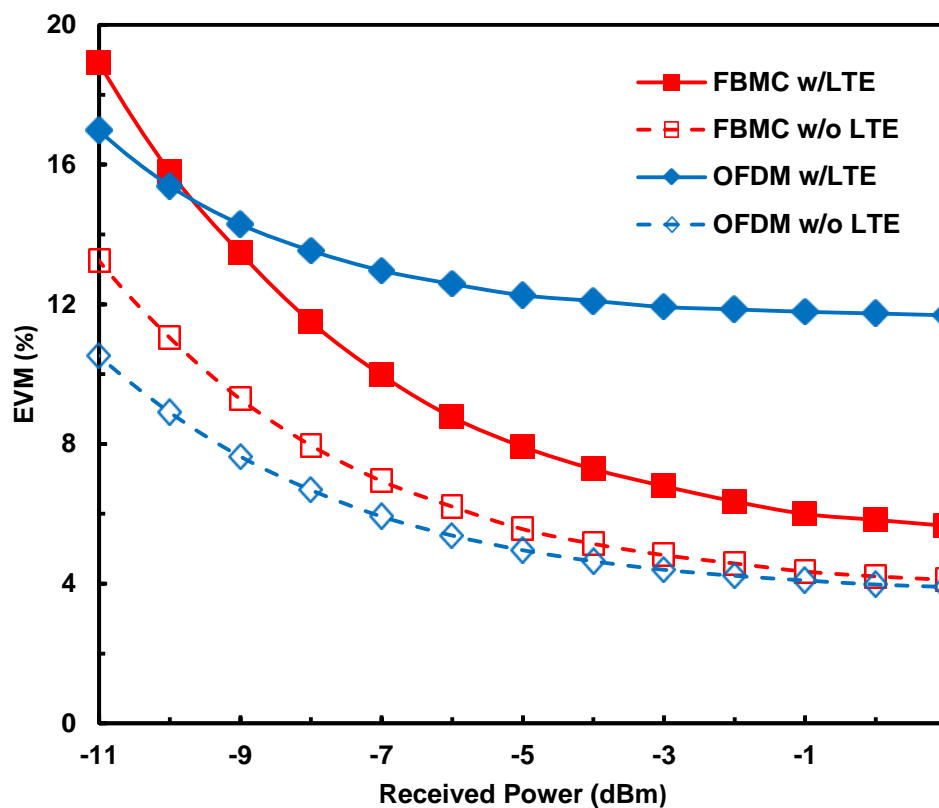


Figure 6.14: EVM as a function of received power for FBMC and OFDM with and without in-band LTE

The EVM as a function of received optical power after 20km fibre is shown in Figure 6.14 considering FBMC and OFDM with and without in-band LTE. The impact of IBI can be noticed by observing the difference in the EVM of OFDM with and without the in-band LTE. The EVM performance of FBMC with in-band LTE is 1.5% higher than the EVM without in-band LTE at +1dBm received power. This reveals that FBMC picks up much less IBI and

also contribute minimal IBI to the LTE signal. Note that the PA is assumed to be operating in the linear regime here.

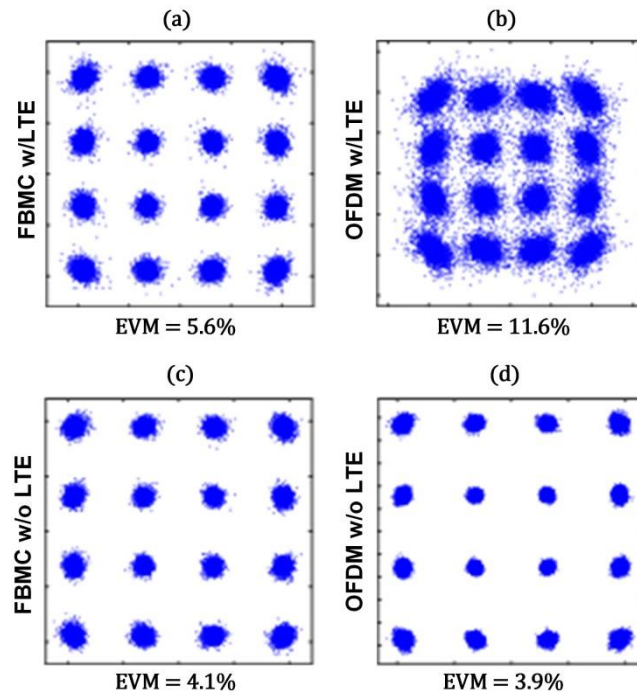


Figure 6.15: Constellation at +1dBm received power (a) FBMC /w LTE (b) OFDM /w LTE (c) FBMC w/o LTE (d) OFDM w/o LTE

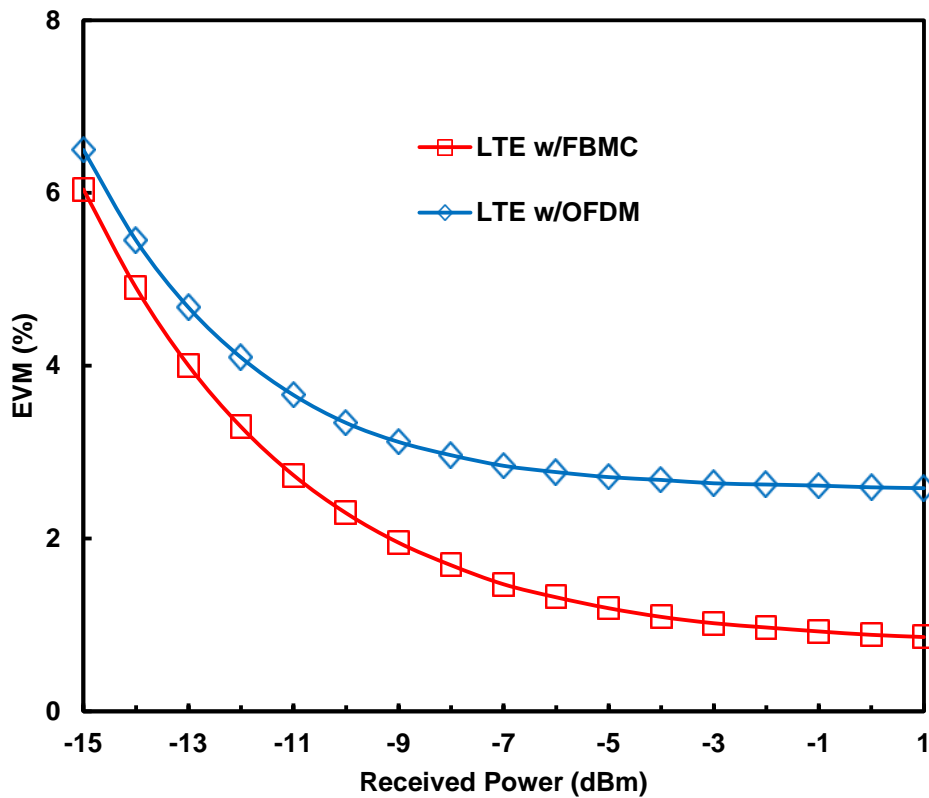


Figure 6.16: EVM of LTE integrated with FBMC and OFDM as a function of received power

Therefore, the result suggests that FBMC can comfortably coexist with legacy services in the future 5G heterogeneous access networks. This benefit can be exploited for a seamless multi-service transmission in the below 6GHz as well as the mmWave frequency bands. The received constellation and corresponding EVM at +1dBm received optical power for FBMC and OFDM with and without in-band LTE is shown in Figure 6.15.

In the same way, the EVM of LTE deployed in-band FBMC and OFDM is plotted in Figure 6.16. Although the EVM performance is generally limited at low received powers by PD noise, the fact that IBI from FBMC to the in-band LTE signal is significantly reduced is obvious as the received optical power increased.

6.5. Impact of PA Nonlinearity in Uplink Multi-User Access Systems

The impact of PA in uplink multi-user access is investigated in this section. For simplicity, the uplink signals are not generated at mmWave frequency but at IF and transported via optical fibre to the CO for uplink Rx DSP. DFT-s-OFDM and DFT-s-FBMC are employed for the evaluation. The subcarrier allocation follows the localised FDMA technique. It should be noted that DFT-s-FBMC has been reported to have higher PAPR[148], which will be further increased by using IAM preamble [142] for CE.

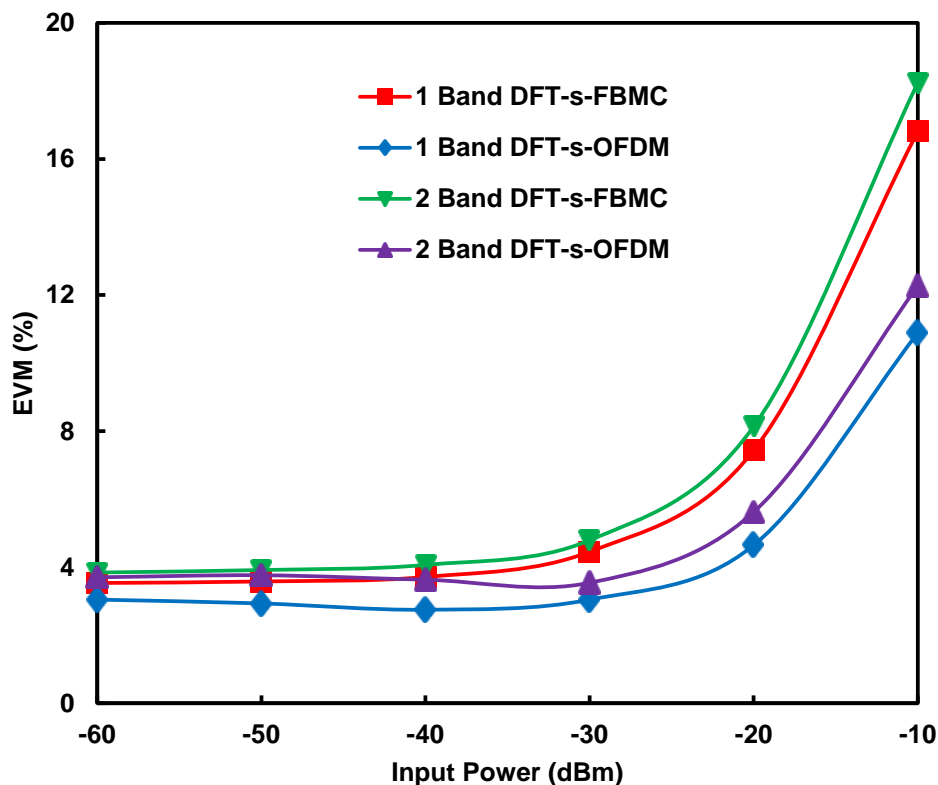


Figure 6.17: EVM as a function of PA Input power for DFT-s-FBMC and DFT-s-OFDM uplink signals

In order to reduce this effect, both waveforms were hard-clipped in MATLAB before being passed to the DAC. The PAPR is 11.5dB and 13.5dB for DFT-s-OFDM and DFT-s-FBMC, respectively. Another phenomenon that common in uplink multi-user transmission is timing misalignment between the uplink signals, leading to loss of orthogonality and consequently ICI [134, 157, 197]. Here, the multiband uplink signals are assumed to be perfectly synchronised in time. Also, frequency bandgap equivalent to the signal bandwidth is inserted between the two bands to emulate non-contiguous CA.

Figure 6.17 shows the EVM as a function PA input power for both waveforms considering 1 and 2 bands uplink transmission. Again, DFT-s-FBMC shows more sensitivity to PA nonlinearity compared to DFT-s-OFDM. However, the EVM performance of both waveforms is similar in the linear regime between -60dBm and -30dBm. This is comparable to Figure 6.5, where FBMC and OFDM are employed in the downlink. However, the difference in EVM is due to the noise added during mmWave upconversion in the DL transmission.

6.6. Summary

In this chapter, the impact of PA-induced IBI in a multi-service over fibre systems has been investigated, considering FBMC and OFDM waveforms. Several coexistence scenarios were considered and the performance of the participating services was evaluated based on the received EVM as a function of the input power to the PA. In a single service transmission scenario, FBMC exhibits higher susceptibility to PA nonlinearity compared to OFDM. In addition, the spectral regrowth in FBMC is much faster as the PA was being driven to the nonlinear regime. In a two service transmission scenario, FBMC and OFDM were deployed as either service 1, service 2 or both and the input power of service 1 was increased relative to the input power of service 2 to assess the impact of IBI on service 2. FBMC and OFDM show similar performance when deployed as service 1 and 2, having the same bandwidth as well as when the bandwidth of service 2 was reduced to half the bandwidth of service 1. However, EVM performance improved by 10% when the bandwidth of service 2 was reduced relative to service 1. This is because most IBI from service 1 fall outside the bandwidth of service 2. Subsequently, FBMC was deployed in service 1 while OFDM was deployed in service 2 and vice versa to investigate the impact of IBI on both waveforms. The enlarged OOB emissions in OFDM due to PA nonlinearity results in significant IBI and thus, degrading the EVM of FBMC. However, the significantly suppressed OOB spectral leakage plays an important role as FBMC introduced much lesser IBI to OFDM, even in the presence of PA nonlinearity.

A novel multi-service transmission scenario was investigated where LTE was deployed in-band a 5G service. The concept is based on the 3GPP Rel.13 standard which allows NB-IoT to be deployed in-band LTE signal. The LTE signal deployed in-band 5G service

emulates the NB since the bandwidth is significantly small compared to the 5G service. OFDM shows much higher sensitivity to guardband, requiring 28 subcarriers to avoid interference with the LTE signal, whereas, 2 subcarriers was sufficient in FBMC to achieve IBI free in-band deployment of LTE signal. Furthermore, FBMC introduces far less IBI to the LTE signal compared to OFDM. However, since FBMC is more sensitive to in-band distortion, the EVM is more degraded compared to OFDM as the input power of LTE increased. To exploit the benefit of low OOB emissions in FBMC, the PA was operated in the linear regime and guardband was reduced to 16 subcarriers. FBMC and OFDM were transmitted with and without in-band LTE and their EVM performance compared. At optimum received optical power of +1dBm, 1.5% EVM degradation was observed in FBMC while the EVM degradation in OFDM was 7.7% with in-band LTE. Despite the sensitivity of FBMC to phase noise of the mmWave generators employed in the architecture, the result shows that FBMC can coexist seamlessly with both legacy and new services in the 5G heterogeneous access network.

Finally, the impact of PA nonlinearity in uplink multi-user transmission system has been investigated employing DFT-s-OFDM and DFT-s-FBMC. Both waveforms show similar EVM performance when the PA was operated in the linear regime. As the input power increased and the PA nonlinearity comes into play, the EVM performance gets worse with DFT-s-FBMC showing more sensitivity to the PA nonlinearity.

7. Coexistence of Multiple 5G Services in a Photonic Millimetre-wave Mobile Fronthaul

7.1. Introduction

In this chapter, a novel scheme is proposed and demonstrated to simultaneously generate multiple mmWave signals at O/E conversion, using only one OLO for heterodyning multiple DL optical signals. In the previous works reported in [90, 110, 111, 120, 151, 198-200], a single mmWave signal was generated using laser heterodyne technique. Recently, an optical-domain band-mapping technique was proposed [103], where IF signals were modulated on different light sources, which were then combined for optical transmission. The IF signals were translated to carrier-aggregated mmWave signals after O/E conversion. The demonstrated technique will, however, result in a scalability problem as a new light source is required every time a new service is added. In [201], the simultaneous generation and transmission of 24GHz and 96GHz mmWave signals was reported. The LO for mmWave upconversion was remotely delivered, extracted at the RRH by an optical BPF, photodetected and subsequently used to upconvert the IF signal to mmWave. However, the RRH configuration significantly increases the system complexity. Moreover, electronic LO is required to downconvert the mmWave to IF at the UE which may be subject to phase noise. The proposed architecture is based on simple remote optical heterodyning of two or more optical carriers to generate mmWave signals. By employing all optical upconversion to realise mmWave carriers, the proposed architecture presents the benefit of reduced implementation cost as different 5G services can coexist in a shared MFH infrastructure. In addition, the architecture is easily scalable and completely reconfigurable, allowing seamless integration of services as needed.

7.2. Simultaneous Generation of Multiple Millimetre-wave Signals based on Optical Heterodyning

The C-RAN architecture is depicted in Figure 7.1, showing the integration of mmWave 5G small cells into the MFH. Note that ARoF is employed for the MFH to avoid the huge data rate requirements in CPRI-based MFH. Due to high propagation loss at mmWave frequencies, a large number of mmWave small cells will be required to provide coverage and capacity in dense urban areas and locations with temporary traffic surge, such as stadiums. As can be seen from Figure 7.1, each mmWave small cell in the MFH is connected to the BBU pool in the CO via optical fibre. This will increase the cost of deploying the small cells,

thus, making the application of densely spaced 5G mmWave small cells in MFH challenging. In order to reduce the number of optical fibre trunk, WDM technology can be deployed in MFH [17]. Figure 7.2 (a) shows the WDM multiplexer and demultiplexer. The 25GHz and 50GHz ITU-T frequency grid for dense WDM (DWDM) are depicted in Figure 7.2 (b) and Figure 7.2 (c), respectively. As shown in Figure 7.2 (b) and Figure 7.2 (c), multiple DL signals are carried on different wavelengths and multiplexed in the CO. At the remote node, the DL signals are demultiplexed and converted to an electrical signal before wireless transmission. In the example depicted in Figure 7.2 (b) and Figure 7.2 (c), the frequency plan is such that three mmWave signals 28GHz, 38GHz, and 60GHz are generated at the RRH for the 5G small cell MFH. As can be seen from Figure 7.2 (b), in the case of 25GHz DWDM grid, λ_1 , λ_2 , and λ_4 are modulated with DL signal and the three wavelengths are separated from λ_3 by the desired mmWave frequency.

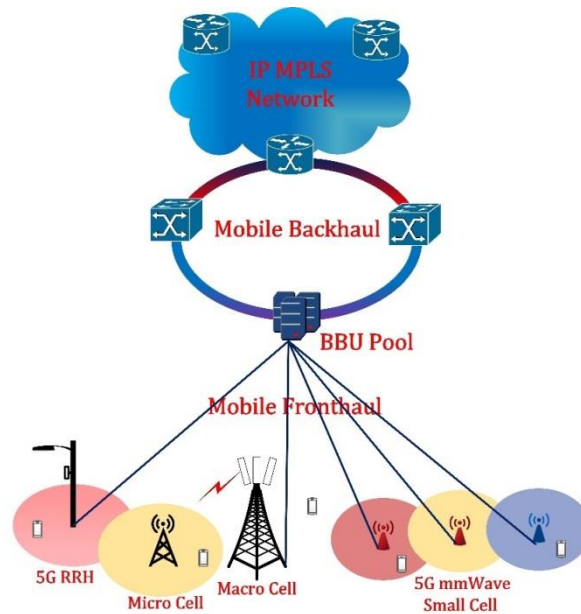


Figure 7.1: The proposed concept of multi-service and multi-operator coexistence in a shared MFH infrastructure

At the RRH, λ_1 , λ_2 , and λ_4 combine with λ_3 individually at O/E conversion to generate the mmWave signals in a heterodyne upconversion. In the case of 50GHz DWDM grid shown in Figure 7.2 (c), due to the wider available bandwidth within each frequency grid and depending on the desired mmWave carrier frequency, the wavelength assignment is different from the 25GHz grid. Also, wider frequency grids such as 100GHz can be utilised, with proper wavelength assignments. In that way, multiple DL signals will be assigned to one WDM channel since the WDM channel filters are chosen according to the wavelength spacing of the adjacent channels. The WDM channel filter will separate each DL signal or group of DL signals from the adjacent channel as shown in Figure 7.2 (c) and Figure 7.2 (d),

respectively, as long as the centre emission frequency of the lasers falls within the bandwidth of that channel.

Moreover, low-cost coarse WDM (CWDM) can be employed to reduce deployment cost. However, DWDM offers more granularity in terms of flexibility of wavelength assignments and scalability since more channels are available (e.g., 160 channels for 25GHz frequency grid). In addition, network monitoring and maintenance can be more achievable with DWDM. Although, the cost of deploying the mmWave small cell solution for 5G MFH is increased by employing DWDM technology, with the need for power supply in the remote node, the benefit of reducing the number fibre trunk while increasing the capacity of MFH is significant. Furthermore, wavelength drifts due to change in laser current and temperature is not an issue as the WDM channel width is reduced (e.g., 25GHz) since ARoF is employed to transport the DL 5G services having bandwidths much smaller compared to the WDM channel width.

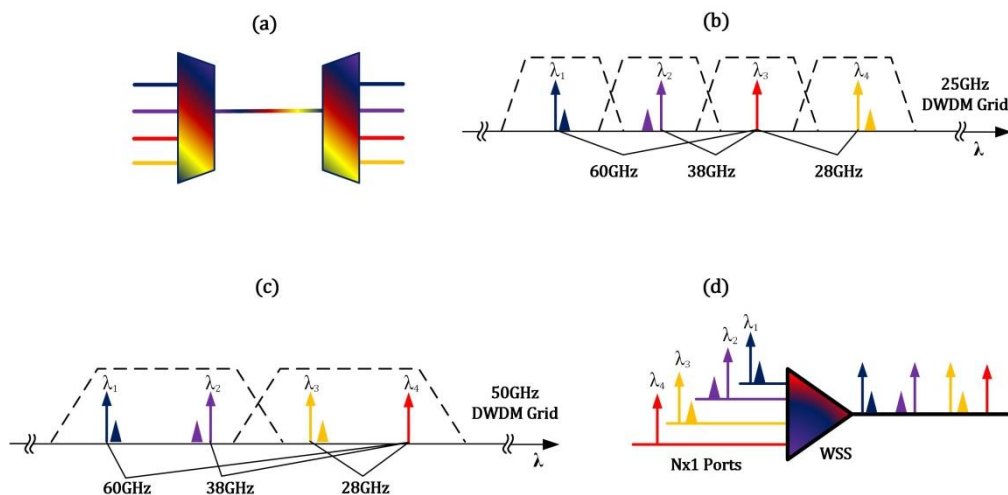


Figure 7.2: Frequency Plan and Multiplexing of multiple services coexistence in a shared MFH infrastructure (a) WDM Multiplexer and Demultiplexer (b) 25GHz DWDM grid (c) 50GHz DWDM grid (d) Nx1 Port WSS

Alternatively, a reconfigurable WSS can be used in case of dedicated fibre infrastructure to dynamically aggregate the DL signals before feeding into an optical fibre for MFH transmission. As shown in Figure 7.2 (d), each DL optical signal is fed into Nx1 WSS and aggregated before they are transported via optical fibre to the RRH. Since the WSS channel is compatible with the DWDM frequency grid, DWDM can be seamlessly integrated as the network capacity increases. In the proposed architecture, WSS is used to aggregate the DL 5G services before optical fibre transmission to the RRH. The optical source, serving as LO for mmWave upconversion can be generated in the CO and delivered alongside the DL signals, or in RRH, using the UL light source.

By delivering the LO from the CO, the complexity of the RRH is further reduced. However, the LO will suffer transmission impairments, and thus degrade the system performance. If the same optical carrier is to be used for UL transmission, optical amplification will be required in the RRH. Using the UL light source as LO will improve the receiver sensitivity and since an optical carrier is needed for UL transmission, the increase in complexity as a result of placing an OLO in the RRH can be justified. In addition, multiple UL services can share the same optical source. In the UL transmission, mmWave signals from the UEs are received by the antennas, downconverted to IF and combined to modulate the UL optical carrier which is then fed into WDM channel for UL transmission to the CO. Multiple WDM channels can be allocated for UL transmission depending on the number of supported services.

Notably, the proposed RoF implementation of 5G mmWave small cell MFH compared to the conventional CPRI-based MFH significantly reduces the CAPEX/OPEX since multiple services and operators can coexist in the MFH network. Moreover, by employing an all-optical upconversion technique to generate mmWave carriers, the complexity associated with multiple upconversion stages in the electrical domain as well as the stringent phase noise requirements at high frequencies are relaxed.

7.3. Simulation Setup

To demonstrate the feasibility of the proposed architecture, an end-to-end simulation testbed was implemented in industry standard VPI Transmission Maker® v9.8 in cosimulation with MATLAB software. Figure 7.3 shows the schematic for the simulation implemented in VPI Transmission Maker®. The components used in VPI such as lasers, MZM and amplifiers have been characterised and their parameters were set to closely match commercially available components. Therefore, the simulation setup can be used as a basis for experimental testbed since the platform presents more flexibility, allowing investigations to be carried out for various transmission scenarios, which may be challenging in practice due to hardware limitations.

As shown in Figure 7.3, three IF signals were used to modulate three tunable DFB lasers having 1MHz linewidth. The centre emission wavelength of the lasers is 1552.524nm, 1552.605nm, and 1552.750nm. The UL laser centre emission wavelength is 1552.299nm. These wavelengths were set to closely match the 25 GHz DWDM ITU-T flexi-grid. Although these wavelengths were set to have frequency difference from the LO laser equivalent to 28GHz, 38GHz and 60GHz mmWave carrier frequencies, it is important to note that the wavelength of the lasers can be detuned from the LO laser wavelength to achieve another frequency difference between the optical carriers to realise different mmWave carriers.

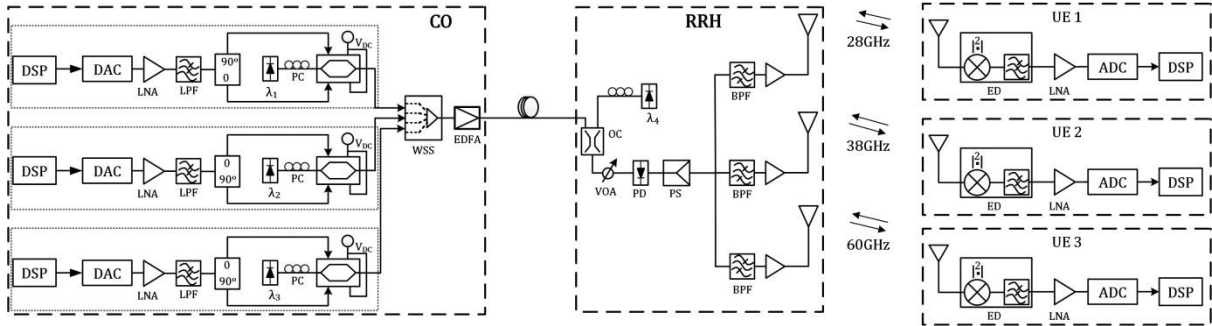


Figure 7.3: Schematic for the simultaneous generation of multiple mmWave signals using one optical LO

Compared to generating the mmWave carriers using multiple stage electrical upconversion, needing precise frequency synchronisation, and expensive PLL to align the phase of the electrical LOs [202], free running lasers are employed in the proposed small cell MFH architecture, for an all-optical heterodyne upconversion. Since data is not encoded on the carrier phase, coherent downconversion is avoided and thus, expensive PLLs are not required. Therefore, an inexpensive ED, which only detects the amplitude variation of the signal, is employed in the UE for mmWave downconversion.

The IF signals used to modulate the lasers in the MZMs were programmed in MATLAB representing 5G services which could be from multiple operators. An OSSB signal was generated in each case by applying a 90° phase shift to one arm of the DE-MZM, biased at quadrature point to ensure maximum linearity. By generating OSSB signal at E/O conversion, the effect of fibre CD is reduced which can potentially allow longer fibre length for the MFH. As illustrated in Figure 7.3, a WSS was used to combine the signals before optical amplification by an EDFA. An optical attenuator placed after the EDFA was used to keep the optical launch power at 9dBm, to avoid fibre nonlinearities. Subsequently, the aggregated DL signals were transported over SMMF for 40km to the RRH where the UL laser was combined with the DL signals before feeding into the PD for optical heterodyning. The 40km fibre length is considered since it has been proposed as the maximum fibre distance that can be supported by MFH [203]. The 28GHz, 38GHz, and 60GHz were employed in the investigation since they have been highlighted as potential carrier frequencies for 5G RATs. However, other mmWave frequencies can be generated by detuning the wavelength of the DFB lasers from the OLO wavelength. Due to the square law characteristics of the PD, unwanted beat signals are generated from the mixing of the modulated optical carriers, besides the desired beat with the OLO. These unwanted signals can fall within the useful bandwidth of the desired mmWave signals, thereby causing interference and degrading the system performance. By properly tuning the centre emission wavelength of the DFB lasers and generating an OSSB signal at E/O conversion, these interfering signals spectrum can be prevented from falling within the useful signal spectrum.

For instance, the beating of λ_1 and λ_3 generate an unwanted signal at around 30GHz; close to the desired 28GHz. In the simulation analysis, various system noise components, including RIN, thermal noise, shot noise and ASE noise were considered. Also, in practical implementation, power loss due to splice and coupling will need to be taking into account and depending on the application scenario, an optical pre-amplification may be required to boost the receiver sensitivity. Finally, fibre nonlinearities, such as cross-phase modulation (XPM) and self-phase modulation (SPM), do not impact the system performance, due to low optical launch power, short fibre length and low data rate considered in the investigation.

After O/E conversion, electrical BPFs centred at the desired mmWave frequencies select the services from the composite signal and a 30dB gain PA was used to amplify each of the mmWave signals before applying the signals to the antennas for up to 2m wireless transmission. Note that several mmWave transmissions scenarios have been studied extensively in the wireless domain, considering longer wireless transmission distance [204-206]. In order to emphasise the impact of optical transmission impairments in MFH on the mmWave 5G services, particularly the increased laser phase noise effect on the detection performance, only the Free Space Path Loss (FSPL) was accounted for in our investigation. An electrical attenuator was used to emulate the FSPL, and the difference in FSPL between the 28GHz, the 38GHz and, the 60GHz at 2m were kept constant by adjusting the transmit/receive antenna gains accordingly. Additionally, to focus on the impact of MFH transmission on the system performance, the FSPL was assumed to be fully compensated at the UE by an LNA. As shown in Figure 7.3, UE1, UE2 and UE3 receive the mmWave signals at 28GHz, 38GHz and 60GHz, respectively and downconvert the signals to IF using an ED. Subsequently, the signals were converted to digital samples before being fed to MATLAB for offline signal processing. For the 5G RATs, OFDM and FBMC were employed for the investigation since they are the most common candidate waveforms for 5G.

For a fair comparison, both waveforms were implemented with similar parameters. The IFFT size was 2048, in which 128 data carriers were modulated with symbol taking from 16QAM alphabets. In OFDM, 128 CP samples were appended in the OFDM symbols. Whereas, the subcarrier pulse-shape function in FBMC was designed based on PHYDYAS prototype filter with overlapping factor $K = 4$, and the PPN scheme ensures FBMC symbol rate is comparable to OFDM without CP. The system parameters used in the simulation are listed in Table 7-1. For the CE, one OFDM symbol modulated with 4QAM was appended in every OFDM frame. The total number of transmitted frames was 20, where each frame consists of 50 OFDM symbols and 1 preamble symbol. Since orthogonality is only guaranteed in the real-field, FBMC symbols suffer IMI at the output of the AFB [142]. Therefore, IAM preamble was appended in each FBMC frame, consisting of 50 FBMC symbols. These preambles were extracted at the receiver to estimate the channel response. By taking the advantage

that channel transfer function is usually highly correlated for adjacent subcarriers, ISFA was employed to enhance the CE. Subsequently, the enhanced channel matrices of the modulated subcarriers were used for ZF equalization, to undo the channel effects. The QAM symbol demapping and EVM computation were performed successively in OFDM receiver after ZF equalisation. In the FBMC receiver block, OQAM Post processing was done prior to QAM symbol demapping and EVM computation.

As shown in chapter 4, the dynamic range of laser heterodyne architecture can be limited by laser phase noise, and since the implementation and configuration of the transceivers are different, it should be expected that the waveforms will exhibit different performance with respect to transmitter nonlinearity and transmission impairments. Moreover, the increased number of optical tones heterodyning at the PD will significantly increase the effect of laser phase noise on the receiver sensitivity. To evaluate the impact of laser phase noise on the system performance, two laser configurations: ECL-ECL and DFB-DFB having an approximately combined linewidth of 200kHz and 2MHz were considered in the simulation.

Table 7-1 System parameters used in the simulation

Parameter	Value	Parameter	Value
Signal Bandwidth	500MHz	Laser Linewidth	100kHz/ 1MHz
Total IFFT/FFT	2048	Laser RIN	-155dB/Hz
Data Subcarriers	128	Laser Power	10dBm
Modulation	16QAM	MZM Insertion Loss	5dB
CP (OFDM)	128	MZM Extinction Ratio	35dB
K (FBMC)	4	Fibre Length	40km
DAC/ADC Sampling Rate	8 /96GSa/s	Fibre Dispersion	17ps/(nm.km)
DAC/ADC Resolution	10bits	Fiber Attenuation	0.2dB/km
Thermal Noise	$10 \times 10^{-12} \text{A}/\text{H}^{1/2}$	EDFA Noise Figure	5dB
ISFA Window Size	22	PD Responsivity	0.68A/W

7.3.1. Performance Evaluation for 28GHz and 38GHz

Firstly, ECL lasers having a combined linewidth of 200kHz were employed in the generation of 28GHz and 38GHz mmWave signal. As shown in Figure 7.3, only λ_1 and λ_2 were modulated with IF signals. OFDM and FBMC waveforms were deployed for the 28GHz and 38GHz and vice versa. The IF centre frequency of the 28GHz signal is 1GHz while that of 38GHz is 1.25GHz. Obviously, the mmWave signals will experience different noise level due to their IF frequencies. Figure 7.4 (a) – (d) shows the optical spectrum before O/E conversion, electrical spectrum after the PD, 28GHz and 38GHz signals after the BPFs, respectively.

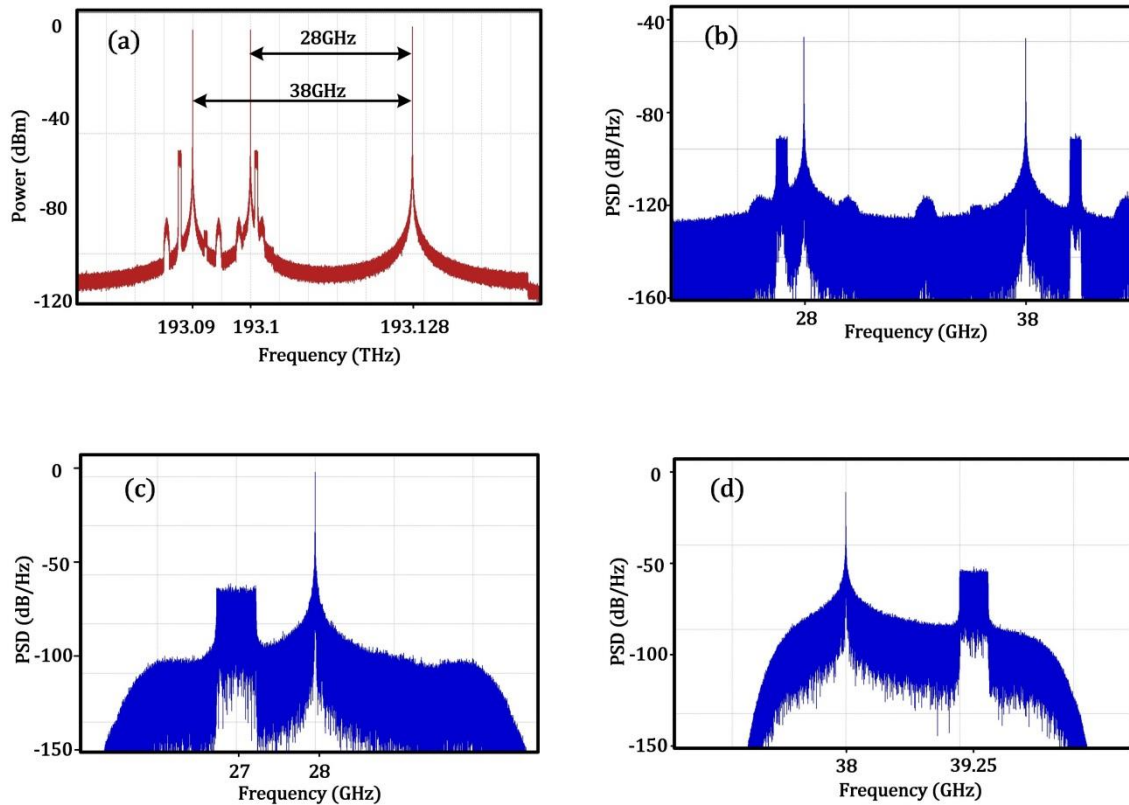


Figure 7.4: Spectrums (a) Optical spectrum before the PD (b) Electrical spectrum after the PD showing 28GHz and 38GHz (c) 28GHz Electrical spectrum (d) 38GHz Electrical spectrum

Figure 7.5 shows the EVM of OFDM and FBMC carried on 28GHz and 38GHz respectively. As can be observed from Figure 7.5 (a), 28GHz FBMC exhibits worse EVM for low received powers compared to 28GHz OFDM without ISFA, but the difference in EVM values reduced as the received power was increased. The EVM is limited at low received powers by a combination of laser phase noise, RIN, ASE noise and receiver noise. As the received power increased the EVM error floor was due to laser phase noise. Moreover, the interaction of CD with the laser phase noise further impacts the EVM performance. However, the EVM performance of FBMC is almost the same as that of OFDM when ISFA was applied. Figure 7.5 (c) and Figure 7.5 (d) show the received constellation at -7dBm corresponding to 28GHz and 38GHz for OFDM and FBMC, respectively.

Next, the ECLs were replaced with DFB lasers having combined linewidth of 2MHz, to investigate the effect of laser linewidth and consequently, laser phase noise on the system performance. Figure 7.6 shows OFDM and FBMC carried on 28GHz and 38GHz generated using DFB lasers having 2MHz combined linewidth. As before, 28GHz FBMC shows worse EVM performance at low received powers but improves as the received power increased. On the hand, 28GHz OFDM exhibits much better EVM performance at low received powers. Moreover, 38GHz OFDM shows slightly lower EVM than 28GHz OFDM and 28GHz FBMC with ISFA at low received power. This can be attributed to the fact that the bandgap between

the optical carrier and the IF signal is larger for 38GHz mmWave signal and thus, reducing the impact of laser phase noise. Nevertheless, it can be observed that the EVM of 38GHz FBMC is still higher than 28GHz OFDM despite the bandgap. Both OFDM and FBMC service, however, show similar EVM performance when ISFA was applied.

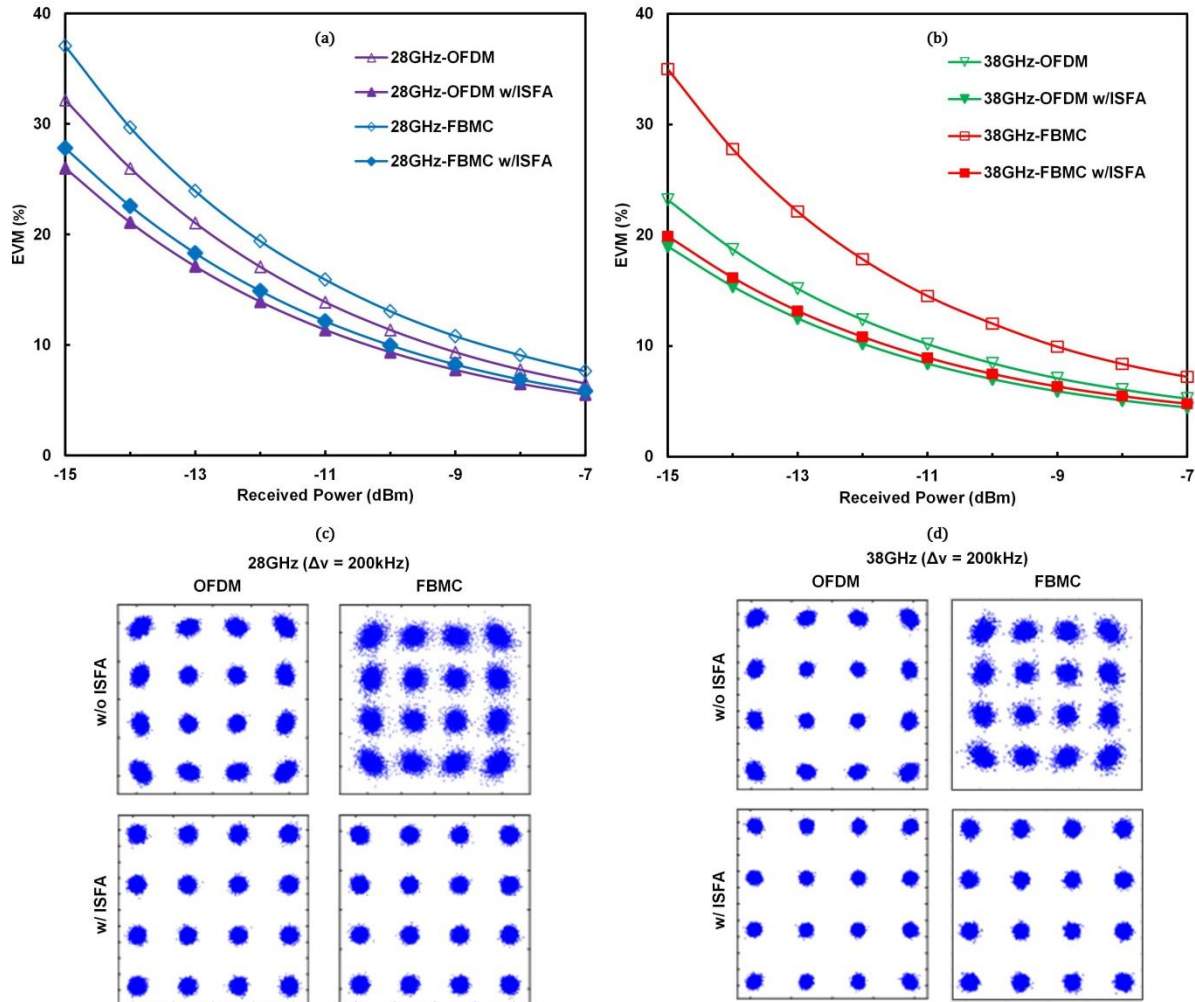


Figure 7.5: EVM as a function of received power using 200kHz combined laser linewidth (a) 28GHz OFDM and FBMC (b) 38GHz OFDM and FBMC (c) Constellation for 28GHz OFDM and FBMC at -7dBm received power (d) Constellation for 38GHz OFDM and FBMC at -7dBm received power

The effect of phase noise can be observed in the received constellations at -7dBm, shown in Figure 7.6 (c) and Figure 7.6 (d) without ISFA, corresponding to 28GHz and 38GHz, respectively. The obtained results demonstrate that the CE process can be enhanced by applying ISFA, to successfully mitigate the effect of noise and CD on the system performance.

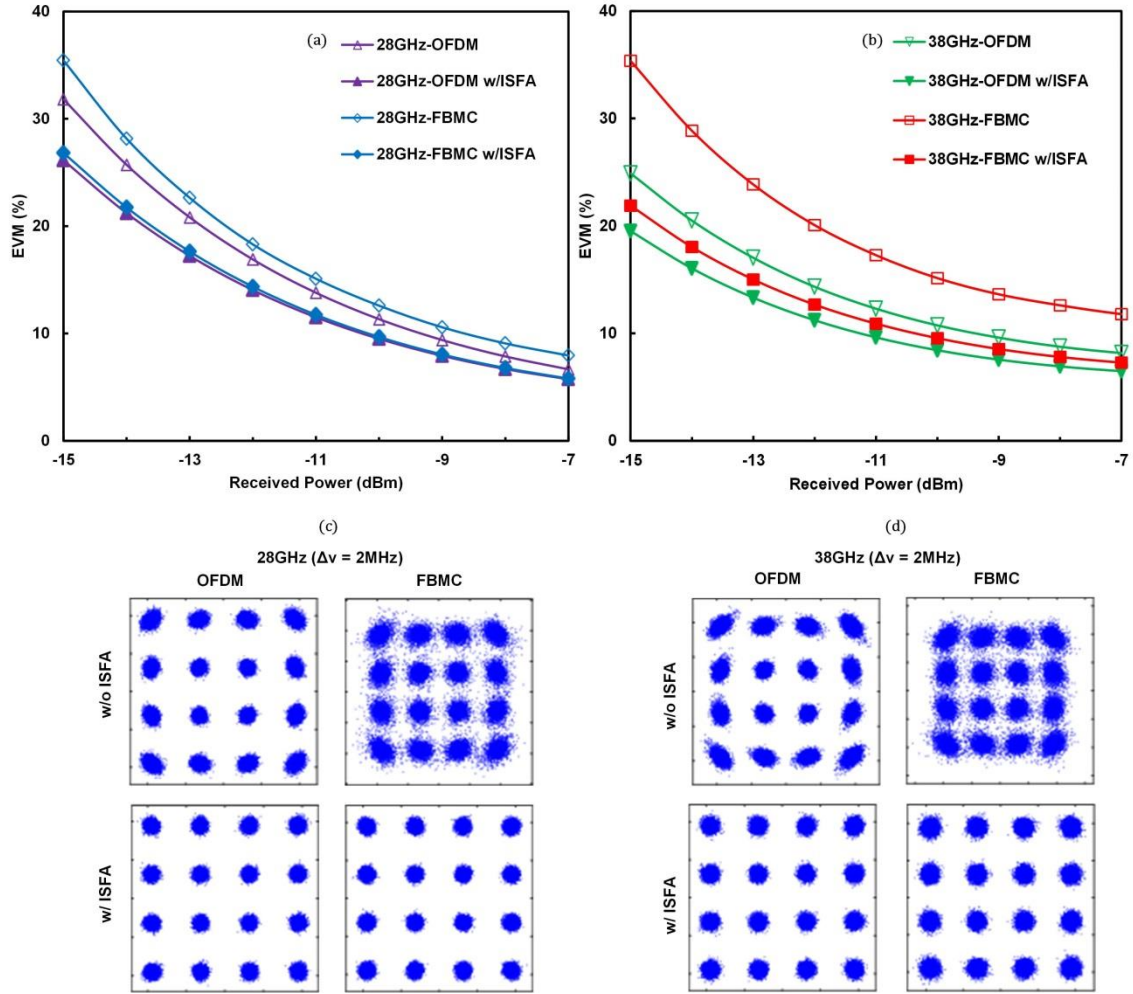


Figure 7.6: EVM as a function of received power using 2MHz combined laser linewidth (a) 28GHz OFDM and FBMC (b) 38GHz OFDM and FBMC (c) Constellation for 28GHz OFDM and FBMC at -7dBm received power (d) Constellation for 38GHz OFDM and FBMC at -7dBm received power

7.3.2. Performance Evaluation for 28GHz and 60GHz

To generate 28GHz and 60GHz mmWave signals, λ_1 and λ_3 were modulated with IF signals from OFDM and FBMC, representing service 1 and service 3, respectively. Here, a slight modification was made to the IF centre frequency of the 28GHz signal and the centre wavelength of the optical carrier. This is to avoid the unwanted beating between the OLO and optical carrier used to generate the 60GHz signal falling on the 28GHz signal spectrum. The IF signal used to generate 28GHz was shifted down in frequency by 250MHz and consequently, the IF centre frequency was 750MHz. Also, λ_1 was detuned by 2GHz, to shift the carrier away from interference from the unwanted beating. Figure 7.7 (a) – (d) shows the spectrum before O/E conversion, after the PD, the 28GHz and 60GHz signals after BPFs. It can be seen from Figure 7.7 (b) that unwanted signal from the 60GHz signal generation falls close to the 28GHz signal. To avoid the unwanted signal from interfering with the 28GHz

signal, the phase shift applied to one arm of the DEMZM was set such that the desired signal is not on the same side with the unwanted signal. Subsequently, BPF was used to extract the 28GHz signal as shown in Figure 7.7(c). In the same way, the 60GHz signal was extracted by a BPF as shown in Figure 7.7(d). Two UEs detect the mmWave signals at 28GHz and 60GHz, downconvert to IF and subsequently, fed the signal to the ADC after which receiver DSP was implemented in MATLAB.

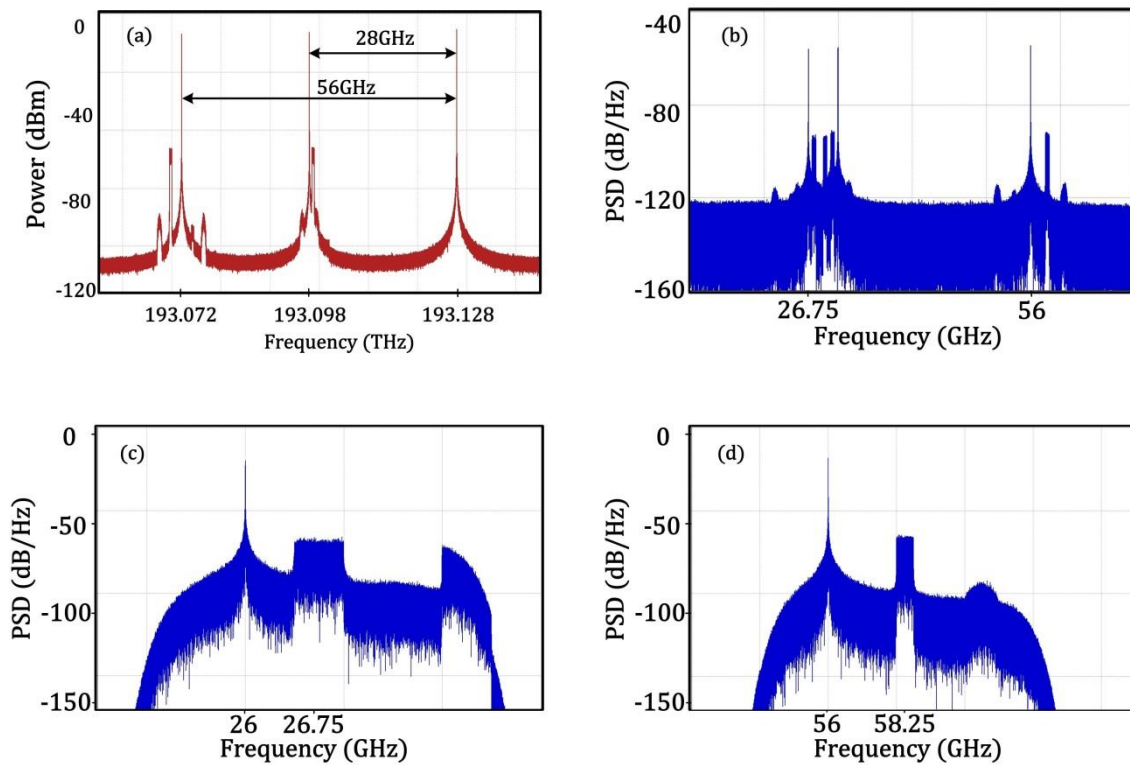


Figure 7.7: Spectrums at (a) Optical spectrum before the PD (b) Electrical spectrum after the PD showing 28GHz and 60GHz (c) 28GHz Electrical spectrum (d) 60GHz Electrical spectrum

The EVM as a function of received power is shown in Figure 7.8 for both waveforms at 28GHz and 60GHz, with and without ISFA. The EVM is similar for both waveforms at 28GHz and 60GHz without ISFA, but when ISFA was employed the EVM of OFDM improved more than the EVM of FBMC at low received powers. The EVM of OFDM at -15dBm received power improved by 12% for 28GHz and 60GHz, respectively, while EVM of FBMC only improved by 6.5%. As can be seen from Figure 7.8, EVM of OFDM is 1% better than that of FBMC for 28GHz and 60GHz at -7dBm received power both with and without ISFA.

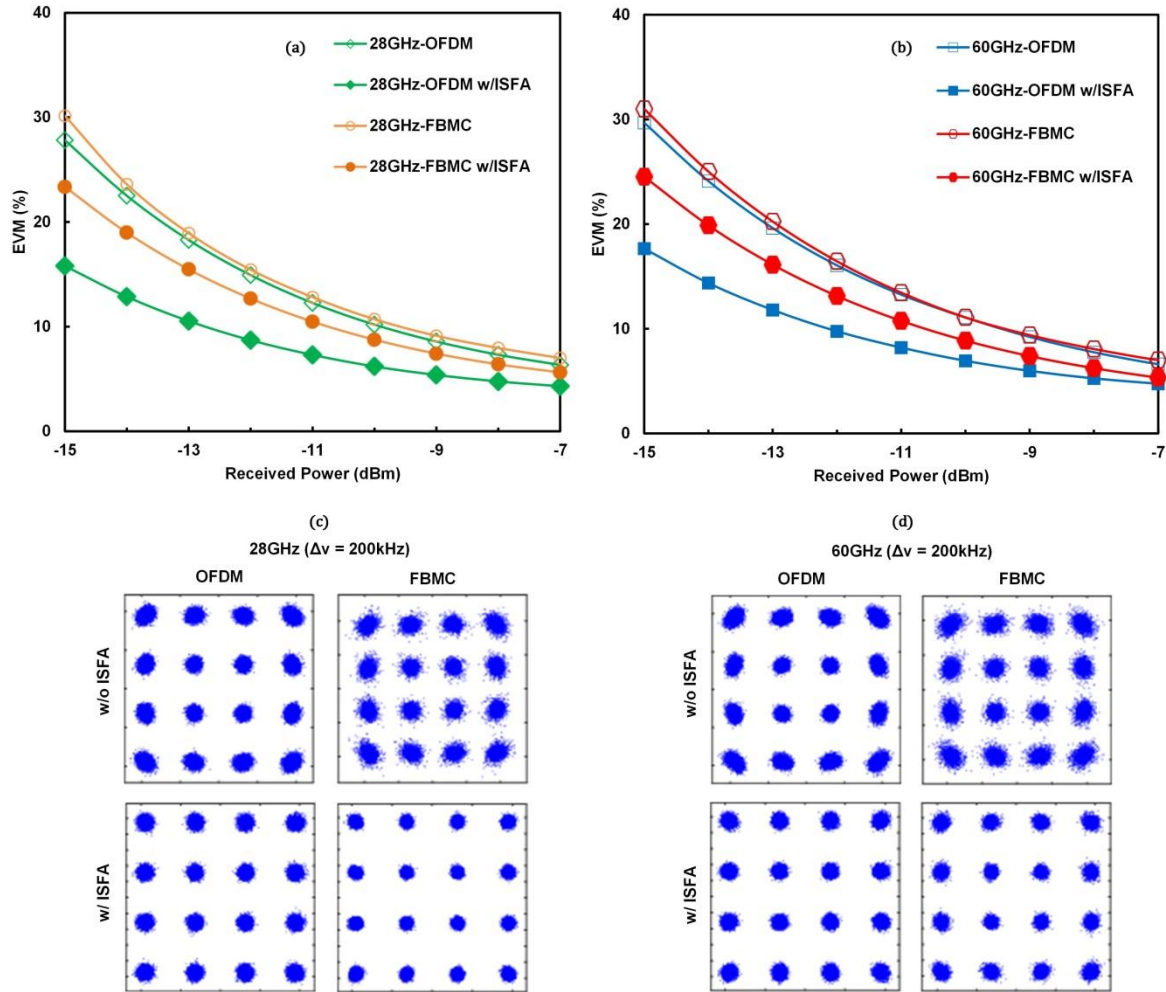


Figure 7.8: EVM as a function of received power using 200kHz combined laser linewidth (a) 28GHz OFDM and FBMC (b) 60GHz OFDM and FBMC (c) Constellation for 28GHz OFDM and FBMC at -7dBm received power (d) Constellation for 60GHz OFDM and FBMC at -7dBm received power

The received constellations at -7dBm received power, with and without ISFA shown in Figure 7.8 (c) and Figure 7.8 (d), demonstrate again that ISFA can improve the system performance in the proposed architecture. Next, the same experiment was repeated with the combined laser linewidth set to 2MHz. Figure 7.9 shows the EVM as a function of received power, with and without ISFA for OFDM and FBMC, respectively. The 28GHz FBMC exhibits high susceptibility to increased laser linewidth. The EVM, however, improved significantly when ISFA was employed from 16.4% to 9.2% at -7dBm received power. Furthermore, an increased EVM error floor can be observed in both 28GHz and 60GHz service as the received power increased, which can be attributed to the increased impact of phase noise as the laser linewidth increased. The 28GHz and 60GHz OFDM service show higher EVM error floor than FBMC with no significant improvement in EVM for 60GHz OFDM, with ISFA. FBMC benefits more from the noise averaging since it is impacted more by noise and this

can be observed from the received constellation of the 28GHz signal, shown in Figure 7.9 (c).

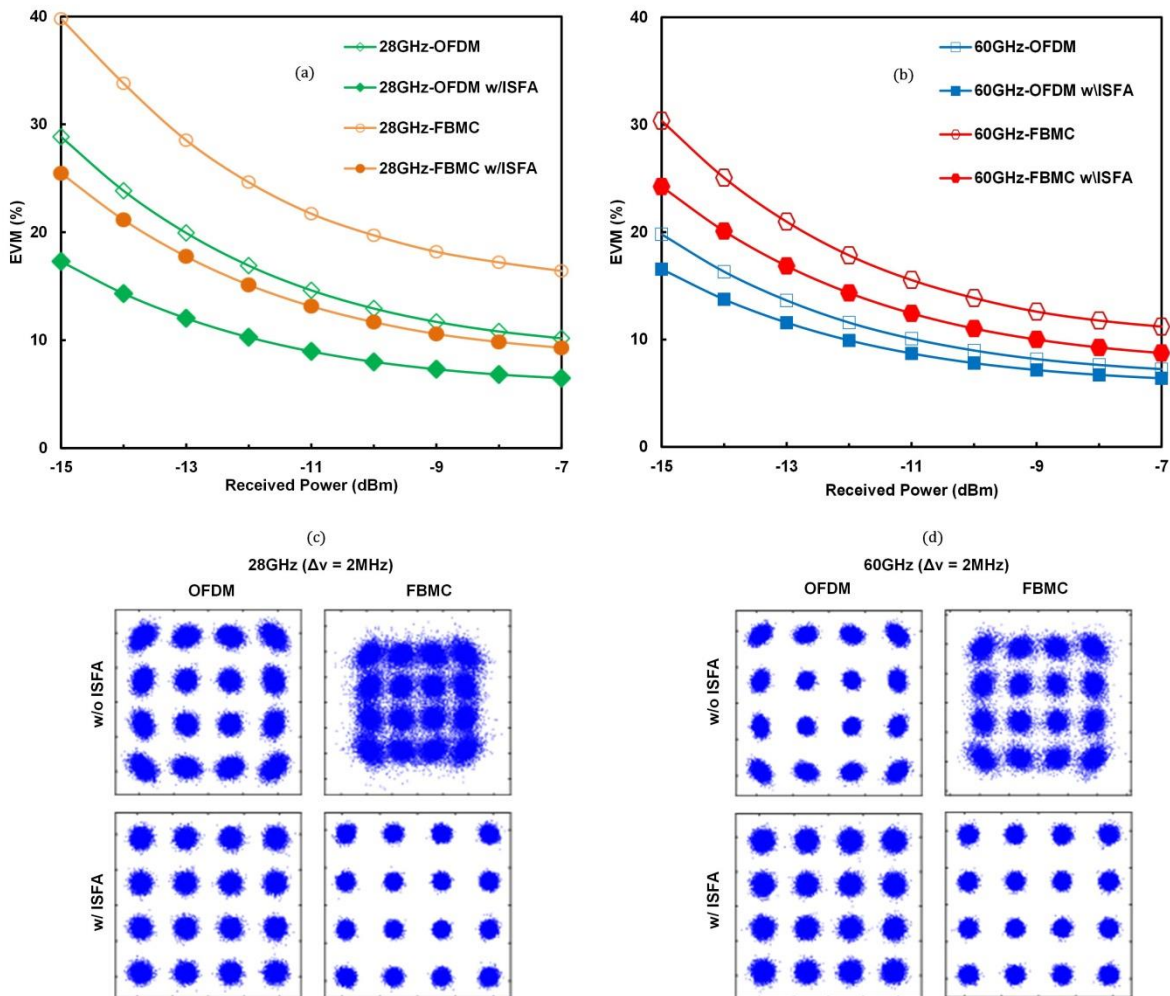


Figure 7.9: EVM as a function of received power 2MHz combined laser linewidth (a) 28GHz OFDM and FBMC (b) 60GHz OFDM and FBMC (c) Constellation for 28GHz OFDM and FBMC at -7dBm received power (d) Constellation for 60GHz OFDM and FBMC at -7dBm received power

Compared to the constellations for 200kHz combined laser linewidth in Figure 7.8, the effect of phase noise is more noticeable in the received constellations of both 28GHz and 60GHz signals, however, this effect can be seen to have completely mitigated when ISFA was applied.

7.3.3. Performance Evaluation for 28GHz, 38GHz and 60GHz

To demonstrate the scalability of the proposed architecture, the three services were transmitted on λ_1 , λ_2 and λ_3 to simultaneously generate 28GHz, 38GHz and 60GHz mmWave signals using the UL optical carrier as the LO. Obviously, as the number of optical carriers heterodyning in the PD is increased, the impact of phase noise on the system performance is expected to increase significantly. OFDM was employed for service 1 and service 2 at

28GHz and 38GHz while FBMC was employed for service 3 at 60GHz. The IF centre frequency of the 28GHz, 38Hz and 60GHz are 0.75GHz, 1.25GHz and 2.25GHz, respectively.

Figure 7.10 shows the EVM as a function of received optical power for simultaneously generated 28GHz OFDM, 38GHz OFDM, and 60GHz FBMC 5G services. The 28GHz OFDM has the worst EVM performance due to reduced bandgap between the carrier and the IF signal. Although OFDM shows better performance than FBMC at 28GHz in all the investigations, the 28GHz service is generally more affected by laser phase noise. While the bandgap is more than 3x the signal bandwidth for the 60GHz FBMC, the EVM performance is almost the same as 28GHz OFDM. The EVM at -7dBm without ISFA is 11%, 7.5% and 11% for 28GHz OFDM, 38GHz OFDM, and 60GHz FBMC, respectively. When ISFA was applied to enhance the CE, the EVM at -7dBm was 9.4%, 6.5%, and 7%, respectively. Although OFDM and FBMC in most transmission scenarios achieve EVM below the 12% threshold for 16QAM LTE signal at high received powers without ISFA, the benefit of applying noise averaging is more noticeable in FBMC for all investigated scenarios.

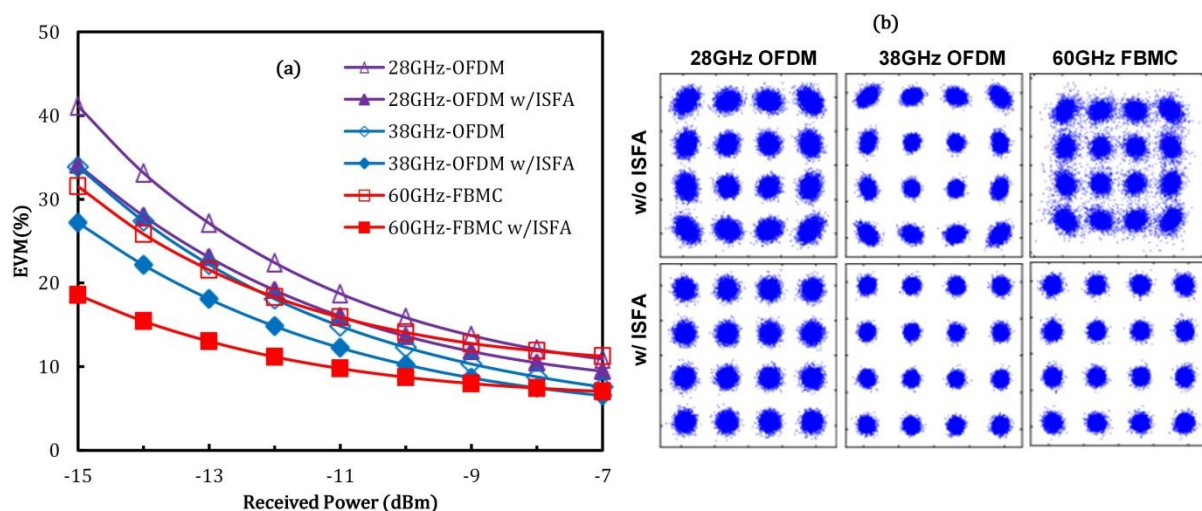


Figure 7.10: (a) EVM as a function of received power for 28GHz OFDM, 38GHz OFDM and 60GHz FBMC (b) constellations at -7dBm received power with and without ISFA using UL laser as LO

To further demonstrate the flexibility of the proposed architecture in terms of system configuration, the UL laser was placed in the CO and the OLO was remotely delivered to the RRH. Figure 7.11 shows the EVM as a function of received optical power and corresponding constellations at -7dBm received power with and without ISFA. Compared to when the LO laser was placed in the RRH, the EVM increased by just 0.1% at -7dBm for 38GHz OFDM and 60GHz FBMC services. The EVM of the 28GHz OFDM signal, however, increased by 2.5%, which is believed to be as a result of increased laser phase noise due to fibre CD.

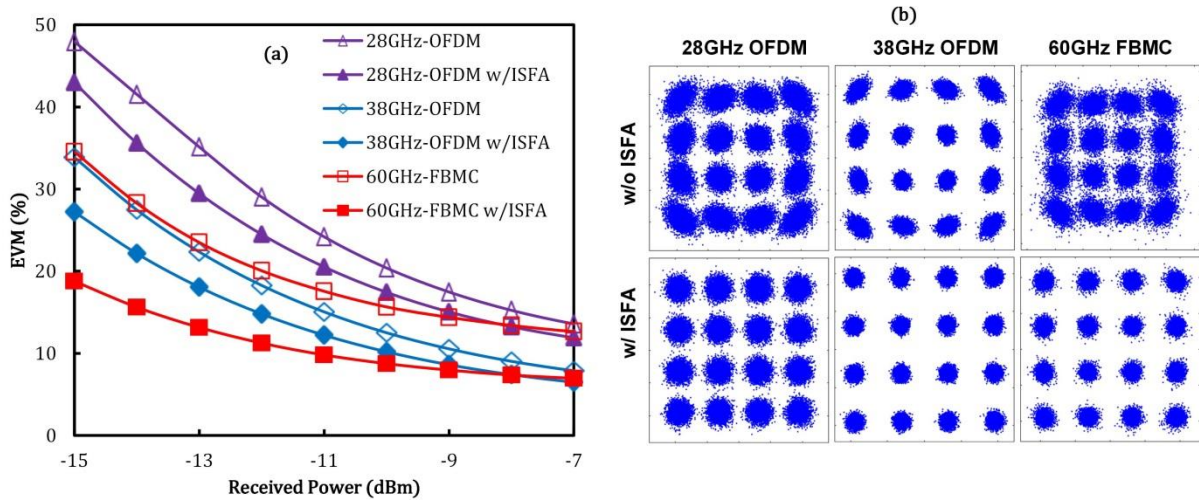


Figure 7.11: (a) EVM as a function of received power for 28GHz OFDM, 38GHz OFDM and 60GHz FBMC (b) constellations at -7dBm received power with and without ISFA using remotely delivered LO

The obtained results demonstrate that the three 5G-like services, simultaneously upconverted to 28GHz, 38GHz and 60GHz after 40km fibre can be successfully recovered after 2m wireless transmission. In terms of the RAT, OFDM presents better resilience to system noise dominated by laser phase noise and thus, better performance, while FBMC is more susceptible to noise. Finally, by applying ISFA to enhance the CE process, the performance of FBMC is significantly improved having similar EVM values with OFDM, allowing for a relaxed receiver sensitivity requirement in the MFH link.

7.4. Summary

A novel coexistence of multiple 5G services in a resilient photonic mmWave small cell MFH was proposed and demonstrated. Notably, the proposed architecture is simple to implement and easily reconfigurable. The UL laser was employed as the LO for generating multiple mmWave signals at O/E conversion, where multiple DL IF signals were simultaneously upconverted to 28GHz, 38GHz and 60GHz mmWave signals. By properly detuning the optical carrier frequency of the IF signals, the IF centre frequencies as well as the phase shift applied to one arm of the DEMZM to generate OSSB modulation, the unwanted beat interference signal is avoided. With such configuration, several services/ operators can share both the fibre link and the RRH, thereby driving down the overall cost and complexity of the small cell MFH infrastructure. Moreover, the OLO can be remotely delivered from the CO, to further reduce the system complexity. ARoF technique was employed to transport the 5G services due to its SE and ability to easily integrate mmWave small cells into the MFH to boost capacity and coverage. Several transmission scenarios were considered in the

simulation considering the coexistence of OFDM and FBMC in a shared photonic MFH infrastructure to investigate their resilience to nonlinearity and noise arising from E/O and O/E conversion. Two laser configurations, having combined linewidth of 200 kHz and 2 MHz was considered to study the impact of laser linewidth and consequently, phase noise on the system performance. In all investigated transmission scenarios, OFDM shows better resilience to system impairments at low SNR compared to FBMC. However, by applying the ISFA technique in the CE process, these effects were effectively mitigated and the 5G services were successfully recovered in all investigated scenarios, with EVM well below the 12% threshold 16QAM LTE signal. It is therefore believed that the proposed architecture facilitates a cost-efficient solution with configurations that can benefit the deployment of densely spaced high capacity mmWave small cell BSs and can be flexibly adopted in the next-generation mmWave small cell MFH.

8. Conclusion and Future Works

8.1. Thesis Summary

As the 5G networks develop, a key feature that is being discussed is the MFH architecture. It is obvious that the present MFH technology based on CPRI cannot support high-capacity and ubiquitous requirements of 5G mobile broadband access. Moreover, up to 1GHz bandwidth as specified in 5G NR for mmWave deployments will overwhelm CPRI based digital MFH due to large overhead data used in the digitisation of IQ signals. Hence, it is more practical to implement mmWave MFH using ARoF technology. Millimetre-wave will play an important role in achieving gigabit access to mobile subscribers due to the vast amount of bandwidth it presents. Since BS configuration is changing in practice from traditional large macro cell structure to compact small cell that can be deployed in 'hot-spot' and 'not-spot', it is anticipated that these small cells will be densely deployed. Moreover, mmWave experiences high propagation loss, which can be exploited for interference mitigation.

To this extent, many research works have been focusing on how to integrate mmWave small cell into MFH taking advantage of optical transport technology based on RoF to photonically realise the mmWave carrier for wireless transmission. However, many of the proposed architecture still feature expensive optical and electrical components. It is well known that noise and nonlinearities inherently limit the system performance in ARoF implementations. Therefore, it is necessary to carry out an in-depth study of these impairments. Several works that have been reported regarding the aforementioned consider OFDM waveform mainly due its wide application in most of today's wireless systems, while other 5G candidate waveforms such as FBMC has not been studied. On the other hand, coexistence of multiple services (i.e. legacy and new) in a shared infrastructure has been discussed in 5G-NR standard. Therefore, it is important to assess the effect of nonlinearity among these services. Investigations that have been carried out so far to this effect either considers only single service or multi-service only on OFDM whereas, such effort has not been put into emerging waveforms such as FBMC.

Given the importance of the above mentioned, especially in gaining an insight to the effects of noise and nonlinearity in FBMC fibre-wireless MFH as against OFDM which has been widely investigated. The work carried out in this thesis aim to explore some of the common implementation of photonic mmWave upconversion techniques employing OFDM and FBMC. The impact of noise in less complex and reconfigurable laser heterodyning mmWave upconversion is comparatively investigated for OFDM and FBMC, respectively. To address the need for in-depth understanding as to how nonlinear distortion can impact the

coexistence of several services in 5G HetNets; the effect of PA nonlinearity is studied for various multi-service coexistence scenarios in DL and UL, considering legacy LTE as well as new class of service based on OFDM and FBMC.

Finally, the ability to generate multiple mmWave carriers with just one OLO delivered is investigated. So far as it is known, upconversion of up to 3 IF signals to different mmWave frequencies is proposed and investigated for the first time using laser heterodyning technique. The main findings of this research work are summarised below:

- An end-to-end simulation testbed was designed in VPI Transmission Maker® in cosimulation with MATLAB to evaluate and compare the performance of 5 mmWave upconversion techniques employing OFDM and FBMC waveforms in terms of E/O conversion and O/E conversion. Theoretical analysis shows that frequency and phase offset can severely degrade the system, where electrical LO is used solely for upconversion/downconversion. Using an ED at the UE eliminates the need for frequency/phase locking or implementing an algorithm which will further increase the system complexity. An OCS was used to generate frequency doubled signal after O/E conversion. Although, LO frequency is reduced by half, high-speed MZM is still an expensive component. On the other hand, all-optical upconversion using laser heterodyning avoids the need for high frequency LO and high-speed MZM. Moreover, it is easily reconfigurable to generate widely tunable mmWave frequencies. In terms of the performance of OFDM and FBMC with these techniques, FBMC exhibits more susceptibility to nonlinearity of the E/O interface compared to OFDM. Further, FBMC exhibits worse EVM at low SNR due to noise at O/E conversion compared to OFDM, but the EVM improves better than OFDM at high SNR.

- An expression for the global system SNR was derived in terms of the PSD of each noise component in the system. The impact each noise component was then investigated to evaluate its contribution to the global system SNR. It was found that RIN dominates the system noise for high RIN values of about -135dB/Hz and all other noise components have no significant effect on the SNR. Laser linewidth and CD play an important role in terms of achievable signal bandwidth. At 18dB threshold for 16QAM signal, achievable signal bandwidth for FBMC and OFDM was 1GHz 1.5GHz when laser linewidth was 10.1MHz and fibre length was 100km, which amounts to ~33% loss in SE for FBMC compared to OFDM. This implies that FBMC exhibits higher susceptible to CD enhanced phase noise, whereas OFDM shows better immunity against CD and laser phase noise.

- To optimise the system throughput in the presence of noise, adaptive modulation was implemented based on CSI feedback from the UE. A computationally efficient ISFA technique was employed to enhance the CE so as to improve the feedback SNR used for bit-loading. It was found that ISFA significantly improve the CE in FBMC more than it does in OFDM and therefore, an increased number of bits were loaded. In most cases investigated, similar number of bits was loaded in OFDM and FBMC, suggesting that ISFA can successfully mitigate the effect of laser phase noise in FBMC.

- A comprehensive investigation was carried out on the impact of PA-induced IBI in multi-service transmission considering several coexistence scenarios for OFDM, FBMC and legacy LTE services. In a single service transmission scenario, FBMC exhibits slightly higher susceptibility to PA nonlinearity compared to OFDM and the spectral regrowth in FBMC is much faster as the PA was being driven to the nonlinear regime. In two service transmission scenario, the input of one service was increased relative to the input power of the other service. Similar EVM performance was observed when both services were either OFDM or FBMC. However, in the coexistence of OFDM and FBMC, increasing the input power of OFDM results in significant OOB emission and consequently IBI in FBMC. On the other hand, increasing the input power of FBMC relative to OFDM results in much lesser IBI to OFDM. For -30dBm input power of FBMC, the EVM of OFDM was 7.3%, while for -30dBm input power of OFDM; the EVM of FBMC was 13.8%. Furthermore, coexistence of LTE service with OFDM and FBMC based 5G service was studied. The in-band deployment of LTE in 5G service follows the pattern specified for NB-IoT deployment in-band LTE. Simulation results shows similar performance to the previous coexistence method since LTE is based on OFDM, demonstrating that LTE service can successfully coexist with 5G FBMC signal in an in-band deployment scenario by properly adjusting the power difference between the two services. In another study, DFT-spread OFDM and FBMC were used to evaluate the impact of PA nonlinearity in uplink RoF. FBMC shows slightly higher EVM performance as the input power increased for both single and multi-user uplink transmission. Given that the PAPR of DFT-s-FBMC was 2dB higher than that of DFT-s-OFDM, the EVM performance is comparable.

- A novel reconfigurable mmWave upconversion that can simultaneously upconvert up to 3 IF signals to different mmWave frequencies have been successfully demonstrated. In the simulations, 3 IF signals were simultaneously generated at

28GHz, 38GHz and 60GHz with just one OLO based on optical heterodyning in the PD. Due to the number of optical tones beating in the PD, phase noise is high in the system. However, by applying ISFA to enhance the CE, results demonstrate the feasibility of simultaneous upconversion of up to 3 IF signals to 28GHz, 38GHz and 60GHz using one OLO for optical heterodyning after 40km fibre.

While the work carried in this thesis demonstrate substantial milestone in research towards fibre-wireless technologies for 5G MFH, there are further areas that can be suggested for future investigations, as listed in the next section.

8.2. Future Works

There are areas of studies that can be suggested as a result of the work carried out in this thesis as next step in the research towards the next-generation MFH technologies:

- Alternative spectrally efficient waveforms, such as UFMC, GFDM or filtered OFDM (F-OFDM) that have been proposed as part of research towards 5G RATs can be investigated for the upconversion techniques presented in this thesis. This will enable comprehensive comparison of the performance of these waveforms in mmWave small cell MFH architecture. Additionally, an extensive study such as was carried out in this thesis for laser heterodyning mmWave upconversion technique can be investigated for the aforementioned candidate multicarrier waveforms.
- In terms of the effect of phase noise particularly in FBMC, phase noise cancellation algorithms [207] can be investigated in order to compare its performance with the ISFA investigated in this thesis, in terms of efficiency and complexity.
- Although, DPD has been widely investigated for RoF systems, a further work that can be carried out in the future is to implement DPD to linearise the system in coexistence of multiple services employing different waveforms. Again, this investigation can be extended to include UFMC, GFDM and F-OFDM. In addition, coexistence of sub-6GHz with mmWave and integrated access backhaul has been highlighted in 5G-NR study and this can be an area of further investigation employing OFDM and other multicarrier waveforms. Deep learning and Artificial Neural Networks algorithms can be employed to predict the nonlinear distortion of MZM or PA and to compensate for its effect [208]. Further, it can be employed in conjunction with ZF to enhance equalisation process [209].
- In order to reduce the effect of PAPR on the system performance, low PAPR FBMC [145] can be employed for bidirectional transmission with the laser heterodyning mmWave upconversion technique employed in this thesis. Further, FBMC-QAM has been proposed as a means of avoiding the complexity that makes the integration of

MIMO challenging. Therefore, FBMC-QAM can be investigated in order to enable the integration MIMO with the small cell MFH architecture.

- Since the main focus of the work carried out in this thesis is the effect MFH transmission impairments on the RATs, investigations can be extended further to incorporate the effect of mmWave wireless channel considering several scenarios, for both downlink and uplink transmission.

References

- [1] *Cisco Visual Networking: Global Mobile Data Traffic Forecast Update(2016-2021)* [Online]. Available: www.cisco.com
- [2] G. K. Chang and L. Cheng, "Fiber-wireless integration for future mobile communications," in *2017 IEEE Radio and Wireless Symposium (RWS)*, 2017, pp. 16-18.
- [3] *TS 36.300 Evolved Universal Terrestrial Radio Access (E-UTRA) and Evolved Universal Terrestrial Radio Access Network (E-UTRAN); Overall description; Stage 2* [Online]. Available: www.3gpp.org
- [4] *TR 36.913 Requirements for further advancements for Evolved Universal Terrestrial Radio Access (E-UTRA) (LTE-Advanced)* [Online]. Available: www.3gpp.org
- [5] G. Ku and J. M. Walsh, "Resource Allocation and Link Adaptation in LTE and LTE Advanced: A Tutorial," *IEEE Communications Surveys & Tutorials*, vol. 17, pp. 1605-1633, 2015.
- [6] *Accelerating the mobile expansion in the 5G Era with LTE Advanced Pro* [Online]. Available: <https://tinyurl.com/ya5w4nfg>
- [7] A. Osseiran, F. Boccardi, V. Braun, K. Kusume, P. Marsch, M. Maternia, *et al.*, "Scenarios for 5G mobile and wireless communications: the vision of the METIS project," *IEEE Communications Magazine*, vol. 52, pp. 26-35, 2014.
- [8] *5th Generation Non-Orthogonal Waveforms for Asynchronous Signalling* [Online]. Available: <http://5gnow.eu/>
- [9] *Millimeter-Wave Evolution for Backhaul and Access (EU Project)* [Online]. Available: <https://www.miweba.eu>
- [10] *Beyond 2020 Heterogeneous Wireless Networks with Millimeter-Wave Small Cell Access and Backhauling (EU Project)* [Online]. Available: <http://www.miwaves.eu/>

- [11] *mm-Wave based Mobile Radio Access Network for 5G Integrated Communications (EU Project)* [Online]. Available: <https://5g-mmmagic.eu/>
- [12] *Dynamically Reconfigurable Optical-Wireless Backhaul/Fronthaul with Cognitive Control Plane for Small Cells and Cloud-RANs '5G XHaul' (EU Project)* [Online]. Available: <https://www.5g-xhaul-project.eu/>
- [13] *G Communication with a Heterogeneous, Agile Mobile network in the Pyeongchang wInter Olympic competitioN (EU Project)* [Online]. Available: <http://www.5g-champion.eu/>
- [14] S. Parkvall, E. Dahlman, A. Furuskar, and M. Frenne, "NR: The New 5G Radio Access Technology," *IEEE Communications Standards Magazine*, vol. 1, pp. 24-30, 2017.
- [15] I. C. Wong, "A deep dive into NR and mmWave for 5G," in *IEEE Comuunication Society Webinar Series*, ed, 2017.
- [16] F. J. Effenberger, "Mobile backhaul and fronthaul systems," in *2016 21st OptoElectronics and Communications Conference (OECC) held jointly with 2016 International Conference on Photonics in Switching (PS)*, 2016, pp. 1-3.
- [17] J. i. Kani, J. Terada, K. I. Suzuki, and A. Otaka, "Solutions for Future Mobile Fronthaul and Access-Network Convergence," *Journal of Lightwave Technology*, vol. 35, pp. 527-534, 2017.
- [18] I. A. Alimi, A. L. Teixeira, and P. P. Monteiro, "Toward an Efficient C-RAN Optical Fronthaul for the Future Networks: A Tutorial on Technologies, Requirements, Challenges, and Solutions," *IEEE Communications Surveys & Tutorials*, vol. 20, pp. 708-769, 2018.
- [19] T. Pfeiffer, "Next generation mobile fronthaul and midhaul architectures [Invited]," *IEEE/OSA Journal of Optical Communications and Networking*, vol. 7, pp. B38-B45, 2015.
- [20] A. Gupta and R. K. Jha, "A Survey of 5G Network: Architecture and Emerging Technologies," *IEEE Access*, vol. 3, pp. 1206-1232, 2015.

- [21] A. Tzanakaki, M. Anastasopoulos, I. Berberana, D. Syrivelis, P. Flegkas, T. Korakis, *et al.*, "Wireless-Optical Network Convergence: Enabling the 5G Architecture to Support Operational and End-User Services," *IEEE Communications Magazine*, vol. 55, pp. 184-192, 2017.
- [22] X. Liu and F. Effenberger, "Emerging optical access network technologies for 5G wireless [invited]," *IEEE/OSA Journal of Optical Communications and Networking*, vol. 8, pp. B70-B79, 2016.
- [23] P. Chanclou, A. Pizzinat, F. L. Clech, T. L. Reedeker, Y. Lagadec, F. Saliou, *et al.*, "Optical fiber solution for mobile fronthaul to achieve cloud radio access network," in *2013 Future Network & Mobile Summit*, 2013, pp. 1-11.
- [24] A. Pizzinat, P. Chanclou, F. Saliou, and T. Diallo, "Things You Should Know About Fronthaul," *Journal of Lightwave Technology*, vol. 33, pp. 1077-1083, 2015.
- [25] J. E. Mitchell, "Integrated Wireless Backhaul Over Optical Access Networks," *Journal of Lightwave Technology*, vol. 32, pp. 3373-3382, 2014.
- [26] N. Carapellese, A. Pizzinat, M. Tornatore, P. Chanclou, and S. Gosselin, "An energy consumption comparison of different mobile backhaul and fronthaul optical access architectures," in *2014 The European Conference on Optical Communication (ECOC)*, 2014, pp. 1-3.
- [27] N. Carapellese, M. Shamsabardeh, M. Tornatore, and A. Pattavina, "BBU Hotelling in Centralized Radio Access Networks," in *Fiber-Wireless Convergence in Next-Generation Communication Networks: Systems, Architectures, and Management*, M. Tornatore, G.-K. Chang, and G. Ellinas, Eds., ed Cham: Springer International Publishing, 2017, pp. 265-291.
- [28] A. Checko, H. L. Christiansen, Y. Yan, L. Scolari, G. Kardaras, M. S. Berger, *et al.*, "Cloud RAN for Mobile Networks-A Technology Overview," *IEEE Communications Surveys & Tutorials*, vol. 17, pp. 405-426, 2015.
- [29] *Common Public Radio Interface (CPRI)* [Online]. Available: <http://www.cpri.info/>

- [30] *Open Base Station Architecture Initiatives (OBSAI)* [Online]. Available: <http://www.obsai.com/>
- [31] *Open Radio Equipment Interface (ORI)* [Online]. Available: <http://www.etsi.org/technologies-clusters/technologies/ori>
- [32] C. Seung-Hyun, P. Heuk, C. Hwan Seok, D. Kyeong Hwan, L. Sangsoo, and L. Jong Hyun, "Cost-effective next generation mobile fronthaul architecture with multi-IF carrier transmission scheme," in *OFC 2014*, 2014, pp. 1-3.
- [33] N. Shibata, S. Kuwano, J. Terada, and H. Kimura, "Dynamic IQ compression technique in mobile front-haul for mobile optical network," in *2014 12th International Conference on Optical Internet 2014 (COIN)*, 2014, pp. 1-2.
- [34] S. Nanba and A. Agata, "A new IQ data compression scheme for front-haul link in Centralized RAN," in *2013 IEEE 24th International Symposium on Personal, Indoor and Mobile Radio Communications (PIMRC Workshops)*, 2013, pp. 210-214.
- [35] T. X. Vu, H. D. Nguyen, T. Q. S. Quek, and S. Sun, "Adaptive Cloud Radio Access Networks: Compression and Optimization," *IEEE Transactions on Signal Processing*, vol. 65, pp. 228-241, 2017.
- [36] G. Bin, C. Wei, T. An, and D. Samardzija, "CPRI compression transport for LTE and LTE-A signal in C-RAN," in *7th International Conference on Communications and Networking in China*, 2012, pp. 843-849.
- [37] N. Z. A. Garcia-Saavedra. (2016). *Proposed options for functional splits for CRAN and fronthaul* [Online]. Available: http://sites.ieee.org/sagroups-1914/files/2016/08/tf1_1608_garcia-saavedra_RAN-split_1.pdf
- [38] M. Jaber, M. A. Imran, R. Tafazolli, and A. Tukmanov, "5G Backhaul Challenges and Emerging Research Directions: A Survey," *IEEE Access*, vol. 4, pp. 1743-1766, 2016.
- [39] G. R. Maccartney, Z. Junhong, N. Shuai, and T. S. Rappaport, "Path loss models for 5G millimeter wave propagation channels in urban microcells," in *Global Communications Conference (GLOBECOM), 2013 IEEE*, 2013, pp. 3948-3953.

- [40] B. Hu, C. Hua, C. Chen, and X. Guan, "Joint Beamformer Design for Wireless Fronthaul and Access Links in C-RANs," *IEEE Transactions on Wireless Communications*, vol. 17, pp. 2869-2881, 2018.
- [41] C. H. Cox, G. E. Betts, and L. M. Johnson, "An analytic and experimental comparison of direct and external modulation in analog fiber-optic links," *IEEE Transactions on Microwave Theory and Techniques*, vol. 38, pp. 501-509, 1990.
- [42] *ITU-T G.supplement 55 Radio-over-fiber (RoF) technologies and their applications*. Available: <http://handle.itu.int/11.1002/1000/12575>
- [43] Y. Yang, C. Lim, and A. Nirmalathas, "Experimental Demonstration of Multi-Service Hybrid Fiber-Radio System Using Digitized RF-Over-Fiber Technique," *Journal of Lightwave Technology*, vol. 29, pp. 2131-2137, 2011.
- [44] A. Nirmalathas, P. A. Gamage, C. Lim, D. Novak, and R. Waterhouse, "Digitized Radio-Over-Fiber Technologies for Converged Optical Wireless Access Network," *Journal of Lightwave Technology*, vol. 28, pp. 2366-2375, 2010.
- [45] Y. Yang, C. Lim, and A. Nirmalathas, "Multichannel Digitized RF-Over-Fiber Transmission Based on Bandpass Sampling and FPGA," *IEEE Transactions on Microwave Theory and Techniques*, vol. 58, pp. 3181-3188, 2010.
- [46] D. Novak, R. B. Waterhouse, A. Nirmalathas, C. Lim, P. A. Gamage, T. R. Clark, *et al.*, "Radio-Over-Fiber Technologies for Emerging Wireless Systems," *IEEE Journal of Quantum Electronics*, vol. 52, pp. 1-11, 2016.
- [47] H. Xin, K. Zhang, Y. Fu, M. Zhang, Z. Guo, H. He, *et al.*, "Quantization noise and sampling jitter impact of ADC/DAC in multi-IFoF based mobile fronthaul," in *2017 16th International Conference on Optical Communications and Networks (ICOON)*, 2017, pp. 1-3.
- [48] J. Wang, Z. Yu, K. Ying, J. Zhang, F. Lu, M. Xu, *et al.*, "Delta-sigma modulation for digital mobile fronthaul enabling carrier aggregation of 32 4G-LTE / 30 5G-FBMC signals in a single- 10-Gb/s IM-DD channel," in *2016 Optical Fiber Communications Conference and Exhibition (OFC)*, 2016, pp. 1-3.

- [49] L. Cheng, Z. Liang, Z. Ming, W. Jing, C. Lin, and C. Gee-Kung, "A Novel Multi-Service Small-Cell Cloud Radio Access Network for Mobile Backhaul and Computing Based on Radio-Over-Fiber Technologies," *Journal of Lightwave Technology*, vol. 31, pp. 2869-2875, 2013.
- [50] Z. Ming, Z. Liang, W. Jing, C. Lin, L. Cheng, and C. Gee-Kung, "Radio-Over-Fiber Access Architecture for Integrated Broadband Wireless Services," *Journal of Lightwave Technology*, vol. 31, pp. 3614-3620, 2013.
- [51] D. A. A. Mello, A. N. Barreto, F. A. Barbosa, C. Osorio, M. Fiorani, and P. Monti, "Spectrally efficient fronthaul architectures for a cost-effective 5G C-RAN," in *2016 18th International Conference on Transparent Optical Networks (ICTON)*, 2016, pp. 1-5.
- [52] S. H. Cho, H. S. Chung, C. Han, S. Lee, and L. Jong Hyun, "Experimental demonstrations of next generation cost-effective mobile fronthaul with IFoF technique," in *2015 Optical Fiber Communications Conference and Exhibition (OFC)*, 2015, pp. 1-3.
- [53] X. Liu, F. Effenberger, N. Chand, L. Zhou, and H. Lin, "Efficient Mobile Fronthaul Transmission of Multiple LTE-A Signals with 36.86-Gb/s CPRI-Equivalent Data Rate Using a Directly-Modulated Laser and Fiber Dispersion Mitigation," in *Asia Communications and Photonics Conference 2014*, Shanghai, 2014, p. AF4B.5.
- [54] X. Liu, F. Effenberger, N. Chand, Z. Lei, and L. Huafeng, "Demonstration of bandwidth-efficient mobile fronthaul enabling seamless aggregation of 36 E-UTRA-like wireless signals in a single 1.1-GHz wavelength channel," in *2015 Optical Fiber Communications Conference and Exhibition (OFC)*, 2015, pp. 1-3.
- [55] X. Liu, H. Zeng, N. Chand, and F. Effenberger, "Efficient Mobile Fronthaul via DSP-Based Channel Aggregation," *Journal of Lightwave Technology*, vol. 34, pp. 1556-1564, 2016.
- [56] K. Hayasaka, T. Higashino, K. Tsukamoto, and S. Komaki, "A theoretical estimation of IMD on heterogeneous OFDM service over SCM RoF link," in *2011 International Topical Meeting on Microwave Photonics jointly held with the 2011 Asia-Pacific Microwave Photonics Conference*, 2011, pp. 328-330.

- [57] J. Wang, C. Liu, M. Zhu, A. Yi, L. Cheng, and G. Chang, "Investigation of Data-Dependent Channel Cross-Modulation in Multiband Radio-Over-Fiber Systems," *Journal of Lightwave Technology*, vol. 32, pp. 1861-1871, 2014.
- [58] O. Omomukuyo, M. P. Thakur, and J. E. Mitchell, "Experimental demonstration of the impact of MZM non-linearity on direct-detection optical OFDM," in *Wireless Communications and Networking Conference (WCNC), 2012 IEEE*, 2012, pp. 3753-3757.
- [59] W. P. Ng, T. Kanesan, Z. Ghassemlooy, and C. Lu, "Theoretical and Experimental Optimum System Design for LTE-RoF Over Varying Transmission Span and Identification of System Nonlinear Limit," *IEEE Photonics Journal*, vol. 4, pp. 1560-1571, 2012.
- [60] A. J. Lowery, "Fiber nonlinearity pre- and post-compensation for long-haul optical links using OFDM," *Optics Express*, vol. 15, pp. 12965-12970, 2007.
- [61] O. Omomukuyo, M. P. Thakur, and J. E. Mitchell, "Experimental demonstration of digital predistortion for linearization of Mach-Zehnder modulators in direct-detection MB-OFDM ultra-wideband over fiber systems," in *2012 Asia Communications and Photonics Conference (ACP)*, 2012, pp. 1-3.
- [62] A. Napoli, M. Mezghanni, D. Rafique, V. Sleiffer, B. Spinnler, and M. Bohn, "Novel digital pre-distortion techniques for low-extinction ratio Mach-Zehnder modulators," in *Optical Fiber Communication Conference*, 2015, p. Th3G. 1.
- [63] G. Paryanti and D. Sadot, "Predistortion of Mach-Zehnder Modulator Using Symmetric Imbalance," *Journal of Lightwave Technology*, vol. 35, pp. 2757-2768, 2017.
- [64] C. Han, S. H. Cho, H. S. Chung, and J. H. Lee, "Linearity improvement of directly-modulated multi-IF-over-fibre LTE-A mobile fronthaul link using shunt diode predistorter," in *2015 European Conference on Optical Communication (ECOC)*, 2015, pp. 1-3.

- [65] H. Chen, J. Li, K. Xu, Y. Pei, Y. Dai, F. Yin, *et al.*, "Experimental investigation on multi-dimensional digital predistortion for multi-band radio-over-fiber systems," *Optics Express*, vol. 22, pp. 4649-4661, 2014.
- [66] J. Wang, C. Liu, J. Zhang, M. Zhu, M. Xu, F. Lu, *et al.*, "Nonlinear Inter-Band Subcarrier Intermodulations of Multi-RAT OFDM Wireless Services in 5G Heterogeneous Mobile Fronthaul Networks," *Journal of Lightwave Technology*, vol. 34, pp. 4089-4103, 2016.
- [67] C. Han, M. Sung, S. H. Cho, H. S. Chung, S. M. Kim, and J. H. Lee, "Performance Improvement of Multi-IFoF-Based Mobile Fronthaul Using Dispersion-Induced Distortion Mitigation With IF Optimization," *Journal of Lightwave Technology*, vol. 34, pp. 4772-4778, 2016.
- [68] T. S. Rappaport, S. Shu, R. Mayzus, Z. Hang, Y. Azar, K. Wang, *et al.*, "Millimeter Wave Mobile Communications for 5G Cellular: It Will Work!," *IEEE Access*, vol. 1, pp. 335-349, 2013.
- [69] P. Zhouyue and F. Khan, "An introduction to millimeter-wave mobile broadband systems," *IEEE Communications Magazine*, vol. 49, pp. 101-107, 2011.
- [70] C. Dehos, Gonza, x, J. L. Iez, A. De Domenico, Kte, *et al.*, "Millimeter-wave access and backhauling: the solution to the exponential data traffic increase in 5G mobile communications systems?," *Communications Magazine, IEEE*, vol. 52, pp. 88-95, 2014.
- [71] R. J. Weiler, M. Peter, W. Keusgen, E. Calvanese-Strinati, A. D. Domenico, I. Filippini, *et al.*, "Enabling 5G backhaul and access with millimeter-waves," in *2014 European Conference on Networks and Communications (EuCNC)*, 2014, pp. 1-5.
- [72] *mmWave: The Battle of the Bands (White Paper)* [Online]. Available: <http://www.ni.com/white-paper/53096/en/>
- [73] K. Sakaguchi, T. Haustein, S. Barbarossa, E. C. Strinati, A. Clemente, G. Destino, *et al.*, "Where, When, and How mmWave is Used in 5G and Beyond," *IEICE Transactions on Electronics*, vol. 100, pp. 790-808, 2017.

- [74] E. Calvanese Strinati, M. Mueck, A. Clemente, J. Kim, G. Noh, H. Chung, *et al.*, "5GCHAMPION—Disruptive 5G Technologies for Roll-Out in 2018," *ETRI Journal*, vol. 40, pp. 10-25, 2018.
- [75] V. Frascolla, M. Faerber, L. Dussopt, E. Calvanese-Strinati, R. Sauleau, V. Kotzsch, *et al.*, "Challenges and opportunities for millimeter-wave mobile access standardisation," in *Globecom Workshops (GC Wkshps), 2014*, 2014, pp. 553-558.
- [76] *5G Is Now, Part 2: High End Performance from Equipment to Devices and Chipsets* [Online]. Available: <https://news.samsung.com/global/5g-is-now-part-2-high-end-performance-from-equipment-to-devices-and-chipsets>
- [77] *5G and Fixed Wireless Access (Ericsson White Paper)* [Online]. Available: <https://tinyurl.com/ybt6msv4>
- [78] *5G Fixed Wireless Access (Samsung White Paper)* [Online]. Available: <https://tinyurl.com/ybl25rdk>
- [79] *Snapdragon X50 Modem, Qualcomm Inc.* [Online]. Available: <https://www.qualcomm.com/products/snapdragon/modems/5g/x50>
- [80] V. Thomas, M. El-Hajjar, and L. Hanzo, "Millimeter-Wave Radio Over Fiber Optical Upconversion Techniques relying on Link Non-Linearity," *IEEE Communications Surveys & Tutorials*, vol. PP, pp. 1-1, 2015.
- [81] J. Beas, G. Castanon, I. Aldaya, A. Aragon-Zavala, and G. Campuzano, "Millimeter-Wave Frequency Radio over Fiber Systems: A Survey," *IEEE Communications Surveys & Tutorials*, vol. 15, pp. 1593-1619, 2013.
- [82] J. Zhensheng, Y. Jianjun, G. Ellinas, and C. Gee-Kung, "Key Enabling Technologies for Optical-Wireless Networks: Optical Millimeter-Wave Generation, Wavelength Reuse, and Architecture," *Journal of Lightwave Technology*, vol. 25, pp. 3452-3471, 2007.
- [83] J. Zhensheng, Y. Jianjun, H. Yu-Ting, A. Chowdhury, C. Hung-Chang, J. A. Buck, *et al.*, "Multiband Signal Generation and Dispersion-Tolerant Transmission Based on

- Photonic Frequency Tripling Technology for 60-GHz Radio-Over-Fiber Systems," *IEEE Photonics Technology Letters*, vol. 20, pp. 1470-1472, 2008.
- [84] H. Ming-Fang, Y. Jianjun, J. Zhensheng, and C. Gee Kung, "Simultaneous Generation of Centralized Lightwaves and Double/Single Sideband Optical Millimeter-Wave Requiring Only Low-Frequency Local Oscillator Signals for Radio-Over-Fiber Systems," *Lightwave Technology, Journal of*, vol. 26, pp. 2653-2662, 2008.
- [85] T. Shao, E. P. Martin, P. M. Anandarajah, and L. P. Barry, "60-GHz Direct Modulation-Direct Detection OFDM-RoF System Using Gain-Switched Laser," *IEEE Photonics Technology Letters*, vol. 27, pp. 193-196, 2015.
- [86] T. Shao, M. Beltrán, R. Zhou, P. M. Anandarajah, R. Llorente, and L. P. Barry, "60 GHz Radio Over Fiber System Based on Gain-Switched Laser," *Journal of Lightwave Technology*, vol. 32, pp. 3695-3703, 2014.
- [87] E. Martin, C. Browning, L. Barry, A. Farhang, L. Doyle, M. H. Hoang, *et al.*, "28 GHz 5G radio over fibre using UF-OFDM with optical heterodyning," in *2017 International Topical Meeting on Microwave Photonics (MWP)*, 2017, pp. 1-4.
- [88] F. Brendel, J. Poette, B. Cabon, T. Zwick, F. v. Dijk, F. Lelarge, *et al.*, "Chromatic Dispersion in 60 GHz Radio-Over-Fiber Networks Based on Mode-Locked Lasers," *Journal of Lightwave Technology*, vol. 29, pp. 3810-3816, 2011.
- [89] R. Khayatzadeh, H. H. Elwan, J. Poette, and B. Cabon, "Impact of Amplitude Noise in Millimeter-Wave Radio-Over-Fiber Systems," *Journal of Lightwave Technology*, vol. 33, pp. 2913-2919, 2015.
- [90] I. G. Insua, D. Plettemeier, and C. G. Schaffer, "Simple Remote Heterodyne Radio-Over-Fiber System for Gigabit Per Second Wireless Access," *Journal of Lightwave Technology*, vol. 28, pp. 2289-2295, 2010.
- [91] A. H. M. R. Islam, M. Bakaul, A. Nirmalathas, and G. E. Town, "Simplified Generation, Transport, and Data Recovery of Millimeter-Wave Signal in a Full-Duplex Bidirectional Fiber-Wireless System," *IEEE Photonics Technology Letters*, vol. 24, pp. 1428-1430, 2012.

- [92] A. H. M. R. Islam, M. Bakaul, and A. Nirmalathas, "Multilevel Modulations for Gigabit Access in a Simple Millimeter-Wave Radio-Over-Fiber Link," *IEEE Photonics Technology Letters*, vol. 24, pp. 1860-1863, 2012.
- [93] S. A. Khwandah, J. P. Cosmas, I. A. Glover, P. I. Lazaridis, N. R. Prasad, and Z. D. Zaharis, "Direct and External Intensity Modulation in OFDM RoF Links," *Photonics Journal, IEEE*, vol. 7, pp. 1-10, 2015.
- [94] L. Cheng, C. Hung-Chang, G. Zhen, J. Wei, C. Estevez, Y. Jianjun, *et al.*, "Optimization of Vector Signal Delivery Over Double-Sideband Carrier-Suppressed Optical Millimeter-Waves Through DC Coupling," *Photonics Technology Letters, IEEE*, vol. 23, pp. 789-791, 2011.
- [95] Z. Yamei and P. Shilong, "Experimental demonstration of frequency-octupled millimeter-wave signal generation based on a dual-parallel Mach-Zehnder modulator," in *Microwave Workshop Series on Millimeter Wave Wireless Technology and Applications (IMWS), 2012 IEEE MTT-S International*, 2012, pp. 1-4.
- [96] C. Lin, Z. Ming, W. Jing, X. Mu, L. Feng, and C. Gee-Kung, "Photonic Precoding for Millimeter-Wave Multicell MIMO in Centralized RoF System," *Photonics Technology Letters, IEEE*, vol. 26, pp. 1116-1119, 2014.
- [97] Y. Song, G. Wanyi, Y. Aiyang, J. Tao, and W. Chonggang, "A Frequency Quadrupling Optical mm-Wave Generation for Hybrid Fiber-Wireless Systems," *IEEE Journal on Selected Areas in Communications*, vol. 31, pp. 797-803, 2013.
- [98] M. Mohamed, X. Zhang, B. Hraimel, and K. Wu, "Analysis of frequency quadrupling using a single Mach-Zehnder modulator for millimeter-wave generation and distribution over fiber systems," *Optics Express*, vol. 16, pp. 10786-10802, 2008.
- [99] M. P. Thakur, P. Laurencio, M. C. R. Medeiros, and J. E. Mitchell, "Optical frequency tripling with improved suppression and sideband selection," in *Optical Communication (ECOC), 2011 37th European Conference and Exhibition on*, 2011, pp. 1-3.

- [100] Y. Zhao, X. Zheng, H. Wen, and H. Zhang, "Simplified optical millimeter-wave generation configuration by frequency quadrupling using two cascaded Mach–Zehnder modulators," *Optics Letters*, vol. 34, pp. 3250-3252, 2009.
- [101] C. Arellano, H. Louchet, I. Koltchanov, and A. Richter, "Important device limitations of transmitter and receiver concepts when designing 100G transmission systems," in *2009 11th International Conference on Transparent Optical Networks*, 2009, pp. 1-7.
- [102] P. T. Dat, A. Kanno, K. Inagaki, N. Yamamoto, and T. Kawanishi, "High-spectral efficiency millimeter wave-over-fiber system for future mobile fronthaul," in *2015 European Conference on Optical Communication (ECOC)*, 2015, pp. 1-3.
- [103] J. Zhang, M. Xu, J. Wang, F. Lu, L. Cheng, M. Zhu, *et al.*, "Carrier aggregation for MMW inter-RAT and intra-RAT in next generation heterogeneous mobile data network based on optical domain band mapping," in *2015 European Conference on Optical Communication (ECOC)*, 2015, pp. 1-3.
- [104] J. Zhang, M. Xu, J. Wang, F. Lu, L. Cheng, H. Cho, *et al.*, "Full-Duplex Quasi-Gapless Carrier Aggregation Using FBMC in Centralized Radio-Over-Fiber Heterogeneous Networks," *Journal of Lightwave Technology*, vol. 35, pp. 989-996, 2017.
- [105] H. Shams, P. M. Anandarajah, P. Perry, and L. P. Barry, "Optical Generation of Modulated Millimeter Waves Based on a Gain-Switched Laser," *IEEE Transactions on Microwave Theory and Techniques*, vol. 58, pp. 3372-3380, 2010.
- [106] E. P. Martin, S. Tong, V. Vujicic, P. M. Anandarajah, C. Browning, R. Llorente, *et al.*, "25-Gb/s OFDM 60-GHz Radio Over Fiber System Based on a Gain Switched Laser," *Journal of Lightwave Technology*, vol. 33, pp. 1635-1643, 2015.
- [107] R. Khayat-zadeh, J. Poette, H. Rzaigui, and B. Cabon, "Coherent and non-coherent receivers in 60-GHz RoF system based on passively mode-locked laser," in *2013 IEEE International Topical Meeting on Microwave Photonics (MWP)*, 2013, pp. 138-141.

- [108] F. Brendel, T. Zwick, J. Poëtte, and B. Cabon, "PLL-stabilized optical communications in millimeter-wave RoF systems," *IEEE/OSA Journal of Optical Communications and Networking*, vol. 6, pp. 45-53, 2014.
- [109] L. Tao, Z. Dong, J. Yu, N. Chi, J. Zhang, X. Li, *et al.*, "Experimental Demonstration of 48-Gb/s PDM-QPSK Radio-Over-Fiber System Over 40-GHz mm-Wave MIMO Wireless Transmission," *IEEE Photonics Technology Letters*, vol. 24, pp. 2276-2279, 2012.
- [110] A. H. M. R. Islam, M. Bakaul, A. Nirmalathas, and G. E. Town, "Simplification of millimeter-wave radio-over-fiber system employing heterodyning of uncorrelated optical carriers and self-heterodyning of RF signal at the receiver," *Optics Express*, vol. 20, pp. 5707-5724, 2012.
- [111] O. Omomukuyo, M. P. Thakur, and J. E. Mitchell, "Simple 60-GHz MB-OFDM Ultrawideband RoF System Based on Remote Heterodyning," *IEEE Photonics Technology Letters*, vol. 25, pp. 268-271, 2013.
- [112] Y. Tian, K. L. Lee, C. Lim, and A. Nirmalathas, "60 GHz Analog Radio-over-Fiber Fronthaul Investigations," *Journal of Lightwave Technology*, vol. PP, pp. 1-1, 2017.
- [113] H. H. Elwan, R. Khayat-zadeh, J. Poëtte, and B. Cabon, "Impact of Relative Intensity Noise on 60-GHz Radio-Over-Fiber Wireless Transmission Systems," *Journal of Lightwave Technology*, vol. 34, pp. 4751-4757, 2016.
- [114] S. Tong, F. Paresys, G. Maury, Y. Le Guennec, and B. Cabon, "Investigation on the Phase Noise and EVM of Digitally Modulated Millimeter Wave Signal in WDM Optical Heterodyning System," *Journal of Lightwave Technology*, vol. 30, pp. 876-885, 2012.
- [115] T. Shao, E. Martin, P. M. Anandarajah, C. Browning, V. Vujicic, R. Llorente, *et al.*, "Chromatic Dispersion-Induced Optical Phase Decorrelation in a 60 GHz OFDM-RoF System," *IEEE Photonics Technology Letters*, vol. 26, pp. 2016-2019, 2014.
- [116] G. Qi, J. Yao, J. Seregelyi, S. Paquet, C. Belisle, X. Zhang, *et al.*, "Phase-Noise Analysis of Optically Generated Millimeter-Wave Signals With External Optical Modulation Techniques," *Journal of Lightwave Technology*, vol. 24, pp. 4861-4875, 2006.

- [117] L. Fan, L. Xinying, Z. Junwen, Y. Jianjun, and C. Zizheng, "Fiber-Wireless-Fiber Link for DFT-Spread OFDM Signal Transmission at W-Band," *IEEE Photonics Technology Letters*, vol. 27, pp. 1273-1276, 2015.
- [118] L. Che-Hao, W. Meng-Fan, L. Chi-Hsiang, and L. Chun-Ting, "W-band OFDM RoF system with simple envelope detector down-conversion," in *Optical Fiber Communications Conference and Exhibition (OFC)*, 2015, pp. 1-3.
- [119] M. A. Hameed and H. Rongqing, "Simplified RF Carrier Extraction and Reuse in OFDM Radio-Over-Fiber Systems," *IEEE Photonics Technology Letters*, vol. 26, pp. 1734-1737, 2014.
- [120] C. Chang-Soon, Y. Shoji, and H. Ogawa, "Millimeter-Wave Fiber-Fed Wireless Access Systems Based on Dense Wavelength-Division-Multiplexing Networks," *IEEE Transactions on Microwave Theory and Techniques*, vol. 56, pp. 232-241, 2008.
- [121] P. T. Dat, A. Kanno, N. Yamamoto, and T. Kawanishi, "Simultaneous transmission of 4G LTE-A and wideband MMW OFDM signals over fiber links," in *2016 IEEE International Topical Meeting on Microwave Photonics (MWP)*, 2016, pp. 87-90.
- [122] M. N. Sakib, B. Hraimel, X. Zhang, M. Mohamed, W. Jiang, K. Wu, *et al.*, "Impact of Optical Transmission on Multiband OFDM Ultra-Wideband Wireless System With Fiber Distribution," *Journal of Lightwave Technology*, vol. 27, pp. 4112-4123, 2009.
- [123] P. Wei-Ren, "Analysis of Laser Phase Noise Effect in Direct- Detection Optical OFDM Transmission," *Lightwave Technology, Journal of*, vol. 28, pp. 2526-2536, 2010.
- [124] M. Sakib, B. Hraimel, X. Zhang, K. Wu, T. Liu, T. Xu, *et al.*, "Impact of Laser Relative Intensity Noise on a Multiband OFDM Ultrawideband Wireless Signal Over Fiber System," *IEEE/OSA Journal of Optical Communications and Networking*, vol. 2, pp. 841-847, 2010.
- [125] B. Farhang-Boroujeny, "Filter bank multicarrier modulation: A waveform candidate for 5G and beyond," *Advances in Electrical Engineering*, vol. 2014, 2014.

- [126] M. Xu, J. Zhang, F. Lu, J. Wang, L. Cheng, H. J. Cho, *et al.*, "FBMC in Next-Generation Mobile Fronthaul Networks With Centralized Pre-Equalization," *IEEE Photonics Technology Letters*, vol. 28, pp. 1912-1915, 2016.
- [127] *VPI Photonic Inc. Simulation Guide* [Online]. Available: <http://www.vpiphotonics.com>
- [128] J. Yao, "Microwave Photonics," *Journal of Lightwave Technology*, vol. 27, pp. 314-335, 2009.
- [129] A. Sahin, I. Guvenc, and H. Arslan, "A Survey on Multicarrier Communications: Prototype Filters, Lattice Structures, and Implementation Aspects," *IEEE Communications Surveys & Tutorials*, vol. 16, pp. 1312-1338, 2014.
- [130] H. Lin and P. Siohan, "OFDM/OQAM with Hermitian Symmetry: Design and Performance for Baseband Communication," in *2008 IEEE International Conference on Communications*, 2008, pp. 652-656.
- [131] M. Xu, J. Zhang, F. Lu, Y. Wang, D. Guidotti, and G. K. Chang, "Investigation of FBMC in mobile fronthaul networks for 5G wireless with time-frequency modulation adaptation," in *2016 Optical Fiber Communications Conference and Exhibition (OFC)*, 2016, pp. 1-3.
- [132] J. Wang, Z. Yu, K. Ying, J. Zhang, F. Lu, M. Xu, *et al.*, "Delta-sigma modulation for digital mobile fronthaul enabling carrier aggregation of 32 4G-LTE / 30 5G-FBMC signals in a single- λ 10-Gb/s IM-DD channel," in *2016 Optical Fiber Communications Conference and Exhibition (OFC)*, 2016, pp. 1-3.
- [133] F. Schaich and T. Wild, "Waveform contenders for 5G ; OFDM vs. FBMC vs. UFMC," in *Communications, Control and Signal Processing (ISCCSP), 2014 6th International Symposium on*, 2014, pp. 457-460.
- [134] B. Farhang-Boroujeny and H. Moradi, "OFDM Inspired Waveforms for 5G," *IEEE Communications Surveys & Tutorials*, vol. 18, pp. 2474-2492, 2016.
- [135] M. Renfors, P. Siohan, B. Farhang-Boroujeny, and F. Bader, "Filter Banks for Next Generation Multicarrier Wireless Communications," *EURASIP Journal on Advances in Signal Processing*, vol. 2010, p. 314193, May 31 2010.

- [136] D. L. R. M. Bellanger, D. Roviras, M. Terré, J. Nossek, L. Baltar, Q. Bai, D. Waldhauser, M. Renfos and T. Ihalainen, "FBMC Physical Layer: A Primer," Technical Report 2010.
- [137] B. Saltzberg, "Performance of an Efficient Parallel Data Transmission System," *IEEE Transactions on Communication Technology*, vol. 15, pp. 805-811, 1967.
- [138] M. G. Bellanger, "Specification and design of prototype filter for filter bank based multicarrier transmission," in *IEEE International Conference on Acoustic, Speech and Signal Processing*, ed USA: Salt Lake City, 2001.
- [139] B. F. Boroujeny, "OFDM versus filter bank multicarrier," *IEEE Signal Process. Mag.*, vol. 28, 2011.
- [140] S. Mirabbasi and K. Martin, "Overlapped complex-modulated transmultiplexer filters with simplified design and superior stopbands," *IEEE Transactions on Circuits and Systems II: Analog and Digital Signal Processing*, vol. 50, pp. 456-469, 2003.
- [141] H. Zhang, D. Le Ruyet, D. Roviras, Y. Medjahdi, and H. Sun, "Spectral Efficiency Comparison of OFDM/FBMC for Uplink Cognitive Radio Networks," *EURASIP Journal on Advances in Signal Processing*, vol. 2010, p. 621808, February 21 2010.
- [142] C. Lélé, J. P. Javaudin, R. Legouable, A. Skrzypczak, and P. Siohan, "Channel estimation methods for preamble-based OFDM/OQAM modulations," *European Transactions on Telecommunications*, vol. 19, pp. 741-750, 2008.
- [143] E. Kofidis, D. Katselis, A. Rontogiannis, and S. Theodoridis, "Preamble-based channel estimation in OFDM/OQAM systems: A review," *Signal Processing*, vol. 93, pp. 2038-2054, 2013.
- [144] S. Hu, G. Wu, T. Li, Y. Xiao, and S. Li, "Preamble Design with ICI Cancellation for Channel Estimation in OFDM/OQAM System," *IEICE Transactions on Communications*, vol. E93.B, pp. 211-214, 2010.
- [145] D. Na and K. Choi, "Low PAPR FBMC," *IEEE Transactions on Wireless Communications*, vol. 17, pp. 182-193, 2018.

- [146] C. An, B. Kim, and H.-G. Ryu, "Waveform comparison and nonlinearity sensitivities of FBMC, UFMC and W-OFDM systems," in *8 th International Conference on Networks & Communications*, 2016, pp. 83-90.
- [147] S. S. K. C. Bulusu, H. Shaiek, D. Roviras, and R. Zayani, "Reduction of PAPR for FBMC-OQAM systems using dispersive SLM technique," in *2014 11th International Symposium on Wireless Communications Systems (ISWCS)*, 2014, pp. 568-572.
- [148] T. Ihalainen, A. Viholainen, T. H. Stitz, M. Renfors, and M. Bellanger, "Filter bank based multi-mode multiple access scheme for wireless uplink," in *2009 17th European Signal Processing Conference*, 2009, pp. 1354-1358.
- [149] S. K. C. Bulusu, H. Shaiek, and D. Roviras, "Potency of trellis-based SLM over symbol-by-symbol approach in reducing PAPR for FBMC-OQAM signals," in *Communications (ICC), 2015 IEEE International Conference on*, 2015, pp. 4757-4762.
- [150] H. Wang, X. Wang, L. Xu, and W. Du, "Hybrid PAPR Reduction Scheme for FBMC/OQAM Systems Based on Multi Data Block PTS and TR Methods," *IEEE Access*, vol. 4, pp. 4761-4768, 2016.
- [151] I. Aldaya, G. Campuzano, G. Castañón, and C. Gosset, "Phase noise insensitivity of RF envelope detection and its application to OFDM radio over fiber systems," *Optics & Laser Technology*, vol. 58, pp. 139-144, 2014.
- [152] P. T. Dat, A. Kanno, N. Yamamoto, and T. Kawanishi, "Full-Duplex Transmission of LTE-A Carrier Aggregation Signal Over a Bidirectional Seamless Fiber-Millimeter-Wave System," *Journal of Lightwave Technology*, vol. 34, pp. 691-700, 2016.
- [153] P. T. Dat, A. Kanno, K. Inagaki, and T. Kawanishi, "High-Capacity Wireless Backhaul Network Using Seamless Convergence of Radio-over-Fiber and 90-GHz Millimeter-Wave," *Journal of Lightwave Technology*, vol. 32, pp. 3910-3923, 2014.
- [154] S. Abramowitz, *Handbook of Mathematical Functions with Formulas, Graphs and Mathematical Tables*.

- [155] H. M. Cheema, "Flexible phase-locked loops and millimeter wave PLL components for 60-GHz wireless networks in CMOS," 2010.
- [156] C. Lim, A. Nirmalathas, M. Bakaul, P. Gamage, K. L. Lee, Y. Yang, *et al.*, "Fiber-Wireless Networks and Subsystem Technologies," *Journal of Lightwave Technology*, vol. 28, pp. 390-405, 2010.
- [157] T. Fusco, A. Petrella, and M. Tanda, "Data-aided symbol timing and CFO synchronization for filter bank multicarrier systems," *IEEE Transactions on Wireless Communications*, vol. 8, pp. 2705-2715, 2009.
- [158] B. Aziz and F. Elbahhar, "Impact of frequency synchronization errors on BER performance of MB-OFDM UWB in Nakagami channels," in *2015 IEEE International Conference on Communications (ICC)*, 2015, pp. 2698-2703.
- [159] G. H. Nguyen, B. Cabon, and Y. L. Guennec, "Generation of 60-GHz MB-OFDM Signal-Over-Fiber by Up-Conversion Using Cascaded External Modulators," *Journal of Lightwave Technology*, vol. 27, pp. 1496-1502, 2009.
- [160] J. Li, T. Ning, L. Pei, C. Qi, X. Hu, and Q. Zhou, "Photonic frequency-quadrupling scheme for millimeter-wave generation by employing feed-forward modulation technique," *Optics Express*, vol. 18, pp. 2503-2508, 2010.
- [161] S. Yu, W. Gu, A. Yang, T. Jiang, and C. Wang, "A Frequency Quadrupling Optical mm-Wave Generation for Hybrid Fiber-Wireless Systems," *IEEE Journal on Selected Areas in Communications*, vol. 31, pp. 797-803, 2013.
- [162] L. Huizi, H. Tianye, K. Changjian, F. Songnian, P. P. Shum, and L. Deming, "Photonic Generation of Frequency-Quadrupled Microwave Signal With Tunable Phase Shift," *IEEE Photonics Technology Letters*, vol. 26, pp. 220-223, 2014.
- [163] M. Mohamed, X. Zhang, B. Hraimel, and K. Wu, "Frequency sixupler for millimeter-wave over fiber systems," *Optics Express*, vol. 16, pp. 10141-10151, 2008.
- [164] S. Po-Tsung, J. Chen, L. Chun-Ting, J. Wen-Jr, H. Han-Sheng, P. Peng-Chun, *et al.*, "Optical Millimeter-Wave Signal Generation Via Frequency 12-Tupling," *Journal of Lightwave Technology*, vol. 28, pp. 71-78, 2010.

- [165] W. R. Peng, "Analysis of Laser Phase Noise Effect in Direct- Detection Optical OFDM Transmission," *Journal of Lightwave Technology*, vol. 28, pp. 2526-2536, 2010.
- [166] X. Liu, H. Zeng, N. Chand, and F. Effenberger, "Experimental demonstration of high-throughput low-latency mobile fronthaul supporting 48 20-MHz LTE signals with 59-Gb/s CPRI-equivalent rate and 2- μ s processing latency," in *2015 European Conference on Optical Communication (ECOC)*, 2015, pp. 1-3.
- [167] A. H. M. R. Islam, M. Bakaul, A. Nirmalathas, and G. E. Town, "Millimeter-Wave Radio-Over-Fiber System Based on Heterodyned Unlocked Light Sources and Self-Homodyned RF Receiver," *IEEE Photonics Technology Letters*, vol. 23, pp. 459-461, 2011.
- [168] X. Liu and F. Buchali, "Intra-symbol frequency-domain averaging based channel estimation for coherent optical OFDM," *Optics Express*, vol. 16, pp. 21944-21957, 2008.
- [169] P. Gallion and G. Debarge, "Quantum phase noise and field correlation in single frequency semiconductor laser systems," *IEEE Journal of Quantum Electronics*, vol. 20, pp. 343-349, 1984.
- [170] R. Tkach and A. Chraplyvy, "Phase noise and linewidth in an InGaAsP DFB laser," *Journal of Lightwave Technology*, vol. 4, pp. 1711-1716, 1986.
- [171] P. Gallion, F. J. Mendieta, and R. Leconte, "Single-frequency laser phase-noise limitation in single-mode optical-fiber coherent-detection systems with correlated fields," *Journal of the Optical Society of America*, vol. 72, pp. 1167-1170, 1982.
- [172] M. R. Salehi and B. Cabon, "Theoretical and experimental analysis of influence of phase-to-intensity noise conversion in interferometric systems," *Journal of Lightwave Technology*, vol. 22, pp. 1510-1518, 2004.
- [173] U. Gliese, S. Norskov, and T. N. Nielsen, "Chromatic dispersion in fiber-optic microwave and millimeter-wave links," *IEEE Transactions on Microwave Theory and Techniques*, vol. 44, pp. 1716-1724, 1996.

- [174] W. K. Marshall, B. Crosignani, and A. Yariv, "Laser phase noise to intensity noise conversion by lowest-order group-velocity dispersion in optical fiber: exact theory," *Optics Letters*, vol. 25, pp. 165-167, 2000.
- [175] C. C. Wei and J. Chen, "Study on dispersion-induced phase noise in an optical OFDM radio-over-fiber system at 60-GHz band," *Optics Express*, vol. 18, pp. 20774-20785, 2010.
- [176] I. Aldaya, G. Campuzano, G. Castanon, *et al.*, "A Tutorial on Optical Feeding of Millimeter-Wave Phased Array Antennas for Communication Applications," *International Journal of Antennas and Propagation*, vol. 2015, p. 22, 2015.
- [177] R. A. Shafik, S. Rahman, and R. Islam, "On the Extended Relationships Among EVM, BER and SNR as Performance Metrics," in *Electrical and Computer Engineering, 2006. ICECE '06. International Conference on*, 2006, pp. 408-411.
- [178] Y. Luo, X. Zhou, F. Effenberger, X. Yan, G. Peng, Y. Qian, *et al.*, "Time- and Wavelength-Division Multiplexed Passive Optical Network (TWDM-PON) for Next-Generation PON Stage 2 (NG-PON2)," *Journal of Lightwave Technology*, vol. 31, pp. 587-593, 2013.
- [179] M. Milosavljevic, M. P. Thakur, P. Kourtessis, J. E. Mitchell, and J. M. Senior, "Demonstration of Wireless Backhauling Over Long-Reach PONs," *Journal of Lightwave Technology*, vol. 30, pp. 811-817, 2012.
- [180] S. L. Jansen, I. Morita, T. C. W. Schenk, N. Takeda, and H. Tanaka, "Coherent Optical 25.8-Gb/s OFDM Transmission Over 4160-km SSMF," *Lightwave Technology, Journal of*, vol. 26, pp. 6-15, 2008.
- [181] A. G. Armada and M. Calvo, "Phase noise and sub-carrier spacing effects on the performance of an OFDM communication system," *IEEE Communications Letters*, vol. 2, pp. 11-13, 1998.
- [182] V. Moles-Cases, A. A. Zaidi, X. Chen, T. J. Oechtering, and R. Baldemair, "A comparison of OFDM, QAM-FBMC, and OQAM-FBMC waveforms subject to phase noise," in *2017 IEEE International Conference on Communications (ICC)*, 2017, pp. 1-6.

- [183] Q. Yang, N. Kaneda, X. Liu, and W. Shieh, "Demonstration of Frequency-Domain Averaging Based Channel Estimation for 40-Gb/s CO-OFDM With High PMD," *IEEE Photonics Technology Letters*, vol. 21, pp. 1544-1546, 2009.
- [184] J. G. Andrews, S. Buzzi, C. Wan, S. V. Hanly, A. Lozano, A. C. K. Soong, *et al.*, "What Will 5G Be?," *IEEE Journal on Selected Areas in Communications*, vol. 32, pp. 1065-1082, 2014.
- [185] F. Boccardi, R. W. Heath, A. Lozano, T. L. Marzetta, and P. Popovski, "Five disruptive technology directions for 5G," *IEEE Communications Magazine*, vol. 52, pp. 74-80, 2014.
- [186] Y. m. Lin and P. I. Tien, "Next-generation OFDMA-based passive optical network architecture supporting radio-over-fiber," *IEEE Journal on Selected Areas in Communications*, vol. 28, pp. 791-799, 2010.
- [187] N. Zhang, S. Zhang, S. Wu, J. Ren, J. W. Mark, and X. Shen, "Beyond Coexistence: Traffic Steering in LTE Networks with Unlicensed Bands," *IEEE Wireless Communications*, vol. 23, pp. 40-46, 2016.
- [188] T. Jiang and Y. Wu, "An Overview: Peak-to-Average Power Ratio Reduction Techniques for OFDM Signals," *IEEE Transactions on Broadcasting*, vol. 54, pp. 257-268, 2008.
- [189] H. Ochiai and H. Imai, "Performance analysis of deliberately clipped OFDM signals," *IEEE Transactions on Communications*, vol. 50, pp. 89-101, 2002.
- [190] H. Ochiai and H. Imai, "On the distribution of the peak-to-average power ratio in OFDM signals," *IEEE Transactions on Communications*, vol. 49, pp. 282-289, 2001.
- [191] T. Araujo and R. Dinis, "On the Accuracy of the Gaussian Approximation for the Evaluation of Nonlinear Effects in OFDM Signals," *IEEE Transactions on Communications*, vol. 60, pp. 346-351, 2012.
- [192] E. Zentner and S. Z. Pilinsky, "Performance limitations in an OFDM system due to non-linearities," in *2009 International Symposium ELMAR*, 2009, pp. 255-258.

- [193] H. Bouhadda, H. Shaiek, D. Roviras, R. Zayani, Y. Medjahdi, and R. Bouallegue, "Theoretical analysis of BER performance of nonlinearly amplified FBMC/OQAM and OFDM signals," *EURASIP Journal on Advances in Signal Processing*, vol. 2014, p. 60, May 05 2014.
- [194] G. U. Maheswari, A. Govindasamy, and S. J. Thiruvengadam, "Performance analysis of filter bank multicarrier system with non-linear high power amplifiers for 5G wireless networks," *IET Signal Processing*, vol. 11, pp. 66-72, 2017.
- [195] M. Van Eeckhaute, A. Bourdoux, P. De Doncker, and F. Horlin, "Performance of emerging multi-carrier waveforms for 5G asynchronous communications," *EURASIP Journal on Wireless Communications and Networking*, vol. 2017, p. 29, February 07 2017.
- [196] Y. P. E. Wang, X. Lin, A. Adhikary, A. Grovlen, Y. Sui, Y. Blankenship, *et al.*, "A Primer on 3GPP Narrowband Internet of Things," *IEEE Communications Magazine*, vol. 55, pp. 117-123, 2017.
- [197] A. Aminjavaheri, A. Farhang, A. RezazadehReyhani, and B. Farhang-Boroujeny, "Impact of timing and frequency offsets on multicarrier waveform candidates for 5G," in *2015 IEEE Signal Processing and Signal Processing Education Workshop (SP/SPE)*, 2015, pp. 178-183.
- [198] A. H. M. R. Islam, M. Bakaul, A. Nirmalathas, and G. E. Town, "Simplified Generation, Transport, and Data Recovery of Millimeter-Wave Signal in a Full-Duplex Bidirectional Fiber-Wireless System," *Photonics Technology Letters, IEEE*, vol. 24, pp. 1428-1430, 2012.
- [199] A. H. M. R. Islam, M. Bakaul, A. Nirmalathas, and G. E. Town, "Millimeter-Wave Radio-Over-Fiber System Based on Heterodyned Unlocked Light Sources and Self-Homodyned RF Receiver," *Photonics Technology Letters, IEEE*, vol. 23, pp. 459-461, 2011.
- [200] A. T. Latunde, M. Milosavljevic, P. Kourtessis, and J. Senior, "OQAM-OFDM RoF with IM-DD remote heterodyne 28 GHz upconversion for 5G millimeter RANs," in *2016 18th International Conference on Transparent Optical Networks (ICTON)*, 2016, pp. 1-4.

- [201] P. T. Dat, A. Kanno, N. Yamamoto, and T. Kawanishi, "Simultaneous transmission of multi-RATs and mobile fronthaul in the MMW bands over an IFoF system," in *2017 Optical Fiber Communications Conference and Exhibition (OFC)*, 2017, pp. 1-3.
- [202] T. S. Rappaport, S. Shu, R. Mayzus, Z. Hang, Y. Azar, K. Wang, *et al.*, "Millimeter Wave Mobile Communications for 5G Cellular: It Will Work!," *Access, IEEE*, vol. 1, pp. 335-349, 2013.
- [203] A. Checko, H. L. Christiansen, Y. Yan, L. Scolari, G. Kardaras, M. S. Berger, *et al.*, "Cloud RAN for Mobile Networks -A Technology Overview," *IEEE Communications Surveys & Tutorials*, vol. 17, pp. 405-426, 2015.
- [204] A. I. Sulyman, A. T. Nassar, M. K. Samimi, G. R. Maccartney, T. S. Rappaport, and A. Alsanie, "Radio propagation path loss models for 5G cellular networks in the 28 GHZ and 38 GHZ millimeter-wave bands," *IEEE Communications Magazine*, vol. 52, pp. 78-86, 2014.
- [205] T. S. Rappaport, F. Gutierrez, E. Ben-Dor, J. N. Murdock, Y. Qiao, and J. I. Tamir, "Broadband Millimeter-Wave Propagation Measurements and Models Using Adaptive-Beam Antennas for Outdoor Urban Cellular Communications," *IEEE Transactions on Antennas and Propagation*, vol. 61, pp. 1850-1859, 2013.
- [206] Y. Azar, G. N. Wong, K. Wang, R. Mayzus, J. K. Schulz, H. Zhao, *et al.*, "28 GHz propagation measurements for outdoor cellular communications using steerable beam antennas in New York city," in *2013 IEEE International Conference on Communications (ICC)*, 2013, pp. 5143-5147.
- [207] T. H. Nguyen, J. Louveaux, S. P. Gorza, and F. Horlin, "Simple Feedforward Carrier Phase Estimation for Optical FBMC/OQAM Systems," *IEEE Photonics Technology Letters*, vol. 28, pp. 2823-2826, 2016.
- [208] S. Liu, M. Xu, J. Wang, F. Lu, W. Zhang, H. Tian, *et al.*, "A Multilevel Artificial Neural Network Nonlinear Equalizer for Millimeter-Wave Mobile Fronthaul Systems," *Journal of Lightwave Technology*, vol. 35, pp. 4406-4417, 2017.

- [209] H. Ye, G. Y. Li, and B. H. Juang, "Power of Deep Learning for Channel Estimation and Signal Detection in OFDM Systems," *IEEE Wireless Communications Letters*, vol. 7, pp. 114-117, 2018.